Elucidating Reaction Kinetics with Time-Resolved Frequency Comb Spectroscopy

by

Bryce J. Bjork

B.A., Gustavus Adolphus College, 2011

A thesis submitted to the

Faculty of the Graduate School of the

University of Colorado in partial fulfillment

of the requirements for the degree of

Doctor of Philosophy

Department of Physics

2017

This thesis entitled:

Elucidating Reaction Kinetics with Time-Resolved Frequency Comb Spectroscopy

written by Bryce J. Bjork

has been approved for the Department of Physics

_____

Jun Ye

_____

Carl Lineberger

Date _____

The final copy of this thesis has been examined by the signatories, and we find that both the content and the form meet acceptable presentation standards of scholarly work in the above mentioned discipline.

Bjork, Bryce J. (Ph.D., Physics)

Elucidating Reaction Kinetics with Time-Resolved Frequency Comb Spectroscopy

Thesis directed by Prof. Jun Ye

The kinetics of the hydroxyl radical (OH) + carbon monxide (CO) reaction, which is fundamental to both atmospheric and combustion chemistry, are complex because of the formation of the hydrocarboxyl radical (HOCO) intermediate. Despite extensive studies of this reaction, HOCO has not been observed under thermal reaction conditions. In this thesis, we report the development of a sensitive and multiplexed technique, time-resolved frequency comb spectroscopy (TRFCS) for the observation of reactive chemical intermediates on the microsecond timescale. Using this technique, we observed deuteroxyl radical (OD) + CO reaction kinetics and detected all relevant reactants and products. By simultaneously measuring the time-dependent concentrations of the OD, *trans*-DOCO, *cis*-DOCO and CO_2, we observed unambiguous low-pressure termolecular dependence of the reaction rate coefficients for N_2 and CO bath gases. These results confirm the HOCO formation mechanism and quantify its yield. Additionally, we observed *cis*-DOCO $\rightleftharpoons$ *trans*-DOCO isomerization and quantified its rate.

Dedication

To my family, for their love and support

Acknowledgements

My interest in physics and mathematics began at a young age. My parents always encouraged me to explore and understand the world. This only increased in the high school classroom of Dennis Symalla. His unique style of teaching conveyed his excitement and passion for physics, pushing us to think critically about the world in which we live. After his classes, the decision to pursue an undergraduate degree in physics was easy. During my undergraduate experience at Gustavus Adolphus College, I had the opportunity to work with a few excellent professors. In particular, I'd like to thank Thomas Huber and Steven Mellema for sharing their knowledge, enthusiasm, and laboratory skills. My interest in optics began midway though college, but I really began my experimental optics at Caltech, as part of the LIGO SURF program. During this experience, I had the opportunity to work with Eric Black and Greg Ogin, who were excellent instructors.

During my time at JILA, I've had the opportunity to work with quite a few amazing people. First and foremost, I am truly grateful for the opportunity to work with Jun. He inspires a laboratory atmosphere of collaboration and innovation, with a driving urgency to solve the problem at hand. I am constantly astounded by his ability to simultaneously manage so many different projects yet maintain a laser-like focus in all of them. Most importantly, however, it is clear that he truly cares about his students and post-docs. I've learned a great deal from Jun about experimental physics, experience that will prove invaluable wherever life takes me.

When I joined the lab, I had the opportunity to work with Alexandra Foltynowicz, Piotr Maslowski, Adam Fleisher, Ben Spaun, and Oliver Heckl on the mid-infrared team, who helped teach me the basics of frequency comb spectroscopy. On the extreme ultraviolet team, I overlapped with Tom Allison, Arman Cingoz, Craig Benko, Francois Labaye, and Linqiang Hua. I am grate-

ful for discussions with all of them - their unique perspectives were very valuable. Additionally, I had the pleasure of interacting with Jan Hall, who was always willing to share his knowledge and enthusiasm. I would like to thank Travis Nicholson, Ben Bloom, Ross Hutson, Toby Bothwell, Wei Zhang, Matt Grau, Will Cairncross, Ed Marti, Shimon Kolkowitz, Dave Reens, Alejandra Collopy, Matt Hummon, Mark Yao, Kevin Cossel, Dan Gresh, Yuval Shagam, and all of the other members of the Ye group with whom I've overlapped.

I would like to thank the current members of the mid-infrared and extreme ultraviolet teams, Thinh Bui, Bryan Changala, Kana Iwakuni, Gil Porat, Christoph Heyl, and Steven Schoun, for excellent discussions. It is clear to me that the future of the group is in good hands. I would like to give a special thanks to Thinh Bui and Oliver Heckl, who have been great friends and colleagues. Thinh has a very broad understanding of chemistry and a unique ability to find problems that are both interesting and technically accessible. Combined with his genial personality and strong work ethic, he is a force to be reckoned with. Oliver was a constant pleasure to have in the lab. His optics expertise and consistently positive outlook brightened the lab's atmosphere.

JILA would not be what it is today without its staff shops. I'd like to thank the staff of the machine and electronics shop, particularly Hans Green, Terry Brown, and Kim Hagen, for sharing their technical expertise, enthusiasm, and positive outlook. I'd like to thank J.R. Raith from the computing department for helping to sort out strange computer issues.

There are a few people outside the lab who I'd like to thank for helping me maintain sanity during the difficulties of grad school. Adam Reed, Steven Moses, Karl Mayer, Adam Keith, Dan Palken, Travis Autry, Felix Vietmeyer, and many others who I have not mentioned have been great friends and activity partners throughout my graduate career.

Finally, I'd like to thank my family for supporting me on this journey. I would not be where I am without them.

Contents

List of Figures

List of Tables

Chapter 1

Introduction

The characterization of chemical reactions has always been a difficult task, placing stringent requirements on instrumentation and techniques. Clean experimental data require low reactant concentrations to avoid secondary reactions, producing even lower concentrations of the reaction products. These reactions reach completion on short timescales, in the μs range for bimolecular processes and approaching the fs level for unimolecular processes. As our understanding of chemical reactions has grown, we have learned that many chemical processes that were previously thought to be bimolecular actually involve bound intermediate species whose signatures are manifested by complex temperature and pressure dependencies[1, 2, 3, 4]. To fully understand these reactions requires the simultaneous detection of many molecules, which is difficult using traditional kinetics techniques.

The carbonylation of hydroxyl radical, $OH + CO \rightarrow H + CO_2$, is one such reaction which has been known since the early 1970s to exhibit complex product branching. Interest in this reaction due to the reaction's importance in atmsopheric and combustion processes has stimulated many experimental and theoretical efforts. One main experimental technique that has been commonly employed in its study is fluorescence spectroscopy; the time-dependent concentration of hydroxyl radical is detected through its fluorescence. The OH+CO reaction rate is then determined by varying the CO concentration and observing its change on the OH loss rate. The primary advantage of this technique is its sensitivity, with detection limits lower than 10^9 molecules cm^{-3}[5], with μs time resolution. However, this technique has two major drawbacks. First, it cannot be applied

to every molecule - there are many chemical intermediate species that do not have convenient fluorescent transitions. In many cases, such as in the OH+CO reaction, this precludes access to critical mechanistic detail, such as branching kinetics. Second, absolute concentrations can be accessed in this manner, but require cumbersome calibration. Even so, this technique has been a workhorse for kinetics measurements for many years and the tabulated OH+CO termolecular reaction rates are entirely determined in this manner[6].

It's not that supplementary techniques do not exist. Step-scan Fourier Transform Infrared (FTIR) has also been used for the determination of reaction rates, which has demonstrated simultaneous access to many molecular species, at μs temporal resolution[7]. However, this technique trades off spectral resolution for sensitivity, with one study achieving a CH_2OO molecular sensitivity of 10^{13} molecules cm^{-3} and 12.5 μs time resolution at the expense of 1 cm^{-1} spectral resolution[8]. On the other hand, highly-sensitive techniques such as cw (continuous-wave) cavity ring-down spectroscopy are able to capture events on the μs timescale, but require scanning over a broad range to capture all species relevant to the reaction[9].

In this thesis, we present a technique to bridge this gap, time-resolved frequency comb spectroscopy, which utilizes the broad bandwidth and spatiotemporal coherence of the optical frequency comb to provide simultaneous access to reactants and products with high molecular sensitivity and μs time resolution[10]. The optical frequency comb, described in Chapter 2, has broad success in frequency metrology, chemical sensing, as well as rf generation. Moreover, many of the components necessary for the study of chemical reactions have already been independently demonstrated in the near-infrared. Broadband molecular spectroscopy of multiple trace gases and the ability to accurately determine their concentrations has been shown for FTIR[11], VIPA[12], and dual-comb[13, 14] detection techniques. The enhancement of molecular sensitivity using an optical enhancement cavity has also been demonstrated[15].

However, molecular absorption cross-sections in the near-infrared are weak, as they mostly consist of combination bands. Therefore, it is necessary to move to the mid-infrared "molecular fingerprint region", above 3 μs, which brings larger absorption cross-sections at the cost of technical

complexity. Laser sources, dielectric coatings, and detection techniques are all significantly less developed and significantly more expensive than their telecom ($\leq$ 1.5 μm) brethren. Common devices which are readily available in the near-infrared such as electro-optic modulators (EOMs) and acousto-optic modulators (AOMs) are still in their infancy. Even alignment and characterization of optical beams requires more time and care, since the invisible beams cannot be detected on fluorescent cards or CCDs. Instead, thermal paper and microbolometer cameras are used, which have slow response times (seconds) and poor detection sensitivities.

Even so, mid-infrared time-resolved frequency comb spectroscopy is already very useful and its utility will continue to grow with mid-infrared instrumentation. The specifics of the technique are described in Chapter 3. Briefly, the technique consists of a 3-5 μm mid-infrared frequency comb source, an optical absorption enhancement cavity, and a spatially-dispersive spectrometer based on the virtually-imaged phased array (VIPA). This technique is first applied to the study of acrylic acid photodissociation, which produces the *trans*-HOCO radical intermediate of the OH+CO reaction.

The atmospheric and combustion implications of OH+CO chemistry are introduced in Chapter 4, along with a brief account of its experimental history. The experimental approach for OH generation, O_3 photolysis, is also introduced. The main results of this thesis are presented in Chapters 5 and 6, in which the absolute concentrations of OD, *trans*-DOCO, *cis*-DOCO, and CO_2 are directly detected from the OD+CO reaction, allowing for the unambiguous determination of reaction branching rates. Additionally, *cis* $\rightleftharpoons$ *trans* isomerization is observed for the first time, illustrating the rich dynamics possible in this system. Finally, Chapter 7 concludes the work and presents an outlook for future investigations.

Chapter 2

Frequency Combs and Molecular Spectroscopy

The development of the optical frequency comb in the 1990s and early 2000s by John Hall[16] and Theodore Hänsch[17] has permitted many new applications including metrology, laser ranging, and absorption spectroscopy. Indeed, we are even now adding new applications to this list. Extensive review articles[18, 19, 20], theses[21, 22, 23, 24] and books[25] exist describing the operation and application of the comb. To understand why the frequency comb has become such a useful tool, it is illustrative to look at its properties in both the time and frequency domain. The frequency comb can be understood in the time domain as a stabilized train of laser pulses. The characteristic "comb" structure is then derived by taking the Fourier transform of this time sequence, as shown in Figure 2.1 and given mathematically (see §A.1) by

$$E(t) = \sum_{n=1}^{n_f} A(t - n\tau) e^{i(\omega_c t - n\omega_c \tau + n\Delta\phi_{ce})} \xrightarrow{FT} \tilde{E}(\omega) = \tilde{A}(\omega - \omega_c) \sum_{n=1}^{n_f} e^{-in\omega\tau + in\Delta\phi_{ce}}. \tag{2.1}$$

The left side of this expression represents the time-domain electric field, $E(t)$, of a sequence of n_f pulses, each with a pulse shape $A(t)$. ω_c and τ are the center angular frequency of the spectrum and time between subsequent pulses, respectively. $\Delta\phi_{ce}$ is the a pulse-to-pulse slip between the pulse envelope, $A(t)$, and the carrier frequency, ω_c, indicated in Fig. 2.2. $\tilde{E}(\omega)$ and $\tilde{A}$ are the fourier transforms of $E(t)$ and $A(t)$, respectively. From this expression, a few things are clear. First, the spectral envelope, $\tilde{A}(\omega)$, is given by the fourier transform of the pulse envelope, $A(t)$. Therefore,

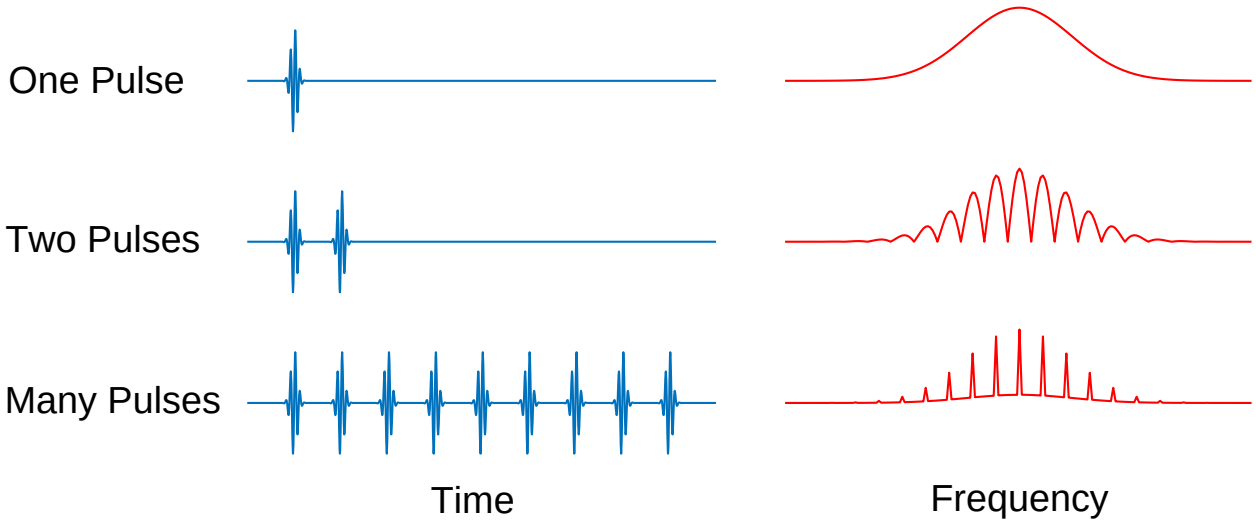

Figure 2.1: The optical frequency comb as an accumulation of stabilized pulses for n_f =1, 2, and 9 pulses.

a broad spectral bandwidth requires a short pulse duration. Second, even through the spectrum of a single pulse is broad, the coherent addition of many pulses creates a series of "comb teeth" underneath the single-pulse envelope. These terms add constructively when $2\pi m = \omega\tau - \Delta\phi_{ce}$. By defining $f_{rep} = 1/\tau$ and $f_0 = \Delta\phi_{ce}/(2\pi\tau)$, we arrive at a precise frequency relationship for the m$^{\text{th}}$ comb tooth, given by[26]

$$f_m = m f_{rep} + f_0. \tag{2.2}$$

where f_m is the optical frequency of the m$^{\text{th}}$ comb tooth, f_{rep} is the pulse repetition rate, and f_0 is the "carrier envelope offset" frequency. This relationship is simple, yet extremely powerful, since f_{rep} and f_0 are in the rf (radio-frequency) domain. These ~100 MHz signals may be detected and stabilized, thus stabilizing the ~100 THz optical comb teeth (f_m).

2.1 Molecular Spectroscopy

Molecular spectroscopy, the study of the interaction between molecules and light, has been around since at least the 1670s, when Sir Isaac Newton used a prism to disperse visible light. Since then, a number of tools and techniques have been developed that allow for the characterization of molecules

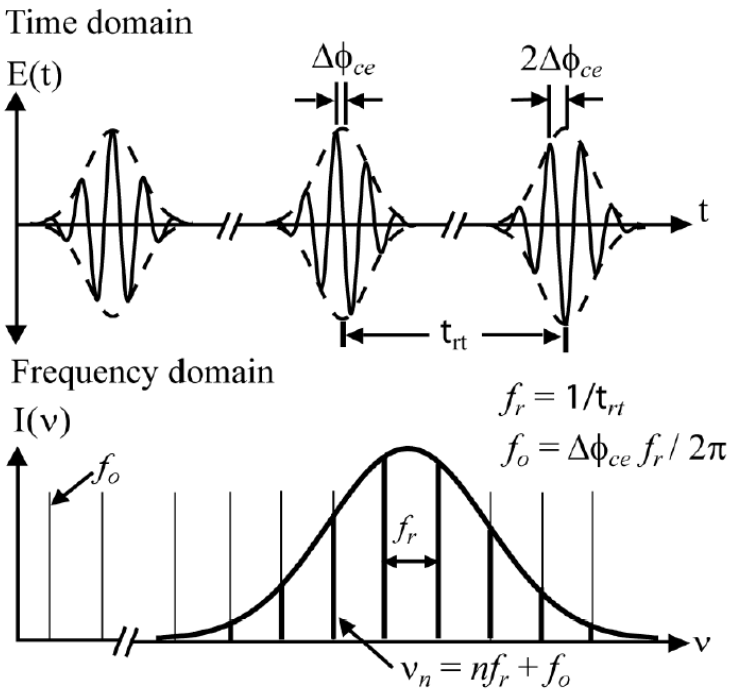

Figure 2.2: Time- and frequency-domain interpretation of f_{rep} and f_0. Reproduced from Ref. [21].

through the spectral response of their interaction with light. Linear absorption spectroscopy is perhaps the oldest technique, but its utility cannot be understated since it allows for the quantitative determination of molecular concentrations. It has been applied to such problems as the detection of gases for manufacturing processes[27, 28, 29], detection of poisonous gasses and explosives[30, 31], human breath analysis for medical applications[32, 33, 34, 35], environmental monitoring[36, 37, 38, 39], and optical ^{14}C dating[40]. Many of these applications require the ability to detect a number of small-amplitude spectral features across a wide bandwidth, in a short amount of time.

Many spectroscopic techniques have been developed to help solve these issues. Absorption spectroscopy based on continuous-wave (cw) techniques can offer high sensitivity, especially when coupled to an optical enhancement cavity for path length increases. However, it is necessary to scan these lasers across the wavelength range of interest in order to acquire a spectrum, with scan time proportional to the desired wavelength range. Still, modulation techniques[41], [42] and optical cavities[43] can provide exceptional sensitivity. NICE-OHMS[44, 45] combines these two techniques. This allows for high signal-to-noise[46] and the ability to measure very small absorption signals[47].

Thermal sources, such as a light bulb or even the sun, have traditionally been simple and robust sources of optical radiation, especially due to their low cost. Their most appealing feature is their broad spectrum, which can easily exceed 100s of THz in bandwidth. However, the lack of spatial and temporal coherence comes with a large cost. The spectral resolution of an instrument using a thermal source will be defined by the spectral resolution of the detector, which can be 10s of GHz in the case of a reflection grating. Additionally, their spatial incoherence decreases the available power and precludes the coupling of these sources to optical cavities with high efficiency to improve their molecular sensitivity. Therefore, these sources typically require much longer averaging times to approach sensitivities comparable to those offered by cw-laser based systems. Globar is a common source of low-cost high-power thermal radiation between 4 and 15 μm[48]. These sources have a high spectral flux (W/Hz), as indicated in Fig. 2.3. However, the focusability of these sources is very poor since the light originates from a macroscopic object radiating in all directions. For example, the Globar source used in Fig. 2.3 is a cylinder 104 mm in length and 6 mm in diameter. Using the concept of etendue (optical phase space volume), this source can at best be focused to a 5 cm diameter spot. This means that fairly standard photodetector with 4 mm^2 active area would only capture 0.2% of this light! A laser source, which can be focused to dimensions approaching its wavelength, does not have this restriction, allowing all of its power to be used. The solid blue curve in Fig. 2.3 reflects the 0.02% "useable power" of the Globar source, in the case of a 4 mm^2 detector active area.

The frequency comb is in its own category, combining the advantages of the thermal and cw techniques. The broad bandwidth of the comb is given by its spectral envelope, while its resolution is given by the narrow spectral width of the comb teeth beneath the envelope. Essentially, the frequency comb is a ~100,000× multiplexed version of the cw-laser. Although the total power available from frequency comb sources may be less than broadband thermal sources, all of this spatially coherent light can be used for measurements (see Fig. 2.3). Finally, we will see in the next section that the frequency comb also permits efficient coupling to an optical enhancement cavity.

The interaction of light with a sample in linear spectroscopy is described by the Beer-Lambert

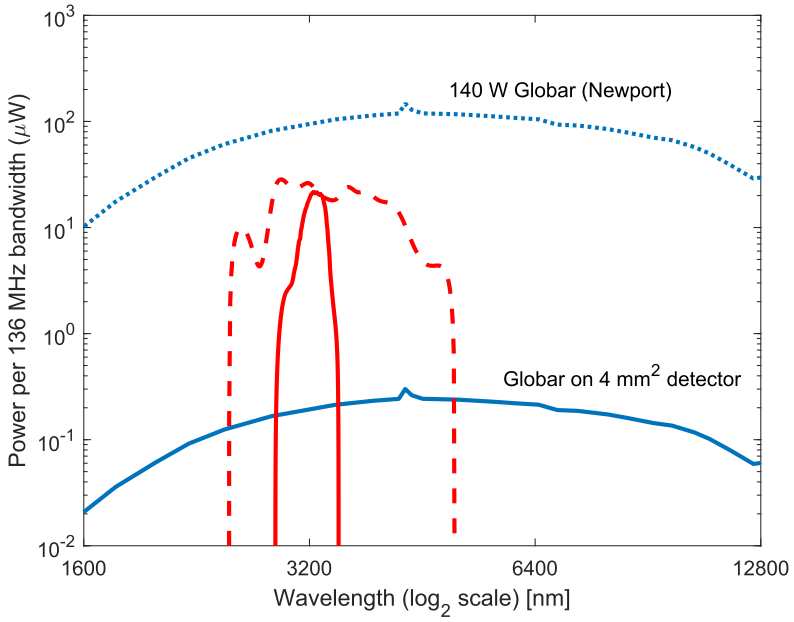

Figure 2.3: Spectral flux of Globar (blue) compared with Mid-Infrared OPO Frequency Comb (red). The y-axis represents power per comb mode (μW) for the the frequency comb and the power per f_{rep} = 136 MHz bandwidth for the Globar source. The solid red curve represents the power at a single center OPO wavelength, while the dashed red curve represents the tuning range of the OPO. The dotted blue curve is the total spectral flux from the globar source, while the solid blue curve is the maximum possible concentrated flux (0.2%) on a typical 4 mm^2 detector area.

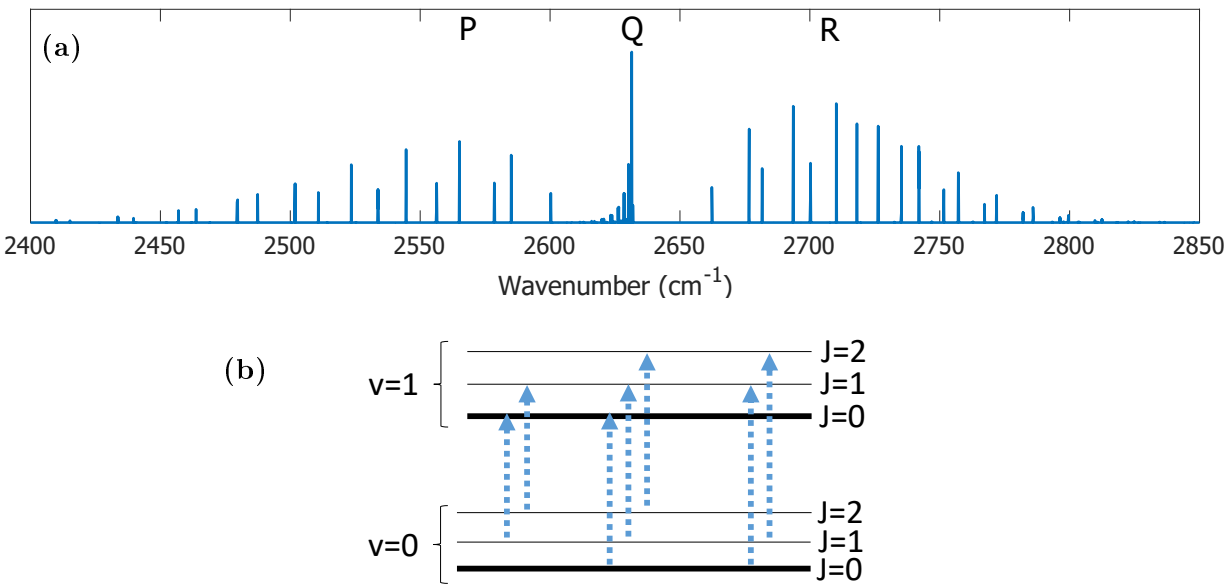

Figure 2.4: (a) The v=0→1 ro-vibrational spectrum of OD, simulated with PGopher[49] using fitted ro-vibrational parameters from Abrams *et al.* (b) Simple ro-vibrational energy level diagram. v and J are the vibrational and rotational quantum numbers, respectively. The P, Q, and R branches correspond to the allowed ro-vibrational transitions $\Delta J = -1, 0, 1$, respectively from the v=0 to v=1 vibrational levels.

law[50],

$$I_t(\nu)/I_0(\nu) = e^{-\alpha(\nu)l}, \tag{2.3}$$

where $\alpha(\nu)$ is the absorption coefficient in cm^{-1}, l is the interaction length in cm, and $I_t(\nu)$ and $I_0(\nu)$ are the transmitted and incident light intensities, respectively. Many molecular transitions contribute to $\alpha(\nu)$: electronic (visible), vibrational (mid-infrared), and rotational (radio frequency), and are typically very spectrally distinct. The mid-infrared spectral region, 2-20 μm, is especially useful for molecular spectroscopy since in this region each molecule has a unique spectral "fingerprint", allowing for identification. A simulated ro-vibrational in this spectral region of the deuteroxyl radical (·OD) is shown in Fig. 2.4a, where the P($\Delta J = -1$), Q($\Delta J = 0$), and R($\Delta J = +1$) branches can be clearly seen. These three sets of transitions arise from the ro-vibrational selection rule $\Delta J = 0, \pm 1$, where J is the angular momentum quantum number[51]. These transitions are indicated in Fig. 2.4b for a few ro-vibrational levels. The narrow Doppler linewidths of these tran-

sitions (~300 MHz) and the breadth of the full spectrum (~300 cm^{-1}) show why the multiplexed capabilities of the frequency comb are very useful. Excellent resources exist[51, 52] summarizing the details of ro-vibrational spectroscopy.

2.2 Enhancement with an Optical Cavity

From Beer's law, it is clear that the strength of the signal (and the minimum detectable concentration) is determined by the interaction length of the light with the sample. For this reason, it is important to make the interaction length as long as possible. One method of increasing this absorption interaction length is simply to use a longer sample. This technique is commonly used in atmospheric sensing, where light from the sun passes through the atmosphere and is detected at the surface of the Earth[53]. Another method of performing this type of sensing is to transmit a laser source through the atmosphere to a mountain-mounted retro-reflector[54] or a mobile drone. However, there are many situations where space is limited and the amount of available sample is small. In these situations, the extra optical path length may be obtained through the use of a White[55] or Harriet[56] cell, in which light reflects many times between two mirrors, before it is eventually ejected for analysis.

Another method for optical enhancement exists, which relies on the coherent properties of light. This device is the optical cavity, which at its simplest, consists of two highly-reflective mirrors. The transmitted electric field of such a device is given by the infinite sum of all possible paths through the two mirrors. Due to the high reflectivity of the mirrors, an average photon will spend a long time inside the cavity, increasing its interaction with the molecular sample. The effective absorption interaction length, l_{eff}, of such a device is given by $l_{eff} = \beta F l_{cav}/\pi$ where $F = \pi/(1-R)$ is the finesse of a cavity formed with mirrors of reflectivity R, l_{cav} is the physical length of the cavity, and $1 \leq \beta \leq 2$ is a parameter dependent on the method used to lock the laser frequency to the cavity[57, 58]. Since finesse values of $F > 3000$ ($R > 99.9\%$) can be easily reached across a broad range of wavelengths, l_{eff} can easily reach values 1000× the physical length of the cavity[1].

[1] Ref. [59, ch. 3] is an excellent resource for the traditional derivation of cw optical cavity reflection and transmission

In order to maintain this large length enhancement, a laser beam must experience constructive interference within the optical cavity. In the time domain, this criterion ensures that the optical field must repeat itself upon one round trip within the cavity. Each laser pulse, upon entering the cavity, must overlap with the pulse already inside the cavity. In the frequency domain, each comb tooth must be uniquely matched to an optical cavity resonance so that it is transmitted by the cavity. A number of methods have been demonstrated for maintaining a resonant frequency relationship between lasers and optical resonators. In most cases, these techniques were initially demonstrated using cw-laser systems and modified later for the frequency comb. The general principle of all of theses techniques is the same; an "error signal", representing the deviation from ideal laser-cavity coupling is generated and this is used to gently nudge the laser's or cavity's frequency towards a more ideal value. Two key requirements exist for this error signal: it must be zero when the laser frequency is matched with a cavity mode and it must be monotonic in detuning near this ideal value[2].

The Pound-Drever-Hall (PDH) technique[61, 62] is a very common method for maintaining a tight lock between an laser source and optical cavity. The error signal for this technique is generated by introducing phase-modulation sidebands to the laser. When these sidebands are at a frequency much larger than the cavity linewidth, they are completely reflected off of the input mirror of the cavity and serve as a "phase reference" for the lock. The carrier (unmodulated) frequency interacts with the cavity and picks up a phase shift upon reflection from the cavity. Demodulating the reflected intensity at the modulation frequency yields a signal proportional to the laser frequency's deviation from the optical cavity mode[3].

An alternative approach is the "sweep lock", where the laser frequency is swept across the cavity mode, with the cavity mode stabilized to the center of the sweep. The total transmitted intensity through the optical cavity is then detected as the integral over the sweep period. This technique significantly reduces frequency-to-amplitude noise conversion on the transmission of the cavity, since

properties.

[2]These techniques fall within the domain of "control theory", which describes the behavior of a dynamical system under feedback[60].

[3]Excellent tutorials for the PDH technique are found in Refs. [62, 59, §4.7].

a small change in the length of the cavity will cause the transmitted cavity pulse to shift within its integration window without changing its total integrated intensity. However, this improved amplitude noise comes with the drawback of reduced intensity, since light is only transmitted through the cavity at the middle of the laser sweep.

As described, these techniques apply to cw-laser systems; modifications must be made to stabilize both parameters, f_{rep} and f_0, of a frequency comb to a cavity. In the PDH technique, this can be done by generating two PDH error signals at the low- and high- wavelength portions of the spectrum and feeding these signals to the appropriate f_{rep} and f_0 actuators in the frequency comb. In the sweep lock, a single error signal is generally used to stabilize f_{rep}, with f_0 stabilized to an rf source. If high-resolution is not required, *e.g.* at high pressures and/or temperatures, f_0 may even be left to freely drift, as it only minimally affects the sweep lock. Other techniques for locking lasers to cavities exist, but were not explored in this thesis work. For example, the Hänsch-Couillaud technique[63] uses an intracavity Brewster plate to generate a frequency-dependent elliptical polarization in the reflected light, thus avoiding frequency modulation of the incident laser beam.

2.3 Mirror Dispersion Characteristics

In Section 2.2, it was suggested that it might be possible to perfectly couple an optical frequency comb to an optical enhancement cavity such that each comb tooth is perfectly resonant with every cavity mode. In general, this is impossible due to the tendency of an optical cavity to change its free spectral range (FSR) with wavelength. To see why this is the case, we look briefly at the reflective and dispersive properties of a standard quarter-wave-stack. The reflectivity and dispersion of a quarter-wave stack is plotted in Fig. 2.5. The changing group delay of the mirrors, $\tau = \frac{\partial \phi}{\partial \omega}$, gives rise to a changing FSR through the formula

$$FSR(\omega) = \frac{c}{2l_{cav} + c\frac{\partial \phi}{\partial \omega}}, \tag{2.4}$$

where l_{cav} is the physical length of the optical cavity and ϕ is the wavelength-dependent spectral phase of the reflected light off of the HR mirror[64]. The wavelength-dependent FSR is also plotted in Fig. 2.5. Due to the changing FSR with wavelength, the comb modes are no longer able to simultaneously maintain resonance with the optical cavity. This causes two problems: (1) the cavity transmission is decreased where the comb-cavity frequency difference is greatest and (2) the molecular dispersion is coupled to the output of the optical cavity. For molecular spectroscopy, (1) can be mitigated by acquiring a reference spectrum prior to the absorption spectrum. However, the transmitted spectrum through the cavity will still be narrowed through the effects of dispersion. This can be seen in the bottom panel of Fig. 2.7, where the "two-point lock" trace is obtained by stabilizing f_{rep} and f_0 using spectrally filtered PDH signals at low wavelength (red trace) and high-wavelength (black trace). A schematic for this scheme is shown in Fig. 2.9a, where the two PDH signals are generated at photodiodes PD1 and PD2. The dashed curves of Fig. 2.7 are obtained by engaging only one lock (pump lock) and detuning the other lock (opo lock), producing a spectrum of narrow bandwith but high intensity. As the lock point is tuned, the peak of the narrow one-lock spectrum traces out the maximum transmission available at a given wavelength. The two-lock value may be compared with this value to determine the wavelength-dependent comb tooth detuning from the cavity mode, assuming a Lorentzian cavity mode lineshape. This detuning is given by

$$\Delta\nu = \Gamma_L \sqrt{\frac{P_1 - P_2}{P_2}}\,, \tag{2.5}$$

where P_1 and P_2 are the transmitted power for the one-point and two-point locks, respectively, and $\Gamma_L = FSR/(2F)$ is the cavity mode's half-width at half max. This wavelength-dependent detuning is plotted in the top panel of Fig. 2.7.

However, (2) remains an issue. The exact formula for the transmission of an enhancement cavity of length L in the presence of an analyte is given by[65, 11]

$$\begin{aligned} \frac{I_t(\nu)}{I_0(\nu)} &= \frac{t^2(\nu)e^{-2\delta(\nu)L}}{1-r^2(\nu)e^{-4\delta(\nu)L}-2r(\nu)e^{-2\delta(\nu)L}\cos[2\phi(\nu)L+\varphi(\nu)]} \\ &= \frac{t^2(\nu)e^{-\alpha(\nu)L}}{1-r^2(\nu)e^{-2\alpha(\nu)L}-2r(\nu)e^{-\alpha(\nu)L}\cos\left[4\pi\nu L(n+n_{analyte}(\nu))/c\right]} \end{aligned}\,, \tag{2.6}$$

where $I_t(\nu)$ and $I_0(\nu)$ are transmission spectra from the cavity with (Sample) and without (Reference) an absorber in the cell. $\delta(\nu)$ and $\phi(\nu)$ are the attenuation and phase shift of the electric field due to the analyte per unit length, given in terms of the analyte's absorption coefficient, $\alpha(\nu)$, and index of refraction, $n_{analyte}(\nu)$ by $\delta(\nu) = \alpha(\nu)$ and $\phi(\nu) = 2\pi\nu n_{analyte}(\nu)/c$. $t(\nu)$ and $r(\nu)$ are the the frequency-dependent intensity transmission and reflection coefficients of the cavity mirrors, respectively. $\varphi(\nu)$ is the round-trip phase shift in the cavity without the analyte. For a buffer gas of refractive index n, this is given by $\varphi(\nu) = 4\pi\nu nL/c$, where c is the speed of light.

At this point, it is common to series expand Eq. 2.6 for small $\alpha(\nu)$, yielding the expression

$$\frac{I_t(\nu) - I_0(\nu)}{I_0(\nu)} \approx \frac{2F(\nu)}{\pi}\alpha(\nu)L, \tag{2.7}$$

where $F(\nu)$ is the cavity finesse, defined as $\pi\sqrt{r(\nu)}/\left[1 - r(\nu)\right]$[65, 11]. This expression may be compared with the equivalent expansion of the Beer-Lambert law, $\left[I_t(\nu) - I_0(\nu)\right]/I_0(\nu) \approx \alpha(\nu)L$, to see the $2F(\nu)/\pi$ path length increase due to the optical cavity.

Additionally, Eq. 2.6 describes the distortion of a molecular lineshape after transmitting through a cavity with non-negligible dispersion properties, where some comb teeth are not perfectly matched with their corresponding cavity modes. In this case, the round-trip intracavity phase shift is given by $\varphi(\nu) = 2\pi\Delta\nu/FSR(\nu) + 2q\pi$, where $\Delta\nu$ is the frequency detuning of the comb tooth from the center of its corresponding cavity mode and q is an integer. Figure 2.6a shows the complex absorption profile of an example molecular feature and Figure 2.6b depicts this feature, as transmitted through an optical cavity with $F = 5000$ and a comb-cavity mismatch of $\Delta\nu = 20$ kHz.

The top panel of Fig. 2.8 shows an experimental spectrum of methane, in which dispersion clearly affects the line shape of the experimental data (black) at low wavelength. This can clearly be seen in the fit residual when the effects of dispersion are not included ($\Delta\nu = 0$, middle panel). The red trace and bottom panel show the improvement in the fit and its residual due to the inclusion of dispersion effects using eq. 2.6.

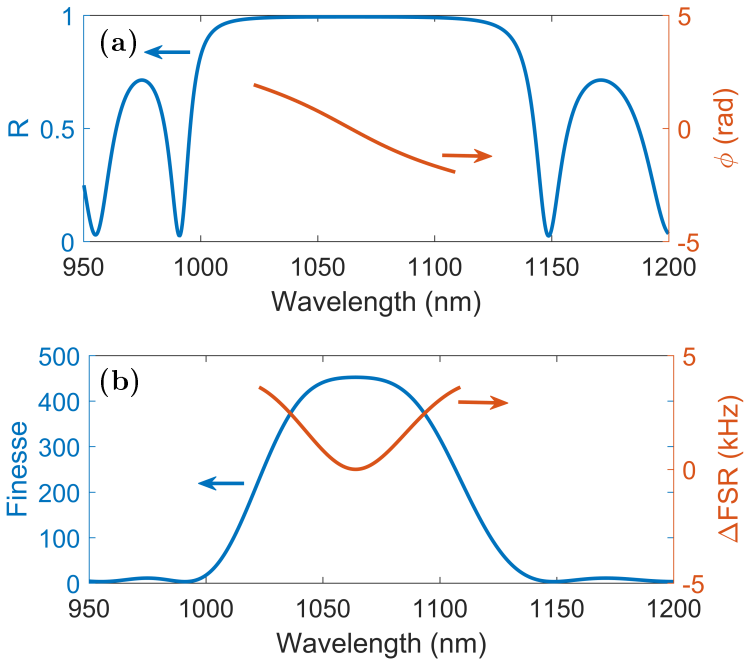

Figure 2.5: Reflectivity and dispersion of a quarter-wave stack. (a) Reflectivity and phase delay. (b) Finesse and wavelength-dependent change in FSR, calculated from (a).

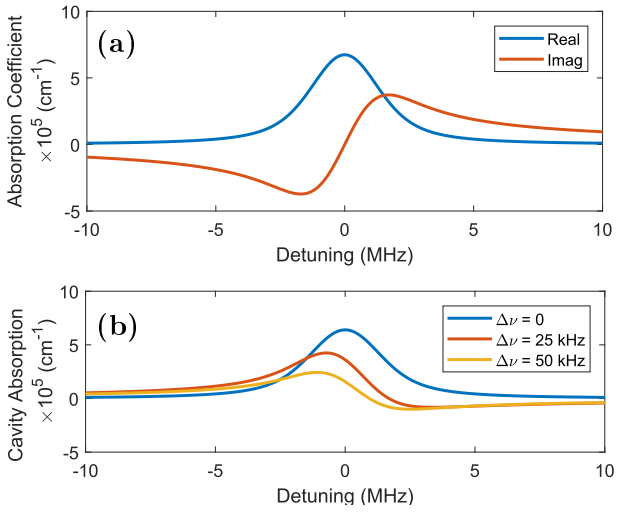

Figure 2.6: Effect of dispersion on cavity absorption features. (a) Real and complex absorption coefficient. (b) The same absorption feature, enhanced by an optical cavity, with laser-cavity detunings of 0, 25 kHz, and 50 kHz. The cavity-enhanced plot is given by $-\log(I_t(\nu)/I_0(\nu))\pi/(2Fl)$, with $I_t(\nu)/I_0(\nu)$ given by eq. 2.6.

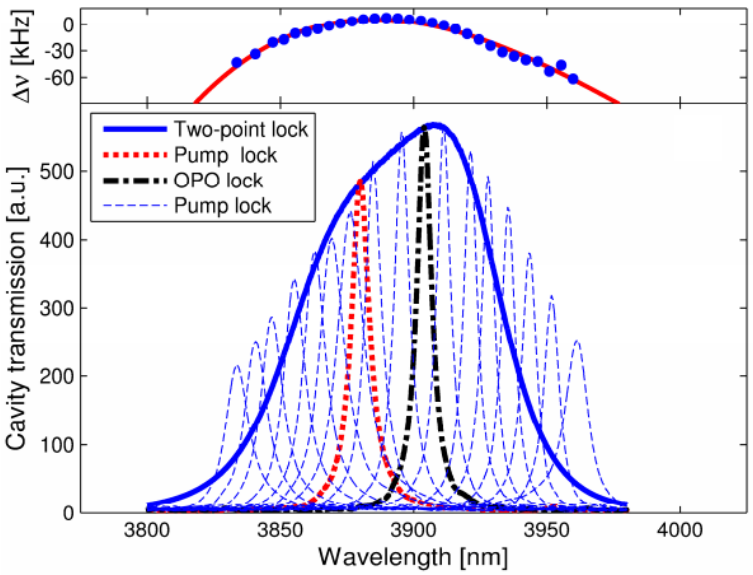

Figure 2.7: Cavity transmission in the presence of dispersion.

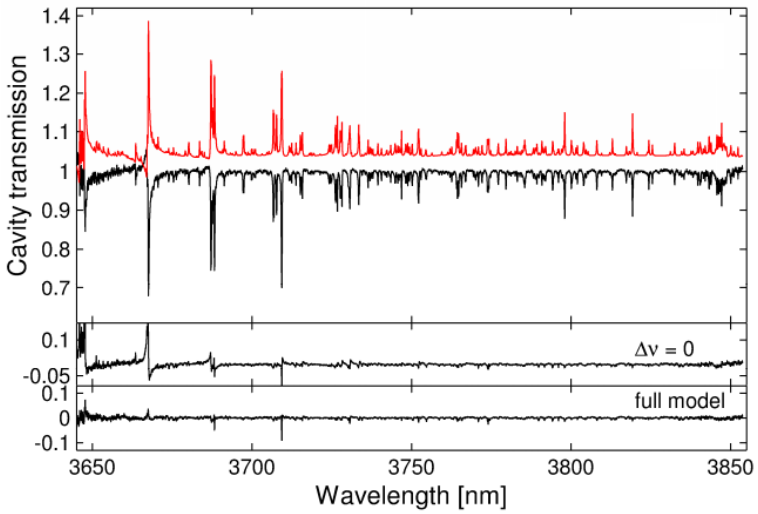

Figure 2.8: Experimental spectra of 10 ppm CH_4 in 760 torr N_2 at room temperature (black curve). The red curve, inverted and offset for clarity, shows model spectra calculated using data from the HITRAN database. With $\Delta\nu = 0$ fixed, the model breaks down at the edge of the mirror bandwidth.

2.4 Detection Methods

Due to the broadband nature of the frequency comb, the transmitted light from the optical cavity must be spectrally resolved in order to obtain information about the molecular sample being probed. Many detection methods have been explored[66], but only two of these have proved useful for the work in this thesis: the Fourier Transform Spectrometer (FTS) and Virtually Imaged Phased Array (VIPA). The FTS has existed for many decades and is widely used across many areas of physics, chemistry, and biology[67]. The general principle of the FTS is to convert optical frequencies to radio frequencies so that they may be detected. This is done using a variable-path-delay Michelson interferometer, shown in Fig. 2.9b. The fourier transform of the light intensity at the interferometer's output yields the intensity spectrum of the light.

An alternative detection technique is the Virtually Imaged Phased Array (VIPA), in which light is spatially dispersed in 2D and detected using a camera. The VIPA technique is discussed in §3.5. Like the FTS, the VIPA can be operated in the "hard lock" configuration, where the frequency comb teeth are always near the center of their respective cavity modes. However, the VIPA permits another "sweep-lock" configuration in which the repetition rate (or offset frequency) is swept across the cavity modes such that the comb is only resonant with the cavity for a short period of time during each sweep. This has the distinct advantage of being fairly immune to mirror dispersion, since each comb tooth will come into resonance with its respective cavity mode during each sweep period. This type of dispersion immunity has not yet been demonstrated in the FTS.

It is worth pointing out that many other detection methods exist, which are not utilized in this thesis. Dual-comb spectroscopy has received great interest due to its ability to acquire spectra quickly and with no moving parts[68]. Additionally, frequency-comb-based streak spectroscopy has been demonstrated, which uses a moving mirror to map time to space, allowing for the acquisition of a broad spectrum with microsecond time resolution[66]. Of course, there is no perfect detection technique; each of the techniques listed here has advantages and disadvantages in time resolution, spectral resolution, complexity, and cost.

2.5 Demonstration: Detection of H_2O_2 in the presence of H_2O

As a demonstration of this technique's ability to simultaneously detect trace concentrations of multiple molecular species, we applied the system to the detection of hydrogen peroxide (H_2O_2) in the presence of a large concentration of water. The increased presence of H_2O_2 in human breath could be used for early diagnostics and monitoring of such diseases as asthma[69, 70, 71], chronic obstructive pulmonary disease[72], or acute respiratory distress syndrome[73, 74], a severe inflammatory condition with up to 50% mortality[75]. The detection of H_2O_2 in human breath is most commonly performed with the creation of a breath condensate and the use of absorption of fluorescence spectroscopic methods, achieving detection limits in the range of a few ppb to a few hundred ppb[76]. Commercial biosensors are available and offer detection limits in the range of a few tens of ppb, but require everyday calibration[77]. Additionally, the need for breath condensation and the use of chemical reactions for analysis precludes the use of these techniques for real-time applications. High-resolution laser spectroscopy has been recognized as a tool for quantitative breath analysis in the gas phase, eliminating the need for sample condensation and pre-filtering[34, 35]. Despite the molecule's importance as a potential marker for numerous diseases, no laser-spectroscopy-based system for its optical detection in human breath has been reported.

One of the main challenges underlying the detection of H_2O_2 in the breath is the large concentration of water, which can approach saturation. Exhaled breath at 35 °C can thus approach a water concentration of 5%. As the breath cools to 21 °C, some of the water will condense, bringing the water concentration to less than 3%. For many techniques, this causes significant contamination and can completely obsure the H_2O_2 signal. To simulate this high-water environment, a solution was prepared with $\sim 27\%$ H_2O_2 in water. This liquid was placed in the removable tray of a specially designed optical cavity, as shown in Fig. 2.9a, and its vapor was allowed to fill the cell. Heaters on the bottom of the cell allowed the temperature of the cell to be tuned from room temperature (23 °C) to a more biologically-relevant temperature of 39 °C. Two flow ports on the top of the cell allowed for a small flow of pure N_2 to reduce the amount of water vapor in the sample, maintain-

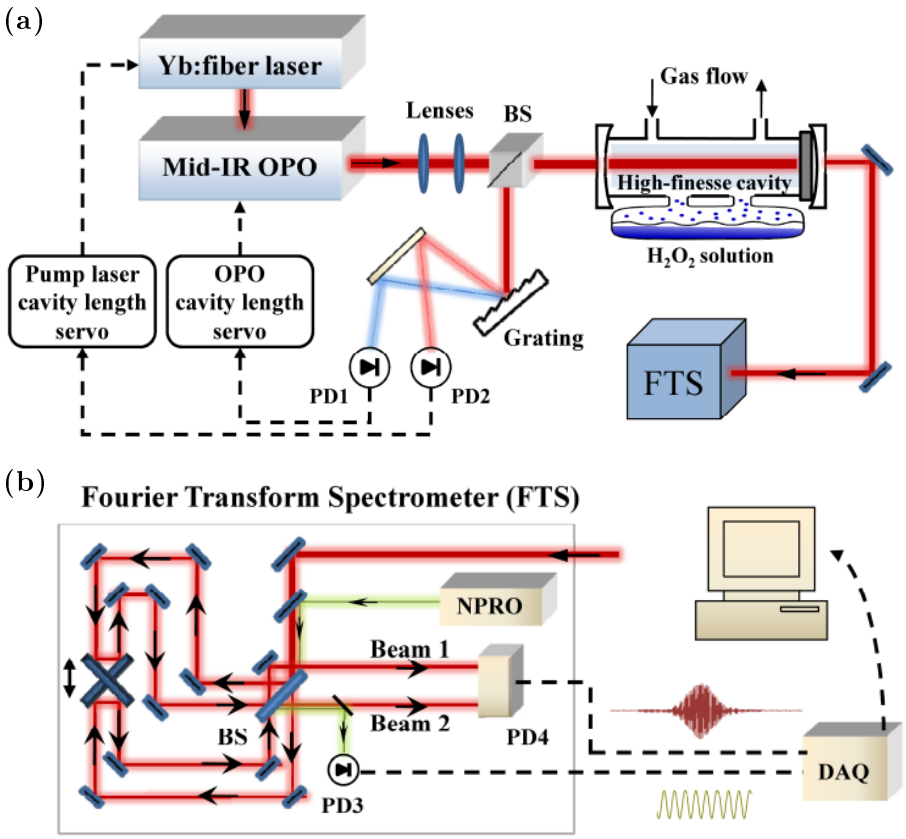

Figure 2.9: Schematic diagrams of the (a) experimental setup and (b) fourier transform spectrometer.

ing the pressure of the cell at an atmospheric pressure of 630 torr. The mirrors were attached to the glass spacer using Torr Seal, after ensuring that the cavity FSR was correctly matched to the frequency comb (27.4 cm, matched to $FSR = 4 \times 136.6$ MHz). A piezo was installed on the output coupler of the cavity, allowing for fine length adjustment.

Observed H_2O_2 spectra are shown in Fig. 2.10a and b, for liquid temperatures of 23 °C and 39 °C, respectively. A sum of model spectra of H_2O_2 and H_2O are fitted to the data, shown in red and blue, respectively. Spectral data for the water lines (H_2O and HOD) are taken from the HITRAN database[78], where the isotopic abundances of 0.99731 and 0.00031 are used, respectively. High-resolution data for the $\nu_2+\nu_6$ combination band of H_2O_2 in this spectral region does not exist, so we used absorbance values from the Pacific Northwest National Laboratory (PNNL) database of quantitative IR data[79]. The PNNL data are intended for open-path monitoring and the experimental spectral are obtained using a conventional FTS with the sample back-pressurized to 760 Torr using dry nitrogen and with absorbance values normalized to a mixing ratio of 1 ppm at a temperature of 296 K and a path length of 1 m[80]. The PNNL absorbance were recalculated by scaling for the path length and the lower atmospheric pressure, 630 torr, in our laboratory. Since the H_2O_2 spectrum is a series of $^{R}Q_0$ sub-branches[81], accounting for the pressure-broadening coefficients is somewhat complicated. Thus, a scaling factor of 0.828 was introduced to partially account for the lower pressure. This pressure discrepency is likely the source of the structure in the fit residual, seen in the bottom panel of Fig. 2.10a, which causes a systematic error in the H_2O_2 concentration retrieved by the fit, which is estimated to be 20%. At the peak absorption at the strongest H_2O_2 line at 3761 nm, we estimate the absorption to be 7×10^{-7} cm^{-1} for 1 ppm at 630 torr. This indicates that the noise equivalent concentration detection limit of H_2O_2 in the absence of water is 8 ppb at 1s averaging time.

In order to determine the concentration detection limit of H_2O_2 in the presence of water at a biologically-relevant (percentage) levels, we measured spectra under the same temperature and pressure conditions as were used for Fig. 2.10 and filled the container with deionized (DI) water only. A sum of H_2O_2 and H_2O was fitted to 100 consecutive water spectra in the wavelength range

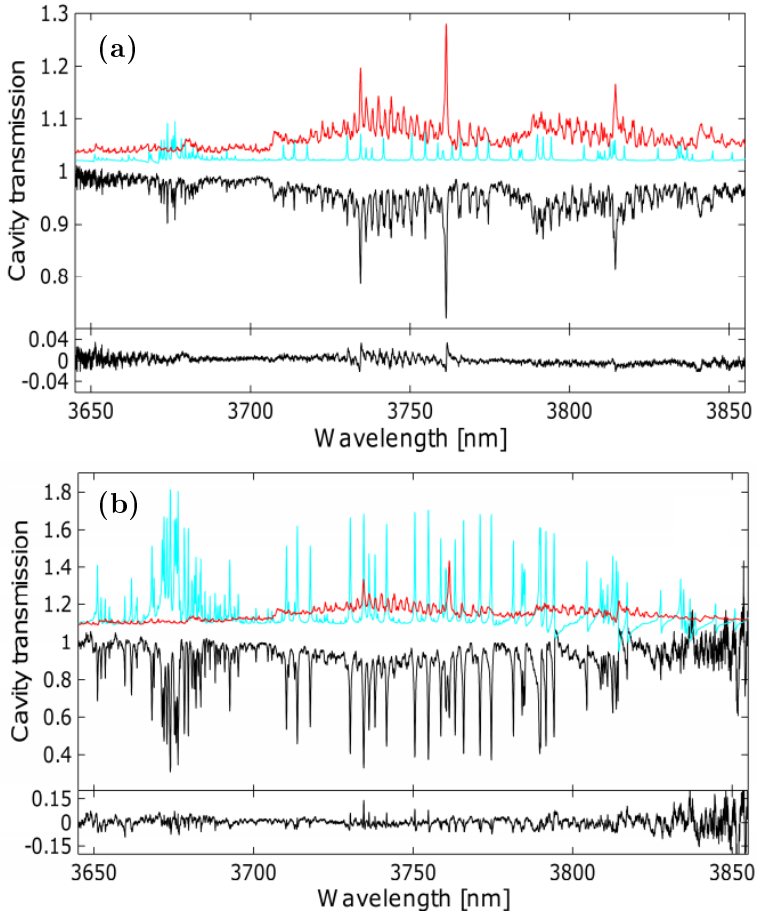

Figure 2.10: Experimental spectra of hydrogen peroxide and water, shown in black, inverted and offset for clarity. Fitted model spectra of H_2O_2 (red) and H_2O (blue) are shown upright. The temperatures and fitted molecular concentrations are (a) room temperature (23 °C), $[H_2O_2]$=3.6ppm, $[H_2O]$=645ppm and (b) T = 39 °C, $[H_2O_2]$=5ppm, $[H_2O]$=1.2 %.

with the highest SNR, i.e. between 3720 and 3790 nm. The mean water concentration returned by the fits was 2.83(6)%, while the mean H_2O_2 concentration was 75 ppb with standard deviation of 130 ppb. Thus, the detection limit of H_2O_2 in the presence of almost 3% of water is 130 ppb. This is worse than the limit determined from the background noise level due to the structure in the fit residual after the model water spectrum is subtracted off. The detection limit could therefore be improved by refining the line-shape model, using more precise spectral data for the water lines, and by reducing the baseline drift in the experiment, but the achieved detection limit of H_2O_2 is already sufficient for medical applications where a typical concentration is $> 10\,\text{ppm}$.

Chapter 3

Time-Resolved Frequency Comb Spectroscopy

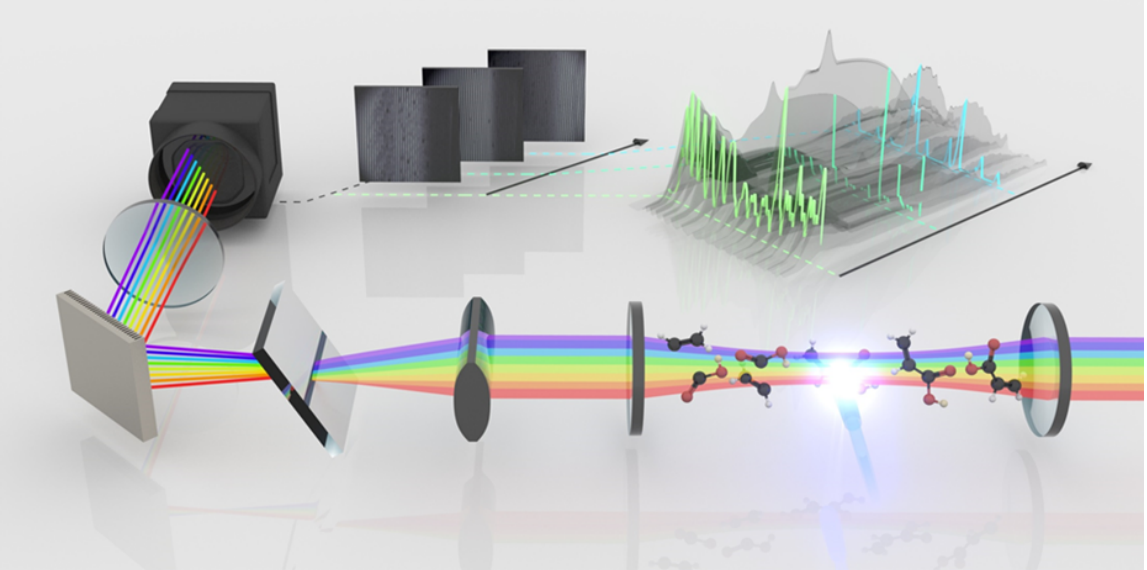

3.1 Overview

Over the past 50 years, spectroscopy has proved a very valuable tool for the study of chemically interesting species in the gas phase. The slow evolution of molecules such as methane and carbon dioxide in the atmosphere are constantly observed by cavity-ringdown techniques[82], differential optical absorption spectroscopy (DOAS) methods[53], and dual-comb spectroscopic techniques[54]. Due to the stability and long lifetime of these molecules, their spectral features can be very narrow, allowing for a simple recovery of the atmospheric molecular concentration. In addition, the long lifetimes of these molecules allow for long averaging and spectral scanning times to collect

broad-bandwidth spectra with high spectral resolution. On the other hand, femtosecond transient absorption spectroscopy allows for the study of unimolecular ps-timescale reactions[83]. In this case, spectral resolution requirements are minimal since the molecular spectral response is lifetime-broadened to some THz.

In this work, we are concerned with the middle ground: the observation and characterization of stable, but highly reactive, molecules which form, re-arrange, and decay on the μs timescale. Lifetime broadening of these molecules should be limited to ~1 MHz, preserving the rich structure of the molecules' spectral response, and thus information about the molecular geometery and its vibrational, rotational, and thermal temperatures. Furthermore, the determination of absolute time-dependent molecular concentrations, especially in the presence of other absorbing species, is considerably simpler. The study of this type of reaction has three main requirements:

1. High temporal resolution
2. Broad spectral bandwidth and high spectral resolution
3. High molecular sensitivity

Traditional broadband absorption techniques such as FTIR have allowed for the detection of some transient species[7], but do not have the molecular sensitivity to observe and characterize trace concentrations. Highly sensitive techniques such as cw cavity ringdown spectroscopy allow for the detection of very small concentrations at short timescales[9, 84] with high spectral resolution, but are unable to scan over a suffiently broad bandwidth to capture a global portrait of the chemical reaction surface. Cavity-enhanced direct frequency comb spectroscopy (CE-DFCS) simultaneously solves all of these problems. The broad bandwidth of the pulsed source allows for many molecules to be observed simultaneously, while the absorption length enhancement of the optical cavity increases the signal amplitude by ~1000×. The transmitted light from the cavity is then spatially dispersed and imaged on a camera to simultaneously detect the broad bandwidth of the frequency comb with a time resolution limited by the ringdown time of the optical cavity (a few μs). Additionally, the spectral resolution of this technique is limited only by the linewidth of the comb teeth, which can be

<1 MHz. At room temperature, this allows the rotational features of small molecules to be resolved so that the molecules may be uniquely identified and characterized. At low temperatures, this high spectral resolution can be utilized to access the narrow features of larger species which have a small rotational spacing[85].

In this chapter, I will first describe the frequency comb source, the optical enhancement cavity, and the dispersive detection system. I will also describe the method used to ensure the proper timing in the experiment and to ensure proper coupling between the cavity and comb. Finally, I will describe the use of this system to measure the photolysis and subsequent reactions of deuterated acrylic acid.

3.2 Mid-Infrared Frequency Comb Source

The mid-IR frequency comb source consists of three parts: oscillator, power amplifier, and optical parametric oscillator (OPO). The oscillator and amplifier are described in Refs. [86, 87], while the OPO is described in Ref. [88]. The oscillator itself is a linear cavity design, with a fiber bragg grating (FBG) output coupler, as shown in Fig. 3.1. Pump light at 976 nm enters the oscillator gain fiber through a wavelength division multiplexer (WDM). The gain fiber is ~15 cm of double-clad fiber from OFS[1]. Directly following the gain fiber is a free-space section, where the free-space light is focused onto a semiconductor saturable absorber mirror (SESAM), which provides the nonlinear reflectivity required to start the mode-locking process. Also in the free-space section is a polarizing beam splitter on a rotation mount for mode-locking through nonlinear polarization rotation. While mode-locked, nonlinear polarization rotation is the main saturable absorber mechanism - the SESAM only serves to make the oscillator self-starting. A spectrum of the oscillator is given in Fig. 3.2, which has the characteristic parabolic shape associated with a similariton pulse[89].

Following the oscillator, the ~90 fs pulse is broadened to ~70 ps using a 30 m long stretcher fiber before injection into the amplifier. The amplifier is based on a 2 m DC-200-40-PZ-Yb fiber and is

[1] Approximately 5 cm of this fiber has been replaced with SMF-28 after a burn of the gain fiber tip. The splice was done using a Fujikura FSM-40 PM fusion splicer in the cladding-alignment mode.

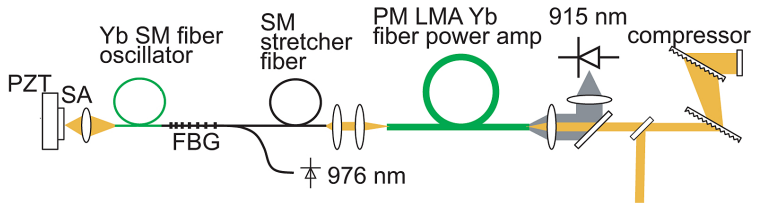

Figure 3.1: Yb comb oscillator and amplifier. Reproduced from Ref. [87].

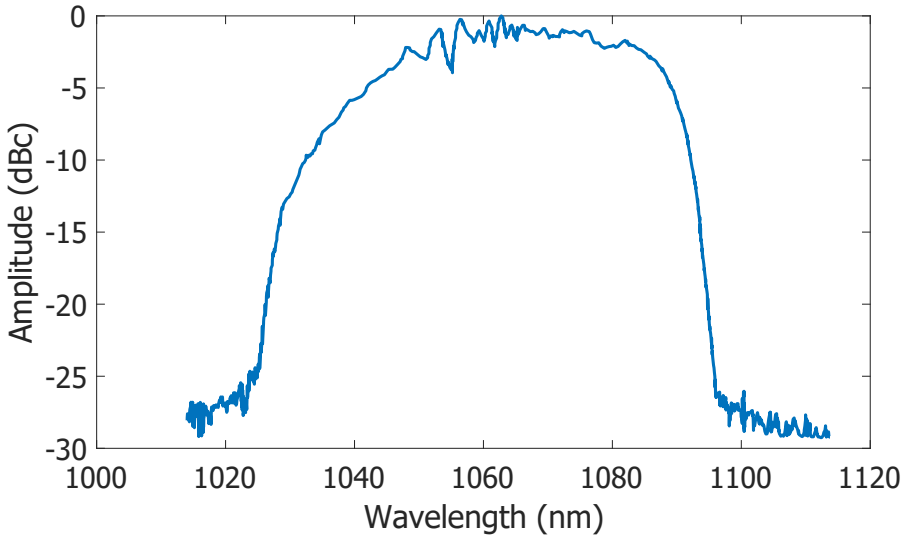

Figure 3.2: Spectrum of Yb:fiber oscillator.

reverse-pumped by 60 W of 976 nm light[2]. This fiber is very common in high-power systems due to its ability to handle high power and its large numerical aperture in the cladding mode (0.6) for the pump. A photo of the amplifier in operation is shown in Fig. 3.3. The input power into the amplifier is 30 mW, while the total output power is 15 W. The output of the amplifier is then sent into a pulse compressor, which compresses the pulses to 110 fs with a power efficiency of 66%.

To generate useful mid-IR light, the compressor output is coupled into an optical parametric oscillator, which features a fan-out PPLN crystal for converting the light to 3-5 μm. The output of the OPO has three key features:

- Broad Bandwidth: The spectrum is approximately 200 nm broad.
- Broad Tunability: The center wavelength of the source may be tuned between 2.8 and 4.8 μm by vertically translating a PPLN crystal.
- High Power: A maximum power of 1.5 W is reached at a center wavelength 3.5 μm

3.3 Frequency Comb Stabilization

In order to use the frequency comb for high-resolution spectroscopy, it is necessary to fix f_{rep} and f_0, ensuring the absolute stability of each comb tooth. Despite efforts to decouple acoustic and thermal processes from the Yb-comb and OPO, some residual noise remains. This residual noise is removed by measuring the f_{rep} and f_0 and applying feedback to the appropriate actuator. In our case, there is a slight twist, since the OPO allows an additional freedom in f_0:

$$f_{0,p} = f_{0,s} + f_{0,i} \ , \tag{3.1}$$

where $f_{0,p}$, $f_{0,s}$, and $f_{0,i}$ are the offset frequencies for the pump, signal, and idler, respectively. The repetition rates of the pump, signal, and idler combs are identical. To stabize f_{rep} and f_0 of the idler comb for spectroscopy, there are a few options. For example, it may seem easiest to simply

[2]Part number K976AA5RN-60.0WN0N-10522B10ENA0 from BWT. The amplifier previously consisted of 8 m of DC-200-40-PZ-Yb fiber, pumped at 915 nm. The fiber and the pump diode were both replaced following catastrophic failure of the fiber's output facet.

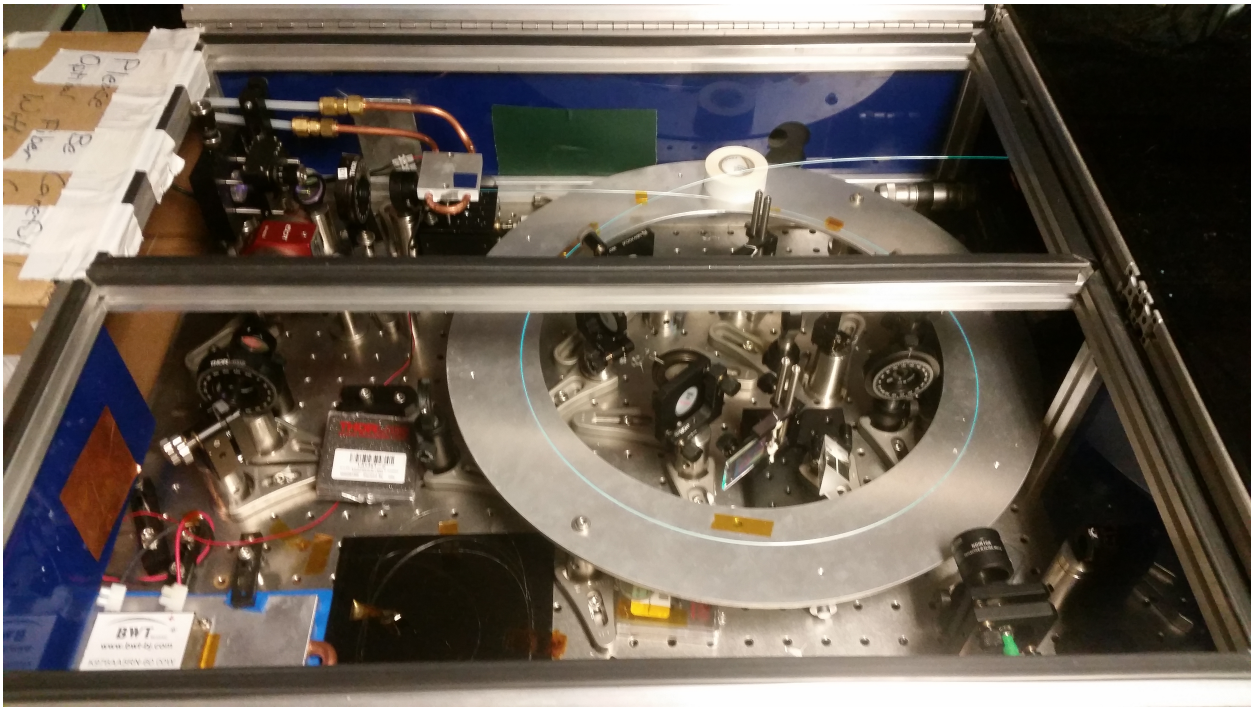

Figure 3.3: Photo of the Yb:fiber amplifier in operation. The NKT fiber is the green glowing fiber on the aluminum ring.

measure f_{rep} and $f_{0,i}$, which in our case are <200 MHz, and stabilize them to radio frequency (rf) sources. This approach does have the advantage of simplicity. Specifically, it allows $f_{0,p}$ and $f_{0,s}$ to drift, unstabilized; only two feedback loops are necessary. However, this simplicity comes with a cost: any noise written to f_{rep} though its feedback loop will be multiplied into the optical domain, limiting the achievable linewidth. For example, typical RF crystal oscillators have a relative frequency instability of 10^{-10}, which will already broaden a 4 μm comb to 7.5 kHz before any in-loop errors are considered. For molecular spectroscopy, where spectral features are typically hundreds of MHz broad, even a linewidth of 1 MHz is sufficient. On the other hand, if a narrower comb tooth linewidth is desired, it is necessary to stabilize f_{rep} with an optical source to remove the noise multiplication process. In practice, there are 6 distinct actuators available in the mid-IR frequency comb:

1. Oscillator pump current (fast)

2. Oscillator fiber stretcher (slow)

3. Oscillator SESAM piezo (fast)

4. Oscillator fiber bragg grating temperature (very slow)

5. OPO bullet mount piezo (fast)

6. OPO translation stage piezo (slow)

With the exception of (5) and (6), which only change the offset frequencies of the signal and idler, these actuators are non-orthogonal in f_{rep} and $f_{0,p}$. Additionally, each of these actuators has a different spectral response.

The oscillator pump current changes f_{rep} and $f_{0,p}$ by shifting the wavelength and changing the self-phase modulation. However, the f_{rep} shift can be minimized by operating the oscillator cavity near zero second-order dispersion[90]. The fiber stretcher and fast piezo should ideally change mostly f_{rep}, but bending in the fiber also causes coupling to f_0. The fiber bragg grating temperature provides the largest actuator for f_0, but is extremely slow. Changing the temperature of the grating changes its effective periodicity through thermal expansion and its thermo-optic coefficient[91]. The group delay of the grating is modified, since the center of the optical spectrum is now reflected off of a different portion of the grating. However, the chirped nature of the grating gives rise to another effect: shorter periods expand less than longer periods, causing dispersion to increase with temperature. Chirped gratings are commonly used for optical dispersion management[92] and their temperature properties are well-described[93].

3.4 Optical Enhancement Cavity

Light from this OPO is sent through two spatial mode-matching lenses into an optical cavity made from 6 m radius of curvature mirrors, separated by 54.88 cm (FSR = $2\times f_{rep}$) such that half of the comb modes are resonant with the cavity. The waist and rayleigh length of the TEM_{00} cavity mode are 1.3 mm and 1.25 m, respectively, using the symmetric cavity equations[59]. The geometry of the absorption-enhancement cell is shown in Fig. 3.4 and a physical picture of the cell is shown in Figure 3.5.

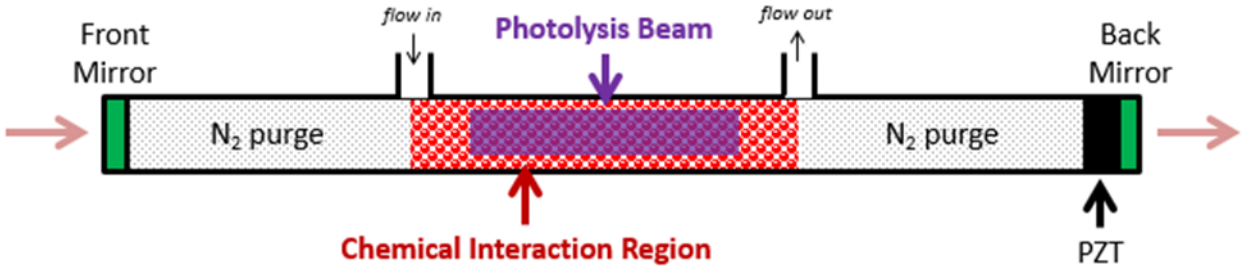

Figure 3.4: Diagram of the flow cell used in the TRFCS work

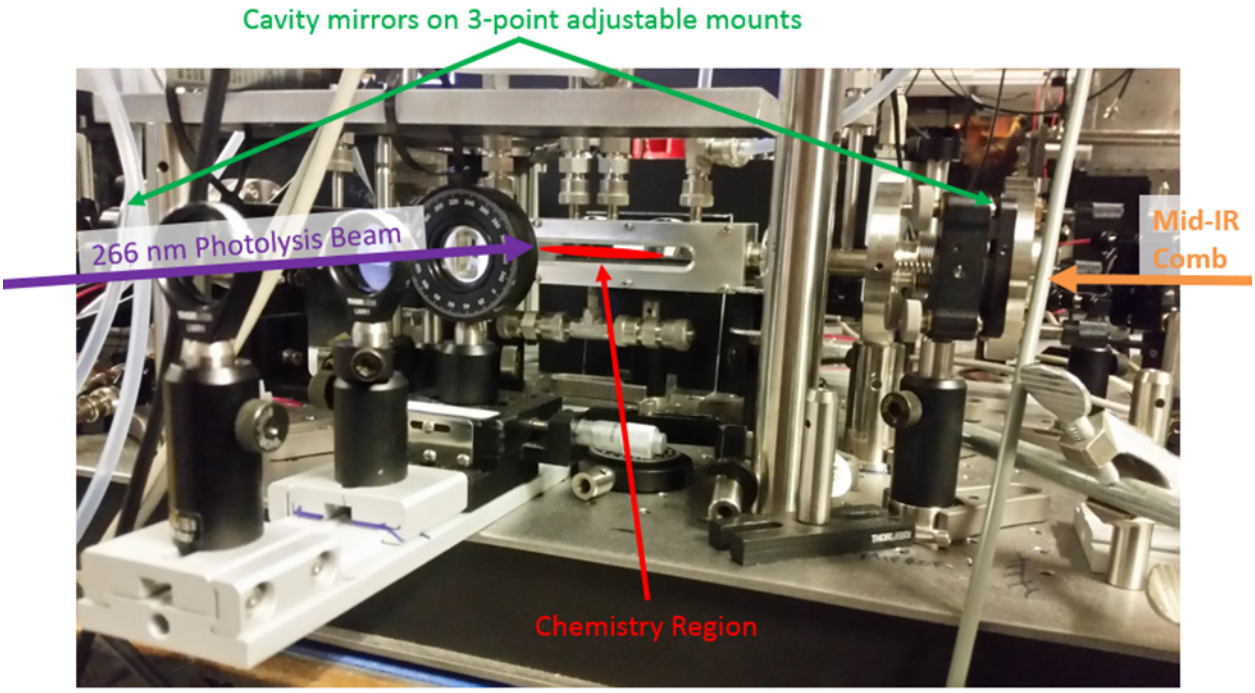

Figure 3.5: TRFCS flow cell

Since the pressure of the cell must be varied over a large range (0-500 torr) for kinetics measurements, it is constantly necessary to re-align the cavity to maintain resonance with the frequency comb. If just the refractive index of N_2 is considered, the effective cavity length will change by 20 μm per 100 torr increase in N_2, which is more than the range of the long-throw piezo on the output coupling mirror. In practice, the length of the cell actually changes much more than this due to pressure-induced mechanical deformations. To allow for easier alignment, two three-point mounts were installed on the input and output of the cavity, shown in Fig. 3.6.

3.5 Virtually Imaged Phased Array (VIPA)

The output of the optical cavity is then spectrally resolved using a mid-infrared Virtually Imaged Phased Array (VIPA)[94], which spatially disperses the light and allows for time-resolved measurements. VIPA etalons were first demonstrated in the near-infrared and optical spectral regions and are currently manufactured in the near-infrared spectral region by several companies. However, these parts are commonly produced with fused silica substrates, which begins to absorb near 2800 nm. This absorption would effectively degrade the quality factor of the VIPA etalon, worsening its transmission and spectral resolution. An alternative material is silicon, which is very transmissive in the mid-infrared.

The VIPA etalon itself consists of a transparent material with a highly-reflective (HR) coating on the input surface (~99.99%) and a partially transmissive (PR) coating on the output surface (~98%), as shown in Fig. 3.8. There is a small anti-reflective (AR) coated entrance window on the input surface, which allows for light to be coupled into the VIPA. The mid-infrared beam is coupled into the VIPA by focusing vertically so that it is transmitted through a small gap in the HR coating on the input surface, as shown in Figure 3.7. The beam size must be constrained such that the beam reflected off of the PR surface does not clip on the input edge.

The light from the mid-IR VIPA etalon is reflected off of a reflection grating, which disperses light along a direction that is transverse to the VIPA dispersion, and then imaged onto an InSb focal plane array. The intensity pattern on the camera then consists of a series of stripes, as shown in

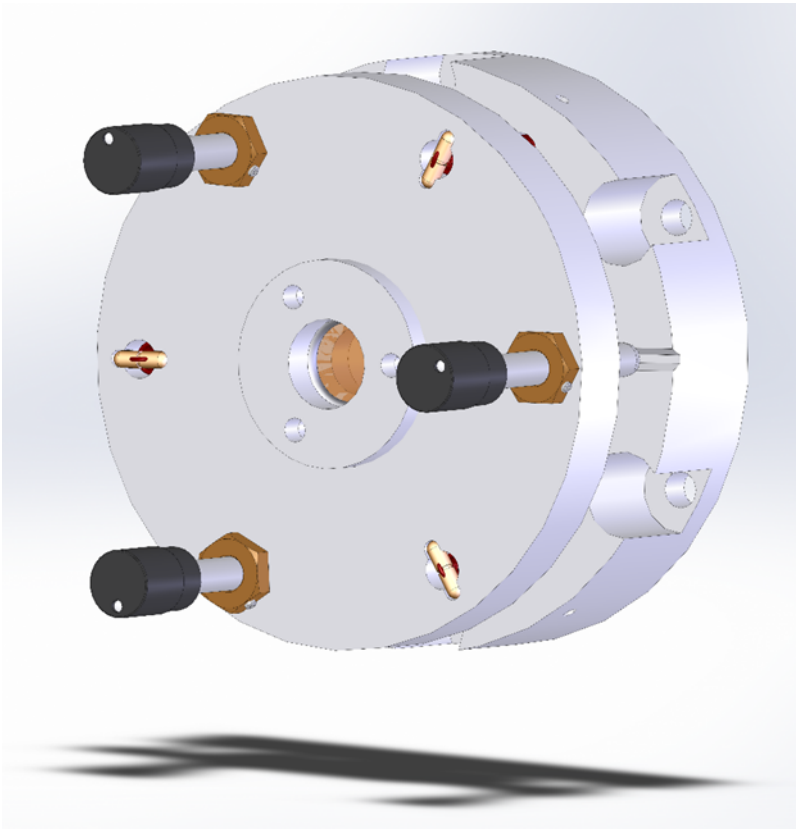

Figure 3.6: Three-point mount installed on the input and output of the reaction cell.

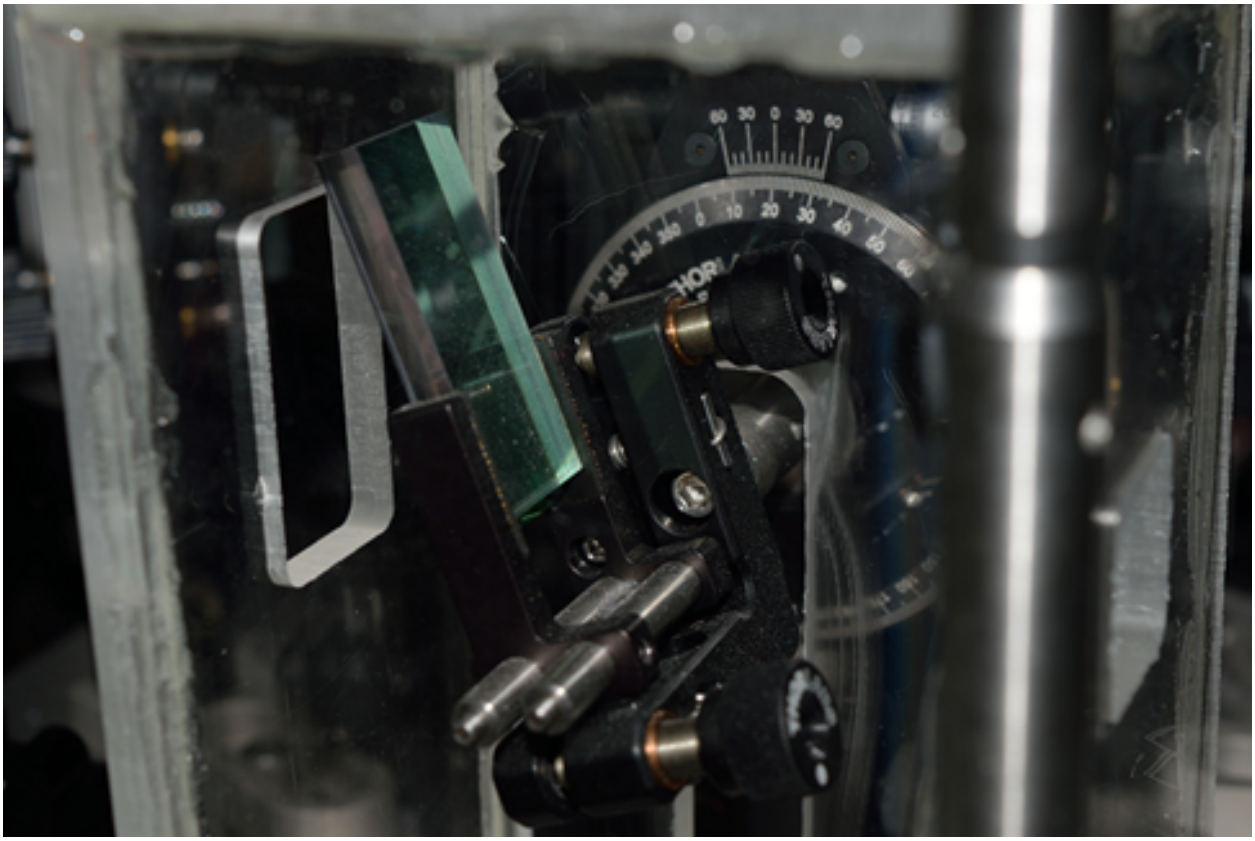

Figure 3.7: Physical picture of VIPA etalon. Mid-IR light is incident from the right. The VIPA etalon is held with a rubber clamp in the center of the image. The large size of the etalon is due to a thick (5 mm) fused silica optical flat for mechanical stability.

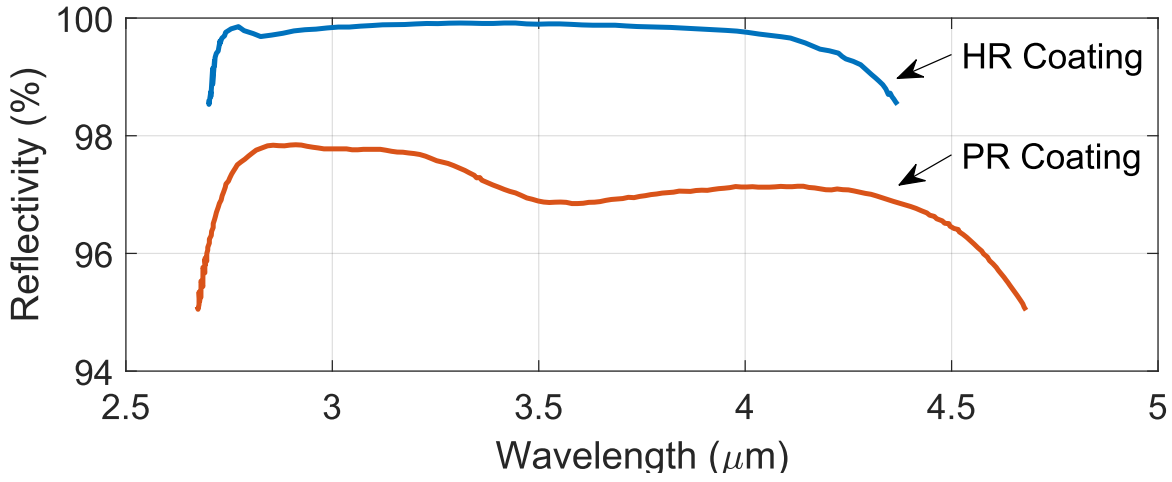

Figure 3.8: Reflection spectrum of the mid-IR VIPA etalon for the input (HR) and output (PR) faces.

Figure 3.9b. Without the grating, these stripes would all overlap, as shown in Figure 3.9a, where the camera response is shown with the grating set to zero-order. Finally, Figure 3.9c shows the camera response with N_2O in the beam path. The black spots in the image indicate strong absorption by N_2O. An alignment strategy for the VIPA spectrometer is described in an earlier thesis of our lab[21].

The intensity pattern at the detector is given[21] by the product of the response functions of the VIPA (y-direction) and grating (x-direction),

$$I_{det}(x,y,\omega) \propto I_{in} e^{-\frac{2f_c^2 y^2}{f^2 w^2}} \frac{1}{(1-Rr)^2 + 4Rr\sin^2(k\Delta/2)} e^{\frac{-2(x-\alpha\omega)^2}{\omega_0^2}} \tag{3.2}$$

$$\Delta = 2tn_r\cos(\theta_v) - 2t\frac{\tan(\theta_v)\cos(\theta_{iv})y}{f} - \frac{t\cos(\theta_v)y^2}{nf^2}\ . \tag{3.3}$$

In these expressions, w is the incident beam radius, $k = 2\pi/\lambda$ is the wavenumber of the beam, and the other parameters are described in Table 3.1. The instrument lineshape functions in the x and y directions are thus Gaussian and Lorentzian, with FWHM of $2/\omega_0^2$ and $\frac{c(1-Rr)}{2\pi tn\cos(\theta_v)\sqrt{Rr}}$, respectively. The frequency dispersion in the y dimension is given by

$$\frac{\Delta\lambda}{\Delta y} = -\frac{2t}{mf}\left[\tan(\theta_v)\cos(\theta_{tv}) + \frac{\cos(\theta_v)y}{nf}\right]\ . \tag{3.4}$$

Parameter	Value	Description
λ	3.8 μm	Wavelength of light
w_0	4 mm	Incident beam collimated size
n	3.3	Index of refraction (silicon)
θ_{iv}	15°	VIPA etalon incident angle
θ_v	4.5°	VIPA internal angle, given by $\sin^{-1}\left(\frac{1}{n}\sin(\theta_{iv})\right)$
t	0.8 mm	Etalon thickness
f	308 mm	Focal length of imaging lens
f_c	254 mm	Focal length of cylindrical lens
R	99.8%	HR surface reflectivity
r	98%	PR surface reflectivity

Table 3.1: VIPA alignment parameters

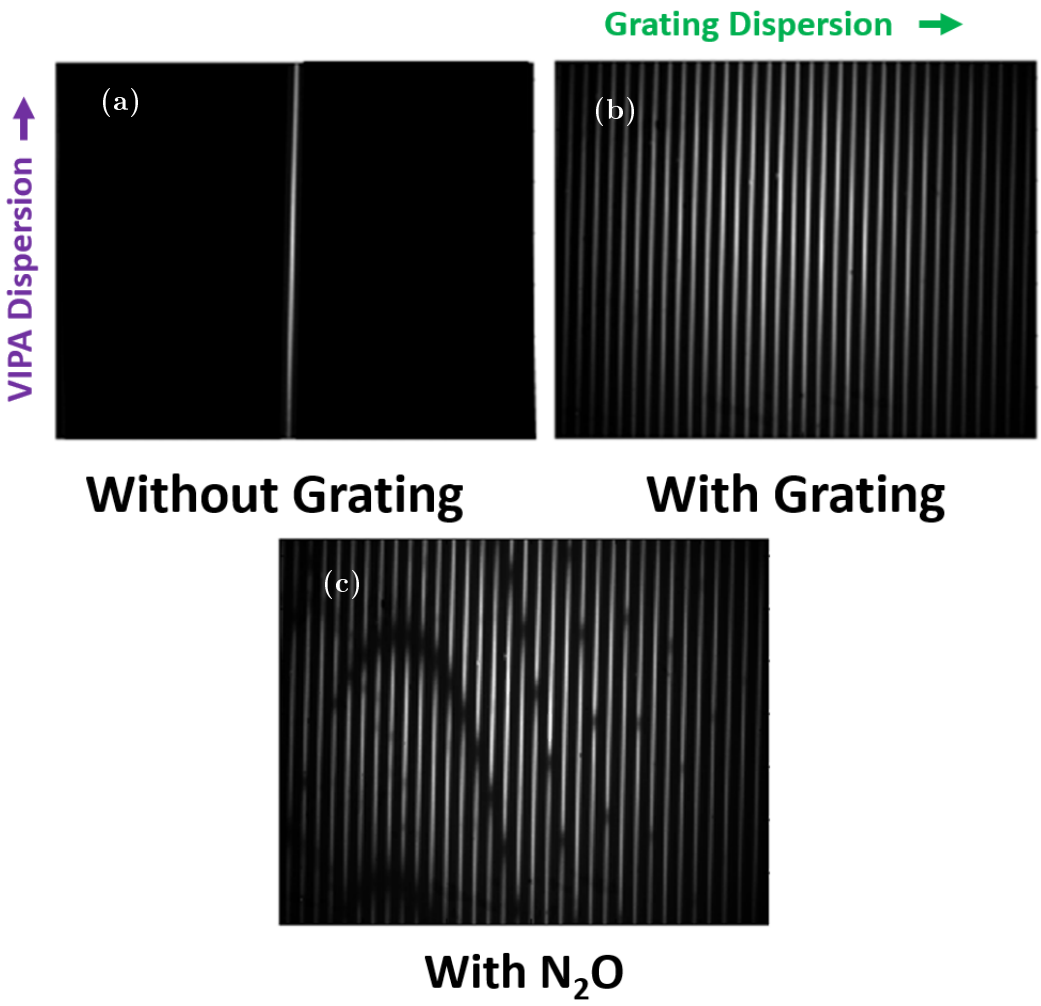

Figure 3.9: Camera image with the grating set to (a) zero and (b) first order. Introduction of N_2O into the beam path results in image (c), where the black bands indicate absorption.

To obtain a 1D spectrum (absorbance vs. wavelength), three steps are followed:

1. Identify (x,y) position of VIPA fringes.
2. Integrate over the horizontal extent of each fringe and construct a matrix consisting of vertical pixel vs. fringe number
3. Identify absorption features and fit to known line positions to determine the wavelength calibration.
4. Flatten these objects to obtain arrays A and $\tilde{\nu}$.

Step (1) is achieved by beginning in the vertical center of the image and walking up and down the fringes, recording their horizontal position. MATLAB code for this procedure is given in Appendix C. Step (2) is simply a discrete convolution operation, which is achieved easily in MATLAB. Step (3) is a bit more complicated. We now have a 2D array of integrated intensities, which we need to associate with corresponding wavelengths. From Eq. 4.1, we note that the VIPA vertical dispersion is approximately given by a second order polynomial in vertical (y) camera position. The horizontal dispersion is given by the FSR of the VIPA. Therefore, the wavelength calibration function, $\tilde{\nu}(n, y)$ is given by $\tilde{\nu}(n, y) = \tilde{\nu}_0 + a_1(n - n_0) + a_2(y - y_0) + a_3(y - y_0)^2$, where n_0 and y_0 are taken to be the center of the fringe image so that $\tilde{\nu}(0, 0)$ is the optical frequency at the center of the images. By observing many molecular features, $\tilde{\nu}_0$, a_1, a_2, and a_3 may be fitted to obtain the calibration.

Since the resolution bandwidth of the VIPA is larger than the repetition rate of our frequency comb, comb teeth cannot be resolved. Without resolving individual comb teeth, the spectral resolution of the system is limited to the VIPA resolution. However, better resolution can be achieved at the expense of total power by filtering the comb. There are generally two methods for doing this. The first option is to build a short cavity with its FSR set to a large multiple of frep, for example FSR $= 20 f_{rep}$. In this case, every 20th comb tooth will be transmitted through the cavity, with all other teeth rejected. The repetition rate of the transmitted comb is thus $20 f_{rep} \cong 2.7$ GHz. A similar option is to match FSR of the filter cavity to a Vernier multiple of the repetition rate, say

FSR $=(8/5)f_{rep}$. In this case, the repetition rate at the output of the cavity will be $8f_{rep}$ (8 being the numerator of the irreducible fraction 8/5). This approach was used in Spaun *et al.* [85].

To determine the spectral resolution of the VIPA, the first approach was used: a filter cavity was constructed with an FSR of 2 GHz, enough to resolve individual comb teeth. A comb-mode-resolved camera image is shown in Fig. 3.10. Since the comb teeth are very narrow relative to the VIPA response function, the vertical and horizontal widths of the spots yield the response functions for the VIPA and grating, respectively.

3.6 Locking the Cavity

As mentioned earlier, there are two main methods of ensuring efficient coupling between comb teeth and cavity modes, the tight lock and the sweep lock. Early on, the tight lock was utilized in the kinetics experiments due to its high on-resonance transmission. However, this can cause problems in photolysis experiments where there is a sudden jump in gas pressure and hence the effective optical path length within the cavity. The sweep lock is significantly less sensitive to this pressure jump and also helps to reduce other frequency-to-amplitude noise conversion processes.

The cavity sweep lock is performed in our case by sweeping the repetition rate, f_{rep}, of the mid-IR frequency comb source with a 50 kHz sine wave. As the frequency comb teeth come into resonance with the cavity modes, the cavity transmits a pulse of light. This transmission signal is mixed with a phase-shifted version of the repetition rate modulation signal, low-passed, and fed back to the cavity piezo. The sweep signals and cavity transmission are shown in Fig. 3.13.

3.7 Timing

Since this is a chemical kinetics experiment, it is necessary to properly synchronize each of the elements of the experiment. A simplified timing diagram is indicated in Fig. 3.11. The repetition rate of the Yb oscillator is swept with a 50 kHz sine or triangle wave (DS345 function generator) using its fast PZT. The 50 kHz synchronization signal from the function generator is used to trigger

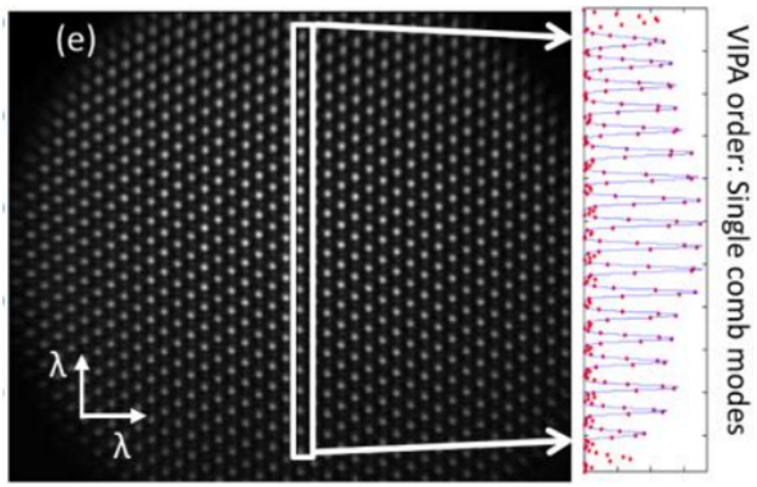

Figure 3.10: Comb mode resolved VIPA image obtained by filtering the 136 MHz comb through a 2 GHz filter cavity.

an Arduino, which generates the YAG, optical shutter, and FLIR camera trigger.

3.8 Temporal Resolution and Sensitivity

There are two key parameters that characterize TRFCS, the temporal resolution and the absorption sensitivity. The temporal resolution is given by the ringdown time of the cavity of length l_{cav} and finesse F,

$$\tau = \frac{F l_{cav}}{\pi c}. \tag{3.5}$$

The absorption sensitivity, however, is determined by the incident power on the camera, I relative to any noise processes, δI, scaled by the effective cavity interaction length, $l_{eff} = \beta F l_{cav}$ (see §2.2). This yields $\alpha_{min} = \frac{\delta I}{I}\frac{1}{\beta F l_{cav}}$. A few noise sources in this experiment include:

1. Intensity noise, ($\delta I_{int} = A_{int} I$). This originates from either intensity fluctuations of the OPO comb or frequency-to-amplitude noise conversion in the cavity.

2. Shot noise, ($\delta I_{shot} = A_{shot}\sqrt{I}$).

3. Camera dark noise, ($\delta I_{dark} = A_{dark}$). There are two main processes here: camera readout (or

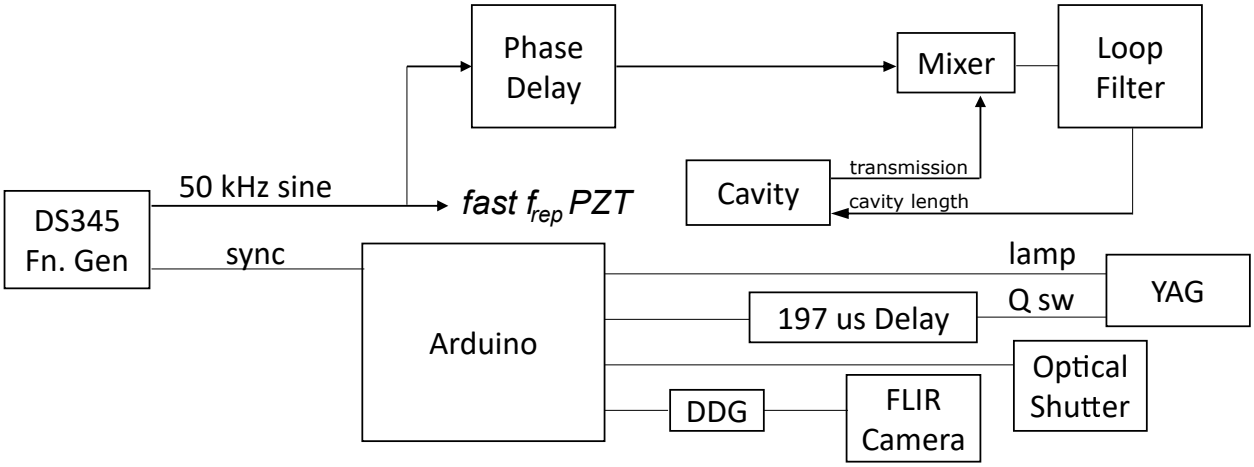

Figure 3.11: Locking diagram for TRFCS experiment.

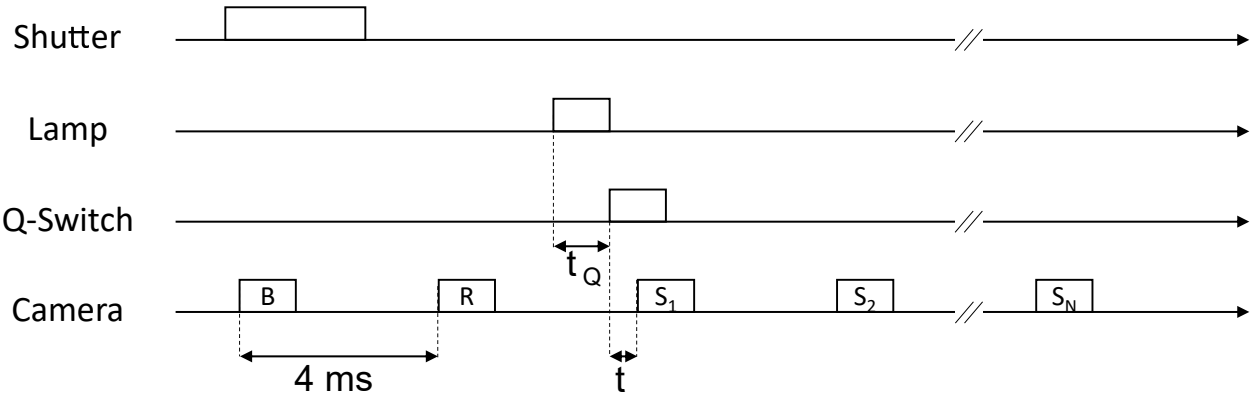

Figure 3.12: Timing diagram for TRFCS experiment.

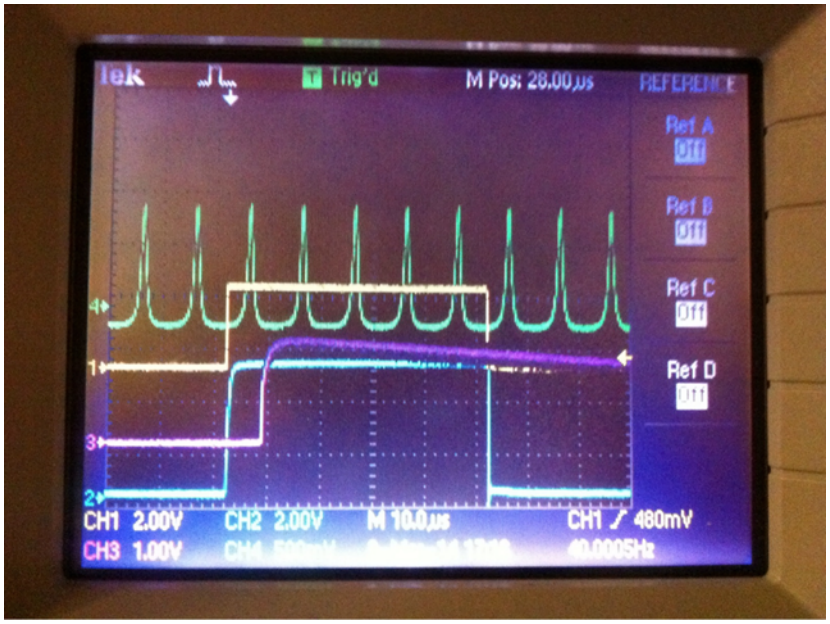

Figure 3.13: Oscilloscope screenshot of sweep signals. The green and yellow signals correspond to the cavity sweep and camera integration window, respectively.

digitization) noise and dark current noise.

In these expressions, A_{int}, A_{shot}, and A_{dark} are the intensity-independent scaling for each process. These noise processes scale with the intensity and camera integration time as

$$(\delta I)^2 = (A_{int} I)^2 + (A_{shot}\sqrt{I})^2 + (A_{dark})^2. \tag{3.6}$$

The minimum detectable absorption is then $\alpha_{min} = \frac{1}{\beta F l}\sqrt{(A_{int})^2 + (A_{shot})^2/I + (A_{dark})^2/I^2}$. In this setup, the δI_{dark} term was dominant, so $\alpha_{min} \propto A_{dark}/(FI)$ was heavily dependent on the total incident intensity on the camera. Practically, there are two elements that mainly limit the total intensity of light on the camera: the optical cavity and the VIPA etalon. Our optical cavity has an on-resonance transmission of approximately 36%, while the VIPA etalon has a transmission of approximately 20%.

3.9 Demonstration of the time-resolved spectrometer: acrylic acid

To demonstrate TRFCS for use in the analysis of chemical reactions, it was applied to the photolysis of acrylic acid. This photolysis pathway has been studied previously and it is a well-known method for generating HOCO/DOCO species[95, 96]. At 193 nm, there are four primary photodissociation pathways[97]:

$$H_2C = CHCOOH + h\nu \rightarrow H_2C = CH + HOCO \tag{3.7}$$

$$\rightarrow H_2C = CHCO + OH \tag{3.8}$$

$$\rightarrow H_2C = CH_2 + CO_2 \tag{3.9}$$

$$\rightarrow H_2C = COH + CO \tag{3.10}$$

Of particular concern is eq. 3.7, the $\pi \rightarrow \pi^*$ C-C transition, which is known to generate *trans*-HOCO. Additionally, partially deuterated acrylic acid, acrylic acid-d_1 (AA-d_1) is used and the OD stretch is monitored to avoid contamination by water lines at 3600 cm^{-1}. AA-d_1 exists as one of two isomers, as shown in Fig. 3.14. Theoretical calculations suggest that the *s-cis* isomer is more stable by about 2.5 kJ mol^{-1}[98]. At room temperature ($\sim$ 2.5 kJ mol^{-1}), this means that about 37% of the molecules will be in the *s-cis* state.

AA-d_1 is a liquid at room temperature, so it is necessary to use a carrier gas (N_2) to introduce it to the reaction cell. This was done using a custom-designed bubbler, shown in Fig. 3.15. The total pressure and temperature of the cell were maintained at approximately 12 torr and 21 °C,

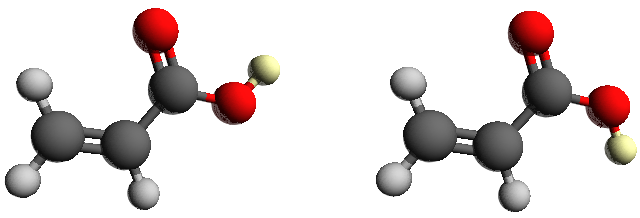

Figure 3.14: AA-d_1 exists in two stable planar forms, s-*cis*-AA-d_1 (left) s-*trans*-AA-d_1 (right) [99].

respectively.

Once in the cell, the concentration of AA-d_1 is readily determined by absorption spectroscopy of its fundamental ν_1 band (OD stretch). An example of such a spectrum is given in Fig. 3.16. Since there are no known spectral information available for AA-d_1, the concentration was determined by shifting and scaling the absorption spectrum from undeuterated acrylic acid. The fine structure that appears in the blue trace is due to periodic baseline oscillations. From this analysis, we determined that the AA-d_1 concentration is approximately 4×10^{14} molecules cm^{-3} over the cell's 12 cm chemical interaction region.

A 10 ns, 193 nm ArF laser (Optex Pro) was used to photolyze the AA-d_1 at a repetition rate of 0.2 Hz, with an energy of 4.8 mJ and a spot size of 1 cm×3 cm. By monitoring the time-dependent concentration of AA-d_1, the fractional photolysis and cell residence time may be estimated, as shown in Fig. 3.17. From the exponential fit, we determine a maximum depletion of $1.61\% \pm 0.04\%$ and a pump-out rate of $k_{pump} = 3.0 \pm 0.1$ (1σ statistical uncertainty from the fit). The expression for the photodepletion of AA-d_1 in terms of its 193 nm absorption cross-section, σ_{AA}, is

$$\frac{[AA]}{[AA]_0} = 1 - \exp(-\sigma_{AA}\Phi H), \tag{3.11}$$

where Φ is the photodissociation quantum yield and H is the 193 photon fluence in photons cm^{-2}. Assuming $\Phi = 1$ and a photon fluence of $H \approx 1.6 \times 10^{15}$ photons cm^{-2} yields $\sigma_{AA} = 1 \times 10^{-17}$ cm^{-2}, which is close to the value (7.5×10^{-18} cm^{-2}) reported in Ref. [100].

In addition to the depletion of AA-d_1, the formation of *trans*-DOCO, HOD, and D_2O were observed, as shown in Fig. 3.18. The P, Q, and R branches of the *trans*-DOCO rovibrational spectrum can clearly be seen within the 40 cm^{-1} bandwidth, but the HOD and D_2O bands are too broad to be seen in their entirety. The formation of *trans*-DOCO from Eq. 3.7 is not surprising, but the prompt formation of HOD is unexpected. A fit of the *trans*-DOCO spectrum from Fig. 3.18A yields a concentration of $(3.1 \pm 0.5) \times 10^{12}$ cm^{-3}. Moving to another spectral region, we are able to observe the ν_3 P-branch of deuterated acetylene, C_2HD, directly following photolysis, shown in Fig. 3.19. This spectrum was assigned using a line list measured by Baldacci *et al* [101]. A

Figure 3.15: Bubbler used to introduce AA-d_1 to the reaction cell.

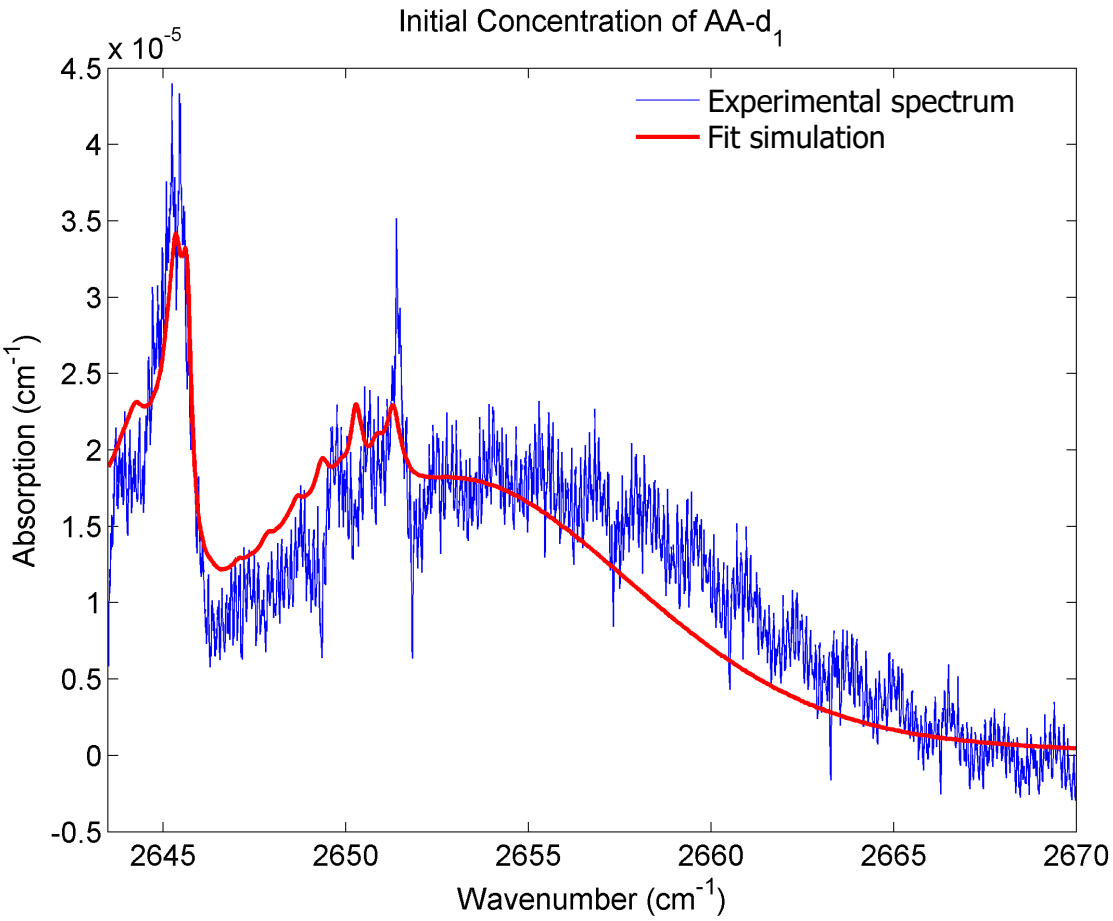

Figure 3.16: Typical broadband absorption spectrum of AA-d_1 in blue. A shifted spectrum (red) of undeuterated acrylic acid is used to fit the concentration.

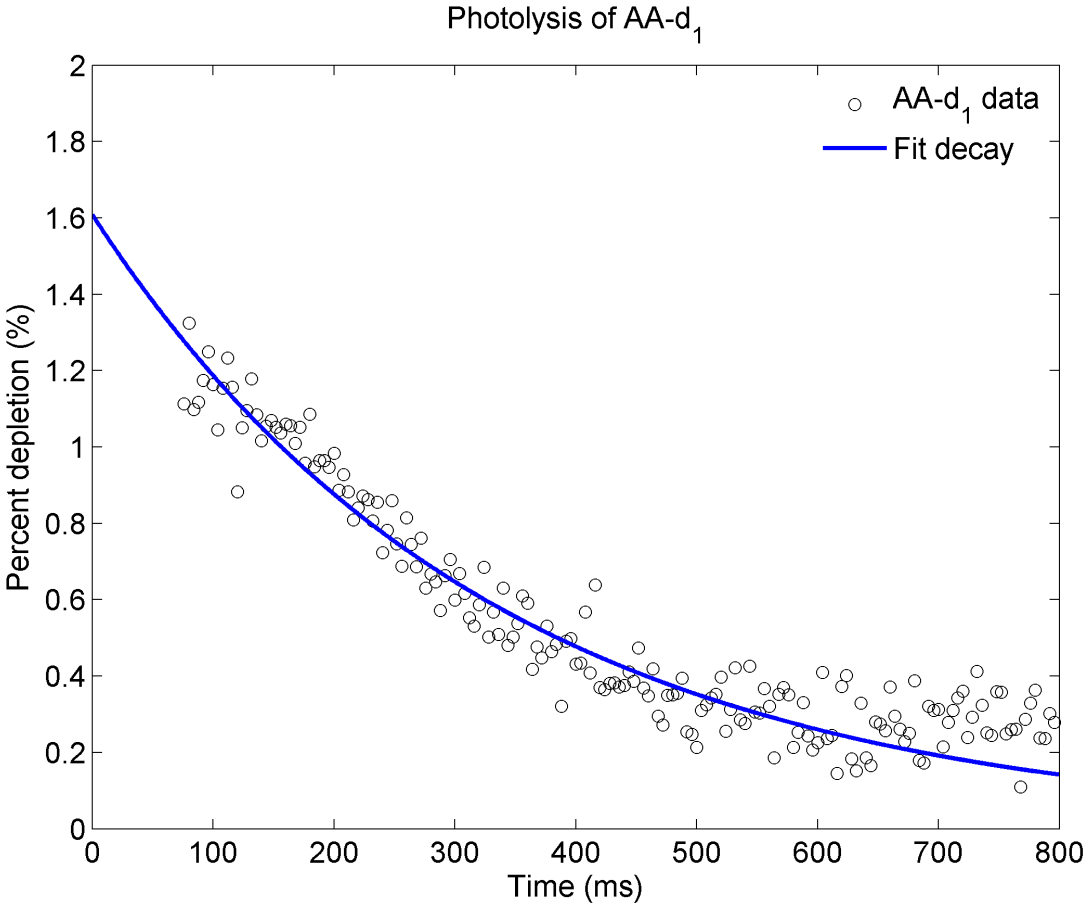

Figure 3.17: Percent depletion of the integrated AA-d_1 band intensity as a function of time (50 μs integration time) after the 193 nm photolysis pulse. An exponential decay fit (blue) reveals a pump-out rate of $k_{pump} = 3.0 \pm 0.1$ s^{-1}.

calculated fundamental band intensity of 20.6 km mol^{-1} was obtained by calculating the optimized geometry and fundamental vibrational frequencies and intensities at the CCSD(T)/aug-pVDZ level using CFOUR[102].

By fitting the time-dependent spectra of all of these species, we are able to see their formation and decay characteristics, as shown in Fig. 3.20. Three species are promptly formed: *trans*-DOCO, HOD, and C_2HD. *trans*-DOCO decays with a lifetime $k_{DOCO} = (9.6 \pm 0.9) \times 10^{-3}\ s^{-1}$, which is similar to the HOCO loss rates observed by Petty *et al*[103], which they attribute to fast bimolecular reactions with other radicals such as the vinyl radical or DOCO. At longer times ($> 200\ \mu s$), D_2O grows as HOD decays, likely due to the isotope exchange reactions HOD+HOD and HOD+AA-d_1.

The observation of prompt HOD and C_2HD is surprising. Bulk phase experiments have found evidence for CO (carbonylation), CO_2 (carboxylation), and HOCO products[104]. In molecular beam experiments, photodissociation leads only to two prompt channels, Eqs. 3.7 and 3.8 [97]. Such high yields of HOD and C_2HD suggest that AA-d_1 undergoes isomerization reactions leading to intramolecular H-atom abstraction, as well as H/D exchange or D-atom insertion. This would yield a full dehydrocarbonylation reaction of the form

$$\begin{aligned} H_2C=CHCOOD + h\nu \rightarrow\ & C_2HD + H_2O + CO \\ \rightarrow\ & C_2H_2 + HOD + CO \end{aligned} \quad . \tag{3.12}$$

The observation of prompt C_2H_2 and H_2O may help elucidate this mechanism. Clusters are another possible pathway for the formation of C_2HD and HOD; acrylic acid is well known to form dimers and larger clusters at room temperature. However, based on the dimerization equilibrium constant of $K_p = 2.6$ torr (measured by Osborne *et al*, Ref. [104]), and the spectroscopically measured partial pressure of AA-d_1, the fraction of dimers is estimated to be $< 1\%$. Therefore, it is unlikely that clusters are responsible for the formation of C_2HD and HOD.

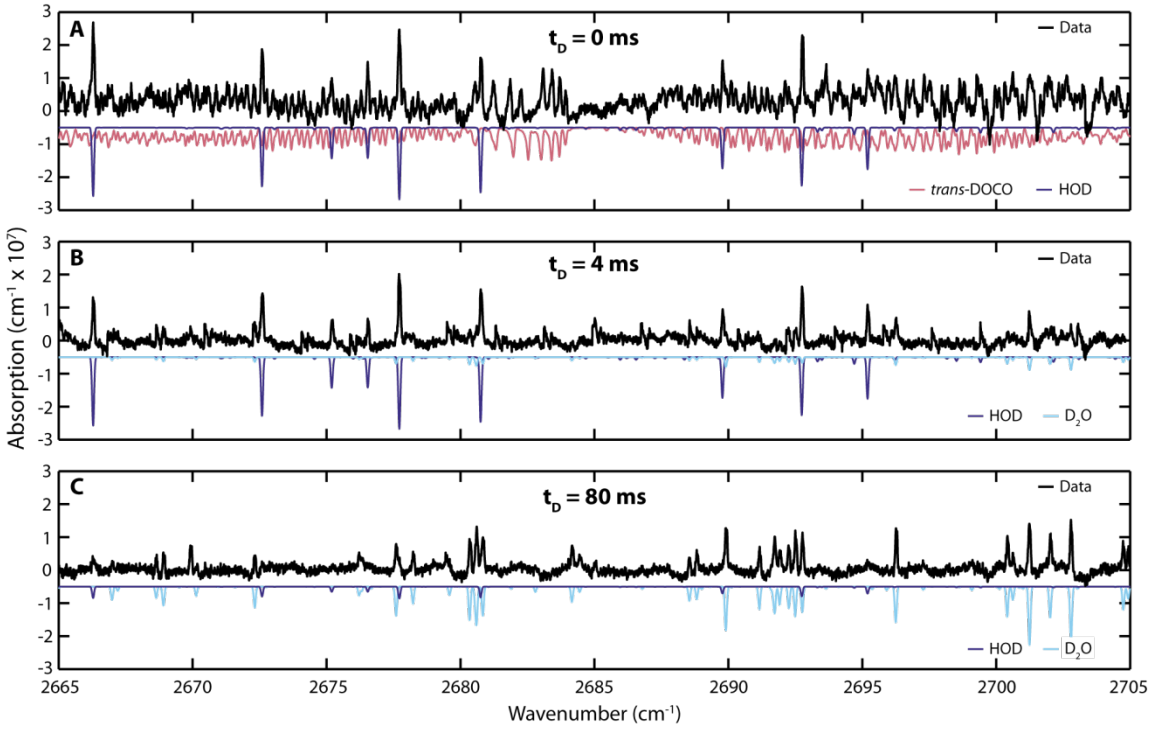

Figure 3.18: Transient absorption following the photolysis of AA-d_1. Experimental data is shown in black and molecular simulations are inverted and shown in magenta, dark blue, and light blue for *trans*-DOCO, HOD, and D_2O, respectively. The camera integration time was set to 50 µs, beginning (A) with the photolysis pulse, (B) 4 ms after photolysis, and (C) 80 ms after photolysis. The four Q-branch transitions in *trans*-DOCO are known to be perturbed by a Coriolis or Fermi interaction [95] and are not included in the fits.

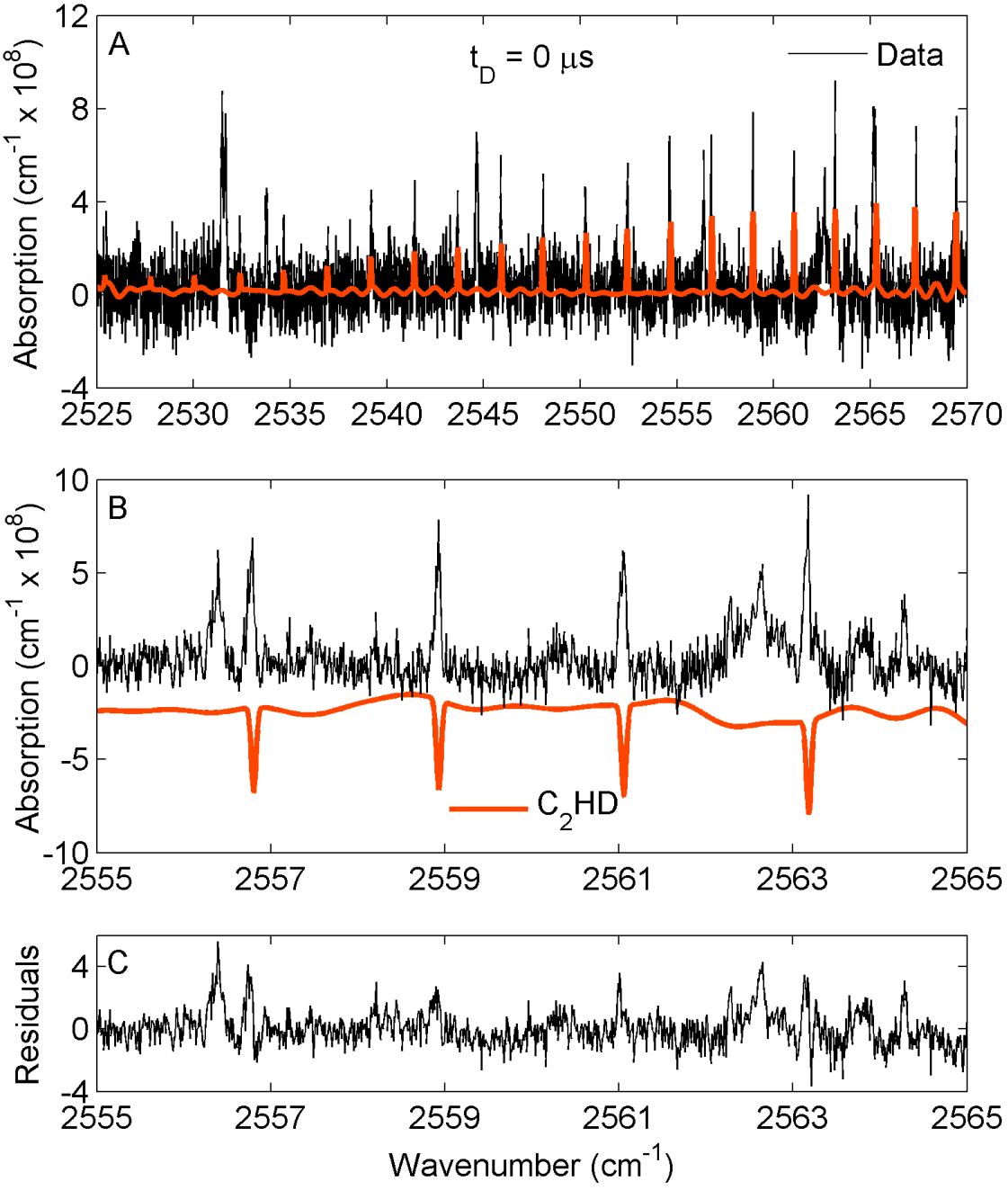

Figure 3.19: Absorption spectrum of C_2HD. Experimental data is shown in black and the fit is shown in red. The full spectrum is shown in panel (a) and a zoomed-in version is shown in panel (b), along with its fit residual in panel (c).

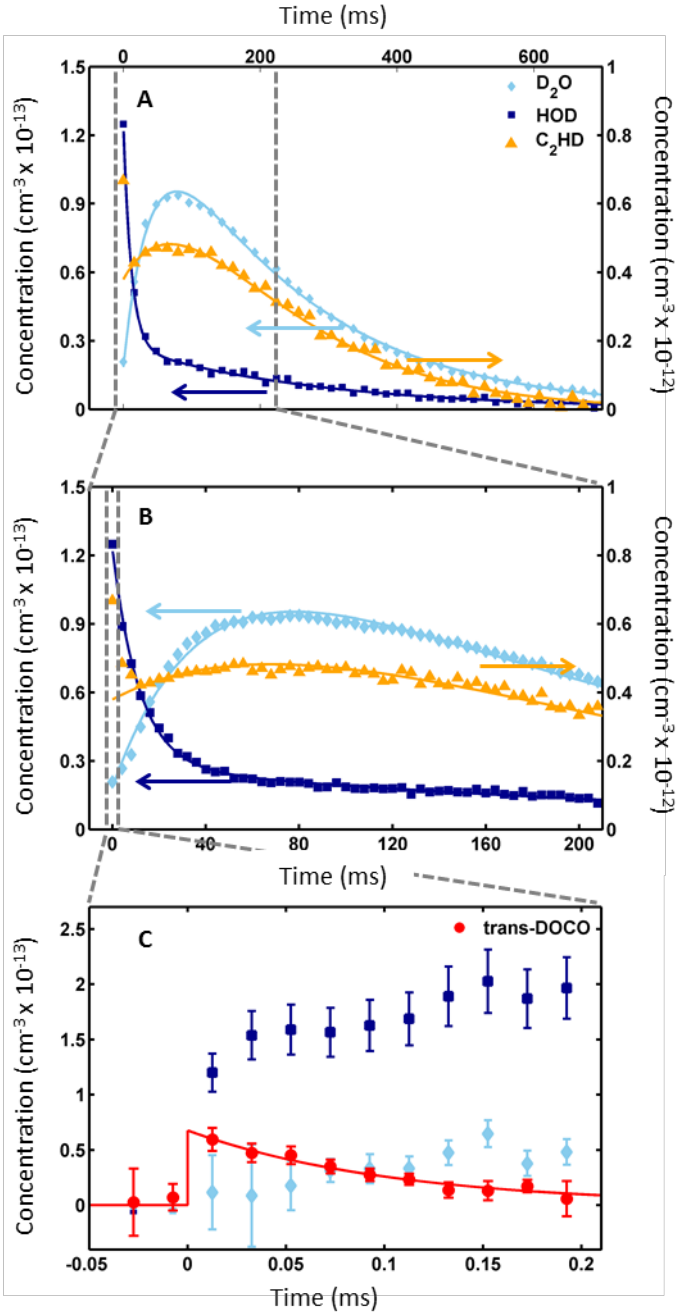

Figure 3.20: Measured absolute concentrations of HOD (dark blue squares), D_2O (light blue diamonds), C_2HD (orange triangles), and *trans*-DOCO (red circles) as a function of time. The CH_2D plot uses the right concentration axis, all other plots use the left axis. Panels A, B, and C are progressively zoomed-in versions of the same data set.

Chapter 4

The OH+CO Reaction: Introduction

4.1 Overview

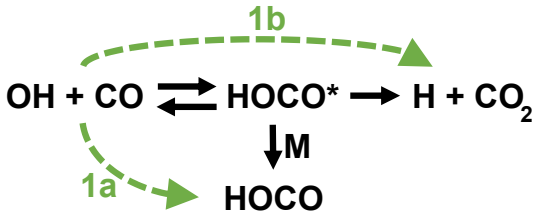

The OH+CO→H+CO_2 reaction has long been studied due to its relevance in atmospheric and combustion chemistry. When OH and CO collide, they form the energetically excited species $HOCO^*$, which may then be collisionally stabilized to ground state HOCO or react to form H + CO_2 . In the first few sections of this chapter, I will discuss the importance of this reaction in atmospheric and combustion chemistry. Later, I'll briefly introduce the history of experimental studies on this reaction.

4.2 Atmospheric Importance

The OH radical participates in many ways to the complex chemistry of the atmosphere. OH radicals are formed in the atmosphere through the photolysis of O_3 to $O(^1D)$ and its subsequent reaction with H_2O. Once formed, OH acts as the primary daytime oxidant in the atmosphere[105, 106], breaking down large organic compounds and removing them from the atmosphere. For this reason,

OH has been referred to as an "atmospheric vacuum cleaner"[107]. Additionally, OH reacts with O_3 and HO_2 to form H_2O_2. The three molecules OH, O_3, and H_2O_2 largely determine the "oxidizing capacity" of the atmosphere[108] and rough average concentrations are given in Table 4.2 along with an example reaction rate with isoprene. It is interesting to note that the atmospheric concentrations of O_3 and H_2O_2 tend to be orders of magnitude larger than OH, but the fast reaction rates of OH more than compensate for the low concentration.

A second effect of OH radicals in the atmosphere is to modulate the concentration of O_3 through their reaction with CO[111]. This modulation occurs in the troposphere through a somewhat complex series of reactions, as shown in Figure 4.1, in which OH acts as a catalyst for the net reaction CO+2 $O_2 \rightarrow$ CO_2 +O_3. Interestingly enough, this effect is reversed in the stratosphere, where OH catalyzes the destruction of O_3.

These effects make clear that any attempt to understand atmospheric chemistry must include a detailed understanding of OH+CO and other OH reactions. However, these reactions are not fully understood; current atmosperic models tend to overpredict the formation of OH and underpredict its loss[112, 113]. Additionally, the OH+CO reaction has many branching channels which may further react to re-form OH. Therefore, it is important to understand the partitioning of this reaction into its many products.

Species	Concentration (molecules cm^{-3})	k(X+isoprene) (molecules cm^{-3} s^{-1})	Rate (s^{-1})
O_3	1.8×10^{12}	9.6×10^{-18} [109]	1.7×10^{-5}
H_2O_2	2.8×10^{10}	–	–
OH	5×10^{5}	1×10^{-10}[109]	5×10^{-5}
NO_3	2×10^{7}	7.2×10^{-13} [110]	1×10^{-5}
Cl	1×10^{5}	4.3×10^{-10} [110]	4×10^{-5}

Table 4.2: Approximate concentrations and reaction rates of a few oxidating species in the atmosphere. k(X+isoprene) is the bimolecular loss rate of the species with isoprene.

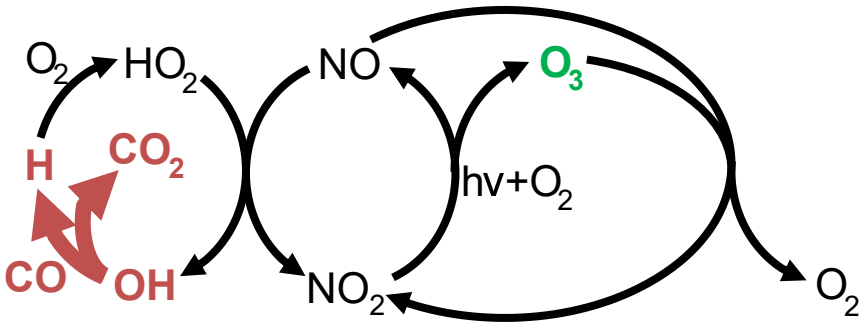

Figure 4.1: Role of OH+CO in the O_3 balance of the atmosphere.

4.3 Combustion Importance and Additional Applications

The OH+CO reaction is also of fundamental importance to combustion chemistry due to the role it plays in CO/CO_2 conversion. This reaction is of particular importance in the combustion of syngas, H_2+CO, where large concentrations of OH are formed during the reaction. The role of the OH+CO→HOCO channel in combustion processes is not yet clear, although preliminary investigations suggest that the channel may not significantly impact the combustion of syngas[114].

HOCO may also play a role in extra-terrestrial atmospheric chemistry. Boxe *et al.* have indicated that HOCO molecules generated on the surface of Mars may have an extrordinarily long lifetime of 30 μs at the Martian surface to 1.2 days at 240 km away from the surface due to the low oxygen content of the Martian atmosphere[115]. Finally, the OH+CO reaction is an important testbed reaction for computational chemistry techniques. Due to the small (3N-6=6) number of degrees of freedom, this reaction can still be tractable with current classical computer systems. Even the addition of a single atom would result in 3 additional degrees of freedom and would exponentially increase the required Hilbert space in the simulation. Quantum computers may help in this regard by allowing for polynomial scaling with system size[116], but no such device is yet powerful enough.

4.4 History of the OH+CO Reaction

The study of the OH+CO reaction has a long history, due primarily to its significance in atmospheric and combustion processes. Until the early 1970s, however, it was believed this reaction followed

a very simple Arrhenius mechanism, shown in Fig. 4.2a, in which there is only a single barrier between the reactants, OH+CO, and products, H+CO_2. In this simple case, the reaction rate may be expressed in the form $k(T) = Ae^{-E_a/(RT)}$, where A and E_a are the pre-exponential factor and the activation energy of the reaction, respectively. In a very simple sense, $e^{-E_a/(RT)}$ is proportional to the fraction of reactants above the reaction barrier and A is a steric factor dependent on the shape of the potential energy surface. The constants A and E_a are typically determined through a linear fit of an "Arrhenius plot", Fig. 4.2b, where ln(k) is plotted vs 1/T.

By 1972, the OH+CO reaction rate had been determined at a variety of temperatures and pressures, but the analysis was proving problematic within the Arrhenius framework: clearly a new approach was needed. This is perhaps most clearly illustrated by a 1972 review of hydroxyl reaction rates which states, "the hydroxyl radical has been a problem species in chemical kinetics. The accepted value for the room temperature rate constant of [OH+CO] has varied by a factor of 1000 over the last 10 years."[117]. The article primarily attributes this inconsistency to the relative difficulty in preparing the reactive OH species in the absence of other competing reactive species. This may have been part of the problem, but a much better explanation soon came from an alternative source: the reaction mechanism itself. In 1973, Smith and Zellner were able to explain the strange behavior of this reaction in terms of a reactive complex, HOCO[118]. The HOCO complex was proposed to be a short-lived, loosely bound, state between the OH+CO reactants and the products, H+CO_2. By adding this complex to the OH+CO reaction surface, as indicated in Fig 4.3a, they were able to explain the anomalous (non-Arrhenius) temperature dependence in Fig. 4.3b.

Work on this reaction accelerated and, through time-dependent studies of OH fluorescence[119, 120], more comprehensive models were developed for OH+CO reaction rate temperature and pressure dependence[119, 120, 121, 122, 123]. Additionally, microwave[124] and infrared studies[96] determined that Smith and Zellner's "HOCO complex" is actually a highly reactive, but tightly bound, molecule consisting of *trans*-HOCO and *cis*-HOCO isomers. A few reaction rates, *trans*-HOCO+O_2 and *trans*-HOCO+NO, were determined[103], showing this very fast reactivity. Progress

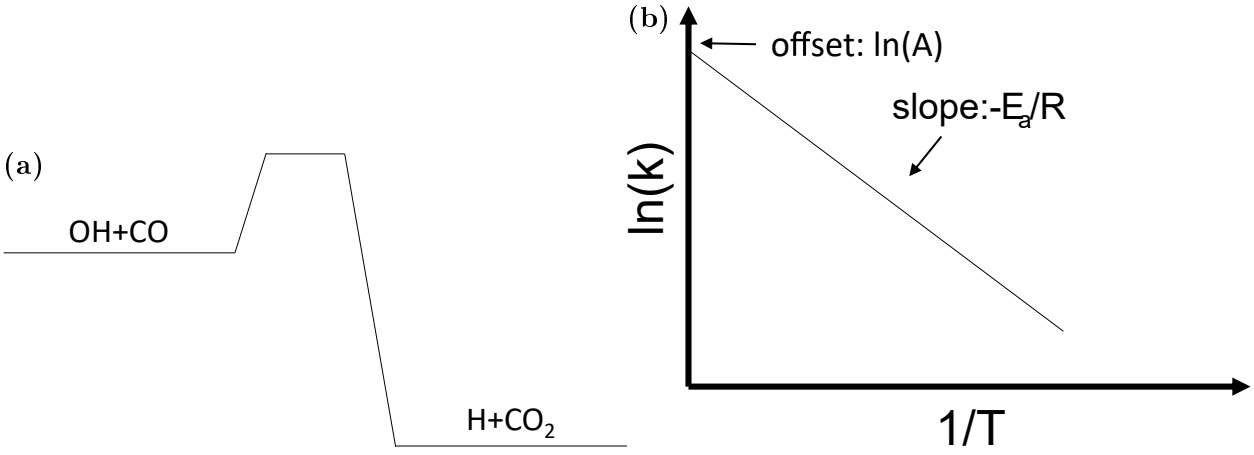

Figure 4.2: (a) Simple Arrhenius reaction surface and (b) expected temperature dependence of such a reaction.

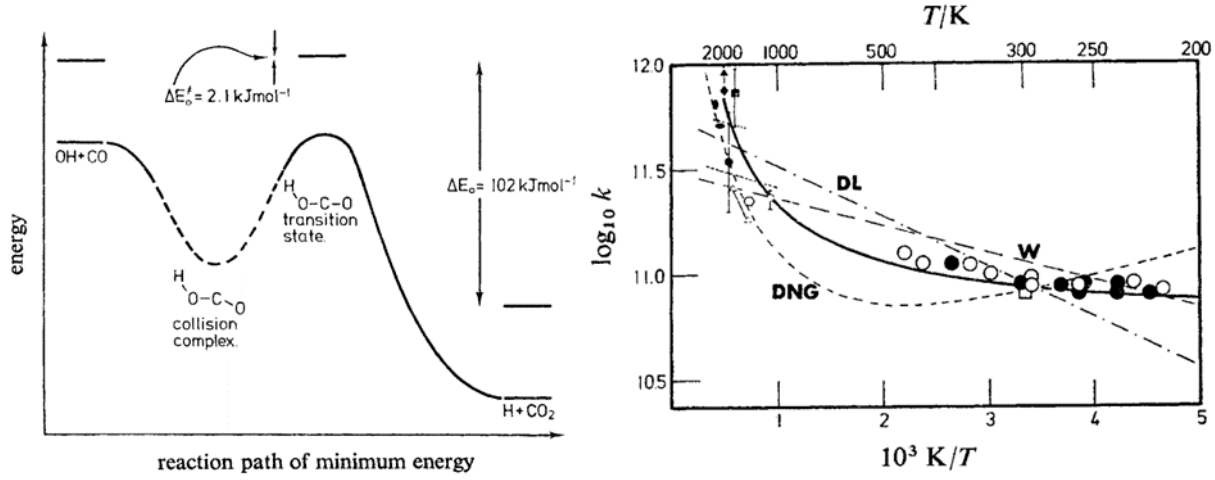

Figure 4.3: (a) Reaction surface and (b) temperature dependence of the OH+CO reaction, as determined by Smith and Zellner in 1973*[118]*. The straight lines correspond to the Arrhenius temperature dependence, which do not fit the experimental data points. These plots are reproduced from Smith *et al.[118]*.

on the deuterated reaction, OD+CO, proceeded largely in tandem, with many of the same results. The microwave and infrared spectra of *trans*-DOCO were obtained, showing its stability in its ground vibrational state[95, 125].

Despite these advances, a few key components of this reaction have remained unexplored. Since the majority of the OH+CO and OD+CO reaction rate studies only observed the loss of OH/OD in the presence of CO, they were unable to directly study the transformation of OD into its respective product channels. In fact, by 2016 there was still no direct observation of HOCO or DOCO formation from the OH+CO or OD+CO reactions. Additionally, infrared vibrational spectra of *cis*-HOCO and *cis*-DOCO had not been observed. The direct observation of *trans*-DOCO, *cis*-DOCO, and D+CO_2 from OD+CO would allow for the characterization of all relevant reaction rates and branching ratios for this reaction, allowing for unprecedented access to the OD+CO potential surface.

4.5 Mechanics of the OH+CO Reaction

The OH+CO reaction and its deuterated analogue proceed on the potential surface indicated in Fig. 4.4, where OH and CO first associate to form the rotationally and vibrationally excited $HOCO^*$ molecule. When isolated, this molecule has a lifetime on the order of ps[126], and dissociates to form H+CO_2. In the presence of large concentrations of a bath gas, however, $HOCO^*$ is vibrationally quenched to its ground vibrational state. This complex reaction pathway can be simplified into an equivalent model, with two pathways, reactions 1a and 1b. The bimolecular reaction 1a, with rate k_{1a}(P,T) describes the formation of ground state *trans*- or *cis*-HOCO, while the bimolecular reaction 1b, with rate k_{1b}(P,T) describes the formation of H+CO_2. The Lindemann mechanism yields a good first-order approximation to these parameters. As applied to the OH+CO reaction and derived in §A.2, this mechanism simply enforces the steady-state approximation for the $HOCO^*$ species ($\frac{d}{dt}[HOCO^*] = 0$) as well as CO ($\frac{d}{dt}[CO] = 0$). With these constraints, effective pressure-dependent rates k_{1a} and k_{1b} for the formation of HOCO and H+CO_2 are

$$k_1 = k_{1a} + k_{1b} \tag{4.1}$$

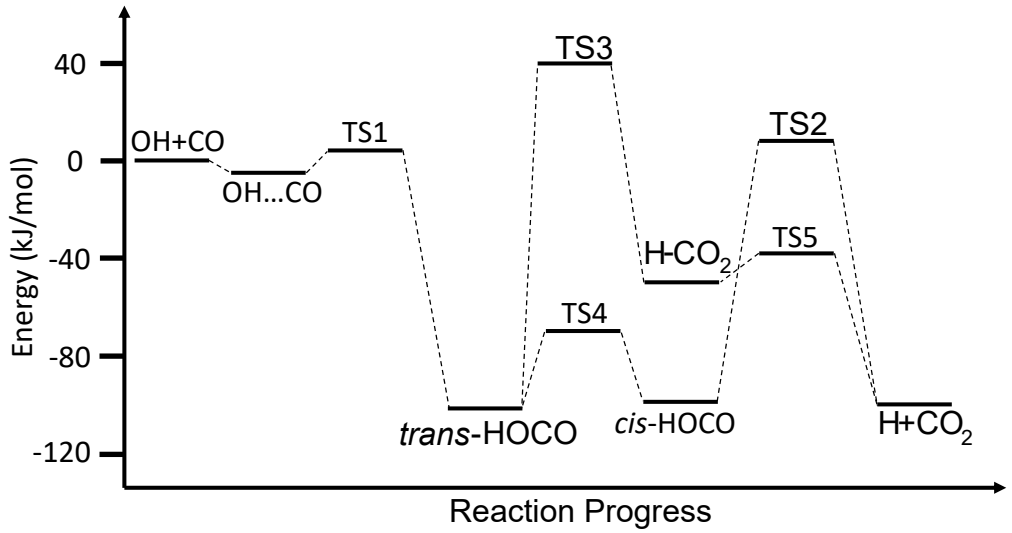

Figure 4.4: One dimensional potential energy surface for OH+CO using values from Nguyen *et al.* [123].

$$k_{1a} = \frac{[M]k_{1a,0}}{1 + [M]k_{1a,0}/k_{1a,\infty}} \tag{4.2}$$

$$k_{1b} = \frac{k_{1b,0}}{1 + [M]k_{1a,0}/k_{1a,\infty}}, \tag{4.3}$$

where the subscripts "0" and "∞" refer to zero pressure and very large pressure, respectively. At low pressures, [M]$\ll k_{1a,\infty}/k_{1a,0}$, the HOCO formation pathway, $k_{1a} \approx k_{1a,0}[M]$, is proportional to pressure and the CO_2 formation pathway, $k_{1b} \approx k_{1b,0}$, is constant with pressure. Figure 4.5 shows k_1, k_{1a}, and k_{1b} vs. [He] using experimentally-determined parameters from Fulle et al. [120]. In this case, $k_{1a,0} = 3.9 \times 10^{-33}$, $k_{1a,\infty} = 1.1 \times 10^{-12}$, and $k_{1b,0} = 1.3 \times 10^{-13}$.

While the Lindemann formalism generally gives the correct behavior of the reaction rate with pressure, it fails to provide a correct quantum treatment of the excited HOCO vibrational and rotational states. An extension to the unimolecular Lindemann theory is the Troe formalism, in which unimolecular Lindemann-type reaction rates are multiplied by broadening factors[4, 127] that affect the pressure dependence in the intermediate pressure range. The bimolecular case of OH+CO is more complicated[120], but the limiting functional form at low and high pressures remain the same

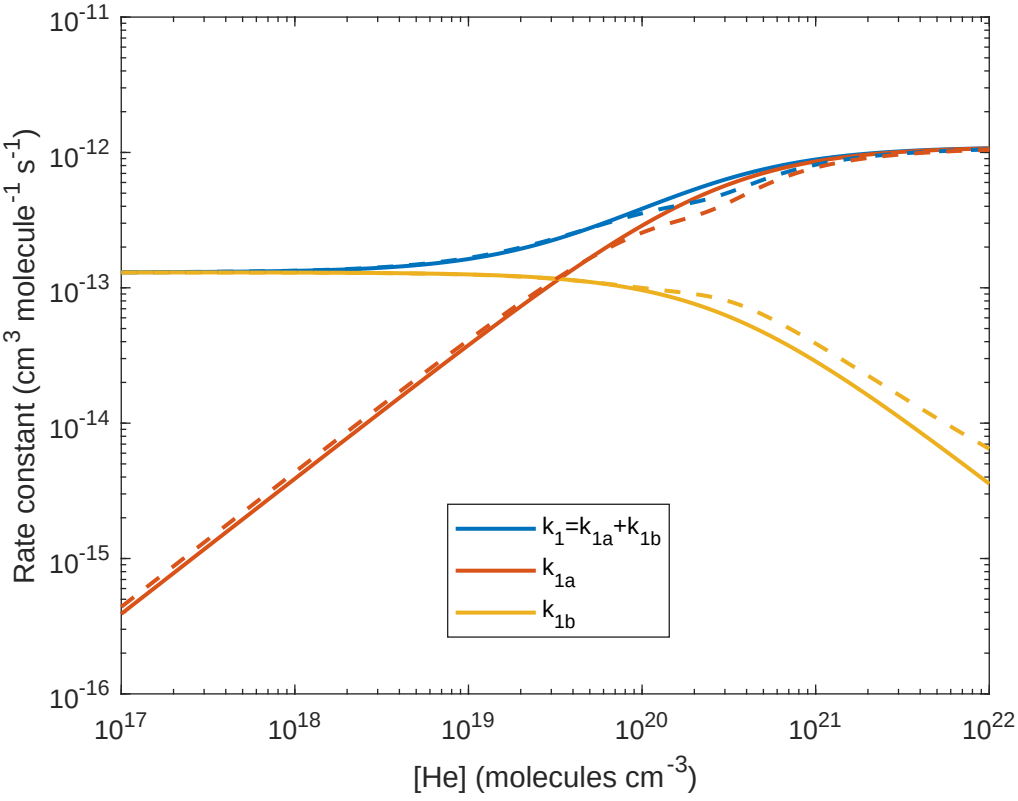

Figure 4.5: Pressure dependence of the OH+CO reaction rate within the Lindemann formalism (solid curves). Fitted reaction rates are taken from Fulle *et al.* [120]. The dashed curves include emperical broadening factors needed to fit the data in Ref. [120].

as in the Lindemann case.

4.6 Experimental Approach: OD Generation

Many methods exist for the generation of OD (and OH) radicals, a few of which are listed in Table 4.3. However, there are benefits and drawbacks associated with each method. For example, the discharge of D_2O can generate a very large concentration of OD radicals, but will inevitably generate[128] other species such as O, DO_2, and D_2O_2. Due to the difficulties in characterizing the species produced in this manner, this approach is not viable. In general, photolysis is the cleanest method of generating these radicals, since a specific molecular bond is broken by the photolysis laser. Of the photolysis-based techniques, we settled on photolysis of O_3 at 266 nm, and its subsequent reaction of $O(^1D)$ with D_2 as the ideal production pathway for OD. This decision allowed us to avoid D_2O_2 and D_2O spectral contamination in the precursor and also provided for significantly higher OD yields when compared with the photolysis of N_2O. The photolysis cross sections for O_3, N_2O, and H_2O_2 are shown in Fig. 4.6, where it is easily seen that the O_3 cross-section dominates by several orders of magnitude. Additionally, high-energy pulses at 266 nm from quadrupled pulsed YAG lasers are readily available.

Ozone itself is fairly reactive and will not live long at room temperatures. The walls of a steel vessel will catalyze its conversion to O_2 within about 1 day. For this reason, the ozone used in our kinetics experiments was generated on-demand using a commercial ozone generator and was purified with a silica-gel ozone trap at low temperature. A trap was originally constructed using the description in Ref. [130], but was modified many times and now looks considerably dissimilar. The final iteration of the trap consists of a U-shaped stainless-steel tube filled with 6-12 mesh silica gel. Due to the implosive hazards of glass dewars, we housed the ozone trap in a durable Nalgene dewar.

The general operating procedure for the ozone trap was:

1. Cool the ozone trap using a LN_2+isopropanol slurry. The slurry will become very viscous,

Pathway	Notes
$O_3+h\nu \rightarrow O(^1D)+O_2$ $D_2+O(^1D) \rightarrow OD+D$ (O_3 Photolysis)	• Very large O_3 photolysis cross-section at 266 nm • Messy D, OD, O_3 regeneration chemistry • $D_2+O(^1D)$ generates OD in high (v=9) vibration • Pure O_3 is difficult to generate and stabilize
$N_2O+h\nu \rightarrow O(^1D)+N_2$ $D_2+O(^1D) \rightarrow$ OD+D (N_2O Photolysis)	• N_2O is stable and can be easily purchased • $D_2+O(^1D)$ generates OD in high (v=9) vibration • Photolysis of N_2O is inefficient, even at low wavelengths
$D_2O_2+h\nu \rightarrow 2$ OD (D_2O_2 Photolysis)	• Pure D_2O_2 is difficult/impossible to obtain, since D_2O_2 degrades to D_2O • Severe spectral contamination by D_2O_2 and D_2O
$D_2O+e^- \rightarrow$products (D_2O Discharge)	• D_2O is readily available and D_2O discharge is well-established • Generates many reactive species • Severe spectral contamination by D_2O

Table 4.3: Methods of OD production.

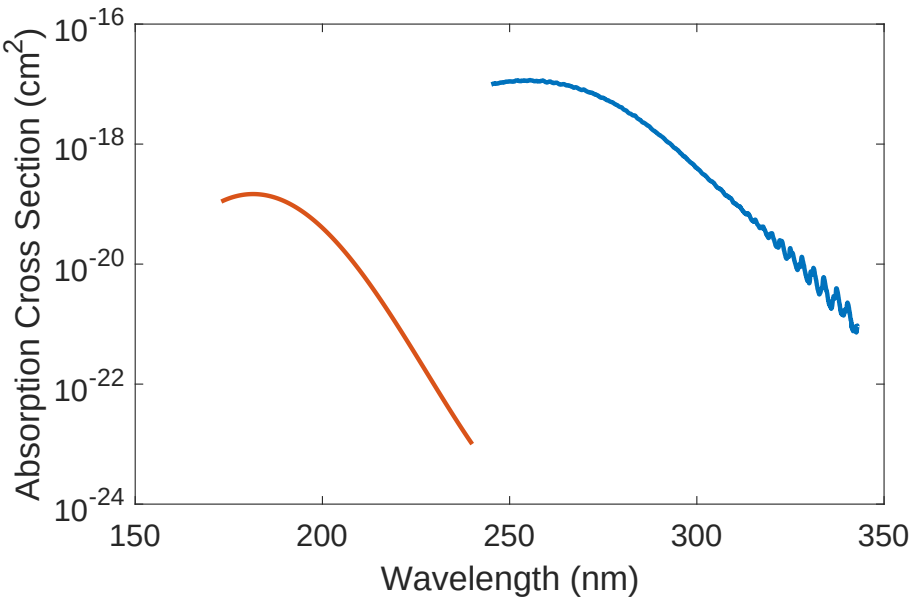

Figure 4.6: UV Photolysis cross sections for O_3 (blue) and N_2O (red). Data for O_3 and N_2O are obtained from HITRAN2012[129] and Burkholder *et al.*[6], respectively.

Figure 4.7: Photo of ozone trap.

but should not solidify.

2. Begin flowing ~2 slm O_3+O_2 over the trap. In our case, the mixture was 8% O_3 in O_2. Wait about 1 hour for the trap to fill. A large concentration of ozone behind the trap is a good indication that the silica gel is close to saturation.

3. Close the O_3 source and flow N_2 over the silica-gel, slowly releasing the ozone into the kinetics cell.

The concentration of ozone in our reaction cell was directly measured by absorption spectroscopy at 270 nm with a UV LED. The spectrum of the LED is shown in Fig. 4.8 along with the ozone cross section across the range. The large variation of ozone cross section with wavelength permits two methods for determining the concentration:

1. A "two-beam" measurement, in which the LED output is split into "reference" and "signal" beams that are sent around and through the chemistry cell, respectively. The ozone concentration in the cell is then simply given by

$$n_{O3} = -\frac{1}{\sigma_{O3} l} \ln\left(\frac{I_S}{I_R}\right) .$$

2. A "single-beam" measurement in which the LED output is sent directly through the chemistry cell onto a spectrometer (Ocean Optics USB2000+). The ozone flow is turned off and a single reference spectrum, $I_R(\lambda)$, is taken. The transmitted LED spectrum with ozone flow, $I_S(\lambda)$, is monitored and the ozone concentration is calculated using a two parameter (n_{O3},δ) linear fit to $-\ln\left(I_S(\lambda)/I_R(\lambda)\right) = n_{O3}\sigma_{O3} l - \delta$, where δ accounts for small fluctuations in the diode transmission due to varying current or slow drifts in alignment. At concentrations of 1×10^{15} molecules cm^{-3}, δ is much smaller than $n_{O3}\sigma_{O3} l$.

The total concentration of trapped ozone was determined by observing the time-dependent concentration of ozone at the exit of the trap. Ozone is trapped using the above protocol and is allowed to warm up at t=0. The measured ozone is integrated vs time to provide a total ozone flow,

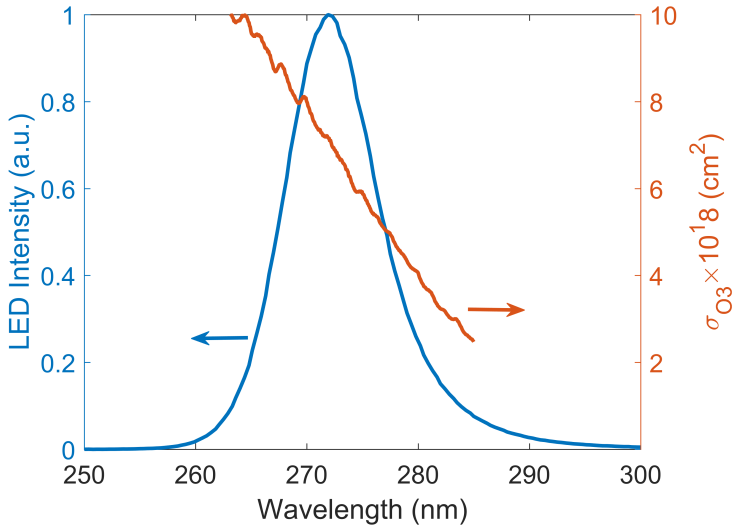

Figure 4.8: UV LED spectrum (blue, left axis) and O_3 absorption cross section (red, right axis).

shown in Fig. 4.9. By 100 mins, the ozone trap is depleted, yielding a total integrated concentration of ~160 torr min. With the measured pumping speed of 193 ml/s, the trapped ozone is determined to be 6.1×10^{22} molecules.

Additionally, extreme care must be taken during the purification process, since ozone is highly explosive[131]. Generally, this risk can be appropriately mitigated by (1) constructing the ozone trap from stainless steel to contain the potential blast and (2) ensuring that the LN_2+isopropanol slurry does not freeze, maintaining O_3 above its condensation temperature of 161 K. Finally, the ozone must be destroyed prior to being pumped out of the system to avoid damage to the pump. In order to achieve this, a copper cylinder was filled with copper mesh and heated to ~140 degrees C. This was installed directly prior to the roughing pump.

4.7 Spectral Characteristics of Key Species

The absorption spectra of a few key species are shown in Figure 4.10. Since our OPO frequency comb is tunable between 2.8 μm to 4.8 μm, we can detect each of these species by tuning our spectrum appropriately. The OD ro-vibrational spectrum is also very broad, allowing for the simultaneous detection of OD+*trans*-DOCO, OD+*cis*-DOCO, or OD+CO_2 in the same spectral window. This

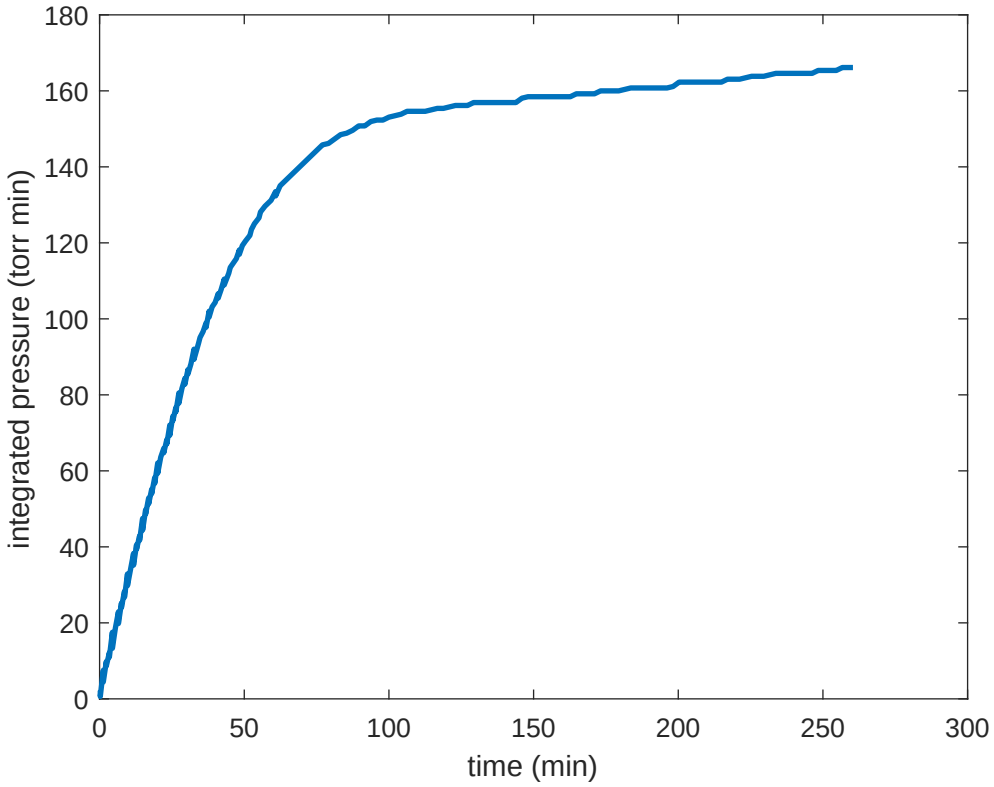

Figure 4.9: Integrated time-dependent ozone concentration.

important feature allows for the removal of the path length (given by the Finesse and photolysis length) from the analysis, since $A_{trans-DOCO}/A_{OD} = n_{trans-DOCO}\sigma_{trans-DOCO}/(n_{OD}\sigma_{OD})$ and similarly for *cis*-DOCO and CO_2. However, the relative cross sections, σ, remain important.

Line positions for OD(v=0,1) were readily available from Abrams et al [132]. Line strengths for OD(v=0,1), however, have not been measured and are necessary to calculate the OD cross section, σ_{OD}. Since the OH(v=0) cross section has been measured by Nesbitt *et al* [133, 134], it was possible to determine the OD(v=0) cross section through mass scaling.

The dipole matrix element, $\mu_{\nu',\nu''}$, is given by

$$\mu_{\nu',\nu''} = \int \psi^*_{\nu'}(r)\mu(r)\psi_{\nu''}(r)\,dr\ , \tag{4.4}$$

where ψ_ν and $\mu(r)$ are the wave function and dipole moment, respectively. Since deuteration does not change the charge of the H or O atoms, the dipole moment function remains the same for OH and OD. However, the wavefunctions are modified under deuteration. A Hamiltonian appropriate

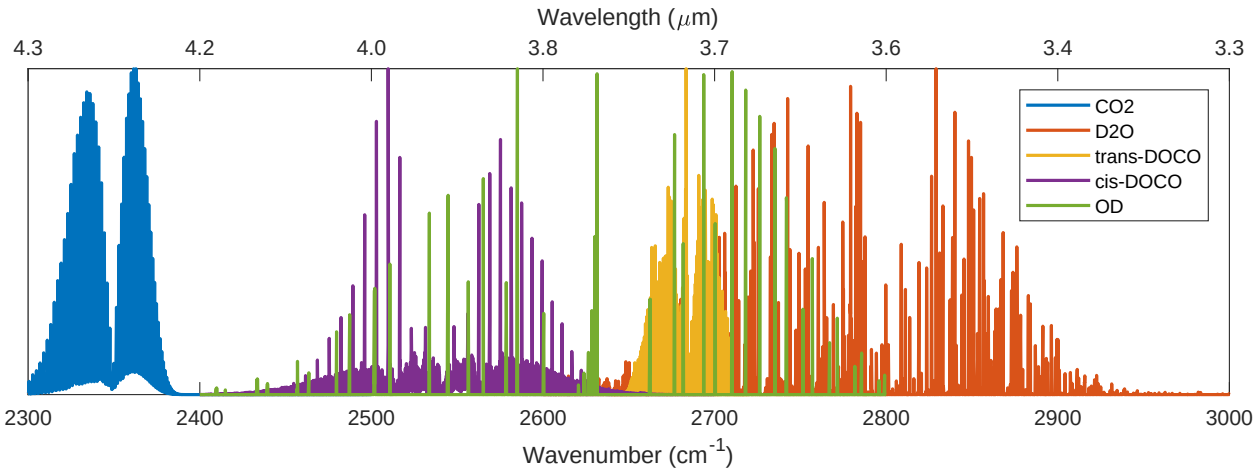

Figure 4.10: Mid-IR Absorption Spectra of Key Species.

for OH is[134]

$$H = T_r + V(r) + A(r)L \cdot S + B(r)R^2 \ , \tag{4.5}$$

where T_r is the kinetic energy operator, $V(r)$ is the OH internuclear potential, $A(r)$ is the spin-orbit coupling constant, $B(r)$ is the rotational constant, and L, S, and R are the electronic orbital, electronic spin, and nuclear end-over-end angular moment, respectively. Since the $A(r)$ and $B(r)$ terms are small, we will neglect them for this calculation. In the continuous position basis, H is

$$H(r, r') = -\frac{\hbar^2}{2m}\frac{d^2}{dr^2}\delta(r - r') + V(r)\delta(r - r') \ , \tag{4.6}$$

where m is the reduced mass. The position variables are discretized, $r, r' \rightarrow r_i, r_j$, and we use the finite difference method to approximate the derivative, $\frac{d^2}{dr^2} \rightarrow \frac{1}{(\Delta r)^2}(\delta_{i.j+1} - 2\delta_{i,j} + \delta_{i,j-1})$. This yields

$$H_{i,j} = -\frac{\hbar^2}{2m(\Delta r)^2}(\delta_{i.j+1} - 2\delta_{i,j} + \delta_{i,j-1}) + V(r_i)\delta_{i,j} \ , \tag{4.7}$$

where Δr is the grid spacing in r_i. Since $V(r)$ remains unchanged under deuteration, we use the measured OH RKR potential (shown in Fig. 4.11a) and scale the kinetic operator for the OD case.

The OH and OD vibrational wavefunctions obtained using this method are shown in Fig. 4.12 along with the OH internuclear potential.

With these wave functions determined, it is possible to calculate the dipole matrix element using the measured OH dipole moment function from Nesbitt et al [134], shown in Fig. 4.11b. Eq. 4.4 was used to calculate the dipole matrix elements for OH(v=0-3) and OD(v=0-3). These values are shown in Table 4.5 along with available experimental values.

Spectral parameters for the ν_1 ro-vibrational band of trans-DOCO have previously been determined by Petty and Moore[95]. Using PGopher, it is possible to obtain the relative line strengths within the ro-vibrational band, but a dipole moment is needed for absolute line strengths. The absolute determination of line strengths for transient reactive species is notoriously difficult, so we turned to theory. Table 4.7 includes theoretical band positions and intensities for *trans*- and *cis*-DOCO.

Finally, CO_2 required no spectral treatment, since comprehensive line positions and strengths already exist in the HITRAN database[129]. D_2O was also observed; line positions and strengths were obtained through private communication with Keeyoon Sung of JPL (see Table 5.2).

Mode	Empirical Dipole[135, 136]	This calculation
OH(01)	0.0342	0.0343
OH(12)	0.041	0.0408
OH(23)	0.040	0.039
OD(01)	–	0.0303
OD(12)	–	0.0386

Table 4.5: Experimental and calculated dipole matrix elements for OH and OD (Debye).

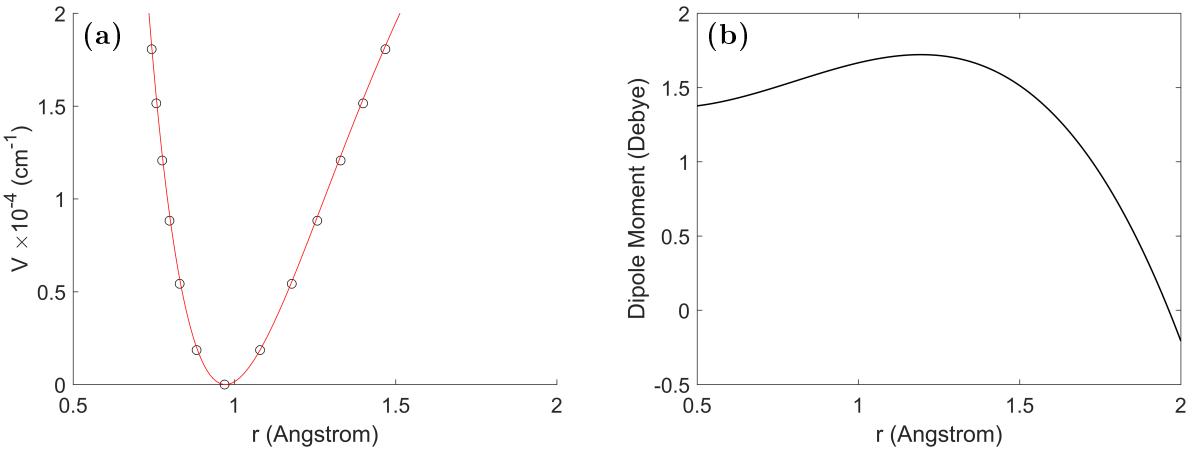

Figure 4.11: Functions used in this calculation. (a) OH RKR potential energy from Nesbitt *et al.*[135, 136] along with fit. (b) Dipole moment function from Nesbitt *et al.*[135, 136].

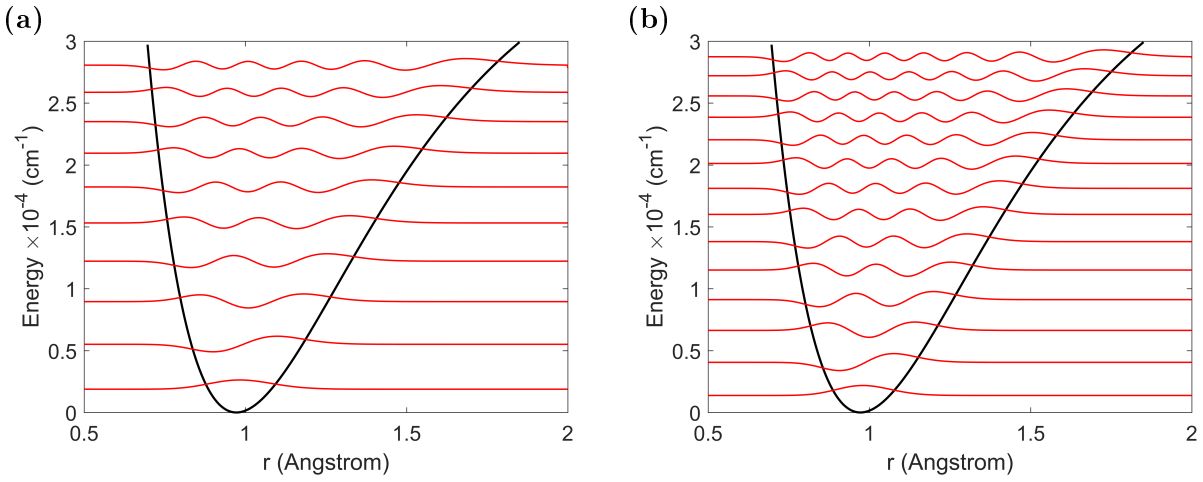

Figure 4.12: Calculated vibrational wavefunctions for (a) OH and (b) OD. Wavefunctions are in red, offset by their vibrational energy. The fitted potential energy surface is in black.

	t-DOCO Position (cm^{-1})	*t*-DOCO Intensity (km mol^{-1})	*c*-DOCO Position (cm^{-1})	*c*-DOCO Intensity (km mol^{-1})
Johnson *et al* (2011) [137]	2688	–	2555	–
Mladenović *et al* (2013) [138]	2691	–	2558	–
Huang et al (2013) [139]	2685.1	47.97	2551.6	14.75
Wang *et al* (2014) [140]	2685	–	2544	–
Stanton, private communication	–	65	–	14.4

Table 4.7: Theoretical ν_1 ro-vibrational band positions and intensities for *trans*- and *cis*-DOCO.

Chapter 5

Direct Measurement of OD+CO→*trans*-DOCO Kinetics

This chapter is published as

B. J. Bjork, T. Q. Bui, O. H. Heckl, P. B. Changala, B. Spaun, P. Heu, D. Follman, C. Deutsch, G. D. Cole, M. Aspelmeyer, M. Okumura, and J. Ye, "Direct Frequency Comb Measurement of OD + CO→DOCO Kinetics", Science 354, 6311 (2016), pp. 444-448. [141]

Abstract: The kinetics of the hydroxyl radical (OH) + carbon monxide (CO) reaction, which is fundamental to both atmospheric and combustion chemistry, are complex because of the formation of the hydrocarboxyl radical (HOCO) intermediate. Despite extensive studies of this reaction, HOCO has not been observed under thermal reaction conditions. Exploiting the sensitive, broadband, and high-resolution capabilities of time-resolved cavity-enhanced direct frequency comb spectroscopy, we observed deuteroxyl radical (OD) + CO reaction kinetics and detected stabilized *trans*-DOCO, the deuterated analog of *trans*-HOCO. By simultaneously measuring the time-dependent concentrations of the *trans*-DOCO and OD species, we observed unambiguous low-pressure termolecular dependence of the reaction rate coefficients for N_2 and CO bath gases. These results confirm the HOCO formation mechanism and quantify its yield.

5.1 Main Text

The apparent simplicity of gas phase bimolecular reaction kinetics of free radicals often belies the complexity of the underlying dynamics. Reactions occur on multidimensional potential energy surfaces that can host multiple pre-reactive complexes and bound intermediate complexes as well as multiple transition states. As a result, effective bimolecular rate coefficients often exhibit complex temperature and pressure dependence. The importance of free radical reactions in processes such as combustion and air pollution chemistry has motivated efforts to determine these rate constants both experimentally and theoretically. Quantitative *ab initio* modeling of kinetics remains a major contemporary challenge[142], requiring accurate quantum chemical calculations of energies, frequencies and anharmonicities, master equation modeling, energy transfer dynamics, and, when necessary, calculation of tunneling and non-statistical behavior. Experimentally, detection of the transient intermediates, which is the key to unraveling the dynamics, is often quite challenging.

The reaction of hydroxyl radical with CO (eq. 5.1),

$$\mathrm{OH} + \mathrm{CO} \rightarrow \mathrm{H} + \mathrm{CO_2},\ \Delta_r E_0 = -103.29\ \mathrm{kJ\ mol^{-1}} \tag{5.1}$$

($\Delta_r E_0$, standard energy of the reaction at 0 K) has been extensively studied over the last four decades because of its central role in atmospheric and combustion chemistry[123]; it has come to serve as a benchmark for state-of-the-art studies of chemical kinetics of complex bimolecular reactions[143, 144]. In Earth's atmosphere, OH is critical as the primary daytime oxidant[105, 106]. CO, a byproduct of fossil fuel burning and hydrocarbon oxidation, acts through eq. 5.1 as an important global sink for OH radicals; this reaction is the dominant OH loss process in the free troposphere. In fossil fuel combustion, OH + CO is the final step that oxidizes CO to CO_2 and is responsible for a large amount of heat released.

The rate of the reaction in eq. 5.1 is pressure dependent and exhibits an anomalous temperature dependence, which led Smith and Zellner[118] to propose that the reaction proceeds through a highly energized, strongly bound intermediate, HOCO, the hydrocarboxyl radical (Fig. 5.1A, inset).

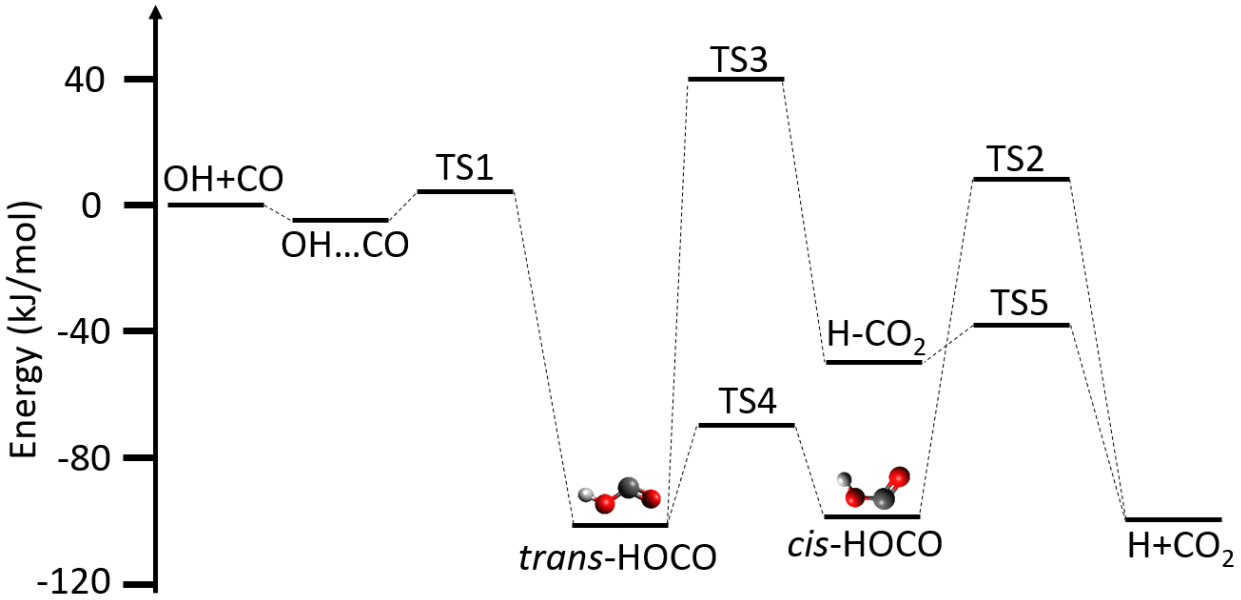

Figure 5.1: Potential energy surface for the OH + CO → H + CO_2 reaction, with energies taken from Nguyen et al. [123]. OH + CO → H + CO_2 proceeds through vibrationally excited HOCO*, which is either deactivated by bath gas M or reacts to form H + CO_2. The inset shows the simplified OH + CO reaction mechanism. TS, transition state.

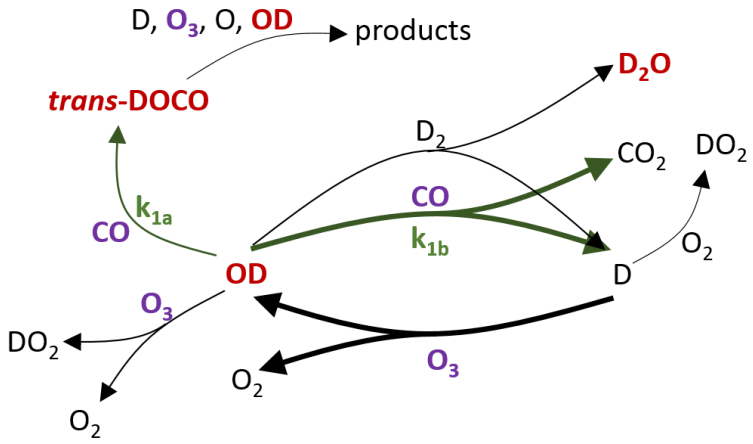

Figure 5.2: Schematic showing the most important reactions in our system. Time-dependent concentrations of trans-DOCO, OD(v = 0), OD(v = 1), and D_2O (red) are measured by cavity-enhanced absorption spectroscopy; the concentrations of the precursors (purple) are set by flow controllers or meters. O_3 is measured by UV absorption.

Formation of H + CO_2 products is an example of a chemically activated reaction. The course of the reaction is governed by the dynamics on the potential energy surface, shown schematically in Fig. 5.1. The OH and CO pass through a pre-reactive weakly bound OH-CO complex to form a highly energized $HOCO^*$ in one of two isomers, trans-HOCO or the less stable *cis*-HOCO[123]. In the low pressure limit at room temperature, $HOCO^*$ primarily back-reacts to OH + CO, but there is a small probability of overcoming the low barrier (8.16 kJ mol^{-1}) and reacting to form H + CO_2. In the presence of buffer gas, energy transfer by collisions with third-bodies M (termolecular process) can deactivate or further activate the $HOCO^*$. Deactivation can lead to the formation of stable, thermalized HOCO products (reaction 1a), which diminishes the formation of H + CO_2 (reaction 1b). Approaching the high pressure limit, HOCO formation becomes the dominant channel and H + CO_2 product formation decreases. The overall reaction rate is characterized by an effective bimolecular rate constant $k_1([\mathrm{M}], T) = k_{1a}([\mathrm{M}], T) + k_{1b}([\mathrm{M}], T)$, where T is temperature [119, 3, 120, 145, 121].

There have been numerous experimental studies of the temperature and pressure dependence of the overall rate coefficient; these all measure OH loss in the presence of CO[119, 120, 121, 146, 147, 148, 149, 150]. In principle, master equation calculations with accurate potential energy surfaces within a statistical rate theory can compute $k_1([M], T)$, but *a priori* kinetics are rarely possible because the energy transfer dynamics are generally not known. A number of studies have thus fit the theoretical models to the observed overall rate constants, using a small number of parameters to describe collisional energy relaxation and activation [119, 120, 148, 149, 151, 152]. Although these previous studies have had success in describing $k_1([M], T)$, they do not capture the dynamics that would be revealed from the pressure-dependent branching between stabilization of HOCO and barrier crossing to form H + CO_2 products. Detection of the stabilized HOCO intermediate and measurement of its pressure-dependent yield would confirm the reaction mechanism and quantitatively test theoretical models. The spectroscopy of HOCO is well established, and recently HOCO has been observed from the OH + CO reaction generated in a discharge[125, 153, 124]; however, measurements under thermal conditions are necessary to derive rate constants.

sTo directly and simultaneously measure the time-dependent concentrations of reactive radical intermediates such as HOCO and OH, we applied the recently developed technique of time-resolved direct frequency comb spectroscopy (TRFCS)[10]. The massively parallel nature of frequency-comb spectroscopy allows time-resolved, simultaneous detection of a number of key species, including intermediates and primary products, with high spectral and temporal resolution. The light source is a mid-IR (≈3-5 μm) frequency comb, generated from an optical parametric oscillator (OPO) synchronously pumped with a high repetition rate (f_{rep} = 136 MHz) mode-locked femtosecond fiber laser [88]. The OPO spectrum is composed of spectrally narrow comb teeth evenly spaced by frep and shifted by an offset frequency, f_0. By matching and locking the free spectral range (FSR) of the enhancement cavity to $2 \times f_{rep}$, we keep the full comb spectrum resonant with the cavity during the data acquisition. The broadband transmitted light (~65 cm^{-1} bandwidth, ~7100 comb teeth) is spatially dispersed in 2D by a virtually-imaged phased array (VIPA) etalon and a grating combination, which is then imaged on an InSb camera (Fig. 5.7). Absorption spectra are constructed from these images as a function of time (with a resolution of 10 μs determined by the camera integration time), which are compared with known molecular line intensities to obtain absolute concentrations. The absorption detection sensitivity is greatly enhanced with our high finesse (F≈4100) optical cavity that employs mid-IR mirrors with low-loss crystalline coatings. These mirrors, with a center wavelength of 3.72 μm and a spectral bandwidth of about 100 nm, have significantly lower optical losses and hence yield enhanced cavity contrast compared with traditional amorphous coatings as covered in detail in Ref. [154], enabling an improved sensitivity by a factor of 10 for the direct detection of *trans*-DOCO.

In this experiment, we studied the deuterium analogue of eq. 5.1, OD + CO→D + CO_2, exploiting the sensitivity and resolution of TRFCS to detect the reactant OD (in both v=0 and v=1 states) and the product trans-DOCO by absorption spectroscopy in a pulsed-laser-photolysis flow cell experiment. We sought to measure the pressure-dependent effective bimolecular rate coefficients and the yield of trans-DOCO at 27 to 75 Torr (3.3 to 10 kPa) total pressure. Such measurements would be especially sensitive to the competition between termolecular DOCO stabilization and

reaction to form D+CO_2. Detection of the deuterated species allowed us to avoid atmospheric water interference in our spectra. We further anticipated that the yield of stable DOCO would be higher, as deuteration substantially reduces the rate of tunneling to form D + CO_2 products while increasing the lifetime of $DOCO^*$ due to the higher density of states.

The OD + CO reaction was initiated in a slow-flow cell by photolyzing O_3 in a mixture of D_2, CO, and N_2 gases with 266 nm (32 mJ, 10 Hz) pulses from a frequency-quadrupled Nd:YAG laser, expanded to a profile of 44 mm × 7 mm and entering the cell perpendicular to the cavity axis. $[O_3]_0$ was fixed at a starting concentration of 1×10^{15} molecules cm^{-3} and verified by direct UV absorption spectroscopy. The initial concentrations of CO, N_2, and D_2 were varied over the range 1 to 47 Torr (0.13 to 6.3 kPa) while the O_3 concentration was restricted to 3 to 300 mTorr (4×10^{-4} to 4×10^{-2} kPa) to minimize secondary reactions. A complete description and tabulation of the experimental conditions is included in (§5.2.1).

Each photolysis pulse dissociated 15% of the ozone (§5.2.1) to form O_2 + $O(^1D)$ at nearly unity quantum yield [155]. The resulting $O(^1D)$ either reacts with D_2 to form OD + D or is quenched by background gases to $O(^3P)$ within 1 s. $O(^1D)$ + D_2 is known to be highly exothermic and produces vibrationally excited OD(v = 0 - 4) with an inverted population peaking at v = 2 and v = 3[156]. Vibrationally excited OD was rapidly quenched or formed D atoms by collisions with CO[157, 158]. Formation of vibrational Feshbach resonances of $DOCO^*$ from collisions of OD(v>0) with CO may be possible, but the lifetimes are on the order of picoseconds, as previously observed for the $HOCO^*$ case[83, 159, 160, 161]. Therefore, only vibrationally/rotationally thermalized OD(v=0) are expected to form DOCO by the mechanism described in Fig. 5.1A inset. OD and DOCO reach a steady-state after 100 μs through cycling reactions depicted in Fig. 5.1B: D atoms produced from OD + CO D + CO_2 reacted with O_3 to regenerate the depleted OD.

Absorption spectra covering a ~65 cm^{-1} bandwidth were recorded at a sequence of delays from the t = 0 photolysis pulse, using a camera integration time of either 10 or 50 μs depending on our sensitivity to *trans*-DOCO signals. The broad bandwidth of the comb covers 6 OD, ~200 D_2O, and ~150 *trans*-DOCO transitions. These spectra were normalized to a spectrum acquired directly

preceding the photolysis pulse and were fitted to determine time-dependent concentrations. With this approach, we captured the time-dependent kinetics of trans-DOCO, OD, and D_2O from OD + CO within a spectral window of 2660 to 2710 cm^{-1}. Representative snapshots at three different delay times are shown in Fig. 5.3. The OD and *trans*-DOCO data were compared to simulated spectra, generated with PGopher [49] using measured molecular constants[95, 132, 162] and known or computed intensities. The simulated spectra are fitted to these experimental data at each time delay to map out the full time trace of the three observed species, as shown in Fig. 5.4A-B, with error bars derived directly from the fit residual. See (SM, §5.2.2) for details of data analysis.

We determined the effective bimolecular rate coefficient for the trans-DOCO channel, $k_{1a}([M], T)$ from simultaneous measurements of both time-dependent *trans*-DOCO and OD. In the low pressure regime studied here, the DOCO formation rate obeys a termolecular rate law, while the effective bimolecular coefficient for the D + CO_2 channel remains close to the zero pressure value, $k_{1a}([M] = 0)$. We measured the dependence of the effective bimolecular rate constant on the concentrations of all of the major species (N_2, CO, D_2, and O_3) present in the experiment.

We analyzed the early-time (t <200 μs) rise of *trans*-DOCO in order to decouple the measurement of k_{1a} from secondary loss channels at longer times. The expected time dependence of the DOCO concentration is given by eq. 5.2.

$$\frac{d[DOCO]}{dt} = k_{1a}[CO][OD](t) - k_{loss}[X][DOCO](t)\,. \tag{5.2}$$

k_{loss} describes a general DOCO decay through a reaction with species X, and [OD](t) refers to the time-dependent concentration of OD in the ground vibrational state. The solution to eq. 5.2 is a convolution of the DOCO loss term with [OD](t), given by the integral in eq. 5.3. [CO] is in large excess and remains constant throughout the reaction.

$$[DOCO](t) = k_{1a}[CO]\int_0^t e^{-(k_{loss}[x])(t-u)}[OD](u)du\,. \tag{5.3}$$

The effective bimolecular rate coefficient k_{1a} can be reduced into two terms dependent on N_2 and

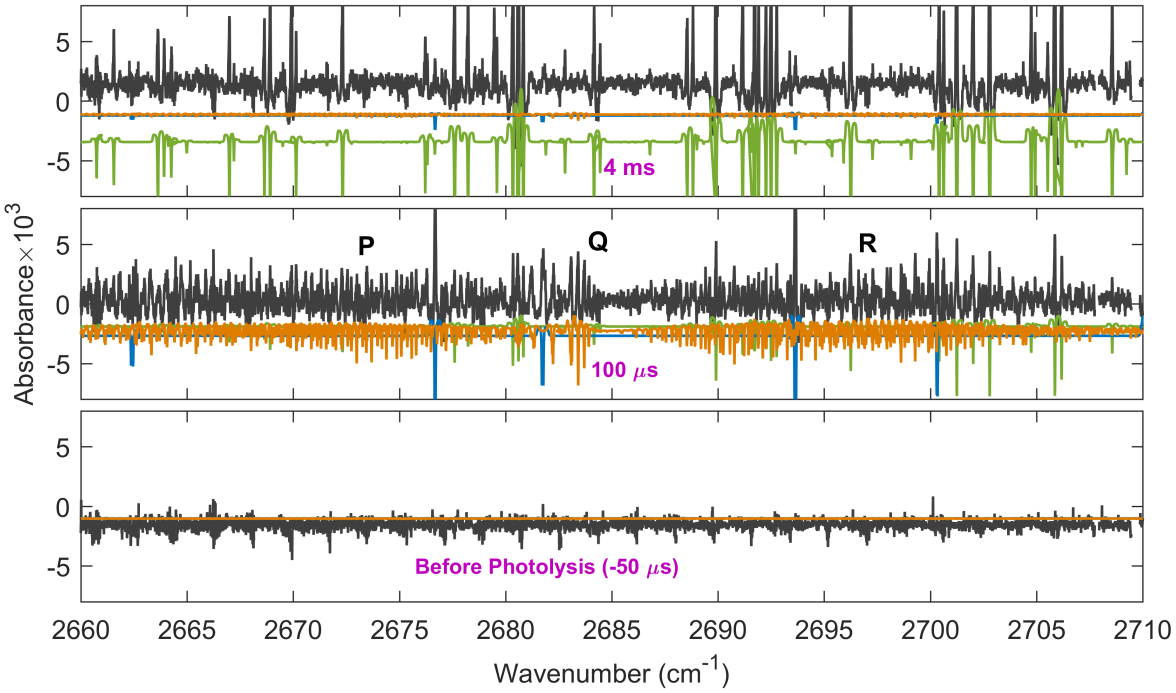

Figure 5.3: Experimental spectra (black) were recorded with an integration time of 50 μs and offsets of –50 ("before photolysis"), 100, and 4000 μs from the photolysis pulse. These spectra were then fitted to the known line positions of OD (blue), D_2O (green), and *trans*-DOCO (orange) to determine their temporal concentration profiles. The P, Q, and R branches of *trans*-DOCO are indicated above the 100-μs experimental trace.

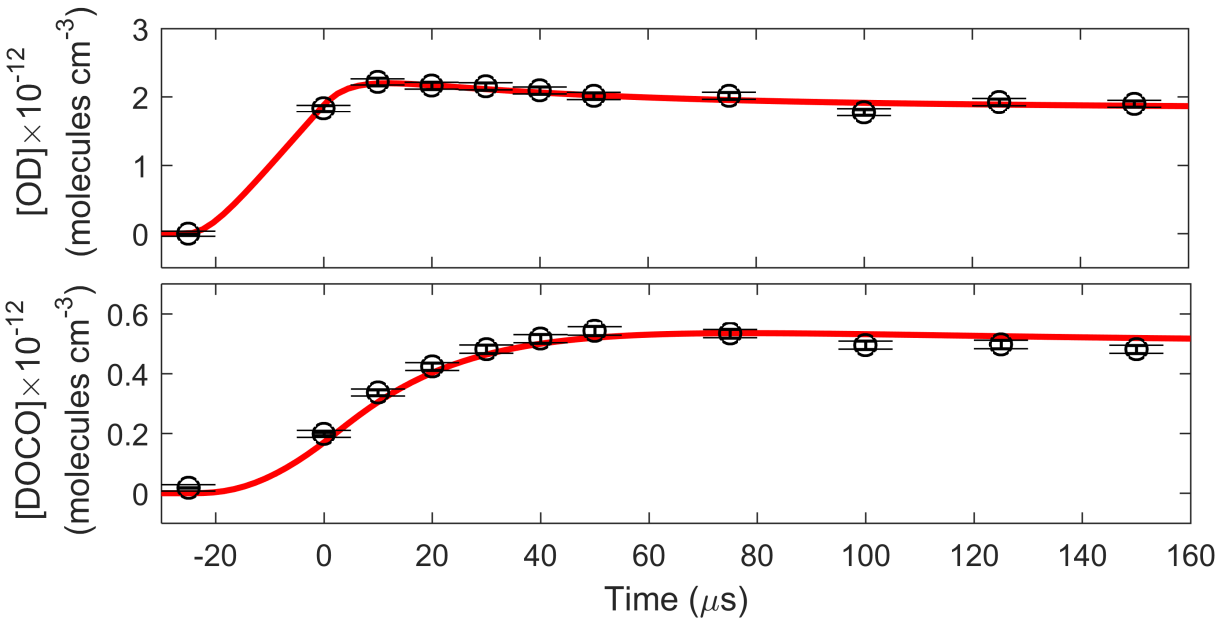

Figure 5.4: (a) An analytical functional form for [OD](t) was obtained by fitting the data (black circles) to a sum of boxcar-averaged exponential functions (red line). At each time, the data point represents ~300 averaged spectra, and the error bars are from statistical uncertainties in the spectral fit. (b) The bimolecular *trans*-DOCO rise rate was obtained by fitting the data (black circles) to Eq. 5.3 (red line). The data in (a) and (b) were obtained at a 10-μs camera integration time and precursor concentrations of [CO] = 5.9×10^{17}, [N_2] = 8.9×10^{17}, [D_2] = 7.4×10^{16}, and [O_3] = 1×10^{15} molecules cm^{-3}.

CO concentrations

$$k_{1a} = k_{1a}^{(CO)}[CO] + k_{1a}^{(N2)}[N_2]\,, \tag{5.4}$$

where $k_{1a}^{(CO)}$ and $k_{1a}^{(N2)}$ are the termolecular rate coefficient dependence on CO and N_2, respectively.

By simultaneously fitting [DOCO](t) and [OD](t) as a function of [CO] and [N_2], we uniquely determined all of the k_{1a} termolecular coefficients. Figure 5.3B shows an early-time segment of our data at 10 μs camera integration for both [trans-DOCO](t) and [OD](t). To fit the nonlinear time-dependence of [OD](t), we used derived analytical functions composed of the sum of boxcar-averaged exponential rise and fall functions (SM, §5.2.3). Equation 5.3 gives the functional form for fitting [*trans*-DOCO](t), which includes the integrated [OD](t) over the fitted time window of -25 to 160 μs. The fitted parameters are k_{1a} and a *trans*-DOCO loss rate, $r_{loss,exp}$ ($\equiv k_{loss}[X]$).

For our first set of data, we varied the CO concentration. At each set of conditions, we acquired data at both 10 and 50 μs camera integration time. By plotting k_{1a} versus [CO] for both 10 μs and 50 μs, we did not observe any systematic dependence on camera integration time. Moreover, we observed a clear linear dependence (with reduced chi-squared,), indicating a strong termolecular dependence of k_{1a} on CO, or $k_{1a}^{(CO)}$ (Fig. 5.5A). The offset in the linear fit comes from the N_2 termolecular dependence of k_{1a}, or $k_{1a}^{(N2)}$. We then varied N_2 concentration and observed a similar linear dependence of k_{1a} from eq. 5.4. A 50 μs camera integration time was used for this second data set due to lower *trans*-DOCO signals at higher N_2 concentrations. The results are shown in Fig. 5.5B. Because both the offset terms from the linear fit to the CO data and the linear fit to the N_2 plot correspond to $k_{1a}(N_2)$, we performed a multidimensional linear regression to eq. 5.4 to determine $k_{1a}(CO)$, $k_{1a}(N_2)$, and r_{loss} simultaneously. Because $r_{loss,exp}$ describes *trans*-DOCO loss, it is expected to be invariant to [CO] and [N_2]. Therefore, $r_{loss,exp}$ serves as a shared, fitted constant in the global fit across the CO and N_2 data sets. From the fits shown in red in Fig. 5.5A-B, we obtained $k_{1a}^{(N2)}$ = ×10^{-33} cm^6 molecules^{-2} s^{-1}, $k_{1a}^{(CO)}$ = ×10^{-32} cm^6 molecules^{-2} s^{-1} and $r_{loss,exp}$ = (4.0±0.4)×10^4 s^{-1}. The statistical and systematic errors in these parameters are collected in Table 5.4.

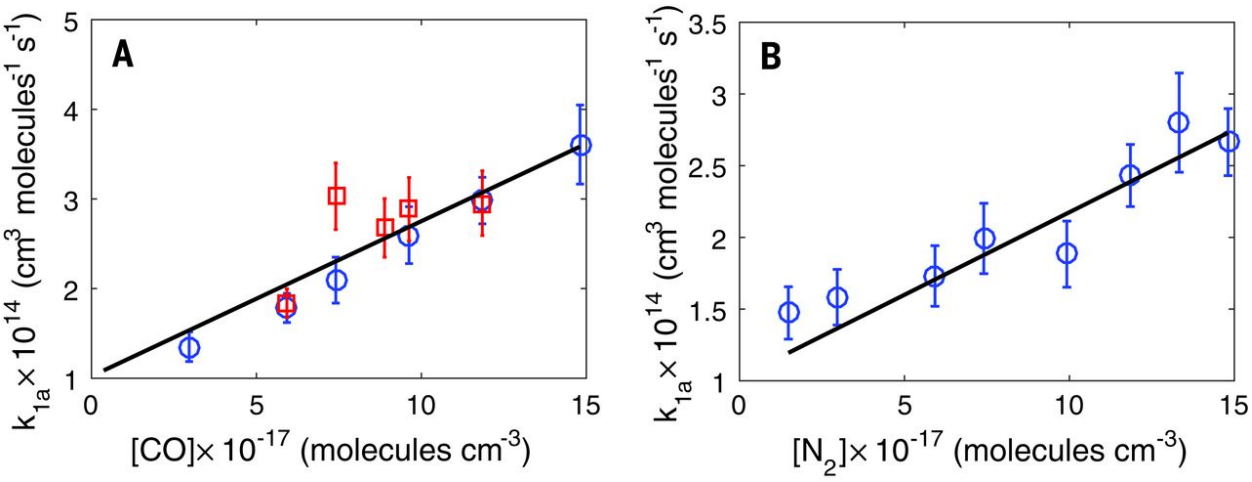

Figure 5.5: Determination of the termolecular *trans*-DOCO formation rate. The bimolecular *trans*-DOCO formation rate coefficient, k_{1a}, is plotted as a function of [CO] and [N_2] to determine the termolecular rate coefficients Embedded Image and Embedded Image. Each point represents one of 26 experimental conditions tabulated in table 5.1. In both panels, the error bars represent uncertainties from fits to Eqs. 5.2 to 5.4 and the measured densities of the gases. (A) k1a is plotted as a function of [CO] while [N_2] = 8.9 × 10^{17} molecules cm^{-3} is held constant. (B) k_{1a} is plotted as a function of [N_2] while [CO] = 5.6 × 10^{17} molecules cm^{-3} is held constant. In both plots, D_2 and O_3 concentrations are fixed at 7.4×10^{16} and 1×10^{15} molecules cm^{-3}, respectively. Blue and red data points indicate 50- and 10-μs camera integration times, respectively. The data in (A) and (B) are simultaneously fitted to Eq. 5.4. The black lines in (A) and (B) are obtained from weighted linear fits. The y offsets in the data arise from the nonzero concentrations of N_2 and CO in (A) and (B), respectively.

To verify the reaction kinetics, we constructed a rate equation model of the OD + CO chemistry, which included the decay channels from secondary chemistry, in order to fit the trans-DOCO and OD time traces up to 1 ms (§5.2.4). We fit one overall scaling factor for both OD and trans-DOCO, which accounts for uncertainties in (i) the optical path length and (ii) photolysis yield and subsequent OD^* quenching reactions that establish the initial steady-state concentration of OD. We also fit an additional *trans*-DOCO loss, $r_{loss,model}$, in order to correctly capture the *trans*-DOCO concentration at t >100 μs.

The *trans*-DOCO + O_3 OD + CO_2 + O_2 rate coefficient (9) (k_{O3}+DOCO ≈ 4×10^{-11} cm^3 $molecules^{-1}$ s^{-1}) and the OD + CO termolecular rate coefficients from our experimentally measured values were fixed in the model. Representative fits for two different conditions using the same rate equation model are shown in Fig. 5.6A-B. We found good fits ($\chi^2_{red} \approx 0.71$) with a single, consistent set of parameters over a wide range of CO, N_2, and O_3 concentrations, giving rloss,model = $(4.7\pm0.7)\times10^3$ s^{-1} for all conditions (Fig. 5.19A). The sum of loss contributions from k_{O3}+DOCO[O_3] and an additional loss from rloss,model gives a total loss of ~4.5×10^4 s^{-1}, consistent with our measured rloss,exp. One possibility for rloss,model is a second product branching channel of *trans*-DOCO + O_3 to produce DO_2 + CO_2 + O. The slight discrepancy of the trans-DOCO data with the rate equation model in Fig. 5.6B is possibly due to the inadequately constrained loss processes at long delay times.

Sources of systematic uncertainty have been carefully evaluated. First, we considered the impact of vibrationally hot OD at early times. We constrained the population of vibrationally excited OD in our system by directly observing several hot band transitions from OD(v=1) (Fig. 5.13). We observed that CO is an efficient quencher of OD vibration, with a measured OD(v=1) lifetime (Fig. 5.14) consistent with the OD(v=1) + CO quenching rate reported by Brunning et al. [150] and Kohno et al. [158]. These measurements reveal that the lifetime is well below the minimum integration time of 10 μs and the total population of [OD(v=1)] is less than 10% of [OD(v=0)] in this time window. As OD(v=1) is expected to produce stabilized *trans*-DOCO less efficiently than OD(v=0), the systematic effect caused by the vibrationally hot OD is estimated to be < 10%, which

has been included in our total error budget (Table 5.4).

Another systematic uncertainty arises from the finite camera integration time, which is large (50 μs) or comparable (10 μs) to the early trans-DOCO rise time. The recovered k_{1a} values from the two integration times are consistent with each other to within 21%, which we have included as a systematic uncertainty in our measurement (Fig. 5.12).

A third source of systematic uncertainty comes from any factors that would cause deviations from eq. 5.2; specifically, we investigated the dependence of k_{1a} on D_2 and O_3 concentrations. Additional experiments were conducted in the same manner as the CO and N_2 experiments but varying [O_3] (1×10^{14} – 4×10^{15} molecules cm^{-3}) and [D_2] (7×10^{16} – 1×10^{18} molecules cm^{-3}). At our experimental conditions and using a 50 μs camera integration window, we observed a weak dependence of k_{1a} on [O_3] (Fig. 5.17) and no statistically significant variation with [D_2] (Fig. 5.16). The O_3 dependence was measured at a CO concentration of 1.5×10^{17} molecules cm^{-3}. From analysis of the early-time *trans*-DOCO rise as a function of [O^3] and [D^2], we determined that O_3 and D_2 contribute additional 11% and 8% statistical uncertainty, respectively, to our total budget (Table 5.4).

We find that CO is approximately 100% more effective as a collision partner than N_2 in promoting the termolecular association of trans-DOCO. This result was missed in previous studies, which minimized the CO concentration ($<4\times10^{16}$ molecules cm^{-3}) to avoid biasing a pseudo-first order kinetics measurement[121]. One might naively expect CO to be similar to N_2 as a third body; the significant difference observed here could be due to (i) near-resonant energy transfer between CO and the CO mode in DOCO, (ii) a stronger interaction potential between CO and DOCO*, or (iii) the influence of more efficient CO on OD(v) quenching which we have not correctly accounted for.

In the low pressure regime, our measurements of the association rate, k_{1a}, can be compared to the pressure dependence of k_1, the overall rate of OD+CO, measured in previous experiments in N_2. Most of the pressure dependence of k1 comes from k_{1a}, because k_{1b} is expected to change only slightly in this range. From earlier studies by Paraskevopoulos et al. [147] and Golden et al. [119], the termolecular (linear) component of their reported k_1 values fall within 1σ of our measured

$k_{1a}^{(N2)}$, which may suggest a k_{1a} contribution to the previously reported k_1. Apparent curvature in the pressure dependence seen elsewhere suggests that k1a may already be in the fall-off regime. In order to estimate the *trans*-DOCO branching yield (% yield $\approx k_{1a}/(k_{1a} + k_1(p = 0))$, we took the average value of k_1 from Paraskevopoulos et al. [147], Golden et al. [119], and Westernberg et al. [163]. Even at low total pressures (75 Torr of N_2), our results show that OD+CO produces a *trans*-DOCO yield of nearly (28±11)%.

Optical frequency comb spectroscopy provides broadband, time-resolved absorption detection of radicals with exceptional sensitivity and high spectral resolution. These results clearly demonstrate the capabilities of time-resolved cavity-enhanced frequency comb spectroscopy to elucidate chemical mechanisms through the quantitative detection of intermediates and primary products in real time. Our quantification of the termolecular dependence reveals additional factors that impact the product branching of the OH + CO reaction, which must be included in future atmospheric and combustion model predictions. For example, sensitivity analyses by Boxe et al. [115] have shown that depending on the branching ratio, HOCO can contribute 25 to 70% of the total CO_2 concentration in the Martian atmosphere. The current experiment can be readily extended to detect other primary products (DO_2, CO_2) as well as to study the OH/HOCO system. Furthermore, dynamics and nonthermal processes such as chemical activation, energy transfer and rovibrational state-specific kinetics can be studied. With the bandwidth of optical frequency comb sources spanning an octave or more, the potential of this approach has not yet been fully realized. The technologies of frequency comb sources, detection methods and mirror coatings are developing rapidly and will allow for more expansive applications of this multiplexed technique to many other classes of important chemistry problems.

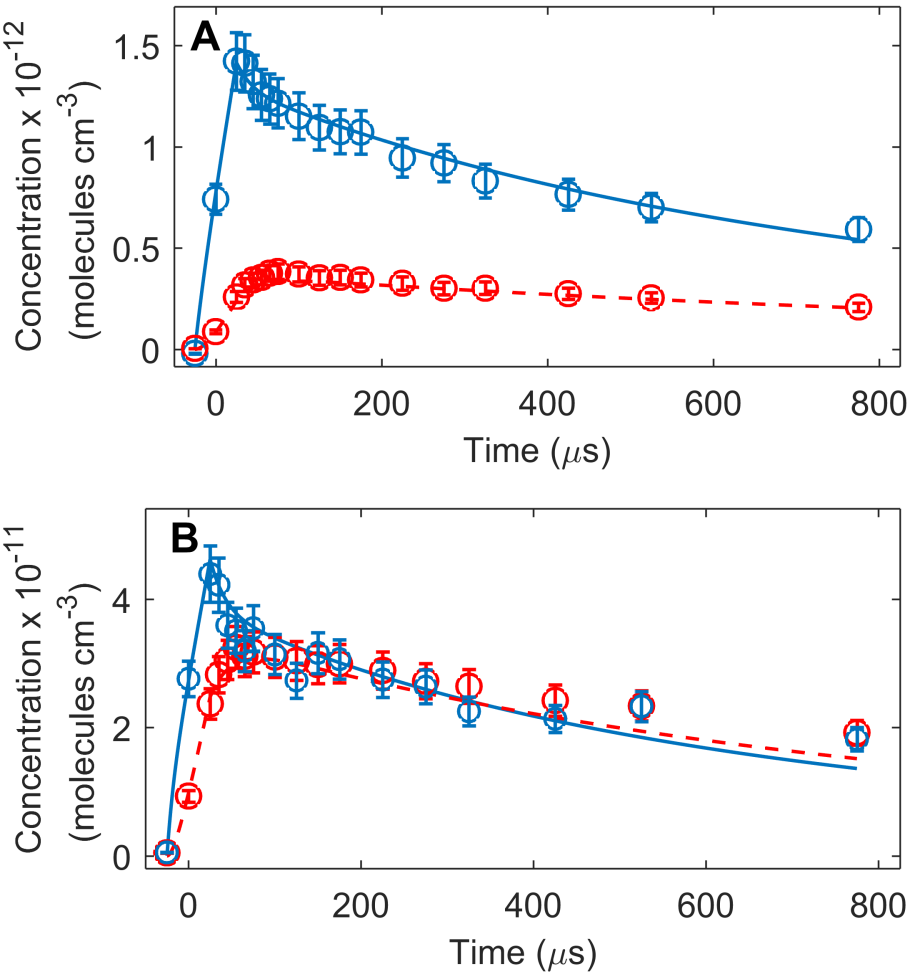

Figure 5.6: Rate equation model fitting. The OD (blue) and *trans*-DOCO (red) traces are weighted fits to the model (solid and dashed lines for OD and trans-DOCO, respectively) described in the Supplementary Material. The integration time was 50 μs. The error bars are from uncertainties in the spectral fit in the same manner as for Fig. 5.3B. The input k_{1a} values for both CO and N_2 were from the early-time *trans*-DOCO rise analysis and were fixed in the fit. The floated parameters included a single scaling factor for the OD and *trans*-DOCO intensities and an extra DOCO loss channel. (A) [CO] = 5.9×10^{17} molecules cm^{-3}; (B) [CO] = 1.2×10^{18} molecules cm-3. [N_2] = 8.9×10^{17}, [D_2] = 7.4×10^{16}, and [O_3] = 1×10^{15} molecules cm^{-3} were fixed for both data sets.

5.2 Supplementary Materials and Methods:

5.2.1 Experimental description and conditions

Scientific Apparatus A schematic of the instrument is depicted in Fig. 5.5 and discussed extensively in the main text.

Generation of OD The ozone used to generate OD in this reaction was generated in a flow-discharge of pure O_2 gas. This mixture contains approximately 8% of O_3 in a buffer of O_2. This mixture was flown across a silica gel trap immersed in an isopropanol/LN_2 bath at -90 °C. The ozone trap was allowed to pump out for about 20 minutes after stopping the O_3/O_2 flow to remove residual O_2. The steady state concentration of O_3 in the reaction cell was measured using the direct absorption of the collimated 270 nm light from a UV LED (UVTOP-270). By comparing this absorption measurement to a static total pressure measurement in the cell, it is estimated that O_3 comprises >70% of the mixture flowing. Frequency quadrupled 266 nm light (beam size: 44 mm × 7 mm, power = 32mJ/pulse) from a Spectra Physics INDI-HG-105 Nd:YAG propagating orthogonal to the mid-IR probe beam was the photolysis beam. In this method, 15% of the O3 in the cavity was photolyzed into $O(^1D)$, $O(^3P)$, and O_2 to start the reaction. OD was then promptly formed from the $O(^1D) + D_2 \rightarrow OD + D$ reaction. O_3 photolysis to $O(^1D)$: In order to accurately simulate the kinetics of the OD + CO chemical system, we measured the fraction of O_3 photolyzed at 266 nm. This was done by measuring the transmission of a 270 nm LED through the photolysis region of the chemical cell before and after the photolysis of O_3 in a buffer of N_2. We measured a photolysis fraction of $f_{phot} = 0.15 \pm 0.02$.

Experimental conditions Table S1 shows the measurement conditions used for determining k_{1a}. The initial concentrations of D_2, CO, N_2, and O_3 were determined by calibrated flow controllers and a capacitance manometer as

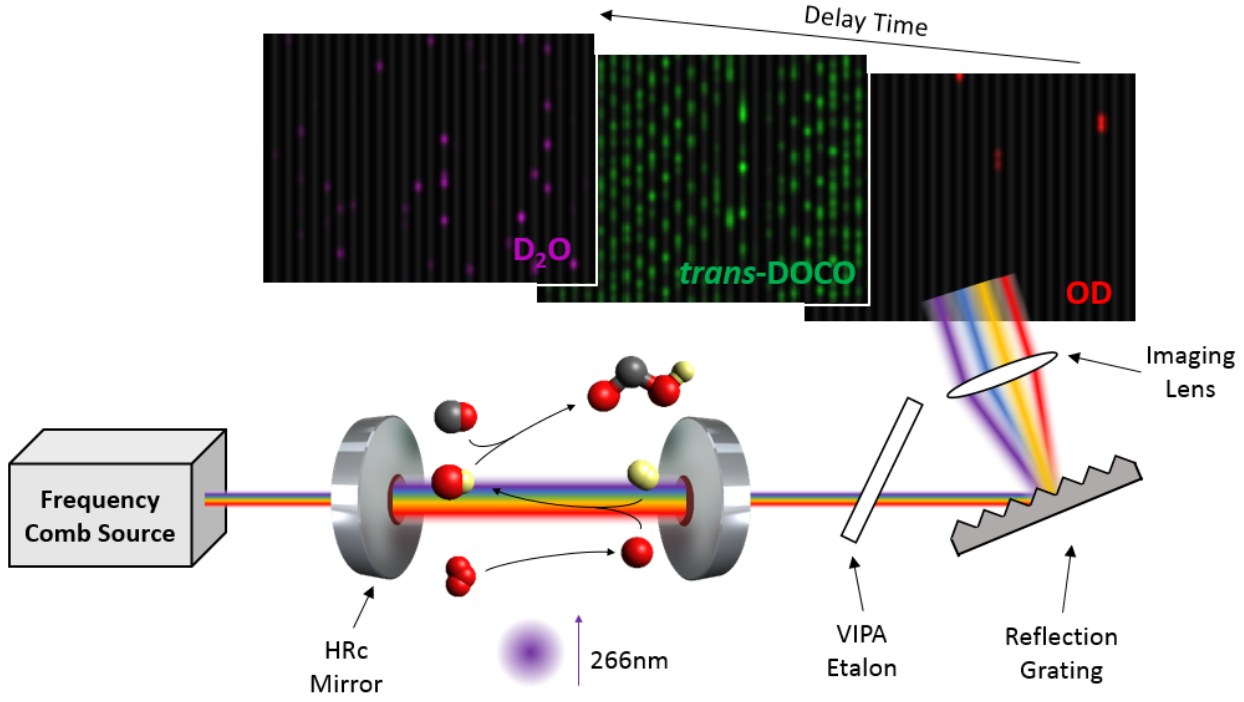

Figure 5.7: A mid-IR frequency comb is coupled into an enhancement cavity, consisting of two high reflectivity crystalline (HRc) mirrors, where a 266 nm laser pulse photolyzes O_3 to initiate the chemistry. The transmission from the cavity is spatially dispersed by a VIPA etalon and a diffraction grating and imaged on an InSb camera. Simulated cavity absorbance images are shown for OD (red), *trans*-DOCO (green), and D_2O (magenta) to illustrate the camera pixel to wavelength mapping.

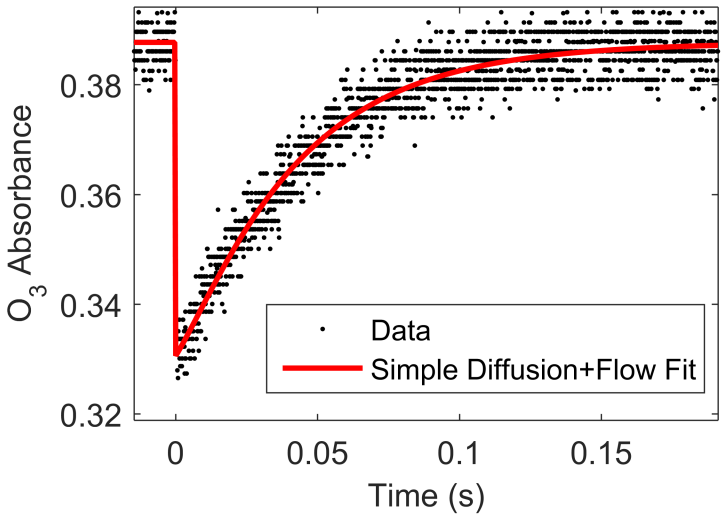

Figure 5.8: Measurement of Ozone photolysis fraction.

$$[N_2]_0 = P\left(\frac{Q_{N2}}{Q_{D2} + Q_{CO} + Q_{N2} + Q_{O3}}\right) \tag{5.5}$$

where P is the total pressure of the reaction cell and the Q_X are the flows of each gas into the reaction cell. By swapping flow controllers and pressure meters, the concentration uncertainty in this method is estimated to be 7%. The initial concentrations of O_3, $O(^1D)$, and O_2 just after photolysis by the YAG beam are given by

$$\begin{aligned} [O_3]_0 &= (1 - f_{phot})[O_3]_{LED} \\ [O(^1D)]_0 &= q_{O(1D)} f_{phot}[O_3]_{LED} \\ [O(^3P)]_0 &= q_{O(3D)} f_{phot}[O_3]_{LED} \end{aligned} \tag{5.6}$$

where $q_{O(1D)} = 0.90$ and $q_{O(3P)} = 0.10$ are the quantum yields [167] of the photolysis of O_3 into $O(^1D)$ and $O(^3P)$, respectively, $f_{phot} = 0.15 \pm 0.02$ the O_3 photolysis fraction, and $[O_3]_{LED}$ is the steady-state concentration of O_3 recorded by the absorption of the 270 nm UV LED.

Table 5.1: Measurement conditions used for the determination of k_{1a}. The units for [CO], [N_2], [D_2], and [O_3] are molecules cm^{-3}.

	[CO]	[N_2]	[D_2]	[O_3]	Int. Time (μs)
CO Scan	7.41×10^{16}	8.89×10^{16}	2.96×10^{16}	1.00×10^{15}	50
	1.48×10^{16}	8.89×10^{16}	7.41×10^{16}	1.00×10^{15}	50
	2.96×10^{16}	8.89×10^{16}	7.41×10^{16}	1.00×10^{15}	10
	2.96×10^{16}	8.89×10^{16}	7.41×10^{16}	1.00×10^{15}	50
	5.92×10^{16}	8.89×10^{16}	7.41×10^{16}	1.00×10^{15}	10
	5.92×10^{16}	8.89×10^{16}	7.41×10^{16}	1.00×10^{15}	50
	5.92×10^{16}	8.89×10^{16}	7.41×10^{16}	1.00×10^{15}	50
	7.41×10^{16}	8.89×10^{16}	7.41×10^{16}	1.00×10^{15}	10
	7.41×10^{16}	8.89×10^{16}	7.41×10^{16}	1.00×10^{15}	50

	[CO]	[N_2]	[D_2]	[O_3]	Int. Time (μs)
	8.89×10^{16}	8.89×10^{16}	7.41×10^{16}	1.00×10^{15}	10
	9.63×10^{16}	8.89×10^{16}	7.41×10^{16}	1.00×10^{15}	10
	9.63×10^{16}	8.89×10^{16}	7.41×10^{16}	1.00×10^{15}	50
	1.18×10^{18}	8.89×10^{16}	7.41×10^{16}	1.00×10^{15}	10
	1.18×10^{18}	8.89×10^{16}	7.41×10^{16}	1.00×10^{15}	50
	1.18×10^{18}	8.89×10^{16}	7.41×10^{16}	1.00×10^{15}	50
	1.48×10^{18}	8.89×10^{16}	7.41×10^{16}	1.00×10^{15}	50
N_2 Scan	5.92×10^{16}	1.48×10^{16}	7.41×10^{16}	1.00×10^{15}	50
	5.92×10^{16}	2.96×10^{16}	7.41×10^{16}	1.00×10^{15}	50
	5.92×10^{16}	5.92×10^{16}	7.41×10^{16}	1.00×10^{15}	50
	5.92×10^{16}	7.41×10^{16}	7.41×10^{16}	1.00×10^{15}	50
	5.92×10^{16}	9.92×10^{16}	7.41×10^{16}	1.00×10^{15}	50
	5.92×10^{16}	1.18×10^{18}	7.41×10^{16}	1.00×10^{15}	50
	5.92×10^{16}	1.33×10^{18}	7.41×10^{16}	1.00×10^{15}	50
	5.92×10^{16}	1.33×10^{18}	7.41×10^{16}	1.00×10^{15}	50
	5.92×10^{16}	1.48×10^{18}	7.41×10^{16}	1.00×10^{15}	50
	5.92×10^{16}	1.48×10^{18}	7.41×10^{16}	1.00×10^{15}	50
O_3 Scan	1.48×10^{16}	8.89×10^{16}	7.41×10^{16}	5.00×10^{14}	50
	1.48×10^{16}	8.89×10^{16}	7.41×10^{16}	1.00×10^{15}	50
	1.48×10^{16}	8.89×10^{16}	7.41×10^{16}	2.50×10^{15}	50
	1.48×10^{16}	8.89×10^{16}	7.41×10^{16}	5.00×10^{15}	50
	2.96×10^{16}	8.89×10^{16}	9.57×10^{16}	1.00×10^{14}	50
	2.96×10^{16}	8.89×10^{16}	8.74×10^{16}	5.00×10^{14}	50
	2.96×10^{16}	8.89×10^{16}	7.41×10^{16}	1.00×10^{15}	50
	2.96×10^{16}	8.89×10^{16}	7.41×10^{16}	2.00×10^{15}	50

	[CO]	[N_2]	[D_2]	[O_3]	Int. Time (μs)
	2.96×10^{16}	8.89×10^{16}	8.16×10^{16}	5.00×10^{15}	50
D_2 Scan	2.96×10^{16}	8.89×10^{16}	1.48×10^{16}	1.00×10^{15}	50
	2.96×10^{16}	8.89×10^{16}	2.96×10^{16}	1.00×10^{15}	50
	2.96×10^{16}	8.89×10^{16}	5.92×10^{16}	1.00×10^{15}	50
	2.96×10^{16}	8.89×10^{16}	8.89×10^{16}	1.00×10^{15}	50
	2.96×10^{16}	8.89×10^{16}	1.18×10^{18}	1.00×10^{15}	50
OD(v=1) lifetime	0	9.98×10^{16}	8.32×10^{16}	1.00×10^{16}	50
	2.06×10^{16}	9.91×10^{16}	8.26×10^{16}	1.00×10^{16}	50
	4.08×10^{16}	9.79×10^{16}	8.16×10^{16}	1.00×10^{16}	50
	5.64×10^{16}	9.67×10^{16}	8.06×10^{16}	1.00×10^{16}	50
	8.19×10^{16}	9.83×10^{16}	8.19×10^{16}	1.00×10^{16}	50
	9.79×10^{16}	9.80×10^{16}	8.16×10^{16}	1.00×10^{16}	50

5.2.2 Data extraction & analysis

Spectral acquisition The transmitted mid-IR light was spatially dispersed using a Virtually Imaged Phased Array (VIPA) and detected using a FLIR SC6000 InSb camera, in the same manner as Fleisher et al.[10]. The camera integration (50 μs or 10 μs integration time) was synchronized to the Nd:YAG photolysis pulse. A digital delay generator sets the variable delay times from the photolysis pulse. Since we are not resolving individual frequency comb modes, we calibrated our frequency axis each day to known D_2O line positions from Ref.[162]. The experiment was conducted at a 10 Hz repetition rate, set by the maximum repetition rate of the pulsed Nd:YAG laser. A "reference" image was collected directly prior to each Nd:YAG pulse and "signal" images were collected at various delay times following the Nd:YAG pulse. Since the InSb camera has a dark current offset that drifts with ambient temperature, a "background" image was also collected at the same repetition rate by briefly blocking the camera with an optical shutter. After collecting each set of images, the absorbance was constructed in the following manner ,

$$A = -\log\left(\frac{S-B}{R-B}\right), \tag{5.7}$$

where S, R, and B are the signal, reference, and background images, respectively. Due to slowly-varying baseline fluctuations in the transmission through the cavity, a sliding average was subtracted from the measured absorbance as a function of wavenumber, forming a "high-passed" signal $\tilde{A} = A - H[A]$, where H is the sliding average function. Following the "high-pass" filter operation, the error at each point in the spectrum is estimated by taking the standard deviation of the surrounding points. In this manner, each collected spectrum is assigned a value and error corresponding to $\tilde{A} \pm \delta\tilde{A}$. Averaging many of these values yields an average value $\tilde{A}_{mean} \pm \delta\tilde{A}_{mean}$. Since this "sliding standard deviation" operation includes some of the absorption peaks in the spectrum, it is a slight overestimate of the error in the spectrum.

Spectral fitting In direct absorption spectroscopy, the concentration of a species is related to the transmission of a probe beam through the relation

$$\frac{I_S(\tilde{\nu})}{I_R(\tilde{\nu})} = e^{-n\sigma(\tilde{\nu})l}\ , \tag{5.8}$$

where and are the light intensities with and without the sample, n is the molecular concentration in molecules cm^{-3},$\sigma(\tilde{\nu})$ is the molecular absorption cross section in cm^2, l is the path length through the sample in cm, and $\tilde{\nu}$ is wavenumber in cm^{-1}. For this experiment, is recorded 4 ms before the photolysis pulse and is recorded after the photolysis pulse by the InSb camera. If multiple species are present, the transmission versus time is now given by

$$-\frac{1}{l}\log\left(\frac{I_S(\tilde{\nu})}{I_R(\tilde{\nu})}\right) = n_A(t)\sigma_A(\tilde{\nu}) + n_B(t)\sigma_B(\tilde{\nu}) + \cdots\ , \tag{5.9}$$

where A and B are two sample molecules. If $\sigma_A(\tilde{\nu}), \sigma_B(\tilde{\nu})$ are linearly independent as a function of wavelength, then $n_A(t), n_B(t)$ are determined uniquely through linear regression. $\sigma(\tilde{\nu})$ is related to the molecular line strength S through $\sigma(\tilde{\nu}) = Sg(\tilde{\nu} - \tilde{\nu}_0)$ where $g(\tilde{\nu} - \tilde{\nu}_0)$ is the area normalized

lineshape function. In our case, $g(\tilde{\nu} - \tilde{\nu}_0)$ is a Gaussian function with FWHM = 900 MHz. This is significantly larger than the molecular Doppler width, so convolution with the molecular lineshape is neglected.

Since we "high-pass" the measured absorbance, $A(\tilde{\nu})$, to reduce the effects of cavity fluctuations, it is also necessary to perform the same operation on the calculated molecular cross sections. This will not affect the fitted concentration values, since the sliding average operation H[A] is a linear function and thus

$$-\frac{1}{l}\log\left(A - H[A]\right) = n_A(t)(\sigma_A(\tilde{\nu}) - H[\sigma_A(\tilde{\nu})]) + n_B(t)(\sigma_B(\tilde{\nu}) - H[\sigma_B(\tilde{\nu})]) + \cdots , \qquad (5.10)$$

where A is the absorbance, given by $A = -\log\left(\frac{I_S(\tilde{\nu},t)}{I_R(\tilde{\nu})}\right)$.

Spectral line intensities Experimental details for obtaining line positions and line intensities for D_2O are found in Ref. [162] and Ref. [164], respectively. Unpublished line intensities (Table 5.2) measured by Dr. Robert A. Toth using a Fourier transform spectrometer[162] are generously provided through private communication with Dr. Keeyoon Sung of JPL. Line positions for OD(v=0,1) were obtained from Ref. [132]. PGopher [49] was used along with fit parameters from Ref. [132] to obtain relative line strengths for each line in the spectrum. The OD v=0 and v=1 transition dipole moments $|\mu_{OD}^{01}| = 0.0303$ and $|\mu_{OD}^{12}| = 0.0386$ D were obtained from mass-scaling the OH transition dipole moments. The $|\mu_{OH}^{01}| = 0.0343$ and $|\mu_{OH}^{12}| = 0.0408$ D transition dipole moments were calculated using the RKR potential and dipole moment functions reported by Nesbitt and coworkers[134, 133]. The error in the transition dipole moments is estimated to be <10% for OD. *trans*-DOCO ν_1 ro-vibrational parameters were obtained from Ref. [95] and used to simulate the ro-vibrational spectrum in PGopher. As there are no known measurements of the *trans*-DOCO band intensity, we assume a trans-DOCO ν_1 band strength of $S_{trans-DOCO} = 65 \pm 5$ km/mol, estimated from a series of anharmonic VPT2 vibrational calculations performed at the CCSD(T)/ANOn (n = 0,1,2) and CCSD(T)/cc-pCVXZ (X = D,T,Q) levels of theory (personal communication with J.

F. Stanton).

Table 5.2: D_2O line positions (cm^{-1}) and intensities (cm $molecule^{-1}$) from Toth et al.[162]. Note that only the line positions are published, whereas the line intensities are provided through private communication with Dr. Keeyoon Sung of JPL.

Position	Intensity	Position	Intensity	Position	Intensity
2640.2345	2.64×10^{-22}	2649.42945	4.41×10^{-21}	2658.5228	3.42×10^{-22}
2640.4272	5.23×10^{-22}	2649.5656	6.13×10^{-23}	2659.1482	1.12×10^{-20}
2641.2913	7.85×10^{-24}	2649.6475	2.37×10^{-23}	2659.9311	1.12×10^{-23}
2641.53603	7.85×10^{-24}	2649.86673	4.86×10^{-21}	2660.1669	1.86×10^{-23}
2642.3123	2.93×10^{-21}	2650.0932	1.2×10^{-21}	2660.57108	4.45×10^{-23}
2642.6734	1.23×10^{-21}	2650.24288	6.78×10^{-21}	2660.7399	3.8×10^{-21}
2643.143	1.38×10^{-22}	2650.52625	3.82×10^{-23}	2661.1383	1.88×10^{-23}
2643.5818	3.23×10^{-22}	2650.61934	2.61×10^{-21}	2661.1527	3.81×10^{-23}
2643.59308	1.27×10^{-23}	2651.0157	1.19×10^{-23}	2661.3546	3.61×10^{-23}
2643.9221	1.73×10^{-21}	2652.1988	1.18×10^{-21}	2661.55001	4.41×10^{-21}
2643.99044	2.82×10^{-21}	2652.7398	2.55×10^{-23}	2661.7319	1.36×10^{-22}
2644.2378	8.58×10^{-24}	2652.8054	7.44×10^{-22}	2663.6125	2.79×10^{-21}
2644.4066	4.29×10^{-24}	2652.8692	3.71×10^{-22}	2663.6323	5.43×10^{-21}
2644.566	6.46×10^{-23}	2654.5461	2.49×10^{-21}	2663.91535	3.88×10^{-21}
2644.6401	3.64×10^{-22}	2654.5589	2.66×10^{-21}	2664.1152	1.13×10^{-21}
2644.7931	8.58×10^{-24}	2655.2742	1.56×10^{-22}	2664.25555	3.61×10^{-21}
2645.1625	2.66×10^{-24}	2655.299	1.01×10^{-22}	2664.4722	1.83×10^{-23}
2645.335	7.64×10^{-22}	2655.7285	1.25×10^{-21}	2664.9705	4.49×10^{-22}
2645.7443	4.41×10^{-22}	2655.8308	7.93×10^{-23}	2664.98852	9.44×10^{-22}
2646.18699	1.9×10^{-21}	2655.928	4.41×10^{-23}	2665.9744	5.8×10^{-23}

Position	Intensity	Position	Intensity	Position	Intensity
2646.68677	2.39×10^{-21}	2657.027	1.13×10^{-23}	2666.5308	1.35×10^{-22}
2646.723	3.85×10^{-21}	2657.1548	5.48×10^{-24}	2666.99383	7.97×10^{-21}
2647.0682	2.12×10^{-21}	2657.4666	3.44×10^{-23}	2667.1147	7.27×10^{-23}
2647.205	1.57×10^{-21}	2657.52565	8.09×10^{-21}	2667.2057	2.58×10^{-21}
2647.34975	4.17×10^{-21}	2657.7129	3.81×10^{-21}	2668.64249	6.78×10^{-21}
2647.3844	1.63×10^{-23}	2657.848	4.37×10^{-23}	2668.91278	1.14×10^{-20}
2648.28	6.95×10^{-21}	2658.12175	3.91×10^{-22}	2669.2846	1.28×10^{-23}
2649.043	1.01×10^{-22}	2658.20235	3.58×10^{-21}	2669.5047	4.45×10^{-22}
2649.061	7.03×10^{-24}	2658.2584	1.99×10^{-22}	2670.13472	5.56×10^{-21}
2649.0898	1.5×10^{-23}	2658.3467	2.37×10^{-23}	2670.54029	5.11×10^{-23}
2670.8972	7.68×10^{-23}	2682.7988	3.24×10^{-21}	2693.6488	1.25×10^{-21}
2670.9733	1.57×10^{-22}	2683.0851	6.7×10^{-23}	2694.1202	2.49×10^{-22}
2671.5212	5.43×10^{-23}	2684.0578	1.64×10^{-22}	2694.23385	4.01×10^{-23}
2671.5883	4.07×10^{-22}	2684.16277	9.19×10^{-21}	2695.3701	1.53×10^{-21}
2671.6725	2.78×10^{-23}	2684.4509	3.24×10^{-21}	2695.516	1.57×10^{-22}
2671.7708	2.28×10^{-23}	2684.5865	4.29×10^{-23}	2695.9146	2.17×10^{-21}
2671.91013	1.38×10^{-23}	2685.00147	2.82×10^{-23}	2696.25256	2.14×10^{-20}
2672.1342	1.73×10^{-23}	2685.2205	1.56×10^{-23}	2696.4641	7.48×10^{-23}
2672.3234	1.27×10^{-20}	2685.4227	3.61×10^{-23}	2696.8033	1.57×10^{-24}
2672.4246	1.25×10^{-22}	2685.7946	7.56×10^{-23}	2697.27755	1.75×10^{-21}
2672.57006	2.55×10^{-23}	2686.09833	5.31×10^{-23}	2697.3128	1.54×10^{-22}
2672.71	1.18×10^{-22}	2686.79348	1.35×10^{-21}	2697.6058	1.5×10^{-22}
2672.7446	1.92×10^{-22}	2686.986	7.48×10^{-23}	2697.7648	1.12×10^{-23}
2672.771	7.36×10^{-23}	2688.01359	7.97×10^{-23}	2697.81728	2.3×10^{-23}
2672.81345	3.01×10^{-23}	2688.5288	3.08×10^{-21}	2698.6272	3.69×10^{-22}

Position	Intensity	Position	Intensity	Position	Intensity
2674.1562	3×10^{-24}	2688.55586	5.97×10^{-21}	2699.0851	1.26×10^{-21}
2674.2478	8.74×10^{-23}	2688.7263	2.68×10^{-23}	2699.09974	9.4×10^{-22}
2675.0847	8.99×10^{-23}	2688.82239	7.64×10^{-21}	2699.39049	4.29×10^{-23}
2675.359	1.17×10^{-22}	2689.0089	1.49×10^{-21}	2700.0094	2.73×10^{-23}
2676.21568	5.27×10^{-21}	2689.3199	2.47×10^{-22}	2700.0249	2.38×10^{-22}
2676.3165	2.67×10^{-21}	2689.4355	2.21×10^{-24}	2700.1138	8.54×10^{-22}
2676.47655	4.7×10^{-23}	2689.90787	2.63×10^{-20}	2700.1409	6.95×10^{-22}
2676.6666	1.25×10^{-21}	2690.1185	4.82×10^{-22}	2700.4127	1.79×10^{-20}
2676.999	1.44×10^{-22}	2690.4366	1.1×10^{-22}	2700.485	5.8×10^{-22}
2677.5985	1.75×10^{-20}	2690.8628	1.52×10^{-24}	2700.62468	7.97×10^{-21}
2678.22986	1.03×10^{-20}	2691.1606	1.36×10^{-20}	2700.8671	7.44×10^{-22}
2679.5902	5.07×10^{-21}	2691.46408	8.74×10^{-23}	2701.0039	1.29×10^{-21}
2679.8475	6.5×10^{-23}	2691.6066	1.98×10^{-21}	2701.1606	5.6×10^{-23}
2679.9658	1.81×10^{-22}	2691.69857	6.46×10^{-21}	2701.24658	3.5×10^{-20}
2680.3429	2.01×10^{-20}	2691.7401	1.21×10^{-20}	2701.4495	8.54×10^{-23}
2680.55718	9.19×10^{-21}	2691.91439	1.09×10^{-20}	2702.01668	1.88×10^{-20}
2680.60718	1.88×10^{-20}	2691.993	2.27×10^{-22}	2702.447	1.51×10^{-22}
2680.83526	1.75×10^{-20}	2692.10628	1.37×10^{-24}	2702.635	2.64×10^{-22}
2680.8799	3.58×10^{-23}	2692.26094	1.29×10^{-20}	2702.6618	5.48×10^{-23}
2681.1146	1.48×10^{-23}	2692.49856	1.79×10^{-20}	2702.76315	1.14×10^{-22}
2681.8938	1.32×10^{-21}	2692.7442	4.25×10^{-23}	2702.79603	3.43×10^{-20}
2682.04028	7.23×10^{-23}	2692.7624	1.53×10^{-20}	2703.0353	1.25×10^{-21}
2682.44429	3.66×10^{-23}	2693.22996	2.42×10^{-24}	2703.1091	5.48×10^{-23}
2704.8754	7.52×10^{-22}	2717.55131	1.06×10^{-20}		
2705.52613	4.99×10^{-21}	2718.0281	8.09×10^{-24}		

Position	Intensity	Position	Intensity	Position	Intensity
2705.86502	3.45×10^{-20}	2718.3284	3.37×10^{-22}		
2706.17996	2.62×10^{-20}	2719.52848	2.19×10^{-20}		
2706.86418	6.13×10^{-22}				
2707.1581	4.66×10^{-22}				
2708.56546	1.31×10^{-20}				
2708.6163	8.05×10^{-22}				
2709.2377	3.24×10^{-21}				
2709.312	3.72×10^{-22}				
2710.24857	6.5×10^{-22}				
2710.57106	3.32×10^{-21}				
2710.7739	9.85×10^{-22}				
2711.0795	5.43×10^{-22}				
2711.21661	4.29×10^{-20}				
2712.35984	2.37×10^{-20}				
2712.45137	4.41×10^{-20}				
2712.5763	8.99×10^{-22}				
2713.3275	3.79×10^{-23}				
2713.37758	8.17×10^{-23}				
2713.48368	1.27×10^{-22}				
2713.6902	1.89×10^{-23}				
2713.7529	3.19×10^{-22}				
2714.0415	1.99×10^{-20}				
2714.63906	1.12×10^{-22}				
2715.016	9.52×10^{-22}				
2715.6114	5.23×10^{-22}				

Position	Intensity	Position	Intensity	Position	Intensity
2715.8032	5.19×10^{-22}				
2715.835	2.41×10^{-22}				
2715.9995	1.03×10^{-21}				
2716.4458	4.33×10^{-22}				
2716.8877	1.73×10^{-21}				
2717.26396	4.29×10^{-23}				

Photolysis Path Length and Finesse In cavity-enhanced spectroscopy, the path length l is given by the physical path length multiplied by a factor of F, where F is the finesse of the optical cavity and $1 \leq \beta \leq 2$ is a parameter that arises when a sweep-lock is used[66]. In addition, the path length is reduced to the width of the photolysis beam, lphot. Thus, the effective optical absorption path length is given by

$$l_{eff} = \frac{\beta F l_{phot}}{\pi}. \tag{5.11}$$

The cavity finesse F as a function of wavelength was measured using cavity ringdown (Fig. 5.9). The photolysis path length, l_{phot}, was determined in two ways: (1) The width (46 ± 5 mm) of the burn spot on a photographic film from YAG beam, and (2) a razor blade scan across the beam and fitting the OD concentration at each point of the scan (Fig. 5.10). The razor blade method gave a beam width of 42 ± 4 mm, which is in agreement with the photographic film method. The weighted average of these two methods is 44 ± 3 mm. The error in the effective path length is given as

$$\delta l_{eff} = l_{eff} \sqrt{\left(\frac{\delta\beta}{\beta}\right)^2 + \left(\frac{\delta F}{F}\right)^2 + \left(\frac{\delta l_{phot}}{l_{phot}}\right)^2}, \tag{5.12}$$

which yields $l_{eff} = 58 \pm 4$ m at the finesse peak of 3725 nm.

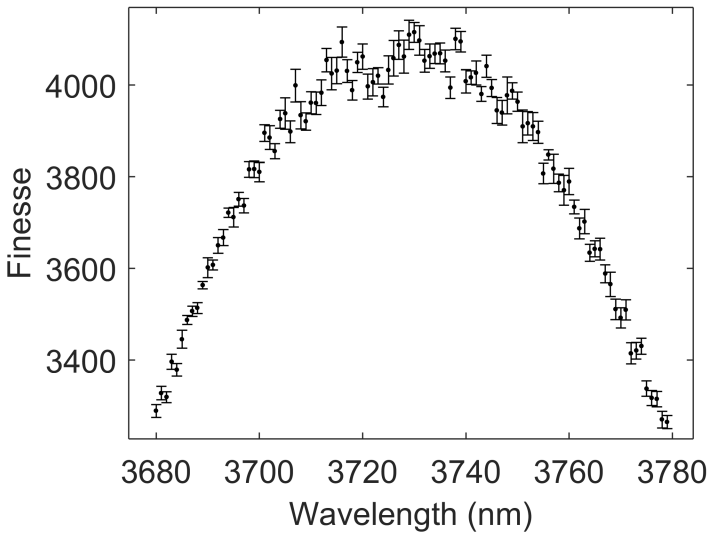

Figure 5.9: Finesse from spectrally resolved cavity-ringdown measurements.

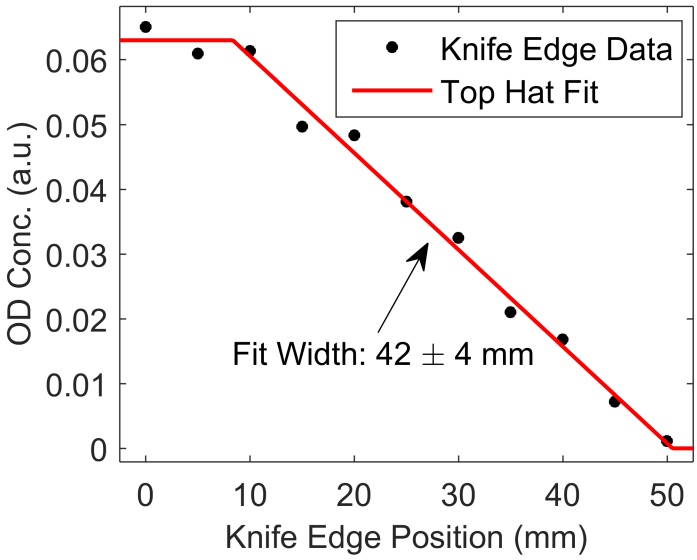

Figure 5.10: Knife edge scan of YAG beam.

Flow cell gas residence time To ensure that fresh gas is introduced into the kinetics cell prior to each photolysis pulse, we measured the residence time by monitoring the D_2O stable product at our flow conditions. Fig. 5.11A shows the D_2O temporal profile at a few CO concentrations, along with a semi-empirical fit for estimating the gas half-life in our flow cell. [D_2O](t) was fit to $[D_2O](t) = A(1 - \alpha e^{-b_1 t} - (1-\alpha)e^{-b_2 t})e^{-b_{fall} t^2}$, where the rise of D_2O is expected to be bi-exponential and the fall is expected to be determined by the spatial profile of the YAG beam as well as diffusion dynamics. We determine the half-life of the cell by setting the fall function to 50%, which yields $\tau_{1/2} = \sqrt{\frac{\ln(2)}{b_{fall}}}$. This parameter is plotted as a function of [CO] in Fig. 5.11B. Since we do not see a systematic variation of the pump out time with [CO], we use the mean, 20.1±0.5 ms, as an estimate of the gas half-life for all conditions. Inserting this back into the pump out function, we estimate that <1% of residual gas remains between photolysis pulses, separated by 100 ms.

5.2.3 Sources of error

Spectral interference from D_2O In performing a linear spectral fit to OD, D_2O, and *trans*-DOCO, it is possible that absorption from one species may interfere with another. This cross-contamination effect can be exacerbated if the lineshape of the fit does not exactly match the experiment. The largest cross-contamination effect in our experiment is between OD and D_2O, since half of the OD lines in our spectral window are contaminated by strong D_2O transitions. However, this is nearly negligible in the first 100 μs, where D_2O concentrations are low. Based on a comparison of contaminated and uncontaminated OD absorption features, we estimate that the systematic error due to cross-contamination is <1%.

Initial Rate Method At early times, we expect DOCO to behave according to the first-order differential equation

$$[DOCO](t) = k_{1a}[CO][OD](t) - k_{loss}[X] \tag{5.13}$$

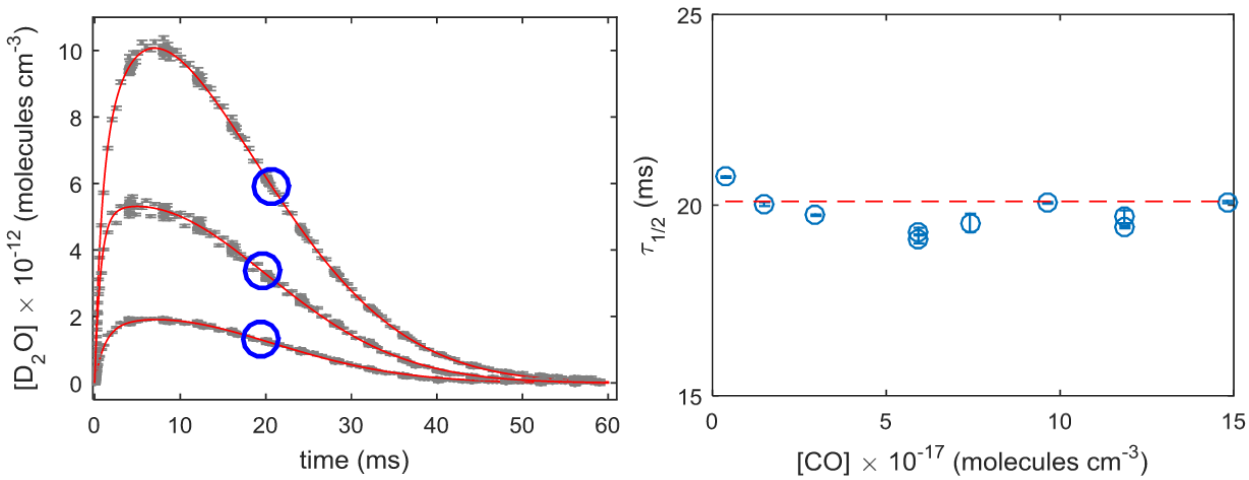

Figure 5.11: (A) Experimental $[D_2O](t)$ (grey dots) for a few CO concentrations, along with temporal fits (red lines), which yield its half-life in the kinetics cell (blue circles). (B) D_2O half-life is plotted as a function of [CO] (blue circles). The mean of these values is indicated by a red dashed line.

where [X] is the primary loss partner for DOCO and [OD](t) refers to the time-dependent concentration of OD in the ground vibrational state, OD(v=0). With the initial condition that [DOCO(t=0)] = 0, we can solve this equation directly for [DOCO](t) in terms of [OD](t), which yields

$$[DOCO](t) = k_{1a}[CO] \int_0^t e^{-(k_{loss}[X])(t-u)}[OD](u)du \; . \tag{5.14}$$

To obtain an analytic form for [OD](t), we fit a sum of exponentials to our experimental data, constrained by [OD](t=0) = 0.

$$[OD](t) = a_1 e^{-b_1 t} + a_2 e^{-b_2 t} - (a_1 + a_2)e^{-b_3 t} \tag{5.15}$$

Here, b_1 and b_2 are bi-exponential decay terms while b_3 is a rise term. The b_3 rise term for OD(v=0) is directly related to the decay of OD(v=1) where it originates. OD(v=1) decay will be discussed in more detail in the following sections. Using this expression for OD(t), DOCO(t) is given by

$$[DOCO](t) = k_{1a}[CO]\left(a_1\frac{e^{-b_1 t} - e^{-r_{loss}t}}{b_1 - r_{loss}} + a_2\frac{e^{-b_2 t} - e^{-r_{loss}t}}{b_2 - r_{loss}} - (a_1 + a_2)\frac{e^{-b_3 t} - e^{-r_{loss}t}}{b_3 - r_{loss}}\right) \tag{5.16}$$

DOCO(t) contains two free parameters in this expression, k_{1a}, and r_{loss} ($\equiv k_{loss}[X]$). We fit a rloss,exp = (4.0±0.4)×10^4 s^{-1} to all data with constant [O_3], while our fit value of k_{1a} varies with N_2 and CO. From our fit values of the bimolecular rate constant k1a, we determine the termolecular rates $k_{1a}^{(CO)}$ and $k_{1a}^{(N2)}$ from a multidimensional linear regression to the expression

$$k_{1a} = k_{1a}^{(CO)}[CO] + k_{1a}^{(N2)}[N_2] \; . \tag{5.17}$$

The statistical error in our values of $k_{1a}^{(CO)}$ and $k_{1a}^{(N2)}$ are established from the variation in the fit residuals. Uncertainty in the Initial Rate Method: To investigate the variation in our fitted k_{1a} values with integration time, we divided our values for k_{1a} (see main text) for 50 and 10 μs and plotted these values as a function of CO concentration. We display this value, $r = \frac{k_{1a,10\mu s}}{k_{1a,50\mu s}}$, with CO in Fig. 5.12.

In order to estimate a general systematic error in a given data set, we calculate the weighted mean and standard deviation of this data, which are and , respectively. We interpret as a systematic shift due to our 50 μs integration time and as an estimate of the statistical variation of k_{1a} with respect to integration time and [CO].

Effect of OD Vibrational Excitation Since vibrationally hot OD(v>0) was generated under our experimental conditions, we investigated the effect of vibrational quenching of hot OD under conditions relevant for fitting the OD + CO DOCO rate. First, O(^{1}D) + D_2 OD + D promptly produces excited OD up to the 4th vibrational state[165]. The second reaction, D + O_3 →OD + O_2, continually generates hot OD up to the 9th vibrational state[166]. Due to the broad bandwidth and high sensitivity of our kinetics apparatus, we were simultaneously able to detect OD(v=0) and OD(v=1) in a time-resolved manner during each experimental run. Fig. 5.13 show an acquired spectrum containing both strong OD(v=0) (blue) and OD(v=1) (red) transitions.

To constrain the extent to which OD(v>0) introduces error into our overall determination of k_{1a}, we conducted experiments to measure both the density and lifetime of OD(v=1) over a range of CO densities. Experiments were conducted with [O_3] = 1×10^{16} molecules cm^{-3}, which provided

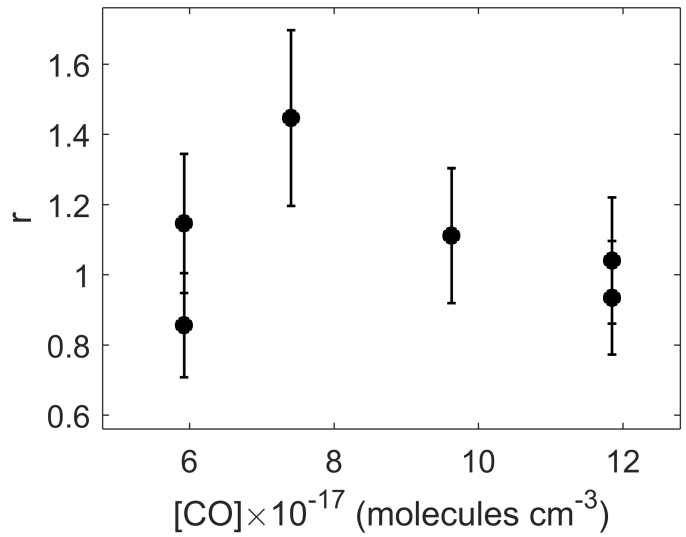

Figure 5.12: The ratio of retrieved k_{1a} values for 50 μs and 10 μs integration times.

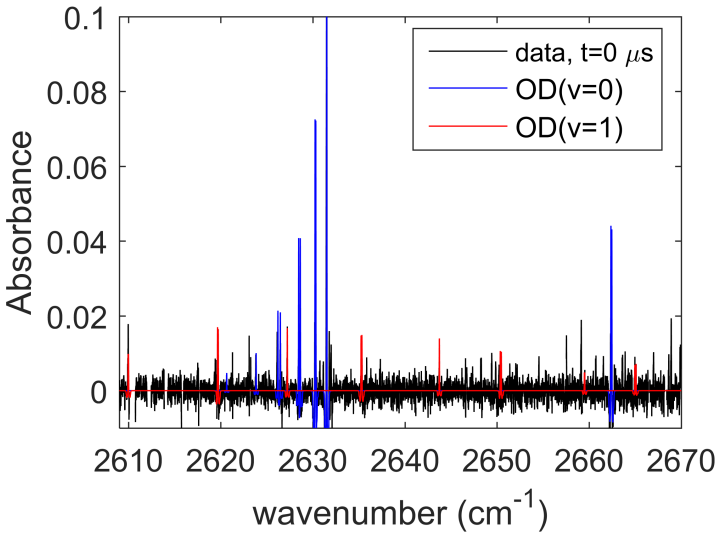

Figure 5.13: Representative spectrum of OD(v=0) and OD(v=1) for measuring [OD(v>0)].

an upper limit for the vibrationally excited OD population. [CO] ranged from 0-9×10^{16} molecules cm^{-3}, which is well below the lowest [CO] used in our k_{1a} measurement. We observed high signal-to-noise ratio OD(v=1) transitions, but not any OD(v>1), indicating that either 1) the densities are too low and/or 2) the lifetimes are too short for higher exited states. The results from this experiment are shown in Fig 5.14. At our operating conditions for determining k_{1a}, the lifetime of OD(v=1) is <5 μs. The measured densities for OD(v=1) are also <10% of OD(v=0). Therefore, even if OD(v>0) forms ground state *trans*-DOCO at the same rate as OD(v=0), this would only introduce a <10% uncertainty in our measurement, which has been included in our systematic error budget (Table 5.4).

OD(v=1) loss is due, at least in part, to quenching to ground state OD(v=0). The equation for [OD(v=0)](t), given by eq. 5.15, is used to fit [OD](t) as a function of [CO]. In eq. 5.15, the fitted parameter b_3, which describes the rise rate of OD, is plotted as a function of [CO] in Fig. 5.15. The fitted slope yields a rise rate constant for OD(v=0) of (3.8±0.5)×10^{-13} cm^3 $molecule^{-1}$ s^{-1}, which is slightly larger than our measured OD(v=1)+CO loss rate, (3.3 ± 0.2)×10^{-13} cm^3 $molecule^{-1}$ s^{-1}. This is expected since OD(v=2) → OD(v=1) quenching competes with OD(v=1) → OD(v=0) loss.

Effect of D_2 In order to determine the systematic effects of large [D_2], we varied [D_2] under constant [N_2]=8.9×10^{17} molecules cm^{-3}, [CO] =3.0×10^{17} molecules cm^{-3}, and [O_3]=1.0×10^{15} molecules cm^{-3}. The results, shown in Fig. 5.16, show no statistically significant variation with [D_2]. While there are no literature estimates of the $DOCO^*$ + D_2 → DOCO + D_2 quenching efficiency, we might expect this rate to be slower than the N_2 rate by about a factor of 2, given similar comparisons in toluene[167]. In this case, we would expect the termolecular rate k_{1a} to change by about 0.5×10^{14} cm^3 $molecules^{-1}$ s^{-1} with a 1×10^{18} molecules cm^{-3} variation in [D_2]. The magnitude of the uncertainty in Fig. 5.16 is about 0.6×1014 cm^3 $molecules^{-1}$ s^{-1}, and hence a termolecular D_2 effect, if it exists, is masked by the noise. Ideally, k_{1a} is determined in the limit of [D_2] → 0. To determine the shift associated with nonzero D_2, we performed a linear fit to this data, resulting in a slope of (1.3 ± 0.8) × 10-33 cm6 molecules-2 s-1 and an offset of (1.44 ± 0.06) × 10^{-14} cm^3 $molecules^{-1}$ s^{-1}. At

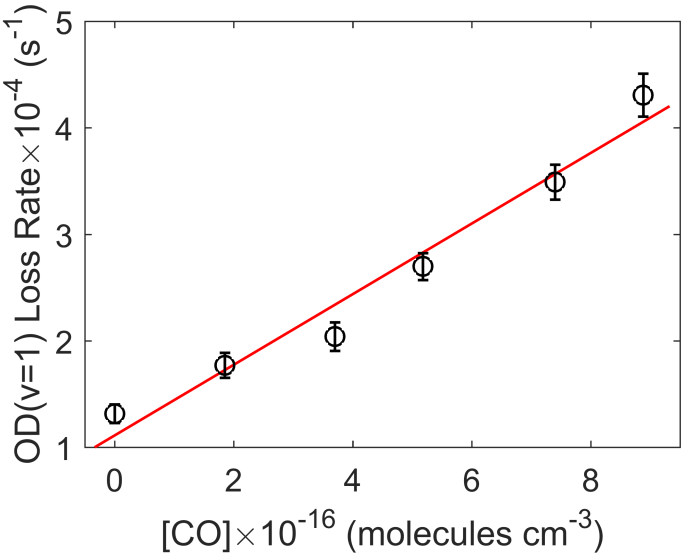

Figure 5.14: First order decay rate of OD(v=1) as a function of [CO]. The fitted rate constant for OD(v=1) loss is (3.3±0.2)×10^{-13} cm^3 $molecules^{-1}$ s^{-1}.

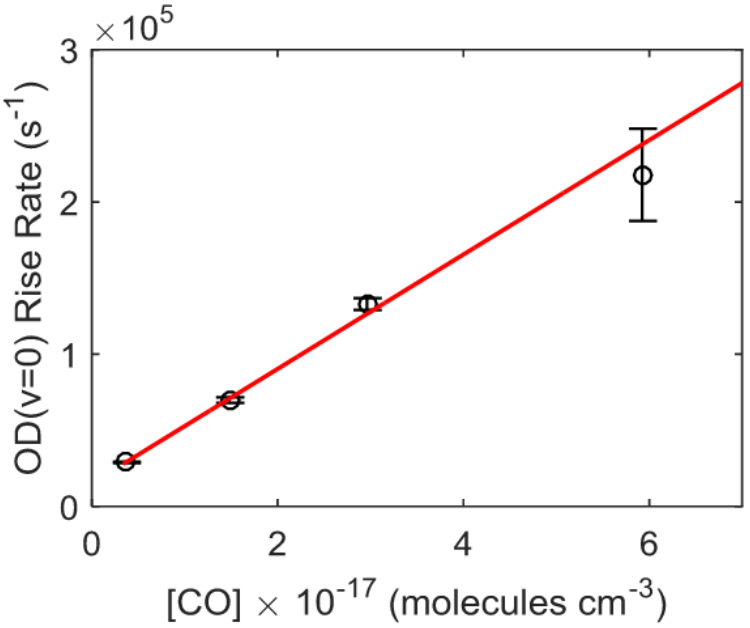

Figure 5.15: OD(v=0) rise as a function of [CO]. The fitted rate constant for OD(v=0) rise is (3.8±0.5)×10^{-13} cm^3 $molecule^{-1}$ s^{-1}.

our typical operating concentration of $[D_2] = 7.4\times10^{16}$ molecules cm^{-3}, this results in a systematic shift of $(0.7 \pm 0.4)\%$. However, this analysis assumes that k_{1a} is linear with D_2. As a much more conservative estimate of our systematic error, we use the mean-normalized standard deviation, , of the data in Fig. 5.16 as the fractional statistical error due to nonzero $[D_2]$.

Effect of O_3 In order to determine the systematic effects of $[O_3]$ in our measurement of $k_{1a}^{(CO)}$ and $k_{1a}^{(N2)}$, we varied $[O_3]$ under constant $[N_2]$=8.9×10^{17} molecules cm^{-3}, [CO]=1.5×10^{17} molecules cm^{-3}, and $[D_2]$= 7.4×10^{16} molecules cm^{-3}. With fixed $[O_3]$=1×10^{15} molecules cm^{-3}, we find our experimental data is consistent with a constant $r_{loss,exp} = (4.0\pm0.4)\times10^4$ s^{-1}, independent of $[N_2]$, $[D_2]$, and [CO]. In the case of varying $[O_3]$, however, we find that a constant $r_{loss,exp}$ term results in poor fits and also an observed systematic variation of k_{1a} with $[O_3]$. We therefore make the assumption that $r_{loss,exp}$ scales with $[O_3]$, i.e. $r_{loss,exp} = k_{O3}[O_3]$, where $k_{O3} = 4.0\times10^{-11}$ cm^3 molecules^{-1} s^{-1} is fixed by the results of the constant $[O_3]$ data. The retrieved values of k_{1a} vs $[O_3]$, shown in Fig. 5.17, display a weak dependence of k_{1a} on $[O_3]$. The weighted mean and standard deviation of this data are and , respectively. Ideally, k_{1a} is determined in the limit of $[O_3] \to 0$. Since we do not see a systematic variation of our retrieved k_{1a} value with $[O_3]$, we interpret as a maximum statistical error due to nonzero $[O_3]$.

5.2.4 Rate Equation Model

A full rate equation model that includes all of the most relevant rates for the reaction of OD + CO is given in Table 5.3. The system of stiff differential equations was integrated using the SimBiology software package from MathWorks and also by the Kintecus software package[168], both of which were in strong agreement. As the experimental data were integrated over 50 or 10 μs, we also boxcar-averaged the results from the rate equation model to fit to experimental data.

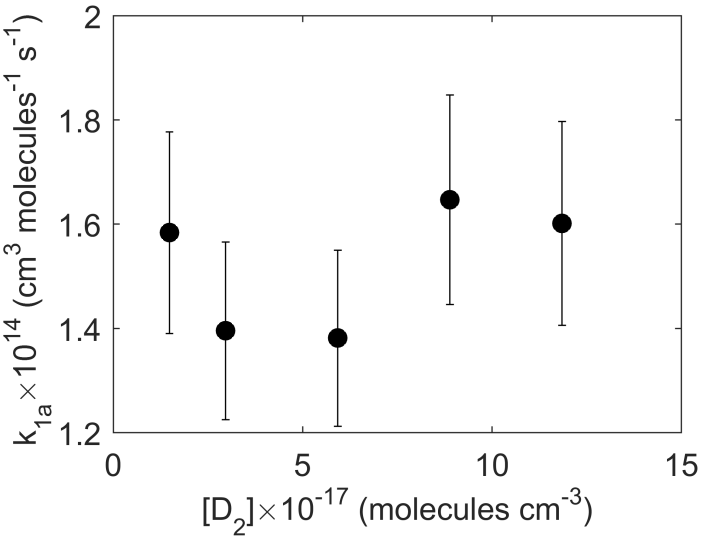

Figure 5.16: Variation of k_{1a} with D_2 concentration.

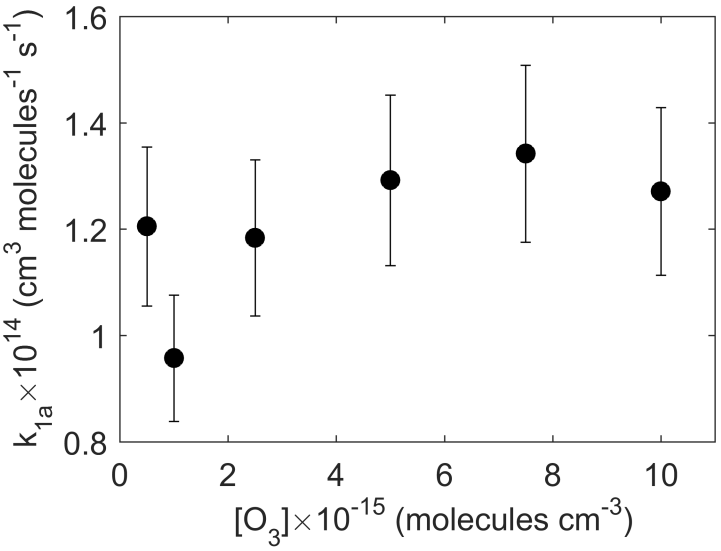

Figure 5.17: Variation of k1a with O_3 concentration.

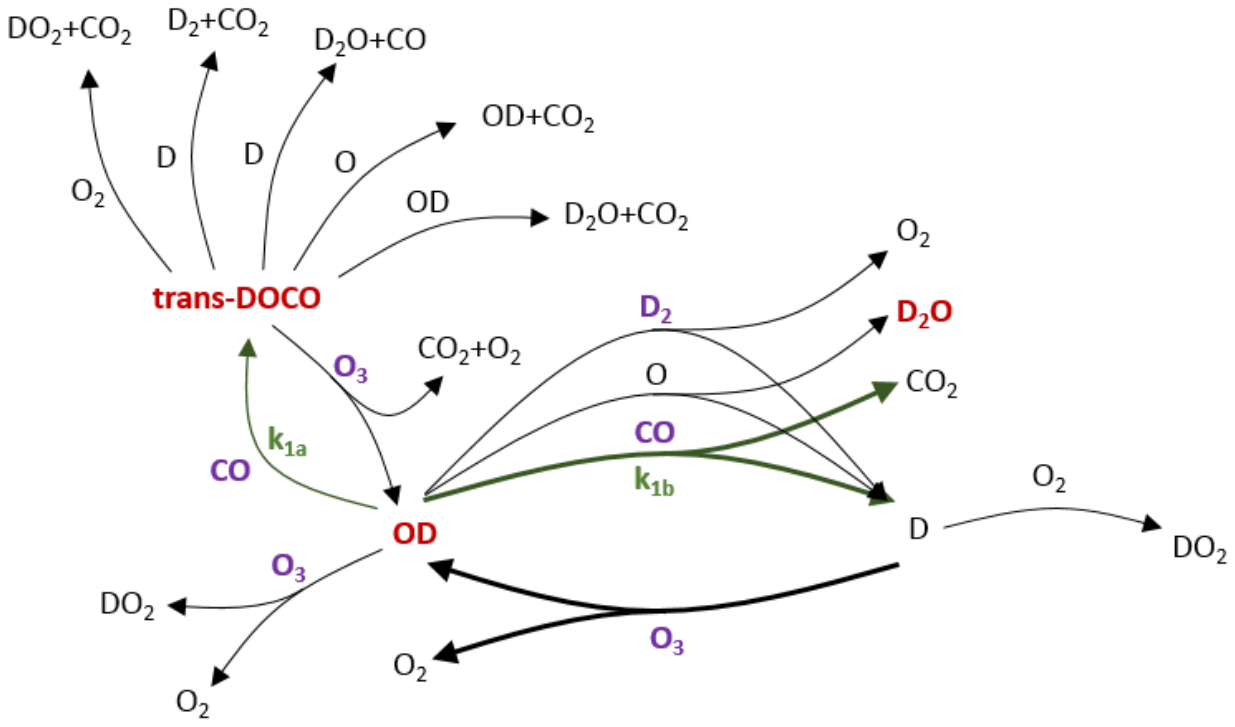

Figure 5.18: Basic schematic of the rate equation model used in the present studies. Absolute time-dependent concentrations of the red molecules (*trans*-DOCO, OD(v=0), OD(v=1), and D_2O) are measured through cavity-enhanced absorption spectroscopy, while the concentrations of the precursors (purple) are fixed by controlling the flows of N_2, CO, and D_2 and measuring the UV absorption of O_3, respectively. The two relevant OD + CO branching reactions are indicated in green.

Table 5.3: Rates used for modelling the OD + CO reaction. Units for termolecular rates are cm^6 $molecules^{-2}$ s^{-1} and cm^3 $molecules^{-1}$ s^{-1} for k_0^{300} and k_∞^{300}, respectively.

Reaction	Rate (cm^3 $molecule^{-1}$ s^{-1})	Source[1]	S_{OD} (%)	S_{DOCO} (%)	Ref(s)
$O(^1D) + N2 \rightarrow O + N_2$	$(3.1\pm0.3)\times10^{-11}$	DM	63	58	[6, 169]
$O(^1D) + CO \rightarrow O + CO$	$(5.8\pm1.2)\times10^{-11}$	DM	12	11	[170]
$O(^1D) + O_2 \rightarrow O + O_2$	$(3.95 \pm 0.4) \times 10\text{-}11$	DM	0	0	[6, 171]
$O(^1D) + O_3 \rightarrow O2 + O_2$	$(1.2\pm0.2)\times10^{-10}$	DM	0	0	[6]
$O(^1D) + O_3 \rightarrow O_2 + O + O$	$(1.2\pm0.2)\times10^{-10}$	DM	0	0	[6]
$O(^1D) + D_2 \rightarrow OD + D$	$(1.1\pm0.1)\times10^{-10}$	DM	75	69	[172]
$OD + O_3 \rightarrow DO_2 + O_2$	$(7.3\pm1.1)\times10^{-14}$	DMH	1	1	[6, 173]
$OD + D_2 \rightarrow D_2O + D$	$(1.65\pm0.13) \times 10^{-15}$	DM	1	1	[174]
$OD + OD \rightarrow D_2O + O$	$(4.34\pm0.63) \times 10^{-13}$	DM	0	0	[175]
$OD + DO_2 \rightarrow D_2O + O_2$	$(3.8\pm0.9) \times 10^{-11}$	DM	0	0	[176]
$OD + D_2O_2 \rightarrow D_2O + DO_2$	$(5.91\pm0.42)\times10^{-13}$	DM	0	0	[177]
$OD + CO \rightarrow D + CO_2$	$(5.6\pm0.2)\times10^{-14}$	DM	28	31	[149, 147, 163, 178]
$OD + CO + N_2 \rightarrow DOCO + N_2$	$(9.1\pm3.6)\times10^{-33}$				(this work)
$OD + CO + CO \rightarrow DOCO + CO$	$(2.0\pm0.8)\times10^{-32}$				(this work)
$OD + OD \rightarrow D_2O_2$	Termolecular: k_0^{300} =6.9×10^{-31} k_0^{300} =2.6×10^{-11}	DMH	0	0	[6]

Reaction	Rate (cm^3 $molecule^{-1}$ s^{-1})	Source[1]	S_{OD} (%)	S_{DOCO} (%)	Ref(s)
O + OD → O_2 + D	$(3.3\pm0.5)\times10^{-11}$	DMH	7	8	[6]
D + O_3 → OD + O2	$(2.9\pm0.3)\times10^{-11}$	DMH	33	45	[6]
D + DO_2 → OD + OD	$(7.2\pm1.4)\times10^{-11}$	DMH	0	0	[6]
D + DO_2 → O + D_2O	$(1.6\pm0.8)\times10^{-12}$	DMH	0	0	[6]
D + DO_2 → D_2 + O_2	$(6.9\pm2.8)\times10^{-12}$	DMH	0	0	[6]
D + O_2 → DO_2	Termolecular: k_0^{300} =4.4×10^{-32} k_0^{300} =7.5×10^{-11}	DMH	0	0	[6]
DOCO + D → D_2O + CO	1.39×10^{-11}	TH	0	2	[179]
DOCO + O_3 → OD + CO_2 + O_2	$(4\pm0.4)\times10^{-11}$ (overall fit)	FIT	2	45	(this work)
DOCO + D → D_2 + CO_2	9.31×10^{-11}	TH	1	14	[179]
DOCO + OD → D_2O + CO_2	1.03×10^{-11}	TH	0	3	[180]
DOCO + O → OD + CO_2	1.44×10^{-11}	TH	0	8	[181]
DOCO + O_2 → CO_2 + DO_2	$(1.9\pm0.2)\times10^{-12}$	DMH	0	3	[103]
DOCO LOSS	(fitted for each trace)				
O + O_3 → O_2 + O_2	$(8.0\pm0.8)\times10^{-15}$	DM	0	0	[6]
O + DO_2 → OD + O_2	$(5.9\pm0.3)\times10^{-11}$	DMH	1	0	[6]
O + D_2O_2 → OD + DO_2	$(1.7\pm0.3)\times10^{-15}$	DMH	0	0	[6]
DO_2 + O_3 → OD + O_2 + O_2	$(1.9\pm0.3)\times10^{-15}$	DMH	0	0	[6]

Reaction	Rate (cm^3 $molecule^{-1}$ s^{-1})	Source[1]	S_{OD} (%)	S_{DOCO} (%)	Ref(s)

[1]The source of the value used in the model is indicated: (TH) indicates a theoretical value, (DMH) indicates a direct experimental measurement of the Hydrogen-substituted reaction, and (DM) indicates a direct experimental measurement. (FIT) indicates a globally fitted reaction rate, specifically DOCO + O_3, which provided the best fit at $(4.0\pm0.4)\times10^{-11}$ cm^3 $molecule^{-1}$ s^{-1} for all scans.

Notes on Specific Reaction Rates OD + CO → D + CO_2 This reaction rate was determined from the weighted average of three measurements from Paraskevopoulos et al. [147], Golden et al. [178], and Westenberg et al. [163]. These values are $k_1 = (5.2\pm0.5)\times10^{-14}$, $(6.6\pm0.4)\times10^{-14}$, and $(5.48\pm0.2)\times10^{-14}$ cm^3 $molecules^{-1}$ s^{-1}, respectively. The result of the weighted average is $k_1 = (5.6\pm0.2)\times10^{-14}$ cm^3 $molecules^{-1}$ s^{-1}. Sensitivity Analysis: In order to determine the sensitivity of the model on each of these parameters, a sensitivity analysis was done, measuring the variation of the DOCO and OD peak concentrations with each of the rate constants. The sensitivity, S_{DOCO}, is defined for a given rate constant k as

$$S_{DOCO} = \frac{k}{[DOCO]_{max}} \frac{\partial [DOCO]_{max}}{\partial k}, \tag{5.18}$$

where $[DOCO]_{max}$ is the maximum concentration of DOCO. S_{OD} is defined in a similar manner. These values essentially represent the fractional fluctuation of [DOCO] or [OD] with a fractional change in k. Values of these parameters are given in Table S3 for the conditions

$[O_3] = 1\times10^{15}$ molecules cm^{-3}

$[D_2] = 1\times10^{17}$ molecules cm^{-3}

$[CO] = 1\times10^{17}$ molecules cm^{-3}

$[N_2] = 1\times10^{18}$ molecules cm^{-3}.

Results of rate equation model fits To compare the rate equation model to the experimental data, two parameters were fitted for each [OD](t), [DOCO](t) trace: an overall scaling factor for both OD and DOCO and a DOCO loss rate. Additionally, we found it necessary to fix the DOCO+O_3 rate as a constant and shared parameter for all traces, which yields a rate constant of 4×10^{-11} cm^3 $molecule^{-1}$ s^{-1}. The scaling factor accounts for uncertainties in both the effective optical path length and the OD^* chemistry involved that establishes the initial OD concentration measured at steady-state. The results of these fits as a function of CO are shown in Fig. 5.19A-B. The averaged values for the overall scaling factor and the DOCO loss rate are 0.14±0.05 and $(4.7\pm0.7)\times10^3$ s^{-1}, respectively. We observe a 65% correlation between the fitted overall scaling factor and DOCO loss rate.

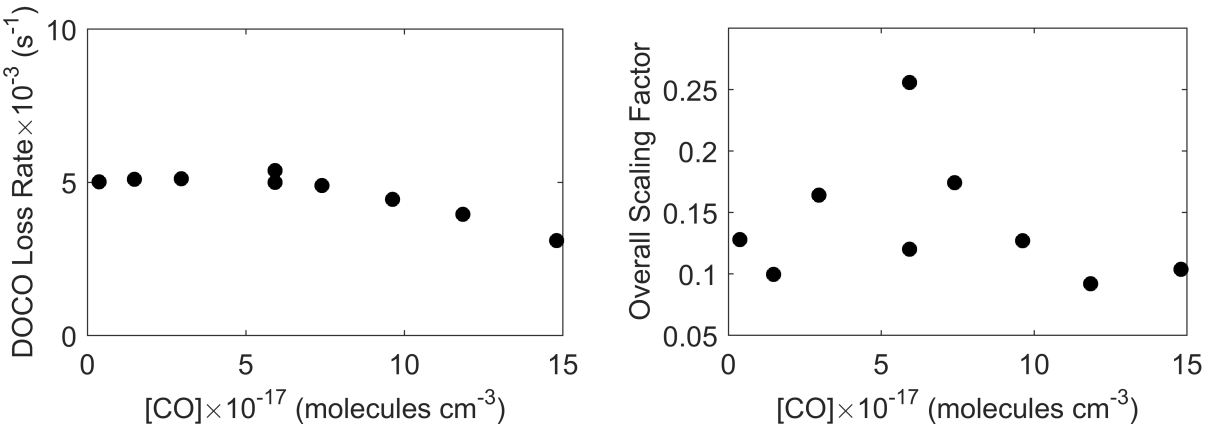

Figure 5.19: Results of fitting the DOCO loss rate (A) and overall scaling factor (B) in the model to the data.

5.2.5 Table of Statistical and Systematic Errors

Table 5.4: Summary of statistical and systematic errors.

	Error Source	$k_{1a}^{(CO)}$	$k_{1a}^{(N2)}$
Statistical Errors	(statistical, from fit residual)	6%	10%
Experimental Control	Flow & Pressure Measurement	7%(stat)	
Molecular Parameters	OD Cross Section	10%(stat)	
	DOCO Cross Section	10%(stat)	
Secondary Reactions	Effect of D_2	8%(stat)	
	Effect of O_3	11%(stat)	
Data Analysis	Cross-contamination of OD and D_2O	-1%(sys)	
	Effect of Integration Time	+9%(sys),21%(stat)	
	OD Vibrational Excitation	-10%(sys)	
	Total Systematic Error Budget	(-11%,+9%)	
	Total Statistical Error Budget	28%	29%
	Total Error Budget	(-39%,+37%)	(-40%,+38%)

Chapter 6

CO_2 and *cis*-DOCO Channels

In the last chapter, we demonstrated the ability of TRFCS to observe the OD+CO→*trans*-DOCO reaction on the microsecond timescale, where it can extract quantitative formation and decay rates for the reactants and products. However, this reaction is still far from being solved; there are still two main product channels, D+CO_2 and *cis*-DOCO, that have not been observed. In this chapter, we will report that the frequency comb is also able to provide quantitative information regarding the branching to these channels.

6.1 The $OD + CO \rightarrow D + CO_2$ Channel

Tuning to lower wavenumber from *trans*-DOCO, we approach the ν_3 asymmetric stretch band of CO_2, with a band center of 2349 cm^{-1}. Due to the large ambient concentration of CO_2 ($\approx$ 400 ppm), it is necessary to strike a balance between sensitivity to CO_2 generated in the kinetics cell and absorption in the lase beam line due to ambient CO_2. In practice, we found the best balance at a spectrum between $2390 - 2450\,cm^{-1}$, as shown in Fig. 6.1. As an additional benefit, we are able to observe OD(v=0) lines within this spectral region, allowing us to determine CO_2 and OD(v=0) concentrations simultaneously. The strongest CO_2 line observed in this window is its R(76) transition at 2390.552 cm^{-1} with a line intensity of $S = 4.140 \times 10^{-22}$ cm molecule^{-1}. The strongest OD(v=0) line is its $P_{1e}(9.5)$ transition near 2433.6 cm^{-1} with a line intensity of $S = 1.64 \times 10^{-21}$ cm molecule^{-1}. The OD line positions and strengths were obtained using the method

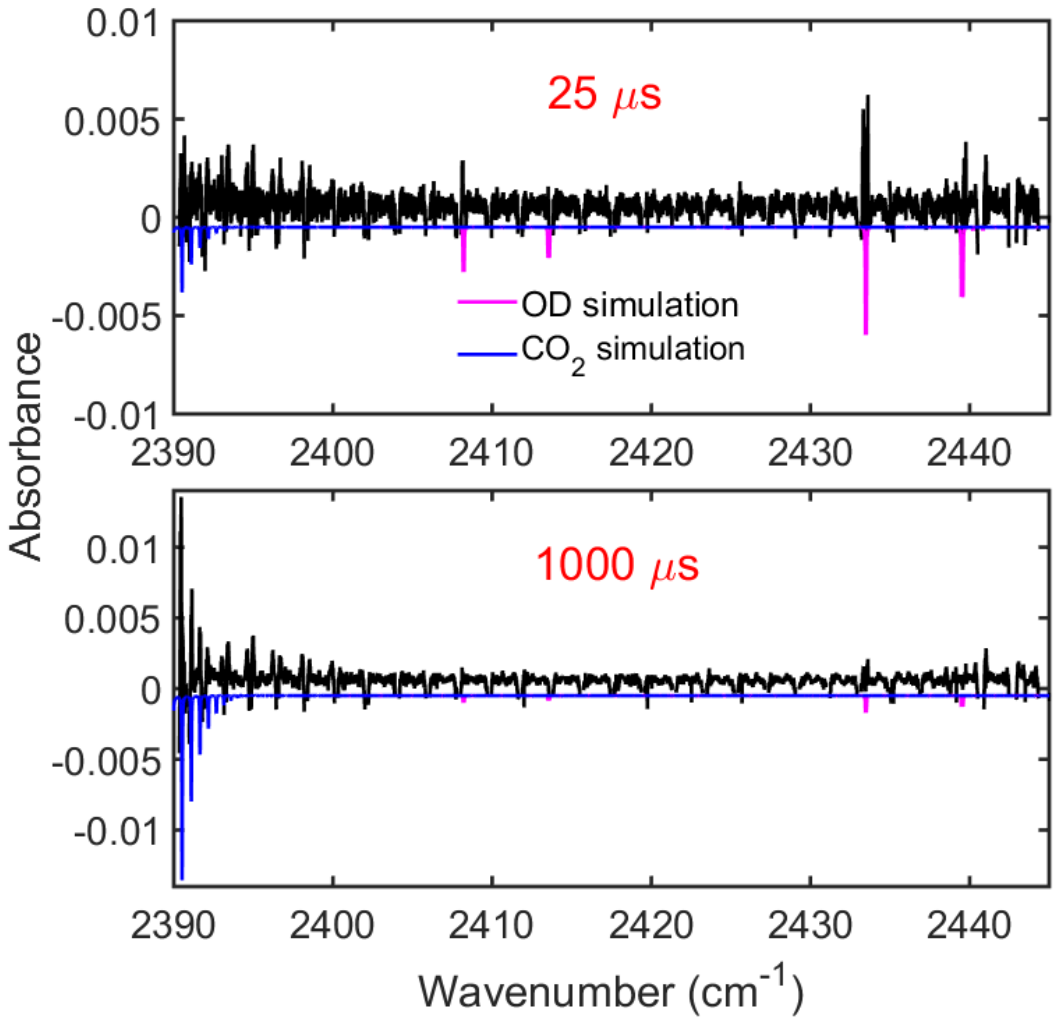

Figure 6.1: Measured spectra (black) at 25 and 1000 μs delay from the photolysis pulse. These spectra are fitted to reference OD(v=0) (magenta) and CO_2(blue) spectra to acquire the temporal profile. The decay of OD(v=0) and the rise of $CO_2$are apparent between 25 and 1000 μs delay.

described in §4.7. The CO_2 line positions and strengths were obtained from the HITRAN2012 database[129].

By fitting the integrated areas for both species, we obtained the time-dependent curves in Fig. 6.2. The error bars on the CO_2 and OD(v=0) concentrations are determined from the fit errors combined with a 7% statistical error due to our flow uncertainty. An emperical sum of box-car-convolved (100 μs integration time) exponential functions, Eq. 5.15, was fit to [OD(v=0)](t), providing a functional form for the data. The OD(v=0) decay is observed to be bi-exponential, with the initial decay (time window ≈ 100 to 300 μs) coming from reactions with CO. The second exponential decay occurs approximately after 300 μs and OD(v=0) approaches steady-state at longer times (t>1 ms). OD(v=0) regeneration reactions D+O_3→OD+O_2 and DOCO+O_3→OD+CO_2+O_2 dominate at longer times. Only the earliest time behavior (<300 μs) captures the initial OD+CO→D+CO_2 branching reaction and is used for the analysis of k_{1b}. The time-dependent concentration for [CO_2](t) in excess [CO] was modeled as a pseudo-unimolecular rise,

$$\frac{d[\mathrm{CO_2}]}{dt} = k_{1b}[\mathrm{CO}][\mathrm{OD(v{=}0)}](\mathrm{t}), \tag{6.1}$$

where k_{1b} is the effective bimolecular rate for OD+CO→D+CO_2. Contrary to DOCO, CO_2 does not have a large loss channel with O_3 at early (< 1 ms) timescales. The solution to this with constant [CO] is the integral of [OD(v=0)](t),

$$[\mathrm{CO_2}](\mathrm{t}) = k_{1b}[\mathrm{CO}] \int_0^t [\mathrm{OD}](u)\, du\ . \tag{6.2}$$

This expression was fit to our experimental data for [CO_2](t), shown in the top panel of Fig. 6.2.

These measurements were performed for CO, N_2, and He bath gases at a variety of pressures. For CO, the concentration range was limited to 3.5×10^{17} to $1.0 \times {}_{10}{}^{18}$ molecules cm^{-3}. At low CO densities, complications arose due to incomplete vibrational quenching of OD(v>0). At high CO densities, the concentration of OD(v=0) was reduced due to the efficient O(^{1}D)+CO→O(^{3}P)+CO quenching reaction. In this intermediate range, OD(v>0) accounts for no more than 10% of the

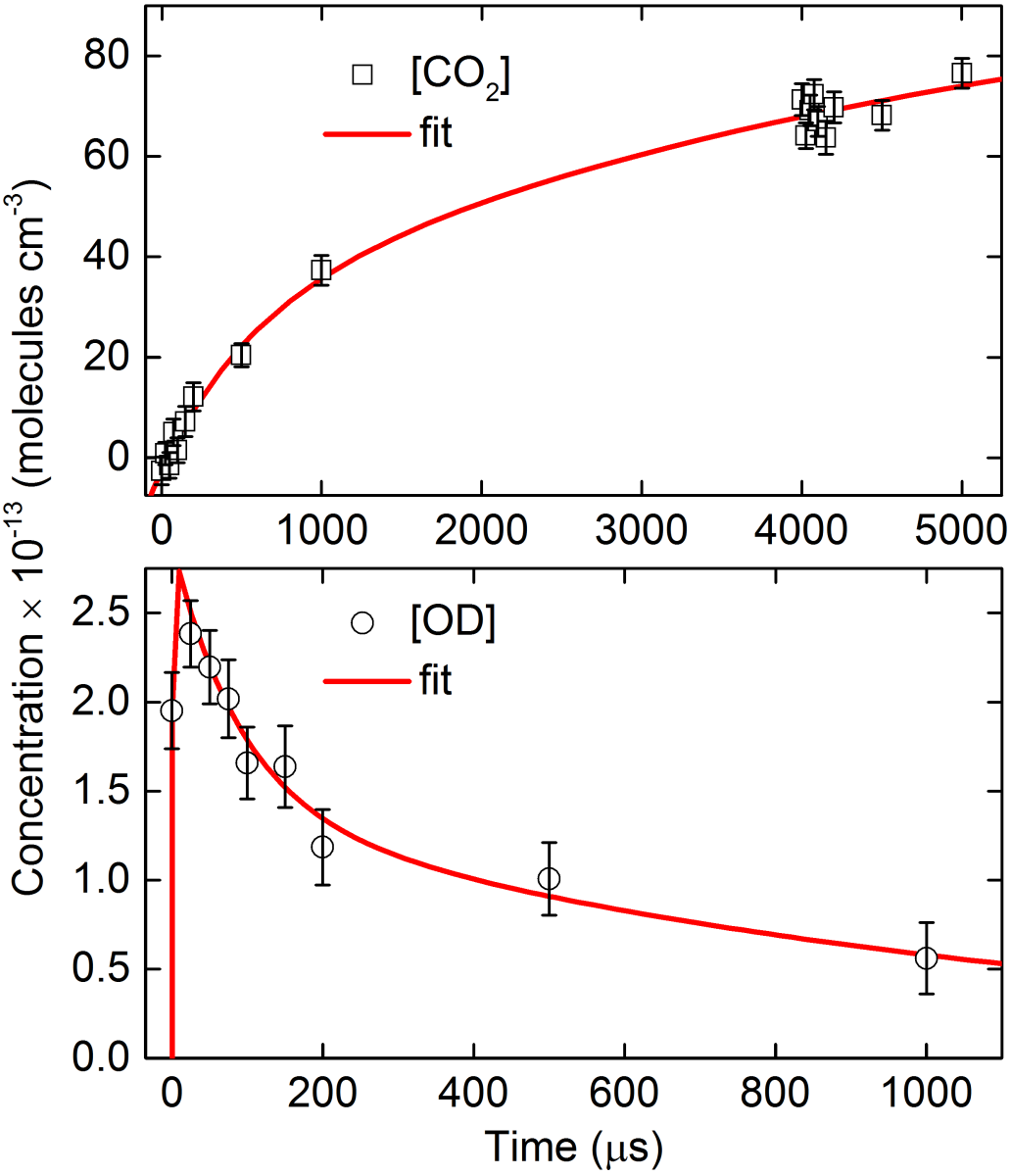

Figure 6.2: Time-dependent concentrations of CO_2 and OD(v=0), obtained by fitting their time-dependent spectra. (bottom) An analytical functional form for [OD](t) is obtained by fitting the data (black circles) to a sum of box-car averaged exponential rise and fall functions (red line). (top) The rise rate of CO_2 is obtained from fitting the data (black squares) to Eq. 6.2 (red line). The error bars include contributions from uncertainties in the spectral fits as well as concentration measurements. The camera integration time was fixed at 100 μs.

total OD. For N_2 and He, the upper limit densities of $\approx 3.5 \times 10^{18}$ molecules cm^{-3} were dictated by technical considerations: high molecular densities result in large mechanical vibrations which affect cavity locking stability. The fits across these three bath gases are shown in Fig. 6.3, which shows that k_{1b} is roughly constant over the measured pressure ranges within its experimental uncertainty. The averaged values for k_{1b} are $5.6(7) \times 10^{-14}$, $6.6(8) \times 10^{-14}$, and $6.1(7) \times 10^{-14}$ cm^3 molecules^{-1} s^{-1} for CO, N_2, and He, respectively.

Another possible source of systematic error could arise from the DOCO+O_3→CO_2+OD+O_2 reaction, which would contribute an additional source of CO_2. To provide a quantitative esitmate for this channel, we measured k_{1b} as a function of O_3 density (2 to 4.5×10^{15} molecules cm^{-3}), and observed no dependence (fit of a flat line to the data yielded a reduced $\chi^2 \approx 0.3$) within the statistical uncertainty. This is consistent with the fact that [DOCO] is much smaller than [CO_2] by more than an order of magnitude, so DOCO+O_3 could contribute at most a 10% error. Nonetheless, 10% systematic error is accounted for in our uncertainty budget.

These results can be analyzed using unimolecular rate theory and the associated Lindemann mechanism expressions given in §4.5. In the low pressure limit, eq. 4.3, $k_{1b}([M] \rightarrow 0)$ is expected to be independent of pressure (See eq. 4.3). Any apparent curvature in the pressure dependence would suggest deviations from the Lindemann mechanism or departure from the low-pressure limit and transition into the fall-off region, which cannot be ruled out given the measurement uncertainties in Fig. 6.3.

6.2 The $OD + CO \rightarrow cis-DOCO$ Channel

The final unquantified channel of the OD+CO reaction is that of *cis*-DOCO. Not a lot is known about *cis*-DOCO or *cis*-HOCO, as they have not been observed in the infrared, let alone as part of the OD+CO or OH+CO reactions. However, the structures of *cis*- and *trans*-HOCO have been measured by McCarthy *et al.* and are shown in Fig. 6.4 . Armed with theoretical band centers (see sec. 4.7), we set out to observe this key species as part of the OD+CO reaction. Since the band center was expected to be well outside of the mirrors we used for the *trans*-DOCO work,

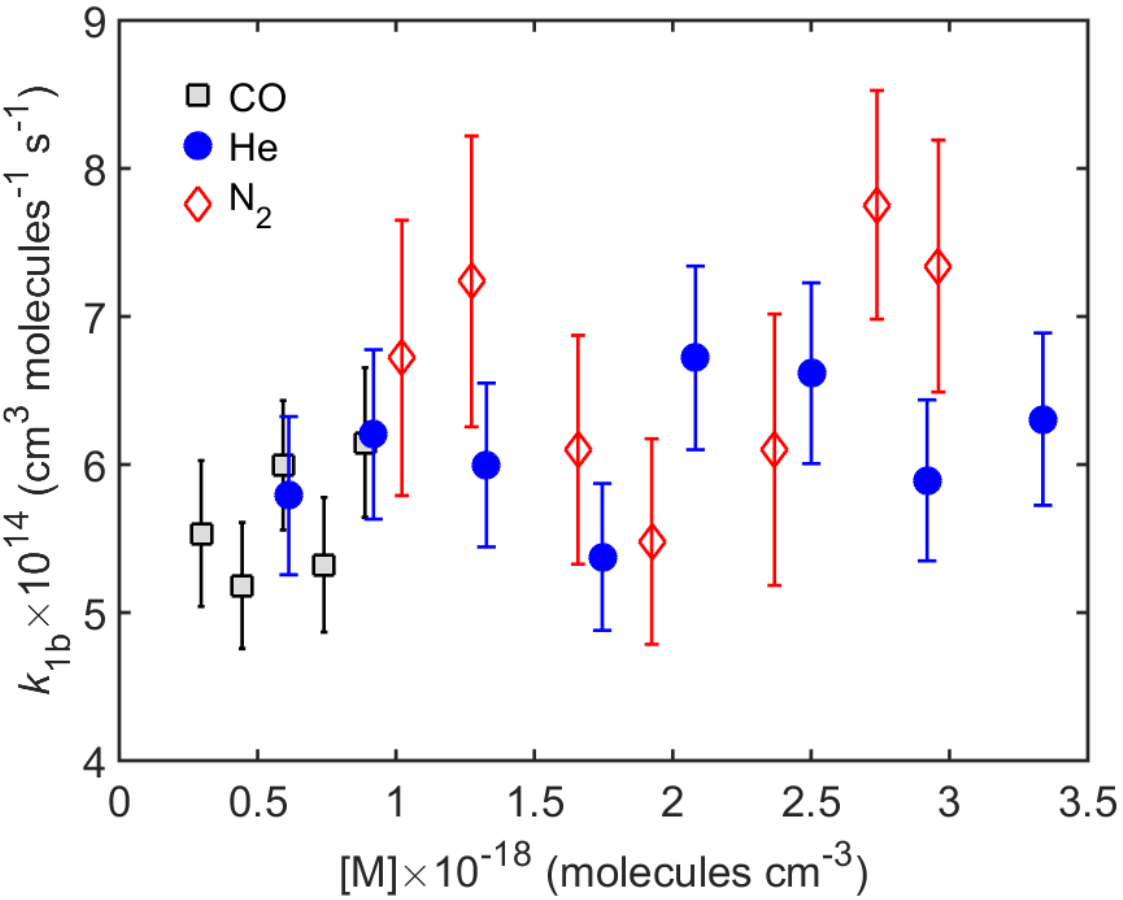

Figure 6.3: The formation rate (k_{1b}) of the activated products, D+CO_2, as a function of bath gases ([M]=N_2 (red diamond), CO (black squares), and He (blue circles)) and pressure. The error bars include contributions from the fit uncertainties as well as concentration measurements.

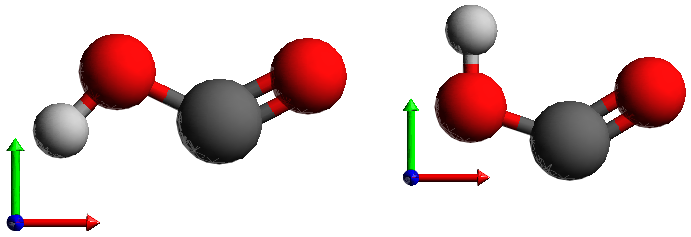

Figure 6.4: Geometry of *trans*- (left) and *cis*-HOCO (right), determined with microwave spectroscopy[125]. The a (red) and b (green) rotational axes are indicated.

we used the same mirrors for the enhancement cavity as in the CO_2 work. Centering the VIPA spectrometer around the expected *cis*-DOCO band center of 2550 cm^{-1}, we observed new spectral features that were present with the addition of CO and absent without. To confirm that these new spectral features belonged to *cis*-DOCO, ^{12}CO was substituted for the ^{13}CO isotopically substituted version, resulting in shifted spectra, as shown in Figs. 6.5 and 6.6.

The simple shift in the spectrum only confirms that the unknown molecule contains carbon, which is a start. The compiled observed transitions and their approximate transition frequencies for both isotopomers are compiled in Table 5.1. Due to Doppler broadening ($\sim$ 300 MHz) and instrument broadening ($\sim$ 900 MHz), we were unable to resolve the individual rotational features of each Q-branch. A Watson A-reduced asymmetric top Hamiltonian was fit to these transitions in PGopher, allowing us to determine the vibrational band origin and A rotational constants for both species. Due to the unresolved Q-branches, it was necessary to fix a few parameters in the fit, the ground state A rotational constant of the ^{12}C species and the B and C rotational constants for both species, to literature values with theoretical isotopic shifts.

The isotopic shifts in these constants can then be compared to theoretical values, shown in Table 6.3. In this table, the "vibrational shift" is given by $A_{12}(v=1) - A_{12}(v=0)$ for ^{12}C and similar for ^{13}C. The "isotopic shift" is given by $A_{13}(v=0) - A_{12}(v=0)$ for v=0 and similar for v=1. The shifts in these constants can seem very esoteric, but there is a simple way of understanding them if the molecular geometry can be assumed to remain approximately constant under the isotopic substitution, which should be an appropriate approximation in our case, since ^{13}C is only slightly heavier than ^{12}C. In this case, the moment of inertia along the a axis of the molecule is given by

$$\frac{h}{2\pi^2 c} \times \frac{1}{A} = I_A = \sum_i m_i ||\bar{r_i} \times \hat{n_a}||^2, \tag{6.3}$$

where m_i and $\bar{r_i}$ are the mass and position of the i^{th} atom in the molecule relative to the center of mass and $\hat{n_a}$ is the unit normal in the direction of the molecule's a-axis such that $||\bar{r_i} \times \hat{n_a}||$ is the perpendicular distance from the i^{th} atom to the a-axis. Under isotopic substitution, the difference between the two moments of inertia is given by

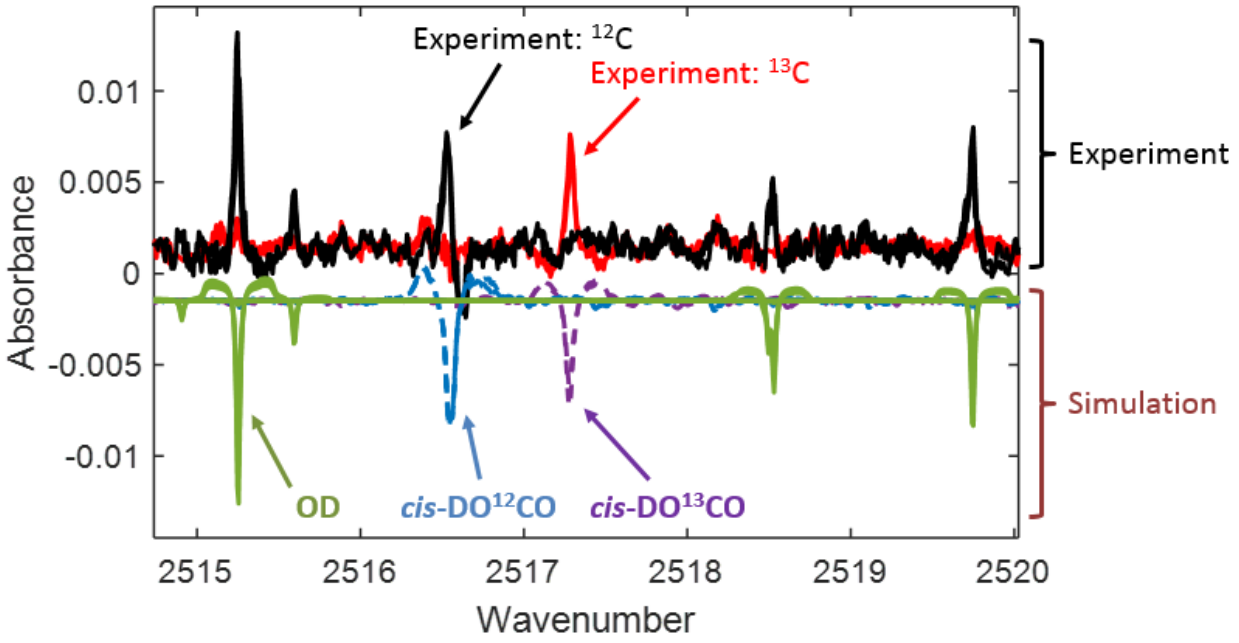

Figure 6.5: Zoomed *cis*-DOCO spectrum.

Table 6.1: Experimental spectral features for *cis*-DO^{12}CO and *cis*-DO^{13}CO and their ro-vibrational assignments. The quantity in parenthesis denotes an estimate of the uncertainty in the line position (in cm^{-1}) due to the FWHM linewidth of the unresolved Q-branch feature.

$k_a^{'}$	$k_a^{''}$	^{12}C Position (cm^{-1})	^{13}C Position (cm^{-1})
7	8	2489.220(0.147)*	2491.106(0.147)*
6	7	2496.040(0.08)	2497.718(0.08)
5	6	2502.931(0.05)	2504.295(0.05)
4	5	2509.764(0.05)	–
3	4	2516.524(0.05)	2517.282(0.05)
2	3	–	–
1	2	–	–
2	1	2548.102(N/A)*	2547.572(N/A)*
3	2	–	–
4	3	2562.550(0.13)	2561.517(0.13)
5	4	2568.954(0.11)	2567.638(0.11)
6	5	2575.191(0.10)	2573.687(0.10)
7	6	2581.414(0.10)	2579.658(0.10)
8	7	–	–

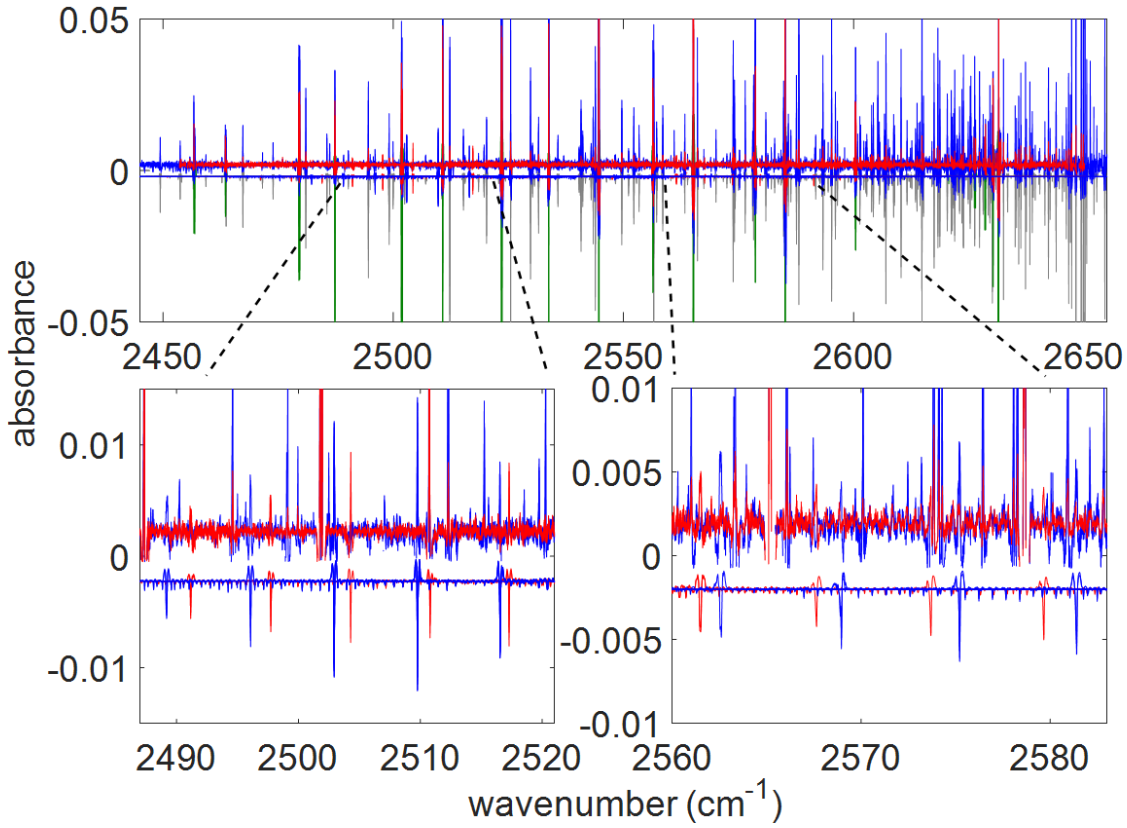

Figure 6.6: The full *cis*-DOCO spectrum. The data and simulation are given by positive and negative absorbance, respectively. The color codes are: *cis*-DO^{12}CO (blue), *cis*-DO^{13}CO (red), OD (green), and D_2O (gray). For clarity, only the simulated *cis-DO*^{12}CO and *cis-DO*^{13}CO are shown for comparison with experimental results in the zoomed-in bottom panels where the two strongest Q branches are located.

Table 6.2: Summary of spectral parameters for *cis*-DO^{12}CO and *cis*-DO^{13}CO. The average fit error is 0.014 cm^{-1}.

	^{12}C(v=0)	^{12}C(v=1)	^{13}C(v=0)	^{13}C(v=1)
Origin (cm^{-1})	0	2539.909(3)	0	2539.725(4)
A (MHz)	110105.52[a]	109313(4)	106124(5)	105423(5)
B (MHz)	11423.441[a]	11422.882[b]	11420.075[c]	11419.559[d]
C (MHz)	10331.423[a]	10324.228[b]	10291.999[c]	10284.951[d]

[a]McCarthy *et al.*, 2016 [125]
[b]^{12}C(v=0) value + VPT2 vibrational shifts
[c]^{12}C(v=0) value + VPT2 isotopic shift
[d]^{12}C(v=0) value + VPT2 isotopic shift & vibrational shift

$$\frac{h}{2\pi^2 c} \times \left(\frac{1}{A_{13}} - \frac{1}{A_{12}}\right) = I_{13,A} - I_{12,A} = (m_{13C} - m_{12C})||\bar{r_i} \times \hat{n_a}||^2, \tag{6.4}$$

where $(m_{13C} - m_{12C})$ is the isotopic shift in mass of the carbon atom, ≈ 1 amu. This shows that the difference in the inverse A constants simply yields the squared distance of the isotopically substituted atom from the molecular a-axis. In our case, this is 0.42 $\AA$ for the v=0 vibrational level. Equation 6.3 can also be used along with the measured molecular geometry of McCarthy *et al* [125] to calculate an isotopic shift in A, again assuming that the geometry does not change with deuteration. This yields a shift of $A_{13}(v = 0) - A_{12}(v = 0) = 4029$ MHz, which is close to our measured value.

Now that the identity of the unknown molecule has been established as *cis*−DOCO, the full reaction kinetics may be studied, including all products. Fig. 6.7 shows the time-dependent concentrations of all four relevant species, *trans*-DOCO, *cis*-DOCO, and CO_2. *trans*-DOCO was re-measured for this study due to new enhancement mirrors and different YAG focusing conditions, with an example spectrum shown in Fig. 6.8 . This data was originally analyzed using the same method as *trans*-DOCO (using Eq. 5.3), but the analysis was changed when it was realized that *trans*⇌*cis* isomerization plays a large role in the kinetics. This was determined by looking at the ratio of *trans*-DOCO to *cis*-DOCO as a function of time on short timescales, as shown in Fig. 6.9. The main feature to note in this plot is the exponential approach to a steady-state or equilibrium value. This is very characteristic of a simple *trans*⇌*cis* isomerization model, as seen in §A.3. In

Table 6.3: Comparison of experimental isotope shifts with theoretical isotope shifts for *cis*-DOCO.

	Experiment	Theory
Vibrational shift in A (MHz)		
^{12}C	-793(4)	-877.296
^{13}C	-701(7)	-797.649
Isotopic shift in A (MHz)		
v=0	-3982(5)	-3976.926
v=1	-3890(6)	-3897.279
Isotopic shift in band origin (cm^{-1})	-0.184	-0.207[e]

[e]VPT2
[f]variational calculation

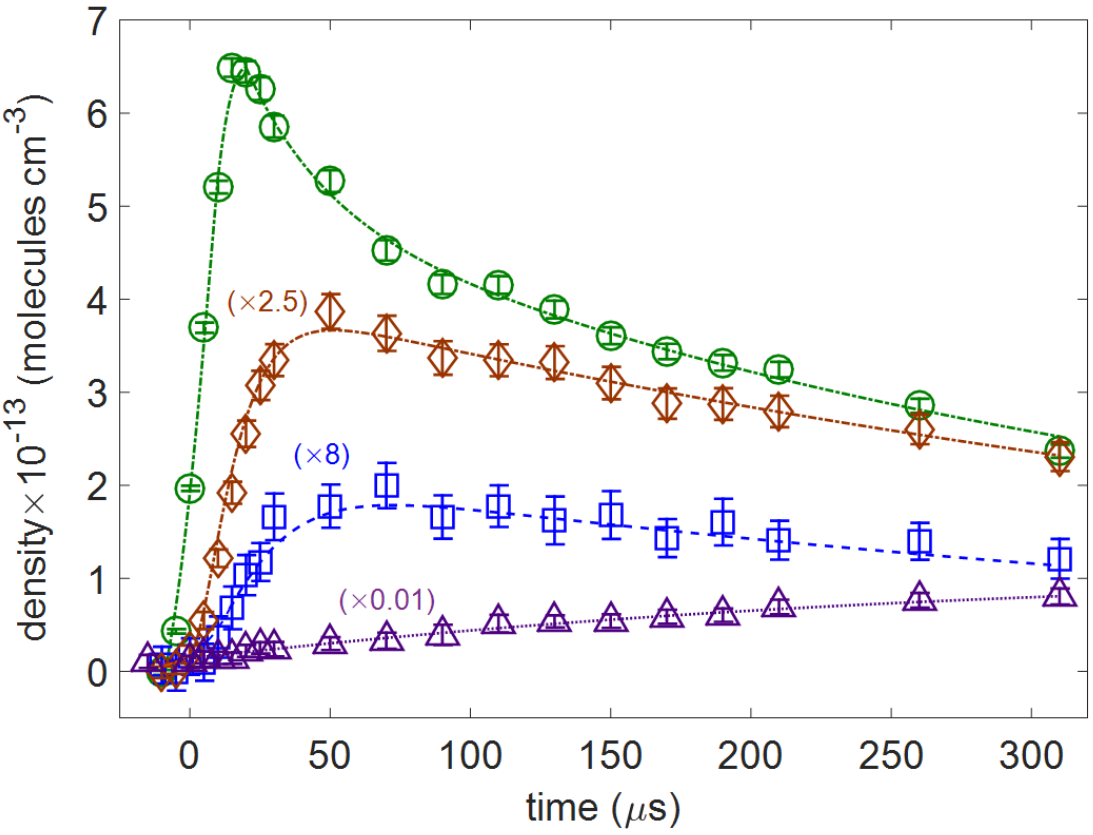

Figure 6.7: The time dependence of reactant OD(v=0) (green circles), intermediates *cis*-DO^{12}CO (blue squares), and *trans*-DOCO (brown diamonds), and product CO_2 (purple triangles) obtained from fitting full experimental spectra for a sequence of time windows after the initiation of the reaction. The quantity in parenthesis is the multiplicative scaling factor for the density. The camera integration time is 20 μs for OD(v=0), *cis*- and *trans*-DOCO, and 50 μs for CO_2.

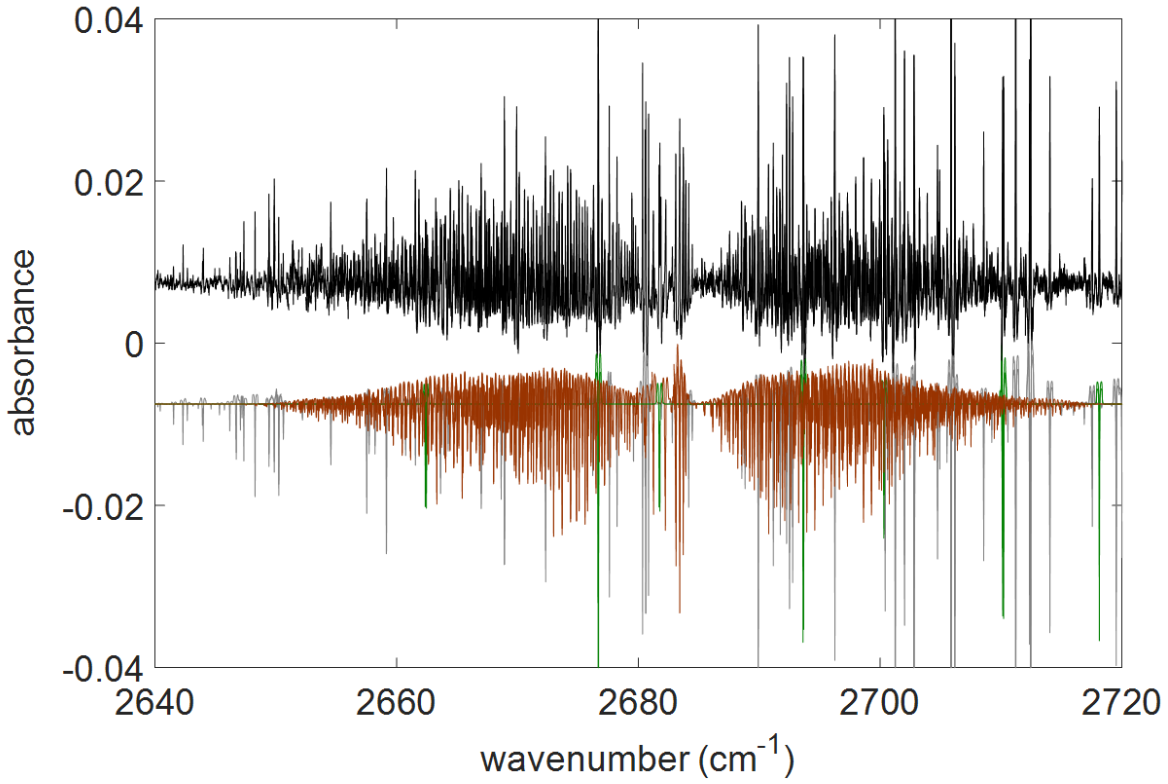

Figure 6.8: The *trans*-DOCO spectrum (black). Simulated *trans*-DOCO (brown), OD (green), and D_2O (gray) are shown as inverted absorbance.

this simplest model, *trans*- and *cis*-DOCO are formed with concentrations $[trans]_0$ and $[cis]_0$, such that the initial ratio is given by $[trans](\text{t=0})/\,[cis](\text{t=0}) = [trans]_0/[cis]_0$. At these initial conditions, the *trans*→*cis* and *cis*→*trans* rates are unbalanced; there is a net flow of population from *trans*→*cis* or *cis*→*trans* until the rates equilibrate, resulting in the plateau shown in Fig. 6.9 . Unfortunately, this model is inadequate, since the true model must include *trans*- and *cis*-DOCO formation, isomerization, and loss rates, given by the coupled equations

$$\begin{aligned} \tfrac{d}{dt}[trans] &= k_{1a,trans}[CO][OD](t) - (r_{loss,trans} + r_{tc})[trans](t) + r_{ct}[cis](t) \\ \tfrac{d}{dt}[cis] &= k_{1a,cis}[CO][OD](t) - (r_{loss,cis} + r_{ct})[cis](t) + r_{tc}[trans](t) \end{aligned} , \tag{6.5}$$

where $k_{1a,trans}$ and $k_{1a,cis}$ are the effective bimolecular formation rates for *trans*- and *cis*-DOCO, $r_{loss,trans}$ and $r_{loss,cis}$ are the effective unimolecular loss rates for *trans*- and *cis*-DOCO (*e.g.* $r_{loss,trans} = k_{O3}[O_3]$ for the *trans*-DOCO+O_3 loss process), and r_{tc} and r_{ct} are the effective unimolecular isomerization rates for the *trans*→*cis* and *cis*→*trans* processes, respectively. The formation rates and unimolecular isomerization rates are expected to be pressure dependent while the loss rates are expected to depend only on the concentration of the loss partner, generally O_3 in our experiments. These expressions are fairly complicated and do not permit a straightforward method for analyzing the kinetics data, especially considering the time window convolution that must be taken into account. To isolate formation from isomerization, the sum of the DOCO isomers may be analyzed, $[\text{DOCO}_{\text{sum}}] \equiv [trans\text{−DOCO}] + [cis\text{−DOCO}]$. This considerably simplifies the model if we also make the assumption that the loss rates for both species are approximately equivalent, $r_{loss} \equiv r_{loss,trans} \approx r_{loss,cis}$. Then, the model simplifies to

$$\frac{d}{dt}[\text{DOCO}_{\text{sum}}] = k_{1a,sum}[\text{CO}][\text{OD}](t) - r_{loss}[\text{DOCO}_{\text{sum}}](t) , \tag{6.6}$$

where $k_{1a,sum} \equiv k_{1a,trans} + k_{1a,cis}$. The solution to this equation is a convolution of the DOCO_{sum} loss term with $[\text{OD}](t)$, given by

$$[\text{DOCO}_{\text{sum}}](t) = k_{1a,sum}[\text{CO}] \int_0^\infty e^{-r_{loss}(t-u)}[\text{OD}](u)\, du . \tag{6.7}$$

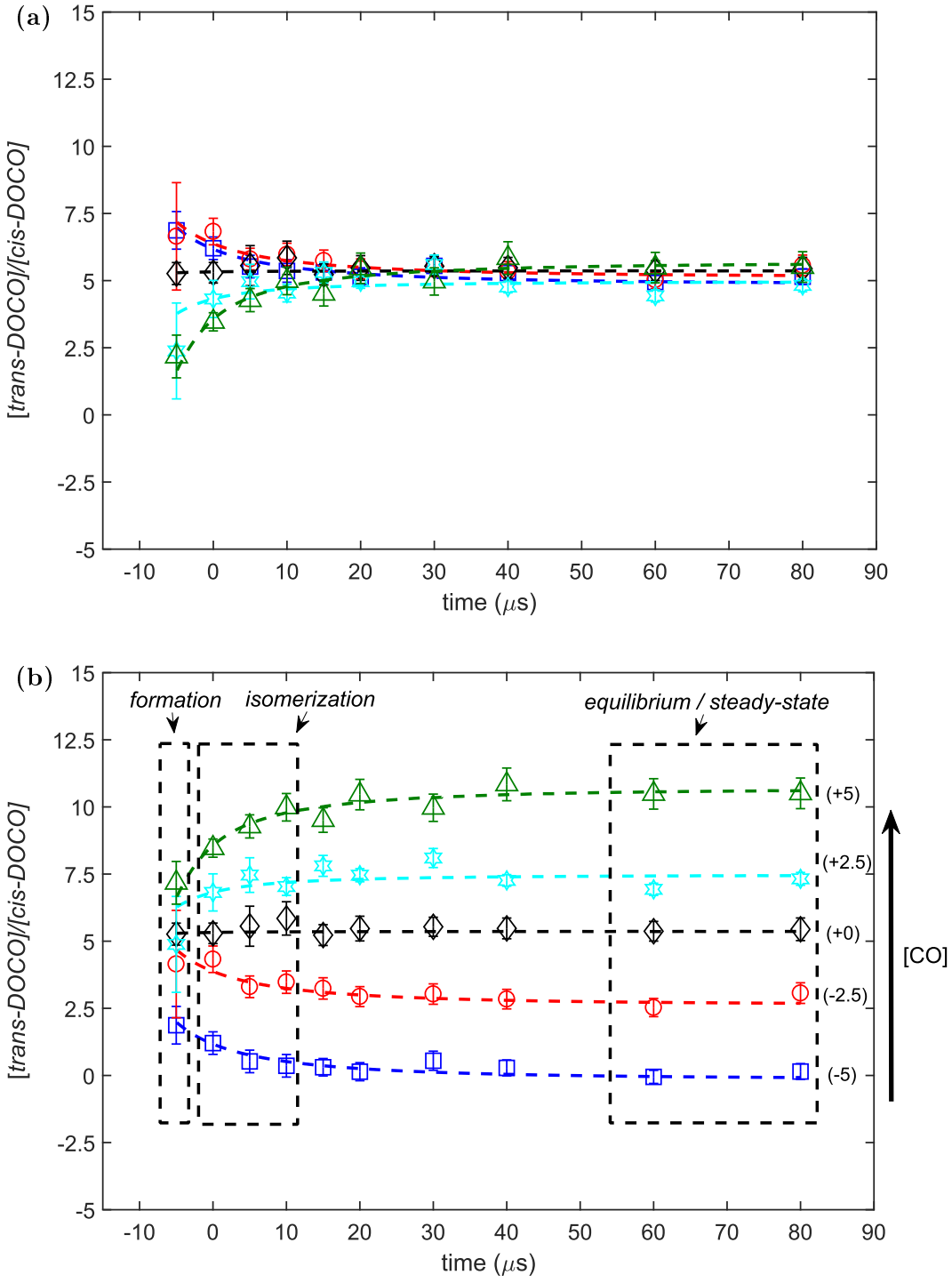

Figure 6.9: The ratio of [*trans*-DOCO] to [*cis*-DOCO] as a function of time for different CO concentrations. The CO concentrations are 5.6, 6.0, 6.4, 6.7, and 7.1 $\times$ 10^{17} molecules cm^{-3} for blue squares, red circles, black diamonds, cyan hexagons, and green triangles, respectively. Arbitrary y-offsets of -5, -2.5, 0, +2.5, and +5, respectively, are added to plot (b) for ease of viewing (plot (a) has no offsets). The dashed lines are fits of the rate equation model to the data.

The effective bimolecular rate constant, $k_{1a,sum}$, can then be decomposed into three terms dependent on the concentrations of the three most abundant gases in our experiment: N_2, CO, and D_2. This yields

$$k_{1a,sum} = k_{1a,sum}^{(CO)}[\mathrm{CO}] + k_{1a,sum}^{(N2)}[\mathrm{N_2}] + k_{1a,sum}^{(D2)}[\mathrm{D_2}] + k_{1a,sum}^{(0)} \,, \tag{6.8}$$

where $k_{1a,sum}^{(CO)}$, $k_{1a,sum}^{(N2)}$, and $k_{1a,sum}^{(D2)}$ are the termolecular rate coefficient dependence on CO, N_2, and D_2, respectively. $k_{1a,sum}^{(0)}$ is an offset term that accounts for additional background species.

The k_{1a} termolecular coefficients were obtained from simultaneously fitting $[\mathrm{DOCO_{sum}}](t)$ and $[\mathrm{OD}](t)$ as a function of [CO], $[\mathrm{N_2}]$ and $[\mathrm{D_2}]$. $[\mathrm{OD}](t)$ were fit using a derived analytical sum of exponential components in the same manner as the *trans*-DOCO analysis (see Eq. 5.15). The functional form for $[\mathrm{DOCO_{sum}}](t)$ was also the same as in the *trans* analysis, given by

$$\begin{aligned}[\mathrm{DOCO_{sum}}](t) = \quad & k_{1a,sum}[\mathrm{CO}]\Bigg(a_1\tfrac{e^{-b_1 t}-e^{-r_{loss}t}}{b_1-r_{loss}} + \\ & a_2\tfrac{e^{-b_2 t}-e^{-r_{loss}t}}{b_2-r_{loss}} - (a_1+a_2)\tfrac{e^{-b_3 t}-e^{-r_{loss}t}}{b_3-r_{loss}}\Bigg) \,,\end{aligned} \tag{6.9}$$

where a_1, a_2, b_1, b_2, and b_3 are determined by the $[\mathrm{OD}](t)$ fit. The only parameters determined by the fit to $[\mathrm{DOCO_{sum}}](t)$ are $k_{1a,sum}$ and r_{loss}. These fits were performed over a temporal range of -25 μs (which accounts for the finite response time of the camera) to 200 μs. Simultaneous fitting of $[\mathrm{DOCO_{sum}}(t)$ and $[\mathrm{OD}](t)$ as a function of [CO], $[\mathrm{N_2}]$ and $[\mathrm{D_2}]$ yields the k_{1a} termolecular coefficients. $r_{loss,sum}$ was determined independently by measuring the time dependence of *cis*-DOCO and *trans*-DOCO while varying the density of O_3, and the results are shown in Fig. 6.10. Here, we obtained a bimolecular rate coefficient for loss to O_3, $k_{O3} \approx 2.5(3) \times 10^{-11}$ $\mathrm{cm^3\,molecules^{-1}\,s^{-1}}$. By constraining $r_{loss,sum}$ to the total loss rate, the fitted termolecular rate coefficients of $\mathrm{DOCO_{sum}}$ with respect to CO, N_2, and D_2 gases are displayed in Figs. 6.12 and 6.11. We performed a multidimensional fit to Eq. 6.8 to determine $k_{1a,sum}^{(CO)}$, $k_{1a,sum}^{(N2)}$, $k_{1a,sum}^{(D2)}$, $k_{1a,sum}^{(0)}$, and r_{loss} simultaneously. As r_{loss} describes DOCO loss to O_3, it is invariant to [CO], $[\mathrm{N_2}]$, and $[\mathrm{D_2}]$. Therefore, r_{loss} serves as a shared, fitted constant in the global

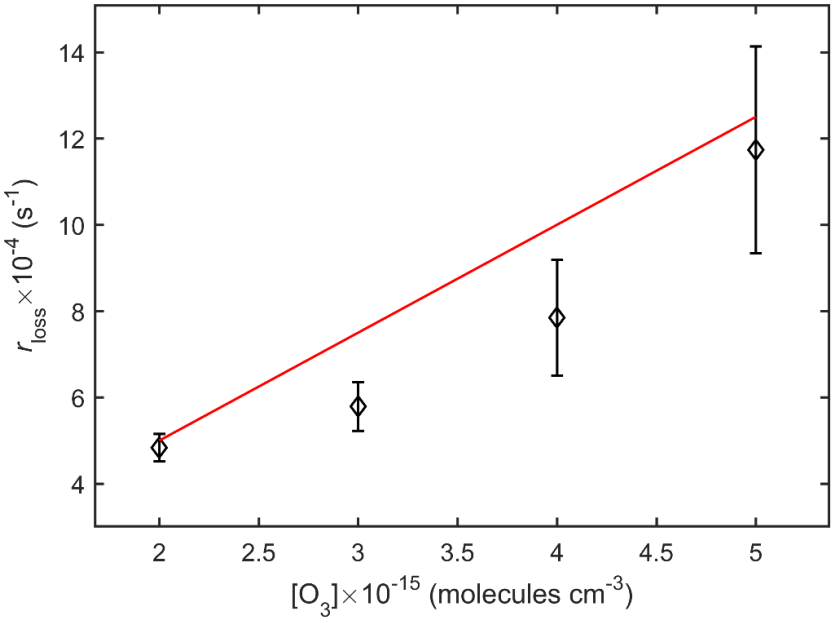

Figure 6.10: Variation of r_{loss} with O_3 concentration.

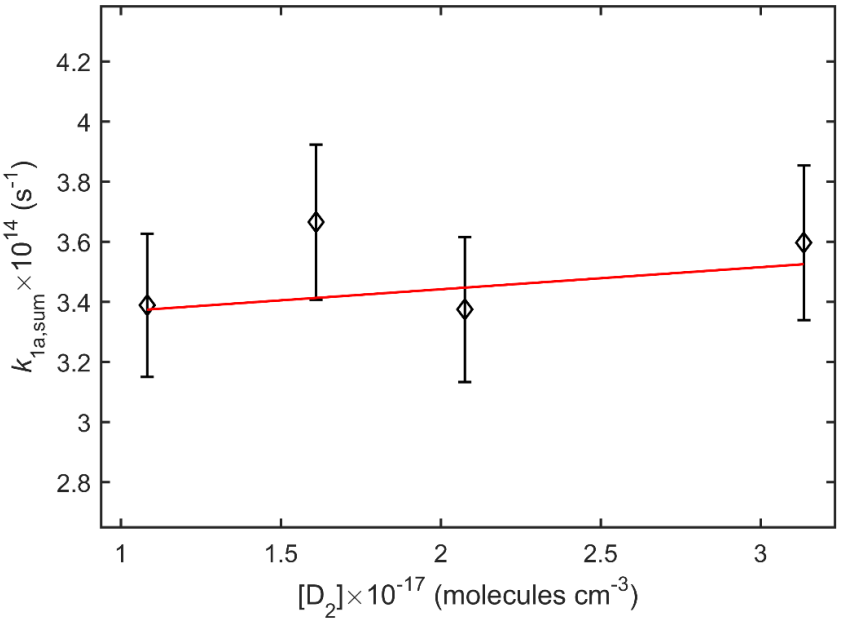

Figure 6.11: Variation of $k_{1a,sum}$ with D_2 concentration.

fit across the CO, N_2, and D_2 data sets. The results obtained from the multidimensional fit are $k_{1a,sum}^{(CO)} = 8.5^{+4.3}_{-5.2} \times 10^{-33}$ cm^6 molecules^{-2} s^{-1}, $k_{1a,sum}^{(N2)} = 1.3^{+0.3}_{-0.4} \times 10^{-32}$ cm^6 molecules^{-2} s^{-1} and $k_{1a,sum}^{(D2)} = 9.6^{+23}_{-24} \times 10^{-33}$ cm^6 molecules^{-2} s^{-1}. We observed an additional offset in the effective bimolecular rate constant, $k_{1a,sum}^{(0)} = 1.5^{+0.7}_{-0.8} \times 10^{-14}$ cm^3 molecules^{-1} s^{-1}. 80% of the offset term, $k_{1a,sum}^{(0)}$, can be accounted for by a combination of the upper limit of $k_{1a,sum}^{(D2)}$ and fit errors from correlations with k_{O3}. Discussion of all statistical and systematic error sources for k_{1a} is found in Table 6.4 .

The analysis up to this point has excluded the DOCO isomerization reactions. We now turn to further analyze the quantitative details of the DOCO formation mechanism in OD+CO. To resolve the dynamical coupling of the isomer-specific formation and isomerization, we measured the time dependence of the trans/cis ratio. Plots of [*trans*-DOCO]/[*cis*-DOCO] as a function of time in Fig. 6.9 reveal clear experimental evidence for a transition between two distinct time-dependent processes: the early-time DOCO formation (k_{1a}) and subsequent *trans*/*cis* isomerization. The decay/rise behavior of the *trans*/*cis* ratio at early times can be qualitatively understood as follows. The nascent *trans*/*cis* ratio from extrapolating back to $t \approx 0$ μs (prior to any isomerization processes) is determined only by the ratio of the formation rate coefficients ($k_{1a,trans}/k_{1a,cis}$). At $0 < t < 50$ μs, the transition between the DOCO formation and isomerization is exemplified by the exponential decay/rise of the *trans*/*cis* ratio as a function of time. The rate of the exponential rise/decay increases with sum of $k_{iso,tc}$ and $k_{iso,ct}$ and is an indication of how fast the *trans* to *cis*

Table 6.4: Summary of statistical and systematic errors for *trans*-DOCO values

		Error Source	$k_{1a,trans}^{(N2)}$	$k_{1a,trans}^{(CO)}$
Statistical Errors		(statistical, from fit residual)	15%	47%
Experimental Control		Flow & Pressure Measurement	7% (stat)	
Molecular Parameters		OD Cross Section	10% (stat)	
		trans-DOCO Cross Section	10% (stat)	
		cis-DOCO Cross Section	10% (stat)	
Data Analysis		Cross-contamination of OD(v=0) and D_2O	-1% (sys)	
		Total Systematica Error Budget	(-11%,+0%)	
		Total Statistical Error Budget	21%	49%
		Total Error Budget	(-32%,+21%)	(-60%,+49%)

populations approach this steady-state. At $t > 50$ μs, the isomerization reaction dominates and establishes steady-state populations of *trans* and *cis* isomers that persists at long times. In the absence of loss processes for DOCO, the *trans*/*cis* ratio is equivalent to $k_{iso,ct}/k_{iso,tc}$, which is the equilibrium constant for isomerization. From this qualitative picture, the relative magnitudes of the ratios of the formation rate ($k_{1a,trans}/k_{1a,cis}$) and isomerization rate ($k_{iso,ct}/k_{iso,tc}$) dictate whether decay or rise behavior is observed.

To provide a more quantitative understanding of the formation and isomerization mechanism, the time-dependent *trans*/*cis* ratio were measured as a function of CO density. The *trans*/*cis* ratios at five representative partial pressures of CO are plotted in Fig. 6.9. The evolution from decay to rise towards the steady-state value at increasing pressure is indicative of the competition between formation and isomerization. To quantify the isomerization and formation rate coefficients, an extended rate equation model of Eq. 6.5, which includes OD formation and decay, is used to fit the time-dependent *trans*/*cis* ratios across nine different CO pressures used in the experiment. The dashed lines (≈ 1 to 2) are results obtained from fitting $k_{1a,sum}$, $k_{iso,tc}$, and $k_{iso,ct}$ to all 9 experimental data sets simultaneously. Here, $k_{1a,sum}$ is taken from the measured value in Fig. 6.12. r_{loss} is independent of CO pressure and is fixed to the fitted value from Eq. 6.6. The fitted isomer specific k_{iso} and k_{1a} are given in Figs. 6.13 and 6.14 , respectively.

The observed trend in Fig. 6.9 can now be explained by comparing the $k_{iso,ct}/k_{iso,tc}$ and $k_{1a,trans}/k_{1a,cis}$ ratios given in the insets of Figs. 6.13 and 6.14, respectively. The transition in behavior from decay to rise occurs at approximately 6.5×10^{17} molecules cm^{-1} of CO, which is the crossing point of the decreasing $k_{iso,ct}/k_{iso,tc}$ and increasing $k_{1a,trans}/k_{1a,cis}$. However, at the lowest CO pressures, loss processes (k_{loss}), which are fixed in the fit, are not negligible relative to k_{1a} and k_{iso} and may introduce additional errors to this analysis. Additional evidence for this complication can be found in the observed ratio of $k_{iso,ct}/k_{iso,tc}$ from the inset of Fig. 6.13. Even though $k_{iso,ct}/k_{iso,tc}$ represents the equilibrium constant at all pressures, we observed a weak dependence at low pressures within our experimental uncertainty. Because k_{1a}, k_{iso}, and k_{loss} are similar in magnitude at the lowest CO pressures, their coupling may interfere with our fitted results. At

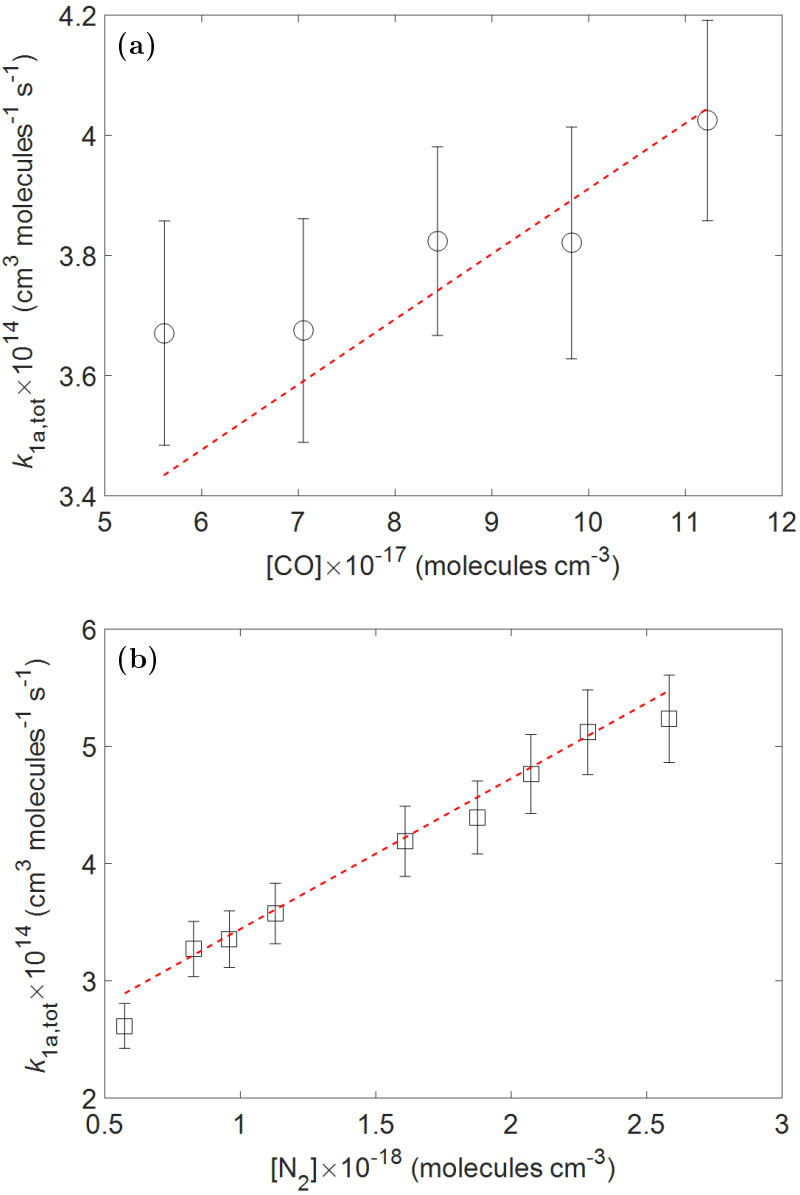

Figure 6.12: The termolecular rate coefficients for $DOCO_{tot}$ are plotted as a function of (a) CO and (b) N_2. The red dashed lines show the fits obtained from a multidimensional linear regression procedure. Data obtained in these plots were taken at 50 μs integration time.

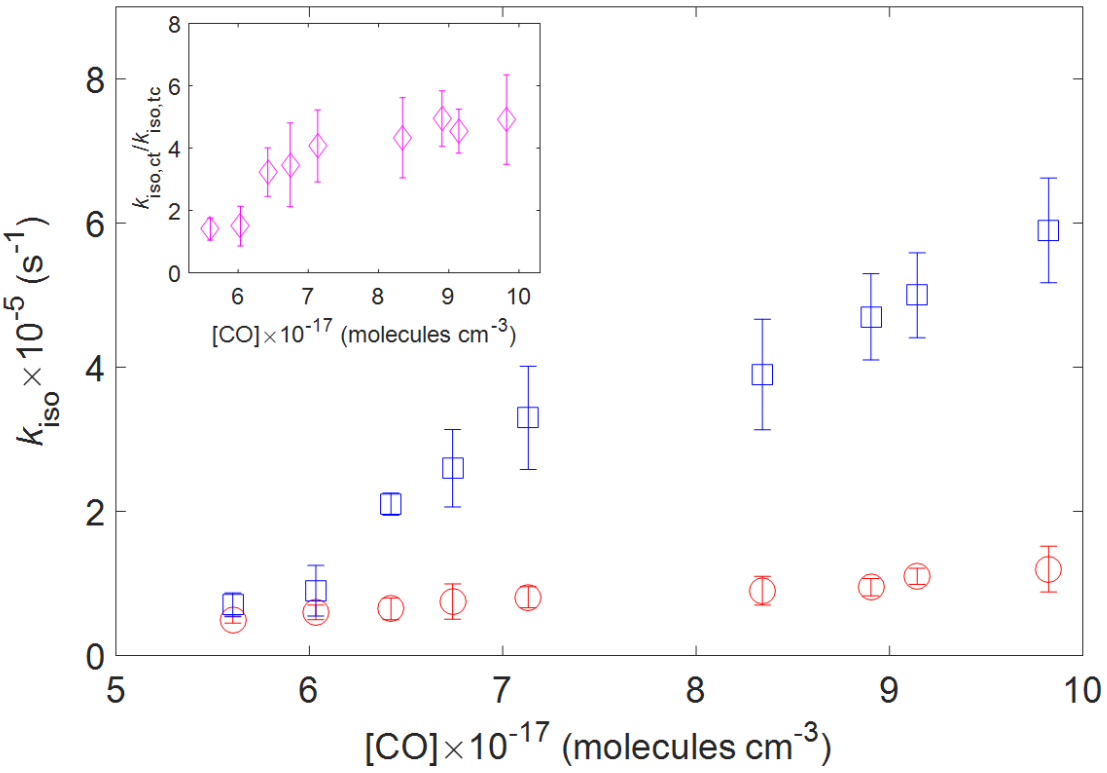

Figure 6.13: The fitted isomerization rate coefficients for *cis*→*trans* ($k_{iso,ct}$, blue squares) and *trans*→*cis* ($k_{iso,tc}$, red circles). The ratio of $k_{iso,ct}/k_{iso,tc}$ as a function of [CO] is given in the inset.

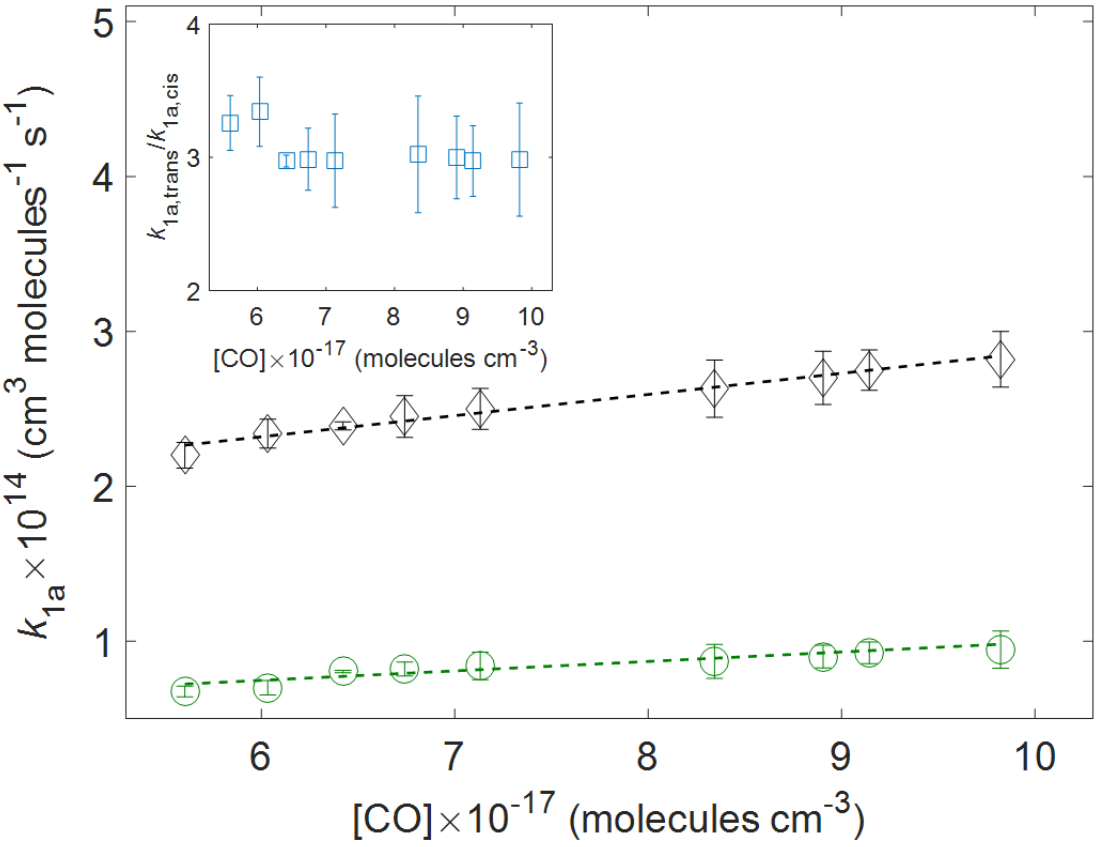

Figure 6.14: The fitted effective bimolecular formation rate coefficients (k_{1a}) for *trans*-DOCO ($k_{1a,trans}$, black diamonds) and *cis*-DOCO ($k_{1a,cis}$, green squares). The ratio of the formation rate coefficients $k_{1a,trans}/k_{1a,cis}$ is given in the inset.

higher pressures ([CO] $> 6.5 \times 10^{17}$ molecules cm^{-3}), k_{iso} dominates and $k_{iso,ct}/k_{iso,tc}$ converges to a constant value. We can compare this fundamental quantity to that predicted by state-of-the-art chemical kinetics theory. Using a theoretical method that combines semi-classical transition state theory with 2-dimensional master equations [123, 151], we predict an equilibrium ratio of $\approx$ 14:1, in comparison with the experimentally observed ratio of ~5:1. A change of $\approx$ 2 kJ/mol in the relative energies of *cis*- and *trans*-DOCO would account for this difference in the measured and predicted equilibrium constants.

New experimental insights into the energy transfer processes are obtained from the formation rate dependence on collision partner and total pressure for both *cis*- and *trans*-DOCO isomers. While the pressure-dependent competition between DOCO and CO_2 is well established [120, 145], DOCO may also exhibit isomer-specific formation rate, which is now resolved for the first time. Fitted linear slopes to the data in Fig. 6.14 gives termolecular formation rate coefficients of $k_{1a,trans}^{(CO)} = 1.4(4) \times 10^{-32}$ cm^6 molecules^{-2} s^{-1} and $k_{1a,cis}^{(CO)} = 6(2) \times 10^{-33}$ cm^6 molecules^{-2} s^{-1}. CO is twice as effective in collisionally stabilizing *trans*-DOCO* compared to *cis*-DOCO*. The unusually large enhancement by the CO collision partner for the *trans*-DOCO isomer relative to *cis*-DOCO may be a consequence of complex formation between *trans*-DOCO* and CO from a stronger interaction potential, which would facilitate energy transfer. This mechanism is further supported by spectroscopic observation of the *trans*-HOCO(CO) complex in the molecular beam environment by Oyama et al. (30).

Finally, the identification and quantification of *cis*-DOCO, *trans*-DOCO, and D+CO_2 amount to all the possible branching pathways for OD+CO. It is now experimentally possible to deconstruct k_1 as a sum of reaction elementary steps, i.e. $k_1([\mathrm{M}], T) = k_{1a,trans}([\mathrm{M}], T) + k_{1a,cis}([\mathrm{M}], T) + k_{1b}([\mathrm{M}], T)$, where $k_{1b}([\mathrm{M}], T)$ is the bimolecular rate coefficient for the D+CO_2 channel [182]. This approximation is valid in the low pressure-limit, provided that k_1 is only strongly dependent on k_{1a} while k_{1b} remains constant with respect to the total pressure and collision partner [120, 145, 182]. Previously, k_1 was determined with only contributions from *trans*-DOCO and CO_2. Mass balance dictates that *cis*-DOCO also contributes to the total k_1, which has been plotted in Fig. 6.15. The observed agreement in k_1 with previous studies by Golden et al. [119] and Paraskevopoulos and

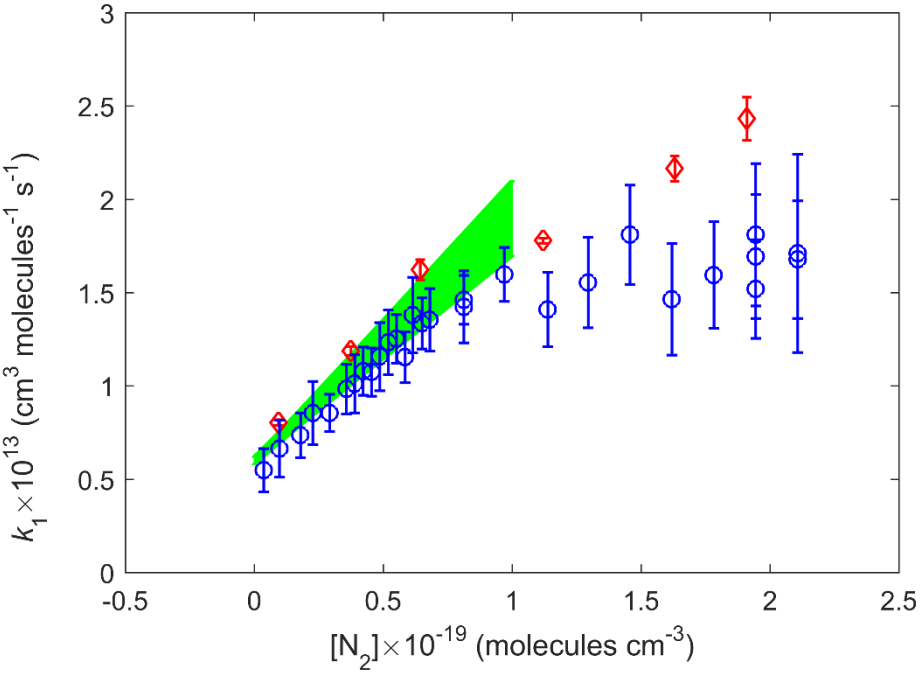

Figure 6.15: The measured k_1 as a function of N_2 are given by the shaded green region (within 1σ uncertainties). Red diamonds and blue circles are the measured k_1 values from Golden *et al.* [119] and Paraskevopoulos & Irwin [147], respectively.

Irwin [147] provides additional confirmation that k_1 can be treated as a sum of the rate coefficients of independent channels, k_{1a} and k_{1b}, in the low-pressure regime.

Chapter 7

Conclusion and Outlook

In this thesis, we have described the a new technique for the analysis of complex chemical reactions on the μs timescale and we have demonstrated its capabilities. Applied to deuterated acrylic acid, the technique allowed for the simultaneous tracking of acrylic acid-d_1, *trans*-DOCO, C_2HD, HOD, and D_2O concentrations. HOD and C_2HD were observed immediately after photolysis, which was unexpected considering previous knowledge of AA-d_1 photolysis kinetics. This may indicate an unknown reaction pathway and warrants further investigation.

Next, we applied the technique to the OD+CO→D+CO_2 reaction, the isotopically-substituted version of the OH+CO reaction. Many experimental efforts have attempted to unravel the complex mechanism of this reaction but have ultimately been unable to directly observe the *trans*- and *cis*-DOCO intermediate species, which are key branching pathways. Using the broad bandwidth, high-resolution, and cavity-enhanced sensitivity of time-resolved frequency comb spectroscopy, we have directly quantified the concentrations of all relevant reactants and products in this reaction, namely OD, *trans*-DOCO, *cis*-DOCO, and CO_2. This allowed us to determine termolecular branching rates for all three product channels. Additionally, we were able to observe *cis*⇌*trans* isomerization and quantify the forward and reverse unimolecular rate constants. Moreover, a class of similar reactions exists where time-resolved frequency comb spectroscopy might be applied. Ozonolysis reactions, for example, produce a so-called "criegee intermediate" as part of their reaction mechanism. One such intermediate, CH_2OO, has been shown to live for 10s of μs[183].

Even with these successes, a much broader range of experiments would be made accessible, or at least simpler, with improved sensitivity. One exciting direction for studies of the OH+CO reaction is cold chemistry in a buffer gas cell[85] at 10K or even ultracold stark-decelerated molecules[184]. These environments would allow access to the OH+CO potential energy surface with unprecedented energy resolution to tunneling, isomerization, and complex formation dynamics. However, there is typically a trade-off between molecular temperature and density, with peak reported densities of 5×10^{12} and 5×10^{10} molecules cm^{-3} for the buffer gas and ultracold environments, respectively. Additionally, only a fraction of the molecules in the cell will react, yielding a much lower density of products so the detection of cold chemistry could be rather challenging.

The multifaceted nature of time-resolved frequency comb spectroscopy makes it difficult to optimize for one particular application. An increase in the cavity finesse will increase the effective path length while degrading the time resultion from the longer ringdown time of the cavity. Similarly, the sensitivity might be increased by reducing the spectral bandwidth of the laser source, but at the cost of molecular accessibility. However, there are a few ways to improve all parameters simultaneously. For example, the total light flux at the camera could be increased by improving the transmission of the optical cavity or VIPA etalon or increasing the power of the laser source. Since the noise in our experiments was dominated by the dark counts of our InSb camera, this would increase sensitivity. The InSb camera is another place for improvement. By improving the cooling of the detector array beyond its current 77K temperature or using a different detection technology, an improvement might be made to the camera's dark noise, increasing sensitivity. Finally, longer wavelengths provide larger band strengths and access to different molecular species. Moving beyond 5 μm would increase the sensitivity and allow for more experimental flexibility[185].

Appendix A

Selected Mathematical Derivations

A.1 The Frequency Comb

We start with a sequence of pulses at a carrier frequency ω_c, each with pulse envelope $A(t)$. Thus, the complex electric field for a pulse train of n_f pulses is given by

$$E(t) = \sum_{n=1}^{n_f} A(t - n\tau) e^{i(\omega_c[t-n\tau]+n\Delta\phi_{ce})}, \tag{A.1}$$

where a pulse-to-pulse phase slip, $\Delta\phi_{ce}$, has also been included. The Fourier transform of this expression yields

$$\begin{aligned} \tilde{E}(\omega) &= \textstyle\sum_{n=1}^{n_f} \int_{-\infty}^{\infty} A(t-n\tau) e^{i(\omega_c[t-n\tau]+n\Delta\phi_{ce})} e^{-i\omega t} dt \\ &= \textstyle\sum_{n=1}^{n_f} e^{-i\omega n\tau} \int_{-\infty}^{\infty} A(t') e^{i(\omega_c t'+n\Delta\phi_{ce})} e^{-i\omega t'} dt' \\ &= \textstyle\sum_{n=1}^{n_f} e^{-i\omega n\tau + n\Delta\phi_{ce}} \int_{-\infty}^{\infty} A(t') e^{-i(\omega-\omega_c)t'} dt' \\ &= \tilde{A}(\omega-\omega_c) \textstyle\sum_{n=1}^{n_f} e^{-i\omega n\tau + in\Delta\phi_{ce}} \end{aligned}, \tag{A.2}$$

where a variable change of $t \to t' + n\tau$ is used in the second line and $\tilde{f}(\omega)$ is the Fourier transform of $f(t)$. In the case of many pulses, i.e. $n_f \to \infty$, we look for constructive interference in the exponential for all pulses, $2\pi m = \omega\tau - \Delta\phi_{ce}$. The frequency of the m^{th} comb tooth, f_m, is then given by

$$f_m = m f_{rep} + \frac{\Delta\phi_{ce}}{2\pi} f_{rep}\,, \tag{A.3}$$

where we have used $f_{rep} = 1/\tau$.

A.2 OH+CO Lindemann Expressions

The system of equations for this system is given below, where brackets are used to indicate the time-dependent concetration of a molecule (i.e. [X] is the time-dependent concentration of X in molecules cm^{-3}).

$$\begin{aligned}
\frac{d}{dt}[CO] &= 0 \\
\frac{d}{dt}[OH] &= k_{a-}[HOCO^*](t) - k_{a+}[OH][CO] \\
\frac{d}{dt}[HOCO^*] = 0 &= k_{a+}[OH](t)[CO] - (k_{a-} + k_{b-}[M] + k_{c-})[HOCO^*](t) \\
\frac{d}{dt}[HOCO] &= k_{b-}[M][HOCO^*] - k_{b+}[M][HOCO^*](t) \\
\frac{d}{dt}[H] &= k_{c-}[HOCO^*] \\
\frac{d}{dt}[CO_2] &= k_{c-}[HOCO^*]
\end{aligned} \tag{A.4}$$

Making this approximation allows us to solve for the steady-state concentration of HOCO*, $HOCO^* = \frac{k_{a+}[OH][CO]}{k_{a-}+k_{b-}[M]+k_{c-}}$. This simplifies the system of equations to

$$\begin{aligned}
\frac{d}{dt}[OH] &= \frac{k_{a-}k_{a+}}{k_{a-} + k_{b-}[M] + k_{c-}}[OH][CO] - k_{a+}[OH][CO] \\
\frac{d}{dt}[HOCO] &= \frac{k_{a+}(k_{b-} - k_{b+})[M]}{k_{a-} + k_{b-}[M] + k_{c-}}[OH][CO] \\
\frac{d}{dt}[H] &= \frac{k_{a+}k_{c-}}{k_{a-} + k_{b-}[M] + k_{c-}}[OH][CO] \\
\frac{d}{dt}[CO_2] &= \frac{k_{a+}k_{c-}}{k_{a-} + k_{b-}[M] + k_{c-}}[OH][CO]
\end{aligned} \quad . \tag{A.5}$$

From these equations, we can determine bimolecular formation and loss rates for OH, HOCO, and CO_2 as k_1, k_{1a}, and k_{1b}, respectively. These are given as

$$k_1 = k_{1a} + k_{1b} \tag{A.6}$$

$$k_{1a} = \frac{k_{a+}(k_{b-} - k_{b+})[M]}{k_{a-} + k_{b-}[M] + k_{c-}} \tag{A.7}$$

$$k_{1b} = \frac{k_{a+}k_{c-}}{k_{a-} + k_{b-}[M] + k_{c-}} \tag{A.8}$$

A.3 *trans*-DOCO $\rightleftharpoons$ *cis*-DOCO Isomerization

In isolation, the cis/trans isomerization may be modelled as a simple A $\rightleftharpoons$ B approach to equilibrium. The system of equations describing this system is

$$\frac{d}{dt}[A] = -r_{AB}[A] + r_{BA}[B] \tag{A.9}$$

$$\frac{d}{dt}[B] = r_{AB}[A] - r_{BA}[B] \tag{A.10}$$

these equations permit the following solutions

$$[A](t) = ([A]_0 - A_{eq})e^{-(r_{AB}+r_{BA})t} + A_{eq} \tag{A.11}$$

$$[B](t) = ([B]_0 - B_{eq})e^{-(r_{AB}+r_{BA})t} + B_{eq} \tag{A.12}$$

$$A_{eq} = ([A]_0 r_{BA} + [B]_0 r_{AB})/(r_{AB} + r_{BA}) \tag{A.13}$$

$$B_{eq} = ([A]_0 r_{AB} + [B]_0 r_{BA})(r_{AB} + r_{BA}), \tag{A.14}$$

where A_{eq} and B_{eq} are the equilibrium values of A[t] and B[t] at long times. It is also useful to define the behavior of the dimensionless quantity $(A[t] - B[t])/(A[t] + B[t])$,

$$\frac{[A](t) - [B](t)}{[A](t) + [B](t)} = \left(\frac{[A]_0 - [B]_0}{[A]_0 + [B]_0} - \frac{K_{A/B} - 1}{K_{A/B} + 1}\right) e^{-(r_{AB}+r_{BA})t} + \frac{K_{A/B} - 1}{K_{A/B} + 1} \tag{A.15}$$

where it is clear that the equilibrium constant, $K_{A/B} = r_{BA}/r_{AB}$, may be recovered from its long-timescale value.

A.4 *trans*-DOCO ⇌ *cis*-DOCO Isomerization with Formation and Loss

In reality, the *trans*-DOCO and *cis*-DOCO species are continually being formed from the reaction OD+CO, isomerize on some timescale, and are lost due to reactions. A simple version of this model may be written

$$\frac{d}{dt}[trans] = r_{+t}[OD] - (r_{-t} + r_{tc})[trans] + r_{ct}[cis] \tag{A.16}$$

$$\frac{d}{dt}[cis] = r_{+c}[OD] - (r_{-c} + r_{ct})[cis] + r_{tc}[trans]. \tag{A.17}$$

At this point, we take the laplace transform of each equation. We now have

$$s\mathcal{L}[trans](s) = r_{+t}\mathcal{L}[OD](s) - (r_{-t} + r_{tc})\mathcal{L}[trans](s) + r_{ct}\mathcal{L}[cis](s) \tag{A.18}$$

$$s\mathcal{L}[cis](s) = r_{+c}\mathcal{L}[OD](s) - (r_{-c} + r_{ct})\mathcal{L}[cis](s) + r_{tc}\mathcal{L}[trans](s). \tag{A.19}$$

Solving for $\mathcal{L}[trans](s)$ and $\mathcal{L}[cis](s)$, we find

$$\mathcal{L}[trans](s) = \frac{r_{+c}r_{ct} + r_{+t}(r_{ct} - r_{lc} + s)}{(r_{ct} - r_{lc} + s)(-r_{lt} + r_{tc} + s) - r_{ct}r_{tc}} \times \mathcal{L}[OD](s) \tag{A.20}$$

$$\mathcal{L}[cis](s) = \frac{r_{+t}r_{tc} + r_{+c}(r_{tc} - r_{lt} + s)}{(r_{ct} - r_{lc} + s)(-r_{lt} + r_{tc} + s) - r_{ct}r_{tc}} \times \mathcal{L}[OD](s), \tag{A.21}$$

which in the time domain is

$$[trans](t) = \frac{1}{2}\left([r_A + \frac{a_A}{r_s}]e^{-(r_t+r_s)/2t} + [r_A - \frac{a_A}{r_s}]e^{-(r_t-r_s)/2t}\right) * [OD](t) \tag{A.22}$$

$$[cis](t) = \frac{1}{2}\left([r_B + \frac{a_B}{r_s}]e^{-(r_t+r_s)/2t} + [r_B - \frac{a_B}{r_s}]e^{-(r_t-r_s)/2t}\right) * [OD](t). \tag{A.23}$$

We now find ourselves interested in the long-timescale dynamics of the above equations. Specifically, we would like to compare with the simple *trans*⇌ *cis* isomerization case. Since the longest timescale

components will occur for $s \to 0$, we can solve for $([trans](t) - [cis](t))/([trans](t) + [cis](t))$ when $t \to \infty$

$$\frac{[trans](t) - [cis](t)}{[trans](t) + [cis](t)}(t \to \infty) = \left(\frac{R(r_t + r_c)}{R(r_t + r_c) + r_t l_c + r_c l_t}\right)\frac{K_{A/B} - 1}{K_{A/B} + 1} + \frac{r_t l_c - r_c l_t}{R(r_t + r_c) + r_t l_c + r_c l_t}, \tag{A.24}$$

which reduces to the long-timescale value of Eq. A.15 when $l_t, l_t \to 0$.

Appendix B

Frequency comb locking notes

This section is primarily meant to be a technical reference for those in our lab wishing to fully lock all parameters of the OPO frequency comb. In the first section, I will briefly discuss locking f_{rep}, which is the least challenging lock, followed by the stabilization of the f_0 of the idler.

B.1 Stabilization of the Repetition Rate

Since many harmonics of the repetition rate are present in the frequency comb's photocurrent signal, one of these harmonics may be used to stabilize the comb, achieving a tighter lock. In our case, we use the 8^{th} harmonic of f_{rep} at $\sim 1092\,\text{MHz}$. This signal is mixed-down with a 1 GHz stable rf source to 92 MHz and sent to one port of a phase-detector. A Discrete Digital Synthesizer (DDS, AD9913 from Analog Devices), clocked to a stable 10 MHz source, provides a 92 MHz reference signal to the other port of the phase-detector. The output of the phase-detector is then low-passed and fed back to the slow f_{rep} actuator (stretcher piezo in the oscillator) to close the loop. This loop can be very slow, operating with ~10s of Hz servo bandwidth, compensating for the drift of the Yb oscillator while relying on its inherent stability at higher frequencies. Moreover, the resolution and phase-continuity of the DDS chip allows for smooth tuning of the repetition rate by ramping the DDS output frequency to the desired value.

B.2 Locking the Carrier Envelope Offset Frequency

The error signal for locking the idler's carrier-envelope-offset frequency, $f_{0,i}$, was generated by heterodyne beating the $p+i$ summing signal (810 nm) from the OPO with the pump supercontinuum (SC, spectrum shown in Fig. B.1). The pump input to the SC fiber (NL-1050-ZERO-2) was 650 mW. With an 810 nm bandpass filter in front of the detector, the repetition rate peak (136 MHz) signal-to-noise was

- SC pump only. -14.7 dBm (300 kHz RBW).
- $p + i$ beam only: -31.0 dBm (300 kHz RBW).
- Both arms: -13 dBm (300 kHz RBW).

This yielded a $(p+i)-p$ beatnote of amplitude -35 dBm (300 kHz RBW). From the repetition-rate-only values, we would expect a beat note of amplitude $1/2\,[(-15\text{ dBm}) + (-31\text{ dBm})] = -23$ dBm. It is likely that the poor spatial quality of the parasitic $p+i$ beam is causing this reduction in signal. Nonetheless, it was possible to feed this signal (through a phase detector) back to the fast and slow piezo actuators in the OPO, resulting in the in-loop error signal shown in Fig. B.2.

B.3 The Fiber Bragg Grating

The effect of the fiber bragg grating (FBG) inside the oscillator is to change both f_{rep} and f_0, since it changes both the group delay and the group delay dispersion. By tuning the temperature of our FBG (total length 5 cm), the f_{rep} and f_0 change by 6.3 Hz/°C and 12.2 MHz/°C, respectively. This can be used as a slow servo for either f_{rep} or f_0 with large dynamic range.

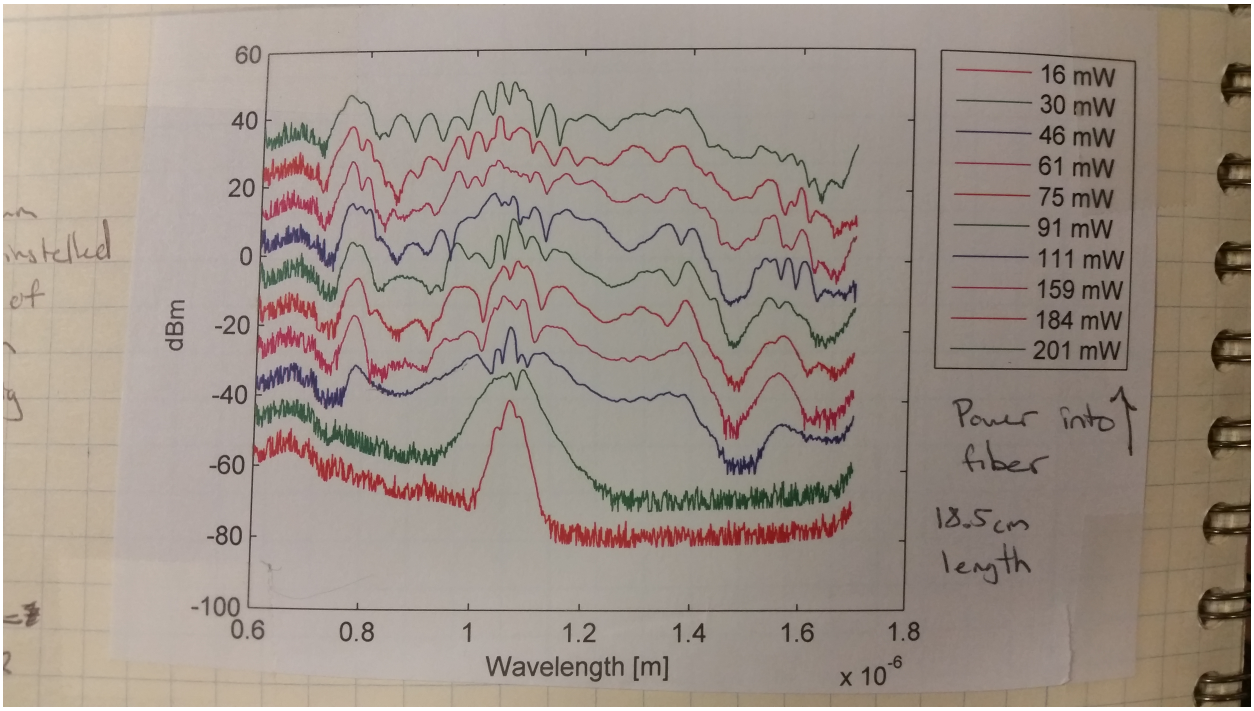

Figure B.1: Supercontinuum Fiber Spectrum.

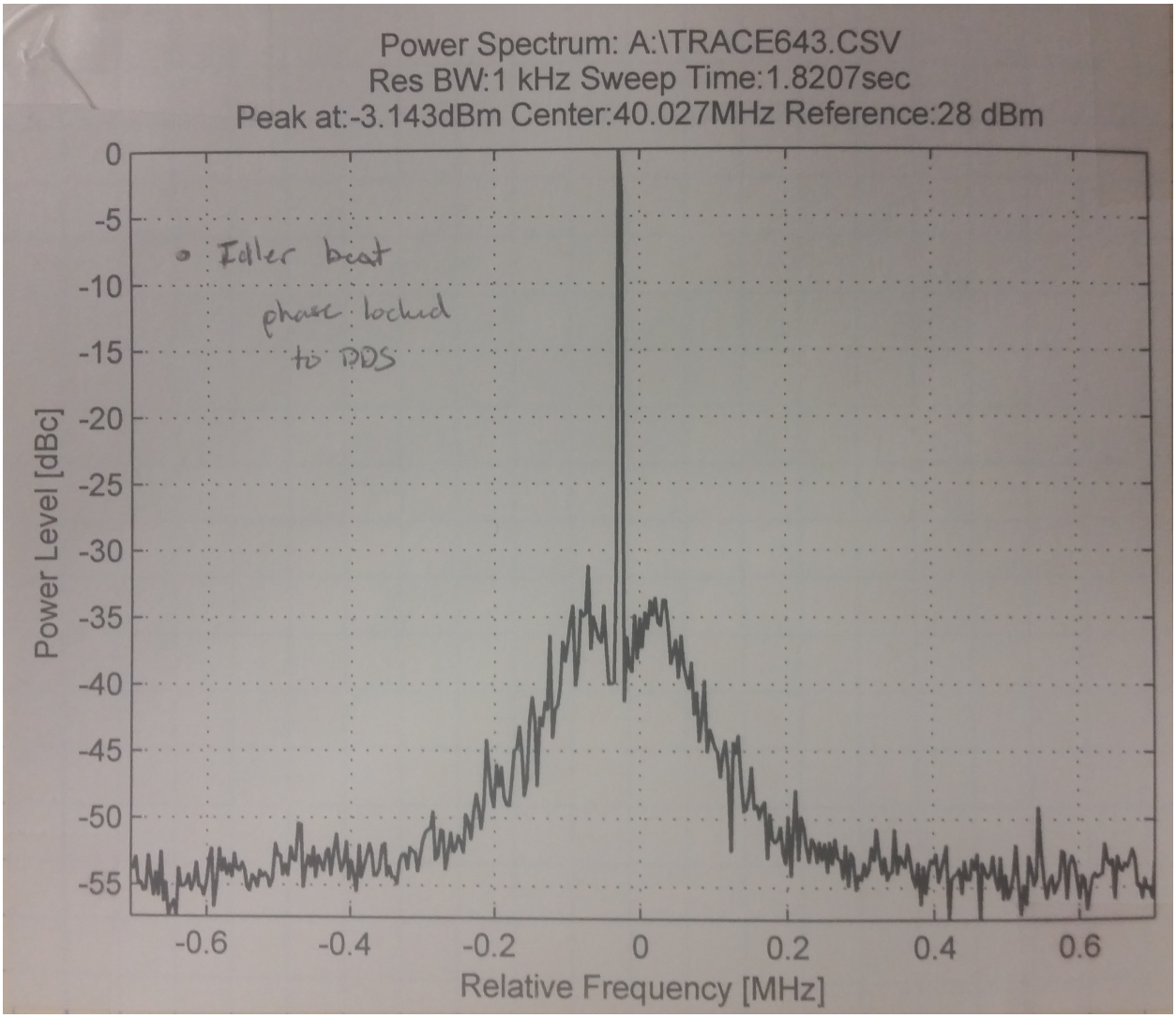

Figure B.2: In-loop error signal from $p + i$ beat with pump supercontinuum.

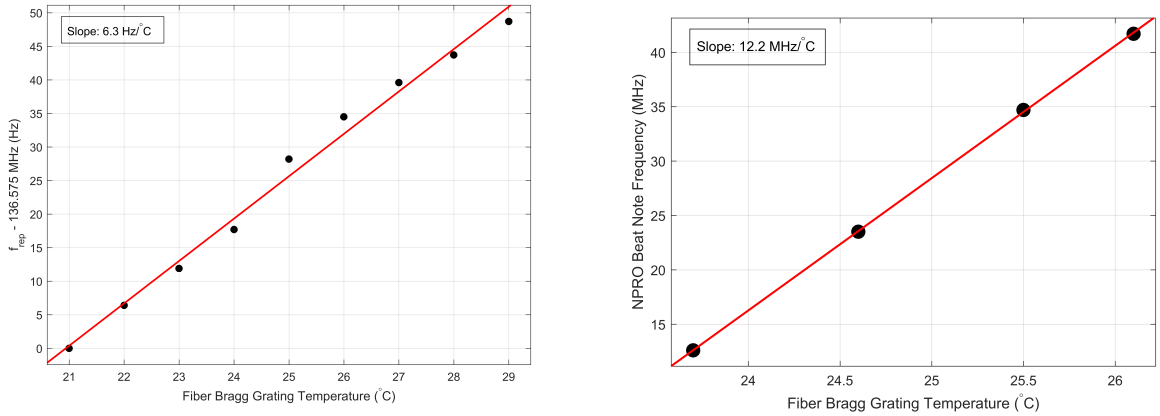

Figure B.3: Response of f_{rep} (left) and f_0 (right) to fiber bragg grating temperature. The data on the right was measured by locking f_{rep} and beating the Yb oscillator with a stable cw laser at 1064 nm.

Appendix C

MATLAB Code

C.1 VIPA Fringe Collection

```
% Uses one variable:
%     fringeImage - the image from which to collect the fringes.

% Bad Pixel Locations
badPixelKernel = [1 1 1; 1 0 1; 1 1 1]/8;
fringeImageConv = fringeImage;
fringeImageConv(isnan(fringeImageConv)) = 0;
badPixelReplace = conv2(fringeImageConv,badPixelKernel,'same');
fringeImage(isnan(fringeImage)) = badPixelReplace(isnan(fringeImage));
fringeImage = fringeImage';
figure;imagesc(fringeImage');

% Identify the zero crossings of the image
windowSize = 30;
fringeImageBase = filter(ones(1,windowSize)/windowSize,1,...
                                                    fringeImage,[],1);
```

```
fringeImageNorm = fringeImage - fringeImageBase;

fringeImageNorm1 = fringeImageNorm(1:end-1,:);
fringeImageNorm2 = fringeImageNorm(2:end,:);
idx = find(sign(fringeImageNorm1)-sign(fringeImageNorm2));
[idxX,idxY] = ind2sub(size(fringeImageNorm1),idx);
isPeak = (-sign(fringeImageNorm1(idx(1:end-1)))+1)/2;
m = (fringeImageNorm2(idx)-fringeImageNorm1(idx));
b = fringeImageNorm1(idx)-m.*idxX;
idxX = -b./m;

% Identify the peaks for each row of the image
thePeaksAndValleysX = (idxX(1:end-1)+idxX(2:end))/2;
thePeaksAndValleysY = idxY(1:end-1);
deltaY = idxY(1:end-1)-idxY(2:end);
thePeaksX = thePeaksAndValleysX((isPeak == 1) & (deltaY == 0));
thePeaksY = thePeaksAndValleysY((isPeak == 1) & (deltaY == 0));

% Group the rows (and sort them)
[uniqueRows,ia,ic] = unique(thePeaksY);

% Iterate over the uniqe rows, selecting peaks and adding them to
% a fringe
fringesX = {};
fringesY = {};
for i = 1:length(uniqueRows)
```

```
        idx = find(thePeaksY == uniqueRows(i));
        for j = 1:length(idx)
                if i == 1
                    fringesX{i,j} = thePeaksX(idx(j));
                    fringesY{i,j} = thePeaksY(idx(j));
                else
                        fringeMatchIdx = [];
                        for k = 1:size(fringesX,2)
                                if ~isempty(fringesX{i-1,k}) & ...
                        (abs(fringesX{i-1,k} - thePeaksX(idx(j))) < 1)
                                        fringeMatchIdx = k;
                                        break;
                                end
                        end

                    if isempty(fringeMatchIdx)
                        fringesX{i,end+1} = thePeaksX(idx(j));
                        fringesY{i,end+1} = thePeaksY(idx(j));
                    else
                        fringesX{i,fringeMatchIdx} = thePeaksX(idx(j));
                        fringesY{i,fringeMatchIdx} = thePeaksY(idx(j));
                    end

                end
        end
end
%figure;imagesc(fringeImageNorm');hold on;
```

```
%scatter([fringesX{:}],[fringesY{:}],'.k');

% Save the fringes to be used laser
for i = 1:numel(fringesX);
    if isempty(fringesX{i})
            fringesX{i} = NaN;
    end
    if isempty(fringesY{i})
            fringesY{i} = NaN;
    end
end
fringesXmat = cell2mat(fringesX);
fringesYmat = cell2mat(fringesY);

% Get the minimum x element from each fringe
fringesStartX = min(fringesXmat,[],1);
[~,idx] = sort(fringesStartX);

% Sort the fringes by fringesStartX
fringesXmatSorted = fringesXmat(:,idx);
fringesYmatSorted = fringesYmat(:,idx);

% Remove fringes that do not cover at least half of the screen and
% that do not have at least 100 points
croppedFringesX = [];
croppedFringesY = [];
fringeHighThresh = 0*size(fringeImage',1);
```

```
fringeLowThresh = 1*size(fringeImage',1);
for i = 1:size(fringesXmatSorted,2)
    if sum(~isnan(fringesXmatSorted(:,i))) > 50 && ...
                    max(fringesYmatSorted(:,i)) > fringeHighThresh && ...
                    min(fringesYmatSorted(:,i)) < fringeLowThresh
            croppedFringesX(:,end+1) = fringesXmatSorted(:,i);
            croppedFringesY(:,end+1) = fringesYmatSorted(:,i);
    end
end

% Save the fringes to be used later
fringeX = newFringesX;
fringeY = newFringesY;
fringeImageSize = size(fringeImage');

% Plot the fringes for the user
figure;imagesc(fringeImageNorm');hold on;
fringesOddX = fringeX(:,1:2:end);
fringesOddY = fringeY(:,1:2:end);
fringesEvenX = fringesX(:,2:2:end);
fringesEvenY = fringesY(:,2:2:end);
scatter(fringesOddX(:),fringesOddY(:),'.k');
scatter(fringesEvenX(:),fringesEvenY(:),'.r');
```

Bibliography

[1] J. Troe. Theory of thermal unimolecular reactions at low pressures. II. Strong collision rate constants. Applications. *The Journal of Chemical Physics*, 66(11):4758–4775, 1977. doi:10.1063/1.433838.

[2] J. Troe. Theory of thermal unimolecular reactions at low pressures. i. solutions of the master equation. *J. Chem. Phys.*, 66(11):4745–4757, 1977. doi:10.1063/1.433837.

[3] J. Troe. Theory of thermal unimolecular reactions at high pressures. *The Journal of Chemical Physics*, 75(1):226–237, 1981. doi:10.1063/1.441829.

[4] J. Troe. Theory of Thermal Unimolecular Reactions in the Fall-off Range. I. Strong Collision Rate Constants. *Berichte der Bunsengesellschaft für physikalische Chemie*, 87(2):161–169, 1983. doi:10.1002/bbpc.19830870217.

[5] Gerald L Newton and Jamie R Milligan. Fluorescence detection of hydroxyl radicals. *Radiation Physics and Chemistry*, 75(4):473–478, 2006. doi:10.1016/j.radphyschem.2005.10.011.

[6] J. B. Burkholder. Chemical kinetics and photochemical data for use in atmospheric studies, evaluation no. 18. *JPL Publication 15-10*, 2015.

[7] Wolfgang Uhmann, Andreas Becker, Christoph Taran, and Friedrich Siebert. Time-Resolved FT-IR Absorption Spectroscopy Using a Step-Scan Interferometer. *Applied Spectroscopy*, 45 (3):390–397, March 1991. doi:10.1366/0003702914337128.

[8] Yu-Te Su, Yu-Hsuan Huang, Henryk A Witek, and Yuan-Pern Lee. Infrared absorption

spectrum of the simplest criegee intermediate ch2oo. *Science*, 340(6129):174–176, 2013. doi:10.1126/science.1234369.

[9] Steven S. Brown, A. R. Ravishankara, and Harald Stark. Simultaneous Kinetics and Ringdown: Rate Coefficients from Single Cavity Loss Temporal Profiles. *The Journal of Physical Chemistry A*, 104(30):7044–7052, August 2000. ISSN 1089-5639. doi:10.1021/jp0013715.

[10] Adam J Fleisher, Bryce J Bjork, Thinh Q Bui, Kevin C. Cossel, Mitchio Okumura, and Jun Ye. Mid-infrared time-resolved frequency comb spectroscopy of transient free radicals. *J. Phys. Chem.*, 5(13):2241–2246, 2014. doi:10.1021/jz5008559.

[11] Aleksandra Foltynowicz, Ticijana Ban, Piotr Mas\lowski, Florian Adler, and Jun Ye. Quantum-noise-limited optical frequency comb spectroscopy. *Physical review letters*, 107(23): 233002, 2011. doi:10.1103/physrevlett.107.233002.

[12] Scott A Diddams, Leo Hollberg, and Vela Mbele. Molecular fingerprinting with the resolved modes of a femtosecond laser frequency comb. *Nature*, 445(7128):627–630, February 2007. ISSN 1476-4687. doi:10.1038/nature05524.

[13] Birgitta Bernhardt, Akira Ozawa, Patrick Jacquet, Marion Jacquey, Yohei Kobayashi, Thomas Udem, Ronald Holzwarth, Guy Guelachvili, Theodor W. Hänsch, and Nathalie Picqué. Cavity-enhanced dual-comb spectroscopy. *Nature Photonics*, 4(1):55–57, 2010. doi:10.1038/nphoton.2009.217.

[14] Patrick Jacquet, Julien Mandon, Birgitta Bernhardt, Ronald Holzwarth, Guy Guelachvili, Theodor W Hänsch, and Nathalie Picqué. Frequency comb fourier transform spectroscopy with khz optical resolution. In *Fourier Transform Spectroscopy*, page FMB2. Optical Society of America, 2009. doi:10.1364/FTS.2009.FMB2.

[15] MJ Thorpe, KD Moll, RJ Jones, B Safdi, and J Ye. Broadband cavity ringdown spectroscopy for sensitive and rapid molecular detection. *Science*, 311(March):1595–1599, 2006. doi:10.1126/science.1123921.

[16] John L. Hall. Nobel Lecture: Defining and measuring optical frequencies. *Reviews of Modern Physics*, 78(4):1279, 2006. doi:10.1103/RevModPhys.78.1279.

[17] Theodor W. Hänsch. Nobel Lecture: Passion for precision. *Reviews of Modern Physics*, 78 (4):1297–1309, November 2006. doi:10.1103/RevModPhys.78.1297.

[18] Steven T Cundiff and Jun Ye. Colloquium: Femtosecond optical frequency combs. *Reviews of Modern Physics*, 75(1):325, March 2003. doi:10.1103/revmodphys.75.325.

[19] S A Diddams. The evolving optical frequency comb. *JOSA B*, 27(11):B51–B62, November 2010. ISSN 1520-8540. doi:10.1364/JOSAB.27.000B51.

[20] Nathan R. Newbury. Searching for applications with a fine-tooth comb. *Nature Photonics*, 5 (4):186–188, April 2011. ISSN 1749-4885. doi:10.1038/nphoton.2011.38.

[21] Michael J Thorpe. *Cavity-Enhanced Direct Frequency Comb Spectroscopy*. PhD thesis, 2009.

[22] Kevin C Cossel. *Techniques in Molecular Spectroscopy: From Broad Bandwidth to High Resolution*. PhD thesis, 2014.

[23] Matt Stowe. *High-Resolution Coherent Control*. PhD thesis, University of Colorado, Boulder, 2008.

[24] Craig Benko. *Extreme Ultraviolet Frequency Combs for Precision Measurement and Strong-Field Physics*. PhD thesis, University of Colorado, 2016.

[25] Jun Ye. *Femtosecond Optical Frequency Comb: Principle, Operation and Applications*. Springer Science & Business Media, 2005. doi:10.1007/b102450.

[26] Steven T Cundiff, Jun Ye, and John L Hall. Optical frequency synthesis based on mode-locked lasers. *Review of Scientific Instruments*, 72(10):3749–3771, 2001. doi:10.1063/1.1400144.

[27] J. P Booth, G Cunge, L Biennier, D Romanini, and A Kachanov. Ultraviolet cavity ring-down spectroscopy of free radicals in etching plasmas. *Chemical Physics Letters*, 317(6):631–636, February 2000. ISSN 0009-2614. doi:10.1016/S0009-2614(99)01424-4.

[28] Susan Y. Lehman, Kris A. Bertness, and Joseph T. Hodges. Detection of trace water in phosphine with cavity ring-down spectroscopy. *Journal of Crystal Growth*, 250(1–2):262–268, March 2003. ISSN 0022-0248. doi:10.1016/S0022-0248(02)02248-0.

[29] Hans H. Funke, Brad L. Grissom, Clark E. McGrew, and Mark W. Raynor. Techniques for the measurement of trace moisture in high-purity electronic specialty gases. *Review of Scientific Instruments*, 74(9):3909–3933, August 2003. ISSN 0034-6748. doi:10.1063/1.1597939.

[30] M. W. Todd, R. A. Provencal, T. G. Owano, B. A. Paldus, A. Kachanov, K. L. Vodopyanov, M. Hunter, S. L. Coy, J. I. Steinfeld, and J. T. Arnold. Application of mid-infrared cavity-ringdown spectroscopy to trace explosives vapor detection using a broadly tunable (6–8 μm) optical parametric oscillator. *Applied Physics B*, 75(2-3):367–376, September 2002. ISSN 0946-2171, 1432-0649. doi:10.1007/s00340-002-0991-8.

[31] C. K. N. Patel. Laser photoacoustic spectroscopy helps fight terrorism: High sensitivity detection of chemical Warfare Agent and explosives. *The European Physical Journal Special Topics*, 153(1):1–18, January 2008. ISSN 1951-6355, 1951-6401. doi:10.1140/epjst/e2008-00383-x.

[32] Claire S. Patterson, Lesley C. McMillan, Christopher Longbottom, Graham M. Gibson, Miles J. Padgett, and Kenneth D. Skeldon. Portable optical spectroscopy for accurate analysis of ethane in exhaled breath. *Measurement Science and Technology*, 18(5):1459, 2007. ISSN 0957-0233. doi:10.1088/0957-0233/18/5/035.

[33] T. H. Risby and S. F. Solga. Current status of clinical breath analysis. *Applied Physics B*, 85 (2-3):421–426, November 2006. ISSN 0946-2171, 1432-0649. doi:10.1007/s00340-006-2280-4.

[34] Chuji Wang and Peeyush Sahay. Breath Analysis Using Laser Spectroscopic Techniques: Breath Biomarkers, Spectral Fingerprints, and Detection Limits. *Sensors*, 9(10):8230–8262, October 2009. doi:10.3390/s91008230.

[35] Terence H. Risby and Frank K. Tittel. Current status of midinfrared quantum and interband

cascade lasers for clinical breath analysis. *Optical Engineering*, 49(11):111123–111123–14, 2010. ISSN 0091-3286. doi:10.1117/1.3498768.

[36] Scott Spuler, Mark Linne, Andy Sappey, and Stuart Snyder. Development of a cavity ringdown laser absorption spectrometer for detection of trace levels of mercury. *Applied Optics*, 39(15): 2480–2486, May 2000. ISSN 1539-4522. doi:10.1364/AO.39.002480.

[37] D. Richter, A. Fried, B. P. Wert, J. G. Walega, and F. K. Tittel. Development of a tunable mid-IR difference frequency laser source for highly sensitive airborne trace gas detection. *Applied Physics B*, 75(2-3):281–288, September 2002. ISSN 0946-2171, 1432-0649. doi:10.1007/s00340-002-0948-y.

[38] M. Bitter, S. M. Ball, I. M. Povey, and R. L. Jones. A broadband cavity ringdown spectrometer for in-situ measurements of atmospheric trace gases. *Atmos. Chem. Phys.*, 5(9):2547–2560, September 2005. ISSN 1680-7324. doi:10.5194/acp-5-2547-2005.

[39] A. Fried, G. Diskin, P. Weibring, D. Richter, J. G. Walega, G. Sachse, T. Slate, M. Rana, and J. Podolske. Tunable infrared laser instruments for airborne atmospheric studies. *Applied Physics B*, 92(3):409–417, September 2008. ISSN 0946-2171, 1432-0649. doi:10.1007/s00340-008-3136-x.

[40] I. Galli, S. Bartalini, S. Borri, P. Cancio, D. Mazzotti, P. De Natale, and G. Giusfredi. Molecular Gas Sensing Below Parts Per Trillion: Radiocarbon-Dioxide Optical Detection. *Physical Review Letters*, 107(27):270802, December 2011. doi:10.1103/PhysRevLett.107.270802.

[41] Hugo Wahlquist. Modulation broadening of unsaturated Lorentzian lines. *The Journal of Chemical Physics*, 35(5):1708–1710, 1961. doi:10.1063/1.1732133.

[42] Gary C. Bjorklund. Frequency-modulation spectroscopy: A new method for measuring weak absorptions and dispersions. *Optics Letters*, 5(1):15–17, January 1980. ISSN 1539-4794. doi:10.1364/OL.5.000015.

[43] Anthony O'Keefe and David AG Deacon. Cavity ring-down optical spectrometer for absorption measurements using pulsed laser sources. *Review of Scientific Instruments*, 59(12): 2544–2551, 1988. doi:10.1063/1.1139895.

[44] Jun Ye, Long-Sheng Ma, and John L. Hall. Ultrasensitive detections in atomic and molecular physics: Demonstration in molecular overtone spectroscopy. *JOSA B*, 15(1):6–15, January 1998. ISSN 1520-8540. doi:10.1364/JOSAB.15.000006.

[45] A. Foltynowicz, F. M. Schmidt, W. Ma, and O. Axner. Noise-immune cavity-enhanced optical heterodyne molecular spectroscopy: Current status and future potential. *Applied Physics B*, 92(3):313, September 2008. ISSN 0946-2171, 1432-0649. doi:10.1007/s00340-008-3126-z.

[46] A. Cygan, D. Lisak, S. Wójtewicz, J. Domysławska, J. T. Hodges, R. S. Trawiński, and R. Ciuryło. High-signal-to-noise-ratio laser technique for accurate measurements of spectral line parameters. *Physical Review A*, 85(2):022508, February 2012. doi:10.1103/PhysRevA.85.022508.

[47] D. K. Havey, D. A. Long, M. Okumura, C. E. Miller, and J. T. Hodges. Ultra-sensitive optical measurements of high-J transitions in the O2 A-band. *Chemical Physics Letters*, 483(1–3): 49–54, November 2009. ISSN 0009-2614. doi:10.1016/j.cplett.2009.10.067.

[48] Newport Web Site. `https://www.newport.com/f/infrared-elements`.

[49] C. M. Western. Pgopher, a program for simulating rotational, vibrational and electronic spectra. *Journal of Quantitative Spectroscopy and Radiative Transfer*, 186:221–242, 2016. doi:10.1016/j.jqsrt.2016.04.010.

[50] Peter Atkins and Julio De Paula. *Elements of Physical Chemistry*. Oxford University Press, 2017. ISBN 0198796706.

[51] Peter F. Bernath. *Spectra of Atoms and Molecules*. OXFORD UNIV PR, 2015. ISBN 0199382573.

[52] Wolfgang Demtröder. *Molecular Physics*. Wiley VCH Verlag GmbH, 2005. ISBN 3527405666.

[53] Ulrich Platt and Jochen Stutz. Differential Absorption Spectroscopy. In *Differential Optical Absorption Spectroscopy*, Physics of Earth and Space Environments, pages 135–174. Springer Berlin Heidelberg, 2008. ISBN 978-3-540-21193-8 978-3-540-75776-4. doi:10.1007/978-3-540-75776-4_6.

[54] G. B. Rieker, F. R. Giorgetta, W. C. Swann, J. Kofler, A. M. Zolot, L. C. Sinclair, E. Baumann, C. Cromer, G. Petron, C. Sweeney, P. P. Tans, I. Coddington, and N. R. Newbury. Frequency-comb-based remote sensing of greenhouse gases over kilometer air paths. *Optica*, 1(5):290–298, November 2014. ISSN 2334-2536. doi:10.1364/OPTICA.1.000290.

[55] John U. White. Long Optical Paths of Large Aperture. *JOSA*, 32(5):285–288, May 1942. doi:10.1364/JOSA.32.000285.

[56] Donald R. Herriott and Harry J. Schulte. Folded Optical Delay Lines. *Applied Optics*, 4(8): 883–889, August 1965. ISSN 1539-4522. doi:10.1364/AO.4.000883.

[57] Florian Adler, Michael J Thorpe, Kevin C Cossel, and Jun Ye. Cavity-enhanced direct frequency comb spectroscopy: Technology and applications. *Annual review of analytical chemistry (Palo Alto, Calif.)*, 3(1):175–205, January 2010. ISSN 1936-1335. doi:10.1146/annurev-anchem-060908-155248.

[58] Christina J. Hood, H. J. Kimble, and Jun Ye. Characterization of high-finesse mirrors: Loss, phase shifts, and mode structure in an optical cavity. *Physical Review A*, 64(3):033804, 2001. ISSN 1050-2947. doi:10.1103/PhysRevA.64.033804.

[59] Warren Nagourney. *Quantum Electronics for Atomic Physics and Telecommunication*. Oxford University Press, 2014. ISBN 0199665486.

[60] Katsuhiko Ogata. *Modern Control Engineering*. PRENTICE HALL, 2009. ISBN 0136156738.

[61] R. W. P. Drever, John L. Hall, F. V. Kowalski, J. Hough, G. M. Ford, A. J. Munley, and H. Ward. Laser phase and frequency stabilization using an optical resonator. *Applied Physics B*, 31(2):97–105, June 1983. ISSN 0946-2171, 1432-0649. doi:10.1007/bf00702605.

[62] Eric D. Black. An introduction to Pound–Drever–Hall laser frequency stabilization. *American Journal of Physics*, 69(1):79–87, December 2000. ISSN 0002-9505. doi:10.1119/1.1286663.

[63] T. W. Hansch and B. Couillaud. Laser frequency stabilization by polarization spectroscopy of a reflecting reference cavity. *Optics Communications*, 35(3):441–444, December 1980. ISSN 0030-4018. doi:10.1016/0030-4018(80)90069-3.

[64] R Jason Jones and Jun Ye. Femtosecond pulse amplification by coherent addition in a passive optical cavity. *Optics letters*, 27(20):1848–50, January 2002. ISSN 0146-9592. doi:10.1364/ol.27.001848.

[65] A. Foltynowicz, P. Maslowski, a. J. Fleisher, B. J. Bjork, and J. Ye. Cavity-enhanced optical frequency comb spectroscopy in the mid-infrared application to trace detection of hydrogen peroxide. *Applied Physics B*, 110(2):163–175, May 2013. ISSN 0946-2171. doi:10.1007/s00340-012-5024-7.

[66] Michael J. Thorpe and Jun Ye. Cavity-enhanced direct frequency comb spectroscopy. *Applied Physics B: Lasers and Optics*, 91(3):397–414, 2008. doi:10.1007/s00340-008-3019-1.

[67] Peter R. Griffiths and James A. De Haseth. *Fourier Transform Infrared Spectrometry*, volume 171. John Wiley & Sons, 2007. doi:10.1002/047010631x.

[68] Gregory Rieker, Fabrizio R. Giorgetta, William C. Swann, Ian Coddington, Laura C. Sinclair, Christopher L. Cromer, Esther Baumann, Adam Zolot, and Nathan R. Newbury. Open-Path Dual-Comb Spectroscopy of Greenhouse Gases. In *CLEO SI*, page CTh5C.9, 2013. ISBN 978-1-55752-972-5. doi:10.1364/CLEO_SI.2013.CTh5C.9.

[69] Ann Wang Dohlman, Hugh R. Black, and James A. Royall. Expired breath hydrogen peroxide

is a marker of acute airway inflammation in pediatric patients with asthma. *Am Rev Respir Dis*, 148(4 Pt 1):955–960, 1993. doi:10.1164/ajrccm/148.4_pt_1.955.

[70] Ildikó Horváth, Louise E Donnelly, András Kiss, Sergei A Kharitonov, Sam Lim, K Fan Chung, and Peter J Barnes. Combined use of exhaled hydrogen peroxide and nitric oxide in monitoring asthma. *American journal of respiratory and critical care medicine*, 158(4):1042–1046, 1998. doi:10.1164/ajrccm.158.4.9710091.

[71] Shamsah Kazani and Elliot Israel. Exhaled breath condensates in asthma: Diagnostic and therapeutic implications. *Journal of breath research*, 4(4):047001, 2010. doi:10.1088/1752-7155/4/4/047001.

[72] P. N. Dekhuijzen, K. K. Aben, Ingrid Dekker, L. P. Aarts, P. L. Wielders, C. L. Van Herwaarden, and AALT Bast. Increased exhalation of hydrogen peroxide in patients with stable and unstable chronic obstructive pulmonary disease. *American Journal of Respiratory and Critical Care Medicine*, 154(3):813–816, 1996. doi:10.1164/ajrccm.154.3.8810624.

[73] Stephen R. Baldwin, Cyril M. Grum, Laurence A. Boxer, Richard H. Simon, Loren H. Ketai, and Larry J. Devall. Oxidant activity in expired breath of patients with adult respiratory distress syndrome. *The Lancet*, 327(8471):11–14, 1986. ISSN 01406736. doi:10.1016/S0140-6736(86)91895-7.

[74] J. Iasha Sznajder, Ana Fraiman, Jesse B. Hall, William Sanders, Gregory Schmidt, Gregory Crawford, Avi Nahum, Phillip Factor, and Lawrence DH Wood. Increased hydrogen peroxide in the expired breath of patients with acute hypoxemic respiratory failure. *Chest*, 96(3): 606–612, 1989. doi:10.1378/chest.96.3.606.

[75] John E. Repine. Scientific perspectives on adult respiratory distress syndrome. *The Lancet*, 339(8791):466–469, 1992. doi:10.1016/0140-6736(92)91067-i.

[76] S Loukides, P Bakakos, and K Kostikas. Exhaled breath condensate: Hydrogen peroxide. *European Respiratory Monograph*, 49, 2010. doi:10.1183/1025448x.00019009.

[77] Wim B. Gerritsen, Pieter Zanen, Anja A. Bauwens, Jules M. van den Bosch, and Fred J. Haas. Validation of a new method to measure hydrogen peroxide in exhaled breath condensate. *Respiratory medicine*, 99(9):1132–1137, 2005. doi:10.1016/j.rmed.2005.02.020.

[78] Laurence S. Rothman, Iouli E. Gordon, Alain Barbe, D. Chris Benner, Peter F. Bernath, Manfred Birk, Vincent Boudon, Linda R. Brown, Alain Campargue, J.-P. Champion, and others. The HITRAN 2008 molecular spectroscopic database. *Journal of Quantitative Spectroscopy and Radiative Transfer*, 110(9):533–572, 2009. doi:10.1016/j.jqsrt.2009.02.013.

[79] Timothy J. Johnson, Robert L. Sams, Sarah D. Burton, and Thomas A. Blake. Absolute integrated intensities of vapor-phase hydrogen peroxide (H2O2) in the mid-infrared at atmospheric pressure. *Analytical and bioanalytical chemistry*, 395(2):377–386, 2009. doi:10.1007/s00216-009-2805-x.

[80] Steven W. Sharpe, Timothy J. Johnson, Robert L. Sams, Pamela M. Chu, George C. Rhoderick, and Patricia A. Johnson. Gas-phase databases for quantitative infrared spectroscopy. *Applied spectroscopy*, 58(12):1452–1461, 2004. doi:10.1366/0003702042641281.

[81] R. L. Redington, W. B. Olson, and P. C. Cross. Studies of Hydrogen Peroxide: The Infrared Spectrum and the Internal Rotation Problem. *The Journal of Chemical Physics*, 36(5):1311–1326, March 1962. ISSN 0021-9606. doi:10.1063/1.1732733.

[82] E. R. Crosson. A cavity ring-down analyzer for measuring atmospheric levels of methane, carbon dioxide, and water vapor. *Applied Physics B*, 92(3):403–408, September 2008. ISSN 0946-2171, 1432-0649. doi:10.1007/s00340-008-3135-y.

[83] Norbert F. Scherer, Lutfur R. Khundkar, Richard B. Bernstein, and Ahmed H. Zewail. Real-time picosecond clocking of the collision complex in a bimolecular reaction: The birth of oh from h+co_2. *The Journal of Chemical Physics*, 87(2):1451, 1987. ISSN 00219606. doi:10.1063/1.453280.

[84] T. Yu and M. C. Lin. Kinetics of phenyl radical reactions studied by the cavity-ring-down

method. *Journal of the American Chemical Society*, 115(10):4371–4372, May 1993. ISSN 0002-7863. doi:10.1021/ja00063a069.

[85] Ben Spaun, P. Bryan Changala, David Patterson, Bryce J. Bjork, Oliver H. Heckl, John M. Doyle, and Jun Ye. Continuous probing of cold complex molecules with infrared frequency comb spectroscopy. *Nature*, 533(7604):517–520, May 2016. ISSN 0028-0836. doi:10.1038/nature17440.

[86] I. Hartl, T. R. Schibli, A. Marcinkevicius, D. C. Yost, D. D. Hudson, M. E. Fermann, and Jun Ye. Cavity-enhanced similariton yb-fiber laser frequency comb: 3×10^{14} w/cm^2 peak intensity at 136 mhz. *Optics letters*, 32(19):2870–2872, 2007. doi:10.1364/OL.32.002870.

[87] T. R. Schibli, I. Hartl, D. C. Yost, M. J. Martin, a. Marcinkevičius, M. E. Fermann, and J. Ye. Optical frequency comb with submillihertz linewidth and more than 10 W average power. *Nature Photonics*, 2(6):355–359, May 2008. ISSN 1749-4885. doi:10.1038/nphoton.2008.79.

[88] Florian Adler, Kevin C. Cossel, Michael J. Thorpe, Ingmar Hartl, Martin E. Fermann, and Jun Ye. Phase-stabilized, 1.5 w frequency comb at 2.8-4.8 μm. *Optics letters*, 34(9):1330–1332, 2009. doi:10.1364/OL.34.001330.

[89] Bulent Oktem, Coşkun Ülgüdür, and F. Ö Ilday. Soliton–similariton fibre laser. *Nature Photonics*, 4(5):307–311, 2010. ISSN 1749-4885. doi:10.1038/nphoton.2010.33.

[90] Ingmar Hartl and Martin E. Fermann. Fiber frequency combs. volume 6453, pages 645313–645313–9, 2007. doi:10.1117/12.717322.

[91] Jocelyn Lauzon, Simon Thibault, Jean Martin, and François Ouellette. Implementation and characterization of fiber Bragg gratings linearly chirped by a temperature gradient. *Optics Letters*, 19(23):2027–2029, December 1994. ISSN 1539-4794. doi:10.1364/OL.19.002027.

[92] Andreas Othonos, Kyriacos Kalli, David Pureur, and Alain Mugnier. Fibre Bragg Gratings. In Dr Herbert Venghaus, editor, *Wavelength Filters in Fibre Optics*, number 123 in Springer

Series in Optical Sciences, pages 189–269. Springer Berlin Heidelberg, 2006. ISBN 978-3-540-31769-2 978-3-540-31770-8. doi:10.1007/3-540-31770-8_6.

[93] Gordon M. H. Flockhart, Robert R. J. Maier, James S. Barton, William N. MacPherson, Julian D. C. Jones, Karen E. Chisholm, Lin Zhang, Ian Bennion, Ian Read, and Peter D. Foote. Quadratic behavior of fiber Bragg grating temperature coefficients. *Applied Optics*, 43 (13):2744–2751, May 2004. ISSN 1539-4522. doi:10.1364/AO.43.002744.

[94] Lora Nugent-Glandorf, Tyler Neely, Florian Adler, Adam J. Fleisher, Kevin C. Cossel, Bryce Bjork, Tim Dinneen, Jun Ye, and Scott A. Diddams. Mid-infrared virtually imaged phased array spectrometer for rapid and broadband trace gas detection. *Optics Letters*, 37(15):3285–3287, August 2012. ISSN 1539-4794. doi:10.1364/OL.37.003285.

[95] Jeffrey T. Petty and C. Bradley Moore. Transient infrared absorption spectrum of the $n1$ fundamental of trans-DOCO. *The Journal of Chemical Physics*, 99(1):47, 1993. ISSN 00219606. doi:10.1063/1.465773.

[96] J.T. Petty and C.B. Moore. Transient Infrared Absorption Spectrum of the $n1$ Fundamental of trans-HOCO. *Journal of Molecular Spectroscopy*, 161(1):149–156, 1993. ISSN 00222852. doi:10.1006/jmsp.1993.1223.

[97] DC Kitchen, NR Forde, and LJ Butler. Photodissociation of acrylic acid at 193 nm. *The Journal of Physical Chemistry A*, 341(97):6603–6610, 1997. doi:10.1021/jp9700241.

[98] Anatoly Kulbida, Mozart N Ramos, Markku Rasanen, Janne Nieminen, Otto Schrems, and Rui Fausto. Rotational isomerism in acrylic acid. a combined matrix-isolated ir, raman and ab initio molecular orbital study. *Journal of the Chemical Society, Faraday Transactions*, 91 (11):1571–1585, 1995. doi:10.1039/ft9959101571.

[99] E. R. Alonso, L. Kolesniková, I. Peña, S. T. Shipman, B. Tercero, J. Cernicharo, and J. L. Alonso. Waveguide CP-FTMW and millimeter wave spectra of s-cis- and s-trans-

acrylic acid. *Journal of Molecular Spectroscopy*, 316:84–89, October 2015. ISSN 0022-2852. doi:10.1016/j.jms.2015.08.002.

[100] Hiroshi Morita, Kiyokazu Fuke, and Saburo Nagakura. Electronic Structure and Spectra of Acrylic Acid in the Vapor and Condensed Phases. *Bulletin of the Chemical Society of Japan*, 49(4):922–928, April 1976. ISSN 0009-2673. doi:10.1246/bcsj.49.922.

[101] A. Baldacci, S. Ghersetti, S. C. Hurlock, and K. Narahari Rao. Infrared bands of 12C2HD. *Journal of Molecular Spectroscopy*, 59(1):116–125, January 1976. ISSN 0022-2852. doi:10.1016/0022-2852(76)90047-3.

[102] Michael E. Harding, Thorsten Metzroth, Jürgen Gauss, and Alexander A. Auer. Parallel calculation of ccsd and ccsd(t) analytic first and second derivatives. *Journal of Chemical Theory and Computation*, 4(1):64–74, 2008. doi:10.1021/ct700152c.

[103] Jeffrey T. Petty, John a. Harrison, and C. Bradley Moore. Reactions of trans-HOCO Studied by Infrared Spectroscopy. *The Journal of Physical Chemistry*, 97(43):11194–11198, 1993. ISSN 0022-3654. doi:10.1021/j100145a013.

[104] Michael C. Osborne, Qiang Li, and Ian W. M. Smith. Products of the ultraviolet photodissociation of trifluoroacetic acid and acrylic acid. *Physical Chemistry Chemical Physics*, 1(7): 1447–1454, January 1999. ISSN 1463-9084. doi:10.1039/A809064E.

[105] J Lelieveld, T M Butler, J N Crowley, T J Dillon, H Fischer, L Ganzeveld, H Harder, M G Lawrence, M Martinez, D Taraborrelli, and J Williams. Atmospheric oxidation capacity sustained by a tropical forest. *Nature*, 452(7188):737–40, 2008. ISSN 1476-4687. doi:10.1038/nature06870.

[106] R. L. Mauldin III, T. Berndt, M. Sipilä, P. Paasonen, T. Petäjä, S. Kim, T. Kurtén, F. Stratmann, V.-M. Kerminen, and M. Kulmala. A new atmospherically relevant oxidant of sulphur dioxide. *Nature*, 488(7410):193–196, 2012. ISSN 0028-0836. doi:10.1038/nature11278.

[107] T. E. Graedel. *Chemical Compounds in the Atmosphere*. Academic Press, 1978. ISBN 0124311865.

[108] Anne M Thompson. The oxidizing capacity of the Earth's atmosphere: Probable past and future changes. *Science*, 256(5060):1157, 1992. doi:10.1126/science.256.5060.1157.

[109] M Karl, Th Brauers, H P Dorn, F Holland, M Komenda, D Poppe, F Rohrer, L Rupp, A Schaub, and A Wahner. Kinetic Study of the OH-isoprene and O3-isoprene reaction in the atmosphere simulation chamber, SAPHIR. *Geophys. Res. Lett.*, 31(5):L05117, 2004. ISSN 0094-8276. doi:10.1029/2003gl019189.

[110] Jiwen Fan and Renyi Zhang. Atmospheric Oxidation Mechanism of Isoprene. *Environmental Chemistry*, 1(3):140–149, December 2004. ISSN 1449-8979. doi:10.1071/EN04045.

[111] Daniel J. Jacob. *Introduction to Atmospheric Chemistry*. Princeton University Press, 1999. ISBN 0691001855.

[112] Shuping Li, Jamie Matthews, and Amitabha Sinha. Atmospheric Hydroxyl Radical Production from Electronically Excited NO2 and H2O. *Science*, 319(5870):1657–1660, 2008. ISSN 0036-8075. doi:10.1126/science.1151443.

[113] Paul O Wennberg and Donald Dabdub. Rethinking ozone production. *Science*, 319(5870): 1624–1625, 2008. doi:10.1126/science.1155747.

[114] E. J. K. Nilsson and A. A. Konnov. Role of HOCO Chemistry in Syngas Combustion. *Energy & Fuels*, 30(3):2443–2457, March 2016. ISSN 0887-0624. doi:10.1021/acs.energyfuels.5b02778.

[115] C. S. Boxe, J. S. Francisco, R. L. Shia, Y. L. Yung, H. Nair, M. C. Liang, and A. Saiz-Lopez. New insights into martian atmospheric chemistry. *Icarus*, 242:97–104, 2014. ISSN 10902643. doi:10.1016/j.icarus.2014.07.023.

[116] Ivan Kassal, James D Whitfield, Alejandro Perdomo-Ortiz, Man-Hong Yung, and Alán

Aspuru-Guzik. Simulating chemistry using quantum computers. *Annual review of physical chemistry*, 62:185–207, 2011. doi:10.1146/annurev-physchem-032210-103512.

[117] Wm E Wilson Jr. A Critical Review of the Gas-Phase Reaction Kinetics of the Hydroxyl Radical. *Journal of Physical and Chemical Reference Data*, 1(2):535–573, 1972. doi:10.1063/1.3253102.

[118] Ian W M Smith and Reinhard Zellner. Rate measurements of reactions of OH by resonance absorption. Part 2. – Reactions of OH with CO, C2H4 and C2H2. *Journal of the Chemical Society, Faraday Transactions 2: Molecular and Chemical Physics*, 69:1617–1627, 1973. ISSN 03009238. doi:10.1039/f29736901617.

[119] D. M. Golden, G. P. Smith, A. B. McEwen, C.-L. Yu, B. Eiteneer, M. Frenklach, G. L. Vaghjiani, A. R. Ravishankara, and F. P. Tully. OH (OD)+ CO: Measurements and an optimized RRKM fit. *The Journal of Physical Chemistry A*, 102(44):8598–8606, 1998. doi:10.1021/jp982110m.

[120] D. Fulle, H. F. Hamann, H. Hippler, and J. Troe. High pressure range of addition reactions of HO. II. Temperature and pressure dependence of the reaction HO+CO↔HOCO→H+CO2. *The Journal of Chemical Physics*, 105(3):983, 1996. ISSN 00219606. doi:10.1063/1.471991.

[121] David C McCabe, Tomasz Gierczak, Ranajit K Talukdar, and A R Ravishankara. Kinetics of the reaction OH+CO under atmospheric conditions. *Geophysical Research Letters*, 28(16): 3135–3138, 2001. doi:10.1029/2000gl012719.

[122] John R Barker and David M Golden. Master equation analysis of pressure-dependent atmospheric reactions. *Chemical reviews*, 103(12):4577–4592, 2003. doi:10.1021/cr020655d.

[123] Thanh Lam Nguyen, Bert C. Xue, Ralph E. Weston, John R. Barker, and John F. Stanton. Reaction of HO with CO: Tunneling is indeed important. *Journal of Physical Chemistry Letters*, 3:1549–1553, 2012. ISSN 19487185. doi:10.1021/jz300443a.

[124] Takahiro Oyama, Wataru Funato, Yoshihiro Sumiyoshi, and Yasuki Endo. Observation of the pure rotational spectra of trans- and cis-HOCO. *Journal of Chemical Physics*, 134(17), 2011. ISSN 00219606. doi:10.1063/1.3578179.

[125] Michael C. McCarthy, Oscar Martinez, Brett A. McGuire, Kyle N. Crabtree, Marie-Aline Martin-Drumel, and John F. Stanton. Isotopic studies of trans- and cis-HOCO using rotational spectroscopy: Formation, chemical bonding, and molecular structures. *The Journal of Chemical Physics*, 144(12):124304, March 2016. ISSN 0021-9606. doi:10.1063/1.4944070.

[126] N. F. Scherer, C. Sipes, R. B. Bernstein, and a. H. Zewail. Real-time clocking of bimolecular reactions: Application to H+CO2. *The Journal of Chemical Physics*, 92(9):5239, 1990. ISSN 00219606. doi:10.1063/1.458531.

[127] R. G. Gilbert, K. Luther, and J. Troe. Theory of thermal unimolecular reactions in the fall-off range. ii. weak collision rate constants. *Berichte der Bunsengesellschaft für physikalische Chemie*, 87(2):169–177, 1983. doi:10.1002/bbpc.19830870218.

[128] Fumiyoshi Tochikubo, Satoshi Uchida, and Tsuneo Watanabe. Study on decay characteristics of OH radical density in pulsed discharge in Ar/H2O. *Japanese journal of applied physics*, 43 (1R):315, 2004. doi:10.1143/jjap.43.315.

[129] L. S. Rothman, I. E. Gordon, Y. Babikov, A. Barbe, D. Chris Benner, P. F. Bernath, M. Birk, L. Bizzocchi, V. Boudon, L. R. Brown, A. Campargue, K. Chance, E. A. Cohen, L. H. Coudert, V. M. Devi, B. J. Drouin, A. Fayt, J. M. Flaud, R. R. Gamache, J. J. Harrison, J. M. Hartmann, C. Hill, J. T. Hodges, D. Jacquemart, A. Jolly, J. Lamouroux, R. J. Le Roy, G. Li, D. A. Long, O. M. Lyulin, C. J. Mackie, S. T. Massie, S. Mikhailenko, H. S. P. Müller, O. V. Naumenko, A. V. Nikitin, J. Orphal, V. Perevalov, A. Perrin, E. R. Polovtseva, C. Richard, M. A. H. Smith, E. Starikova, K. Sung, S. Tashkun, J. Tennyson, G. C. Toon, Vl. G. Tyuterev, and G. Wagner. The HITRAN2012 molecular spectroscopic database. *Journal of Quantitative Spectroscopy and Radiative Transfer*, 130:4–50, November 2013. ISSN 0022-4073. doi:10.1016/j.jqsrt.2013.07.002.

[130] R. E. Stevens, C. W. Hsiao, Linh Le, N. J. Curro, B. J. Monton, B. Y. Chang, C. Y. Kung, C. Kittrell, and J. L. Kinsey. A partial pressure monitor and controller for stable ozone flow from a silica gel trap. *Review of Scientific Instruments*, 69(6):2504–2509, 1998. ISSN 00346748. doi:10.1063/1.1148950.

[131] Kunihiko Koike, Masaharu Nifuku, Koichi Izumi, Sadaki Nakamura, Shuzo Fujiwara, and Sadashige Horiguchi. Explosion properties of highly concentrated ozone gas. In *Journal of Loss Prevention in the Process Industries*, volume 18, pages 465–468, 2005. doi:10.1016/j.jlp.2005.07.020.

[132] Mark C. Abrams, Sumner P. Davis, M. L. P. Rao, and R. Engleman. High-resolution Fourier transform spectroscopy of the vibration-rotation spectrum of the OD radical. *Journal of Molecular Spectroscopy*, 165(1):57–74, 1994. doi:10.1006/jmsp.1994.1110.

[133] David D. Nelson, Aram Schiffman, David J. Nesbitt, and David J. Yaron. Absolute infrared transition moments for open shell diatomics from J dependence of transition intensities: Application to OH. *The Journal of Chemical Physics*, 90(10):5443–5454, May 1989. ISSN 0021-9606. doi:10.1063/1.456450.

[134] David D. Nelson, Aram Schiffman, and David J. Nesbitt. The dipole moment function and vibrational transition intensities of OH. *The Journal of Chemical Physics*, 90(10):5455–5465, May 1989. ISSN 0021-9606. doi:10.1063/1.456451.

[135] David D. Nelson Jr, Aram Schiffman, and David J. Nesbitt. The dipole moment function and vibrational transition intensities of OH. *The Journal of Chemical Physics*, 90(10):5455–5465, 1989. doi:10.1063/1.456451.

[136] David D. Nelson Jr, Aram Schiffman, David J. Nesbitt, and David J. Yaron. Absolute infrared transition moments for open shell diatomics from J dependence of transition intensities: Application to OH. *The Journal of Chemical Physics*, 90(10):5443–5454, 1989. doi:10.1063/1.456450.

[137] Christopher J Johnson, Michael E Harding, Berwyck L J Poad, John F Stanton, and Robert E Continetti. Electron affinities, well depths, and vibrational spectroscopy of of cis- and trans-hoco. *J. A. Chem. Soc.*, 133(49):19606–19609, 2011. doi:10.1021/ja207724f.

[138] Mirjana Mladenovic. Rovibrational energies of the hydrocarboxyl radical from a rccsd (t) study. *The Journal of Physical Chemistry A*, 117(32):7224–7235, 2013. doi:10.1021/jp401151n.

[139] Xinchuan Huang, Ryan C. Fortenberry, Yimin Wang, Joseph S. Francisco, T. Daniel Crawford, Joel M. Bowman, and Timothy J. Lee. Dipole surface and infrared intensities for the cis - And trans -HOCO and DOCO radicals. *Journal of Physical Chemistry A*, 117(32):6932–6939, 2013. ISSN 10895639. doi:10.1021/jp3102546.

[140] Jun Wang, Jun Li, Jianyi Ma, and Hua Guo. Full-dimensional characterization of photoelectron spectra of hoco- and doco- and tunneling facilitated decay of hoco prepared by anion photodetachment. *The Journal of chemical physics*, 140(18):184314, 2014. doi:10.1063/1.4874975.

[141] B. J. Bjork, T. Q. Bui, O. H. Heckl, P. B. Changala, B. Spaun, P. Heu, D. Follman, C. Deutsch, G. D. Cole, M. Aspelmeyer, M. Okumura, and J. Ye. Direct frequency comb measurement of OD + CO $\rightarrow$ DOCO kinetics. *Science*, 354(6311):444–448, October 2016. ISSN 0036-8075, 1095-9203. doi:10.1126/science.aag1862.

[142] Ahren W. Jasper, Kenley M. Pelzer, James A. Miller, Eugene Kamarchik, Lawrence B. Harding, and Stephen J. Klippenstein. Predictive a priori pressure-dependent kinetics. *Science*, 346 (6214):1212–1215, December 2014. ISSN 0036-8075, 1095-9203. doi:10.1126/science.1260856.

[143] Joseph S. Francisco, James T. Muckerman, and Hua Gen Yu. HOCO radical chemistry. *Accounts of Chemical Research*, 43(12):1519–1526, 2010. ISSN 00014842. doi:10.1021/ar100087v.

[144] Christopher J Johnson, Rico Otto, and Robert E Continetti. Spectroscopy and dynamics of the HOCO radical: Insights into the OH + CO $\rightarrow$ H + CO2 reaction. *Physical chemistry chemical physics : PCCP*, 16(36):19091–105, 2014. ISSN 1463-9084. doi:10.1039/c4cp02593h.

[145] C. W. Larson, P. H. Stewart, and D. M. Golden. Pressure and temperature dependence of reactions proceeding via a bound complex. an approach for combustion and atmospheric chemistry modelers. application to ho + co → [hoco] → h + co_2. *International journal of chemical kinetics*, 20(1):27–40, 1988. doi:10.1002/kin.550200105.

[146] George Paraskevopoulos and Robert S. Irwin. The pressure dependence of the rate constant of the reaction of OH radicals with CO. *The Journal of chemical physics*, 80(1):259–266, 1984. doi:10.1016/0009-2614(82)83680-4.

[147] George Paraskevopoulos and Robert S. Irwin. The pressure dependence of the rate constant of the reaction of OD radicals with CO. *Chemical Physics Letters*, 93(2):138–143, 1982. doi:10.1016/0009-2614(82)83680-4.

[148] Michael J. Frost, Paul Sharkey, and Ian WM Smith. Energy and structure of the transition states in the reaction oh + co → h + co_2. *Faraday Discussions of the Chemical Society*, 91: 305–317, 1991. doi:10.1039/DC9919100305.

[149] Michael J. Frost, Paul Sharkey, and Ian WM Smith. Reaction between hydroxyl (deuteroxyl) radicals and carbon monoxide at temperatures down to 80 K: Experiment and theory. *The Journal of Physical Chemistry*, 97(47):12254–12259, 1993. doi:10.1021/j100149a027.

[150] John Brunning, D. Wyn Derbyshire, Ian WM Smith, and Martin D. Williams. Kinetics of OH (v= 0, 1) and OD (v= 0, 1) with CO and the mechanism of the OH+ CO reaction. *Journal of the Chemical Society, Faraday Transactions 2: Molecular and Chemical Physics*, 84(1):105–119, 1988. doi:10.1039/f29888400105.

[151] Ralph E. Weston Jr, Thanh Lam Nguyen, John F. Stanton, and John R. Barker. HO+ CO reaction rates and H/D kinetic isotope effects: Master equation models with ab initio SCTST rate constants. *The Journal of Physical Chemistry A*, 117(5):821–835, 2013. doi:10.1021/jp311928w.

[152] Wei-Chen Chen and R. A. Marcus. On the theory of the CO+ OH reaction, including

H and C kinetic isotope effects. *The Journal of chemical physics*, 123(9):094307, 2005. doi:10.1063/1.2031208.

[153] Chih Hsuan Chang, Grant T. Buckingham, and David J. Nesbitt. Sub-doppler spectroscopy of the trans -HOCO radical in the OH stretching mode. *Journal of Physical Chemistry A*, 117 (50):13255–13264, 2013. ISSN 10895639. doi:10.1021/jp403386d.

[154] Garrett D Cole, Wei Zhang, Bryce J Bjork, David Follman, Paula Heu, Christoph Deutsch, Lindsay Sonderhouse, John Robinson, Chris Franz, Alexei Alexandrovski, Mark Notcutt, Oliver H Heckl, Jun Ye, and Markus Aspelmeyer. High-performance near- and mid-infrared crystalline coatings. *Optica*, 3(6):647–656, 2016. ISSN 2334-2536. doi:10.1364/OPTICA.3.000647.

[155] J. C. Brock and R. T. Watson. Ozone photolysis: Determination of the O (3P) quantum yield at 266 nm. *Chemical Physics Letters*, 71(3):371–375, 1980. doi:10.1016/0009-2614(80)80185-0.

[156] J. E. Butler, R. Glen Macdonald, D. J. Donaldson, and J. J. Sloan. Vibrational excitation of oh($\chi^2\pi$) produced in the reaction of o(^{1}d) with h_2. *Chemical Physics Letters*, 95(3):183–188, 1983. doi:10.1016/0009-2614(83)87228-5.

[157] M. Brouard, D. W. Hughes, K. S. Kalogerakis, and J. P. Simons. The product rovibrational and spin-orbit state dependent dynamics of the complex reaction h+co_2→oh($^2\pi$;ν,n,ω,f)+co: Memories of a lifetime. *J. Chem. Phys.*, 112(10):4557–4571, 2000. doi:10.1063/1.481081.

[158] Nanase Kohno, Mari Izumi, Hiroshi Kohguchi, and Katsuyoshi Yamasaki. Acceleration of the Reaction OH+ CO→ H+ CO2 by Vibrational Excitation of OH. *The Journal of Physical Chemistry A*, 115(19):4867–4873, 2011. doi:10.1021/jp200220f.

[159] S. I. Ionov, G. A. Brucker, C. Jaques, L. Valachovic, and C. Wittig. Subpicosecond resolution studies of the h + co_2 → co + oh reaction photoinitiated in co_2 - hi complexes. *The Journal of chemical physics*, 99(9):6553–6561, 1993. doi:10.1063/1.465847.

[160] David C. Clary and George C. Schatz. Quantum and quasiclassical calculations on the OH + CO → CO2 + H reaction. *The Journal of chemical physics*, 99(6):4578–4589, 1993. doi:10.1063/1.466057.

[161] Marta I. Hernández and David C. Clary. A study of HOCO resonances in the OH + CO → co_2+H reaction. *The Journal of chemical physics*, 101(4):2779–2784, 1994. doi:10.1063/1.467593.

[162] Robert A. Toth. HDO and D_2O low pressure, long path spectra in the 600-3100 cm^{-1} region: Ii. D_2O line positions and strengths. *Journal of molecular spectroscopy*, 195(1):98–122, 1999. doi:10.1006/jmsp.1999.7815.

[163] A. A. Westenberg and W. E. Wilson. ESR Intensity Relations and Some Gas-Phase Chemical Kinetics of the OD Radical. *The Journal of Chemical Physics*, 45(1):338–342, 1966. doi:10.1063/1.1727330.

[164] Robert A. Toth. Air-and N2-broadening parameters of HDO and D2O, 709 to 1936 cm^{-1}. *Journal of molecular spectroscopy*, 198(2):358–370, 1999. doi:10.1006/jmsp.1999.7966.

[165] J. E. Butler, G. M. Jursich, I. A. Watson, and J. R. Wiesenfeld. Reaction dynamics of o(^{1}d$_2$)+h_2, hd, d_2: Oh, od($\chi^2\pi_i$) product internal energy distributions. *J. Chem. Phys.*, 84 (10):5365–5377, 1986. doi:10.1063/1.449947.

[166] G. E. Streit and H. S. Johnston. Reactions and quenching of vibrationally excited hydroxyl radicals. *The Journal of Chemical Physics*, 64(1):95–103, 1976. doi:10.1063/1.431917.

[167] Beatriz M. Toselli, Jerrell D. Brenner, Murthy L. Yerram, William E. Chin, Keith D. King, and John R. Barker. Vibrational relaxation of highly excited toluene. *The Journal of Chemical Physics*, 95(1):176–188, July 1991. ISSN 0021-9606. doi:10.1063/1.461473.

[168] James C. Ianni. Kintecus, windows version 6.01, 2017. URL `http://www.kintecus.com`.

[169] A. R. Ravishankara, E. J. Dunlea, M. A. Blitz, T. J. Dillon, D. E. Heard, M. J. Pilling, R. S. Strekowski, J. M. Nicovich, and P. H. Wine. Redetermination of the rate coefficient for the reaction of O (1D) with N2. *Geophysical research letters*, 29(15), 2002. doi:10.1029/2001gl014850.

[170] J. A. Davidson, H. I. Schiff, Terry J. Brown, and Carleton J. Howard. Temperature dependence of the deactivation of O(1D) by CO from 113–333 K. *The Journal of Chemical Physics*, 69 (3):1216–1217, August 1978. ISSN 0021-9606. doi:10.1063/1.436657.

[171] Mark A. Blitz, Terry J. Dillon, Dwayne E. Heard, Michael J. Pilling, and Ian D. Trought. Laser induced fluorescence studies of the reactions of o(^{1}d$_2$) with n$_2$, o$_2$, n$_2$o, ch$_4$, h$_2$, co$_2$, ar, kr and *n*-c$_4$h$_{10}$. *Physical Chemistry Chemical Physics*, 6(9):2162–2171, 2004. doi:10.1039/B400283K.

[172] Ranajit K. Talukdar and A. R. Ravishankara. Rate coefficients for O(^{1}D) + H_2, D_2, HD reactions and H atom yield in O(^{1}D) + HD reaction. *Chemical Physics Letters*, 253(1):177–183, April 1996. ISSN 0009-2614. doi:10.1016/0009-2614(96)00203-5.

[173] Li-Ping Ju, Ke-Li Han, and António JC Varandas. Variational transition-state theory study of the atmospheric reaction OH+ O_3→ HO_2+ O_2. *International Journal of Chemical Kinetics*, 39(3):148–153, 2007. doi:10.1002/kin.20226.

[174] Ranajit K. Talukdar, Tomasz Gierczak, Leah Goldfarb, Yinon Rudich, BS Madhava Rao, and A. R. Ravishankara. Kinetics of hydroxyl radical reactions with isotopically labeled hydrogen. *The Journal of Physical Chemistry*, 100(8):3037–3043, 1996. doi:10.1021/jp9518724.

[175] Y. Bedjanian, G. Le Bras, and G. Poulet. Kinetic study of OH+ OH and OD+ OD reactions. *The Journal of Physical Chemistry A*, 103(35):7017–7025, 1999. doi:10.1021/jp991146r.

[176] Yuri Bedjanian, Veronique Riffault, Georges Le Bras, and Gilles Poulet. Kinetics and Mechanism of the OH and OD Reactions with BrO. *The Journal of Physical Chemistry A*, 105(25): 6154–6166, 2001. doi:10.1021/jp010369q.

[177] Ghanshyam L. Vaghjiani, A. R. Ravishankara, and N. Cohen. Reactions of hydroxyl and hydroxyl-D with hydrogen peroxide and hydrogen peroxide-D2. *The Journal of Physical Chemistry*, 93(23):7833–7837, 1989. doi:10.1021/j100360a021.

[178] D. M. Golden, G. P. Smith, a. B. McEwen, C.-L. Yu, B. Eiteneer, M. Frenklach, G. L. Vaghjiani, a. R. Ravishankara, and F. P. Tully. OH(OD) + CO: Measurements and an Optimized RRKM Fit. *J. Phys. Chem. A*, 102(44):8598–8606, 1998. ISSN 1089-5639. doi:10.1021/jp982110m.

[179] Hua-Gen Yu and Joseph S. Francisco. Energetics and kinetics of the reaction of HOCO with hydrogen atoms. *The Journal of chemical physics*, 128(24):244315, 2008. doi:10.1063/1.2946696.

[180] Hua Gen Yu, James T. Muckerman, and Joseph S. Francisco. Direct ab initio dynamics study of the OH + HOCO reaction. *Journal of Physical Chemistry A*, 109(23):5230–5236, 2005. ISSN 10895639. doi:10.1021/jp051458w.

[181] Hua-Gen Yu, James T. Muckerman, and Joseph S. Francisco. Quantum force molecular dynamics study of the reaction of O atoms with HOCO. *The Journal of chemical physics*, 127 (9):094302, 2007. doi:10.1063/1.2770463.

[182] Thinh Q. Bui, Bryce J. Bjork, P. Bryan Changala, Oliver H. Heckl, Ben Spaun, and Jun Ye. OD + CO $\rightarrow$ D + CO_2 branching kinetics probed with time-resolved frequency comb spectroscopy. *arXiv preprint arXiv:1701.00832*, 2017. doi:10.1016/j.cplett.2017.04.061.

[183] Oliver Welz, John D Savee, David L Osborn, Subith S Vasu, Carl J Percival, Dudley E Shallcross, and Craig A Taatjes. Direct kinetic measurements of criegee intermediate (ch2oo) formed by reaction of ch2i with o2. *Science*, 335(6065):204–207, 2012. doi:10.1126/science.1213229.

[184] Benjamin K. Stuhl, Matthew T. Hummon, Mark Yeo, Goulven Quéméner, John L. Bohn, and Jun Ye. Evaporative cooling of the dipolar hydroxyl radical. *Nature*, 492(7429):396–400, December 2012. ISSN 0028-0836. doi:10.1038/nature11718.

[185] Oliver H. Heckl, Bryce J. Bjork, Georg Winkler, P. Bryan Changala, Ben Spaun, Gil Porat, Thinh Q. Bui, Kevin F. Lee, Jie Jiang, Martin E. Fermann, and others. Three-photon absorption in optical parametric oscillators based on OP-GaAs. *Optics Letters*, 41(22):5405–5408, 2016. doi:10.1364/ol.41.005405.